Exploring Solid State NMR Spectroscopy As A Tool To Study F-Actin And Its Complexes

Pace, Nicola

Awarding institution:
King's College London

Exploring Solid State NMR Spectroscopy

As A Tool To Study F-Actin And Its Complexes

Thesis submitted for
The degree of Doctor of Philosophy
At the King's College London

by

Pace Nicola

Cardiovascular Division

King's College London

January 2016

Acknowledgments

Firstly, I would like to express my gratitude to Dr. Mark Pfuhl for the essential help he has constantly provided during these years. With his patience and knowledge he has helped unravelling and solving the many different challenges met in this project.

I would like to thank my colleagues, Dr. Zaleska, Dr. Rotskova, Mr Fisentzos and Miss Amos for the time spent in the laboratory together talking about science, the feedback in my project and the happy moments that we have shared in these past years.

I would like to thank Dr. Lewandowski, Dr. Trent and Prof. Brown from the University of Warwick for the comments, feedbacks, suggestions and insights they have provided in all my visits to the Department of Physics at University of Warwick. Without them it would not have been possible to reach the successes and new perspective achieved in this work.

A special mention to Dr. Atkinson, manager of the NMR facility at King's College London, for the help in developing the experiments for the investigation of the charged side chain at physiological pH by solution NMR.

I would like to thank Dr. Hansen and Prof. Middleton for their insightful comments and questions which helped me widen my research by approaching it from different perspectives and angles.

I could write an entire book to explain all the reasons to thank my family: the love of my life, Matilde, my parents and my brother and sister. They never failed to express all their support. They never missed to encourage me to never give up even when the frustration and tiredness were an impossible burden to bare alone. Thank you.

Last but not least, all the friends that have shared my path in the last few years. Eleonora, Vivienne, Andrea, Giulia, Alan and Alessia, I am very glad to have had the chance to meet you all and proud to call you friends.

ABSTRACT

Actin plays a central role in eukaryotic cells in various physiological processes, such as cell motility, cell division and DNA transcription. In addition, actin is the key protein in cardiac muscles, forming filaments that are crucial to its function. The possibility to have the structure of these actin filaments at atomic resolutions is fundamental to understand the molecular mechanism of these events. Although the atomic structure of the monomer of actin has been already characterized, only models based on data at low resolution are available for the structure of actin filaments. This is mainly due to the impossibility of exploiting the full potential of the two most common techniques used in structural biology: NMR in solution and x-ray crystallography. The former cannot be used because the size of actin exceeds the limit of detection, the latter because of the intrinsically disorder contained in a sample of actin filaments which does not allow the growing of a useful crystal. This work aims to investigate the possible application of solid state NMR spectroscopy to the study of actin filament and its complexes, as this technique is not affected by the above mentioned limitations.

In order to simplify the approach to this technique we decided to start with the study of a small actin binding domain, the Villin Head Domain (VHD), complexed with F-actin. Despite the limited number of VHD residues (67), its assignment in the bound state is not still complete, meaning that the structure of the complex is not available yet. Nevertheless, thanks to the implementation of phosphorous and Double-Quantum ssNMR spectroscopy, alongside the possibility to acquire proton spectra at high resolution, it has been possible to create a platform of experiments that can be used to approach the study of thin filament complexes in order to solve their structure.

The availability of the structure of F-actin and its complexes at atomic resolution will be the starting point for further investigations to understand how actin is implicated in health and disease.

Abbreviations

ABD	Actin Binding Domain
ABLIM2	Actin-binding LIM2
ABP	Actin Binding Protein
ADP	Adenosine Diphosphate
ATP	Adenosine Triphosphate
Apo/olo protein	Respectively protein in free/bound state
BMG	Buffered Minimal Glycerol medium
BMGY	Buffered Minimal Glycerol-complex medium
BMM	Buffered Minimal Methanol medium
BMMY	Buffered Minimal Methanol-complex medium
CH domain	Calponin homology domain
CLR	Calponin-like repeats
CP	Cross Polarization
DARR	Dipolar Assisted Rotational Resonance
DMSO	Dimethyl sulfoxide
DQ coherence	Double Quantum coherence
DSS	4,4-dimethyl-4-silapentane-1-sulfonic acid
DTT	Dithiothreitol
EDTA	Ethylene Diamine Tetraacetic Acid
EGTA	Ethylene Glycol Tetraacetic Acid
EM	Electron microscopy
F-actin	Filamentous actin
G-actin	Globular actin
HSQC	Heteronuclear Single Quantum Coherence
INEPT	Insensitive Nuclei Enhanced by Polarization Transfer
IPTG	Isopropyl β-D-1-thiogalactopyranoside
LB	Luria-Bertani medium
MAS	Magic Angle Spinning
MGY	Minimal Glycerol medium
MM	Minimal Methanol medium
MST	MicroScale Thermophoresis
NMR	Nuclear Magnetic Resonance
PCR	Polymerase Chain Reaction
SBR	Symmetry-based recoupling
SDS-PAGE	Sodium Dodecyl Sulfate PolyAcrylamide Gel Electrophoresis
ssNMR	Solid state Nuclear Magnetic resonance
TEM	Transmission Electron Microscopy
TMS	Tetramethylsilane

VHD	Villin Head Domain
WT	Wild Type
YPD	Yeast extract Peptone Dextrose medium

Table of content

1 Introduction

1.1 The importance of studying Actin

Actin is one of the most abundant proteins in eukaryotic cells. It was identified for the first time in skeletal muscle by Straub in 1942 and, since then, actin was extensively and deeply studied. Actin plays a key role in several different physiological events, such as locating and transporting protein complexes in cells through the internalization of membrane vesicles, cell motility and DNA transcription, establishing and maintaining cellular polarity, driving cell shape changes, sensing environmental forces and dividing the cell in two [1-4]. Actin is involved in these events especially through its ability to dynamically assemble and disassemble in filaments, existing in a dynamic equilibrium between its monomer state, called globular actin or G-actin, and its polymerized state, called filamentous actin or F-actin [2]. It was found that actin is one of the major constituents of two different kinds of filaments: *microfilaments*, one of the most important structures in the cytoskeleton of various different cell types, and *thin filaments*, the working partner of the thick filaments involved in the muscle contraction [3, 5].

To emphasized even more the importance of actin, in the ’60, for the first time, actin was also found in plants, covering similar functions than in the other eukaryotic cells such as intracellular movement of organelles and vesicles, exo- and endocytosis and a role in the plant’s cell cycle [5].

For these reasons “[..], knowledge of the atomic structure of the polymer is necessary to clarify the mechanism underlying the functions of actin in cells” [1].

1.1.1 Structure of the monomer of actin (G-actin)

Actin is 42kDa globular protein found in all the eukaryotic cells. In vertebrates actin is expressed in three main different isoforms, α-isoforms of skeletal, cardiac, and smooth muscles and the β- and γ-isoforms expressed in nonmuscle and muscle cells [6]. The three isoforms differ in few residues mostly only at the N-terminus.

The tendency of G-actin to polymerize in filaments at the salt concentration required to grow a crystal makes difficult to obtain an ordered crystal of G-actin. Nevertheless, it was demonstrated that the presence of actin binding proteins or modification on actin sequence that inhibit the polymerization into filaments promote the generation of ordered crystal. In 1990, Kabsch and its coworkers were the first to solve at atomic resolution the structure of rabbit skeletal actin complexed with DNAse I both in ATP and ADP state by x-ray diffraction at a resolution of, respectively, 2,8Å and 3Å (PDB:1ATN for ATP state)(Figure 1.1)[7]. Since then more than 80 structure of G-actin were deposited but most of them were solved in complex with an actin binding protein and a small molecule or on mutate actin that has lost the ability to polymerized [6]. It is interesting to know that, actually, the first to be able to obtain a crystal of actin in absence of any actin binding proteins or modifications in actin sequence was Christine Oriol-Audit in 1977 but limitations in the technology of x-ray sources did not allow the acquisition of data due to the small size of those crystals [8].

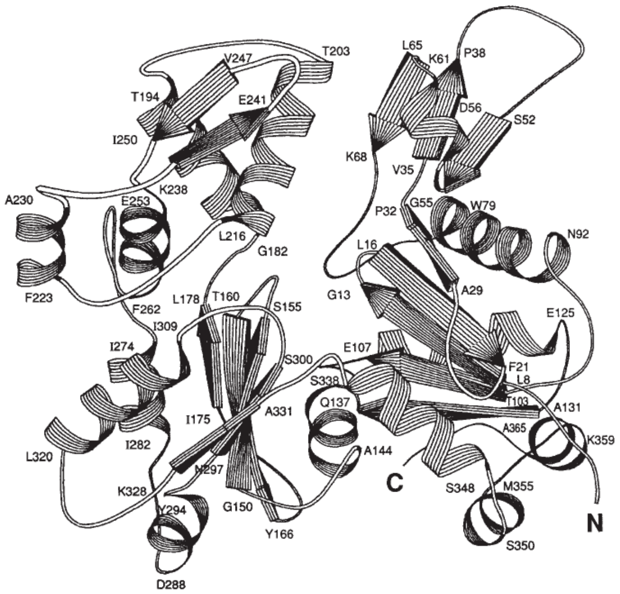

Figure 1.1 Schematic representation of the structure of rabbit skeletal actin complexed with DNAse I in ATP state [7].

The structure of G-actin can be divided into two main domains, referred to as inner and outer domains on the basis of their position relative to the axis of the filament, each composed of two subdomains (S1–4). Historically, the two domains were called small and large domain, identifying, respectively, the outer and inner domain. The C- and N-terminus are both located in the smaller domain [7]. The main domains are separated by a cleft containing a tightly bound adenosine-derived nucleotide in complex with a divalent cation (some studies suggest should be magnesium in the physiological state of actin) (Figure 1.2).

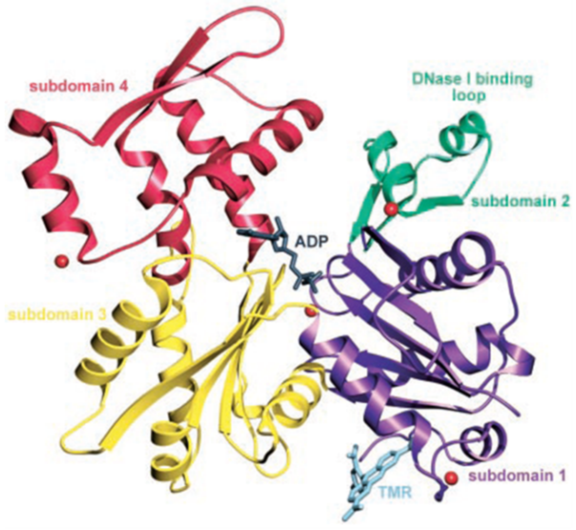

Figure 1.2 Schematic structure of uncomplexed actin modified with a covalently bonded Tetramethylrhodamine-5-maleimide (TMR) molecule to Cys374 in the ADP state. The four subdomains of actin are represented in different colors: subdomains 1 (purple), 2 (green), 3 (yellow), and 4 (red). The cleft between the two main domains contains a molecule of ADP (1J6Z).

It was possible to observe three different conformations that the two domains could assume in relation to their arrangement: open and twisted, closed and twisted and closed and untwisted (flat) (Figure 1.4)[1]. The reciprocal position of the domains is determinate by the size of the cleft between the domains (b_1) defined as the distance between the C_α of glycine 15 and aspartate 157 and the angle the domains assume in respect to each other (θ)(Figure 1.3).

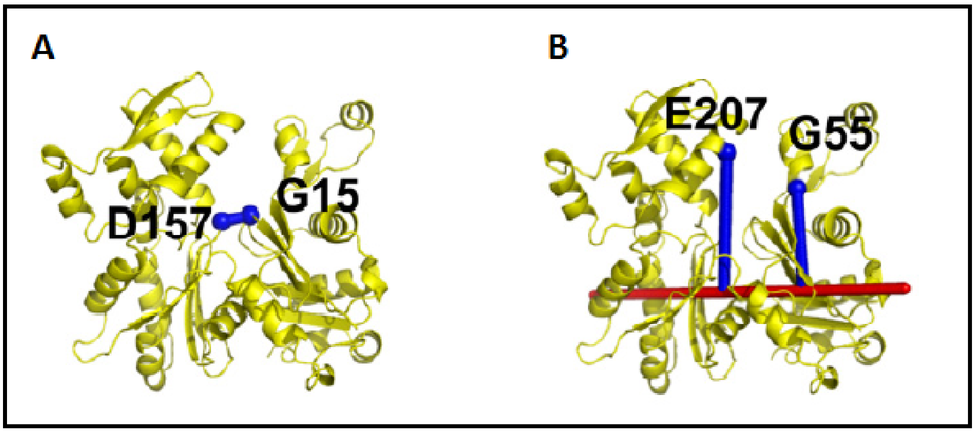

Figure 1.3 Definition of the parameters that characterize the conformations that the two domains can assume in respect of each other. Panel A defines the size of the clamp as distance between C_α of G15 and D157 while panel B the meaning of the twist angle between the two domain as the angle between the normal vectors of the two planes, one containing G55 and the axis of rotation (the red rod), and the other containing E207 and the axis of rotation [1].

The size of the clamp identified the structure as closed when lower of 6Å and open when higher of 7Å. It has been suggested that the transition from the closed conformation to the open one releases the bound nucleotides. The opening and closing of the cleft are due to the movement of the two domains quantifiable as variation in the value of (θ). The twist angles of the G-actin crystal structures are widely distributed in the range of 16–25°, with an average of 20°. In contrast, the angle (θ) in subunit in a filament is 8° (flat arrangement) [1, 2].

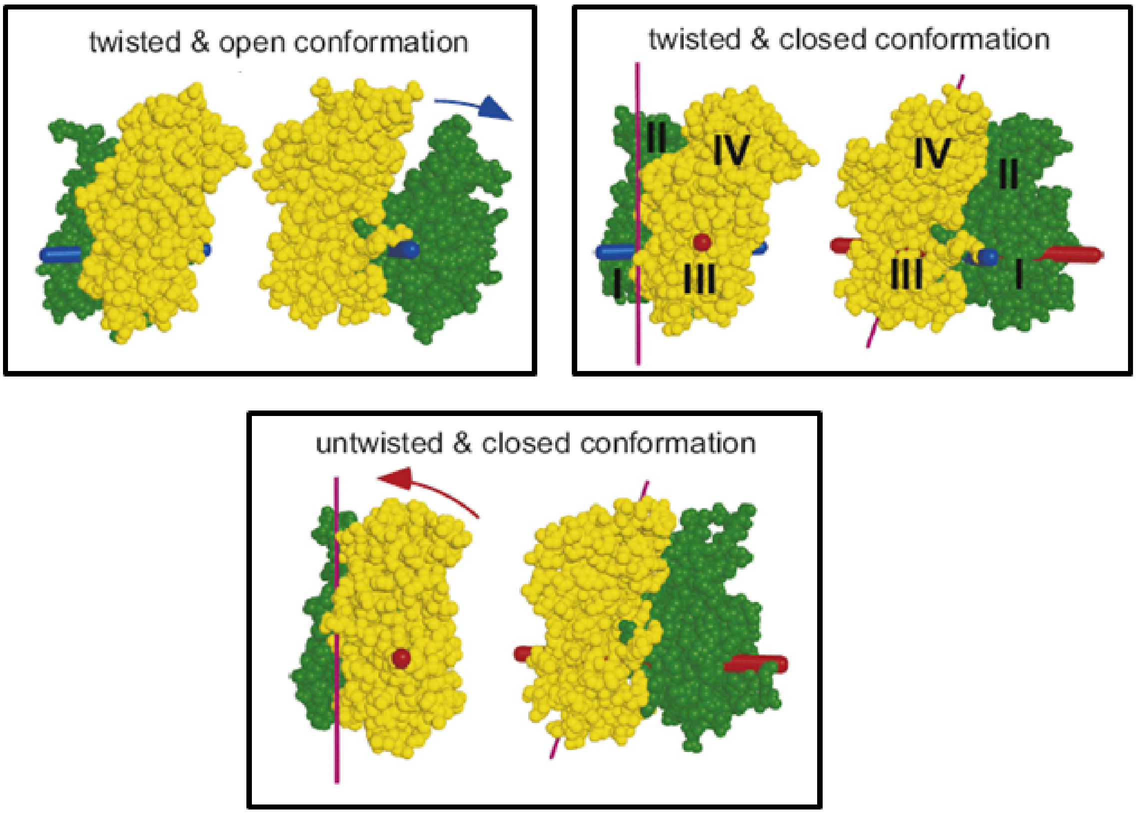

Figure 1.4 The different conformation of actin monomers. The two major domains, the domain consisting of subdomains I+II and the domains consisting of subdomains III+IV, are shown in green and yellow, respectively. The open conformation in (A) is obtained from (B) by a rotation of one major domain relative to the other about the axis of rotation (shown as the blue rod). The flat conformation in (C) is obtained by a rotation of the two major domains relative to each other around the axis of rotation (shown as the red rod). The magenta axis is a helix axis of F-actin [1].

1.1.2 From G-actin to F-actin

At physiologic conditions (high-salt solution) when the amount of G-actin is higher than the critical concentration, the actin monomers polymerize into filaments. The formation of filaments is not an event that it is associated with a refolding process, but with surface-surface contacts. The process of polymerization to F-actin is endothermic and is driven by a large positive entropy change generated by the decreasing in the water-excluded volume created during the polymerization (ΔH=89.0kJmol^{-1}, ΔS=0.413 kJK^{-1}mol^{-1}, ΔC_p=−1.16kJK^{-1}mol^{-1} at 298.15K) [1]. The packing of three side chains will be used as a model to easily explain how this positive entropy is generated (Figure 1.5). The presence of a folded side chain generates an excluded volume that cannot access by molecules of waters. When the side chains are packed the water-excluded volume overlaps and the total volume available to the molecules of water increase as consequence. This accompanies an increase in the number of accessible conformations of water molecules and, therefore, an increase in the entropy of the solvent. The polymerization of actin monomers into filaments acts in the same way of protein folding reducing the water excluded volume and increasing the entropy of the solvent [9].

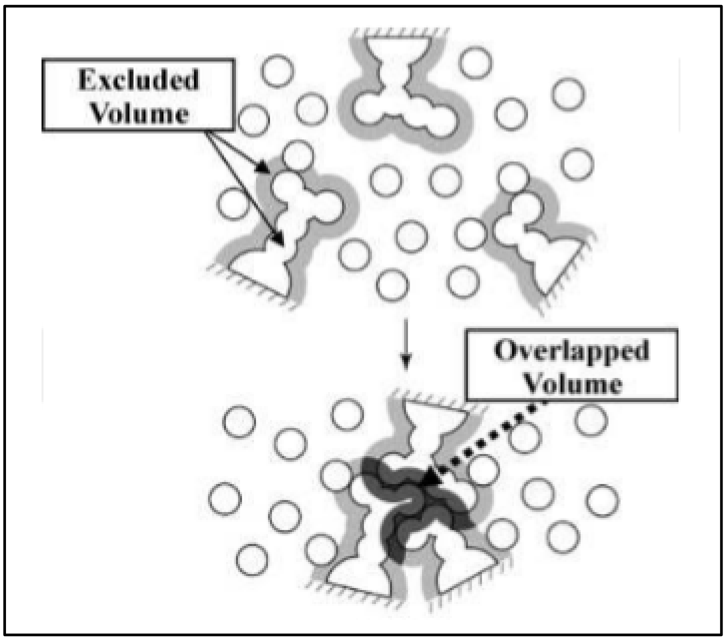

Figure 1.5 The packaging of three side chains can be used as a simplification to easily explain how the gain in the entropy of the solvent that drives the polymerization of an actin filament is generated. The excluded volume is defined as the volume that includes the side chain itself and the volume highlighted in gray. When side chains are packed the excluded volume overlaps increasing the total volume available to the water molecules [9].

Actin polymerization proceeds through kinetically distinct steps (Figure 1.6). In the first step, called also lag-period, there is the formation of unstable nuclei of actin (dimers or trimers of actin). In the presence of other proteins, called “actin nucleators”, the actin nucleus became more stable and it promotes the elongations phase where more monomers of actin are incorporated. The elongation has a polarity (the monomers binds preferentially the barbed end or plus end) and it is mediated by proteins that translocate along the growing filament and simultaneously catalyze the addition of monomers to the filament. The critical concentration for actin addition at the two ends of the filaments are different, 0.1µM for the plus (barbed) end and 0.8µM for the minus. The process continues whilst the rate of elongation is greater than the loss of ADP-F-actin from the other end of the filament. When the two rates (assembling and disassembling) are equal the length of the actin filaments remains the same because actin monomers continue to associate and dissociate from the ends at the same rate (this phenomenon is called treadmilling) [10].

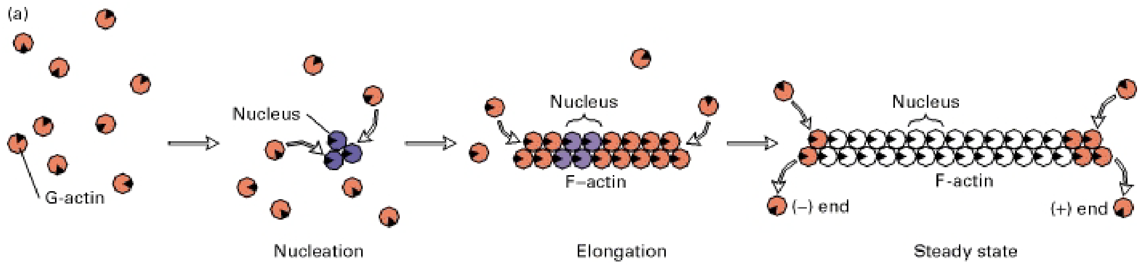

Figure 1.6 Schematically representation of G-actin polymerization into F-actin [10]. G-actin starts to assemble in nuclei of two or three monomers. More monomers of actin assemble on the filament assisted by actin binding proteins that promote the elongation of the polymer. When the rate of polymerization and depolymerization is equal the filaments enter in the steady state where the length of the polymers do not change anymore.

Actin monomers bind either ATP or ADP, and both forms of G-actin are competent for polymerization. However, the nature of the bound nucleotide modulates the kinetics of association and dissociation, with distinct effects at the barbed and pointed ends of the filament [11]. It is interesting to consider that the monomers of actin are incorporated in the filament as ATP-G-actin and the hydrolysis of the nucleotide occurs later after the incorporation. After the hydrolysis the nucleotide in the actin cleft is contained as ADP.Pi. The cleavage of ATP results in a highly stable filament with bound ADP.Pi while the consequent releasing of the phosphate will destabilize the filament [12].

Figure 1.7 During the polymerization of the filament the incorporation of monomers of ATP-G-actin is faster than the hydrolysis of the nucleotide leaving a pool of ATP-F-actin at the barbed-end. Along the filament, behind the barbed-end there will be a pool of ADP.Pi-F-actin while near the pointed-end (where the depolymerization of the filament is occurring) the majority of the actin is in the form of ADP-F-actin [12].

1.1.3 Structure of filamentous actin

In 1990, the same year the first structure of G-actin was published, the first model of actin filament with a resolution of 8Å by Holmes and coworkers was published [13]. This structure was obtained by fitting the atomic structure of G-actin by simple rigid body rotation into the experimentally obtained X-ray fiber diffraction pattern of oriented F-actin gels Figure 1.8.

Figure 1.8 Holmes model representing eight monomers of F-actin helix. For clarity each monomer is shown in different colours. Each amino acid residue is represented by a sphere of radius 2.7Å. The small domain is at large radius. Amino acid residues that cross-link to myosin in the actomyosin complex are shown in green"[13] .

Nearly twenty years later, in 2009, Oda and its coworkers published an improved model of actin filaments with a resolution of 3.3Å in the radial and 5.6Å in the equatorial directions [2].

In the filamentous state, the conformation of actin subunits is affected by changes in structure which result in the untwisting of the two domains even if the closed cleft remains unaltered. G-actin and the subunits in the filaments differ by a 20° rotation of the two main domains around the axis passing along the front of subdomain 1 and the side of subdomain 3. In this subunit an extended D-loop is suggested to fit the surface of the upper subunit along the strand (Figure 1.9) [2].

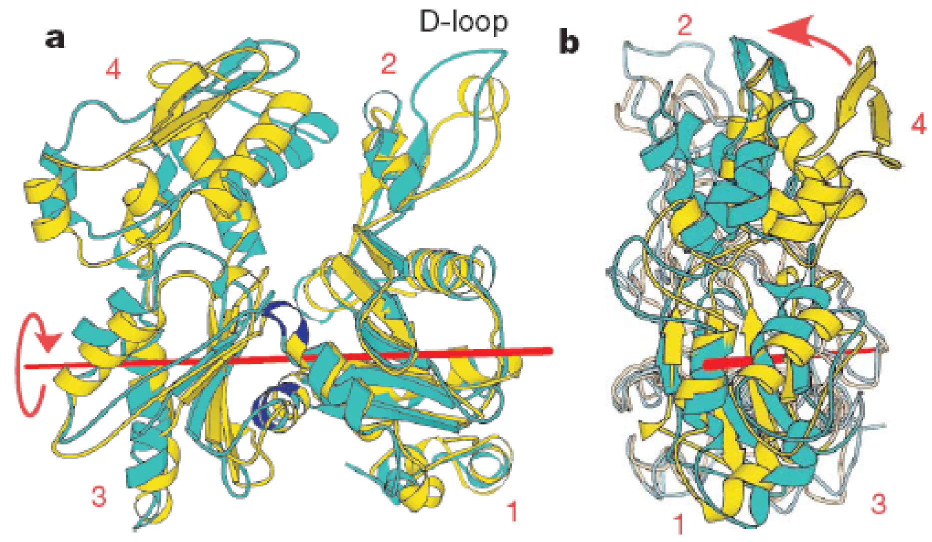

Figure 1.9 Schematically representation of the transition from the G-actin conformation (yellow) to the conformation in F-actin (light blue, PDB code 1J6Z). In the panel a) is presented the front view and in panel B the side view. The rotation of 20° in subdomains II and IV respect to subdomains I and III (reported by the red arrow) is associated with bends of the polypeptide chain at residues 141–142 and 336–337, as indicated in dark blue [2].

The stability of filaments is enhanced by the extensive contacts among the different subunits. It is possible to divide these contacts in intra-strand and inter-strand interface contacts (Figure 1.10). For an exhaustive list of contacts refer to [1] and [2].

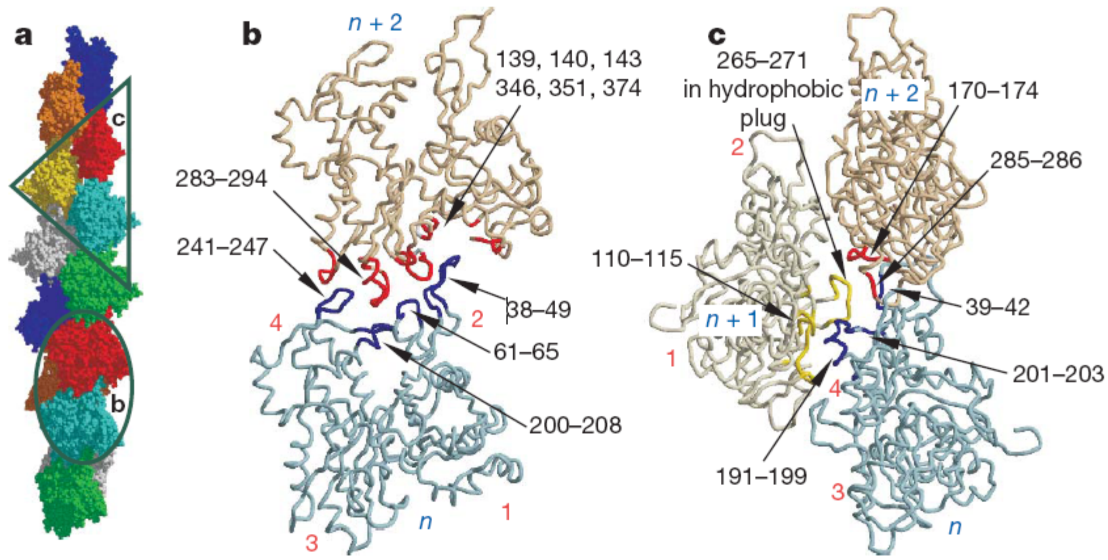

Figure 1.10 Intra- and inter-strand contacts within Oda's F-actin model. Panel a) the model of the F-actin structure including 13 subunits. The two subunits marked by the oval are magnified in Panel b) and the three subunits marked by the triangle are magnified in Panel c). Panel b) and Panel c) represent the residues contributing to the intra-strand contacts between subunits and those facilitating the inter-strand contacts [2].

As shown in Figure 1.8 an actin filament is made by two chains of actin monomers that turn gradually around each other to form a right-handed, two-chained long helix. The actual symmetry is a single left-handed genetic helix with approximately 13 molecules repeating every six turns in an axial distance of 35.9nm. The distance between molecules along the helix axis is 27.6Å. However, because the twist per molecule (−166.6°) is close to 180°, the structure actually appears like two slowly turning right-handed chains. The width of the filament is within the range of 7–10nm (Figure 1.11) [6].

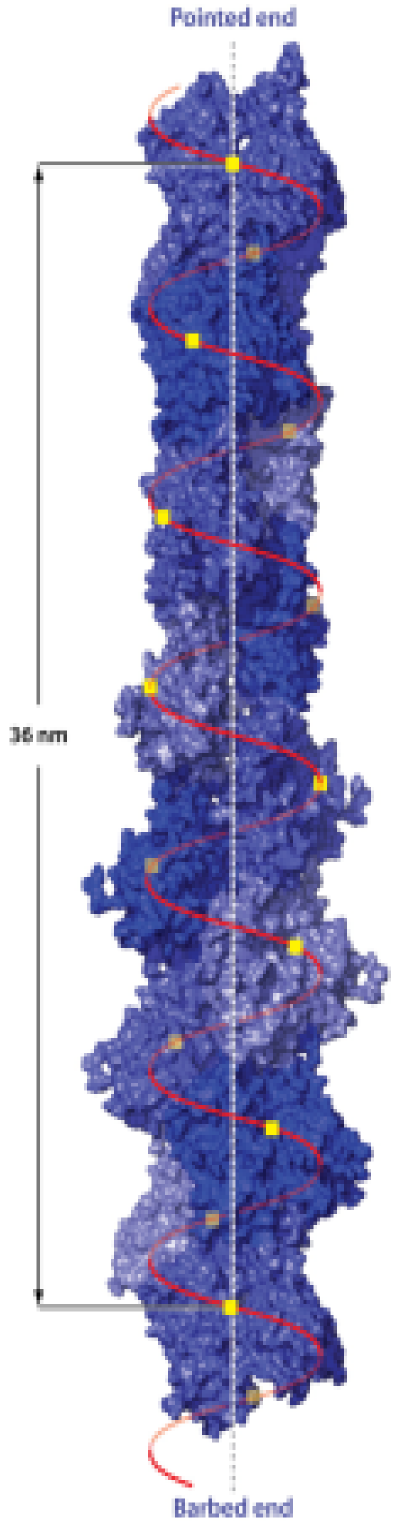

Figure 1.11 The helical structure of F-actin. The symmetry is a single left-handed helix with approximately 13 molecules repeating every six turns [6].

1.2 Proteins and small drugs that interact and modulate the actin filaments

Actin can interact with more than 100 other proteins and their interaction can modulate the assembly of actin filaments or the functions that the filaments play in the eukaryotic cells [5, 14] affecting the conformation of the polymers. The proteins able to interact to actin filaments are called actin binding proteins (ABPs). Many structure models of ABPs bound to filaments have already been solved and are available in the literature. The analysis of the loci on the filaments that contact the ABPs showed that different ABPs can share the same binding site on a filament, suggesting that a sort of binding competition has to be involved [15, 16]. It is also reported in the literature that actin can binding also more than 30 other ligands (among them toxins and drugs) that can stabilize the filaments or promote their depolymerization [16]. Exhaustive lists of ABPs and other ligands are available in literature and are continuously updated.

1.2.1 Actin Binding Proteins (ABPs)

Originally the actin binding proteins were classified according to their functional properties and/or effect on actin organization, leading to groupings such as actin monomer-binding proteins, capping proteins, crosslinking proteins, membrane-associated proteins and so on [15]. Unfortunately, it is not possible to univocally clusterize the ABPs in relation with their structure or their function anymore. Actually, it has been shown that each grouping method accounts for several proteins that cannot be classified univocally because they show more than a specific feature, placing them in a group of proteins called “orphan proteins”. Nearly 15 years ago, trying to determine an easy and unambiguous grouping method, a different classification was published based only on common structural features that the different actin binding modules share [15]. The actin modules were divided into seven different groups:

- the gelsolin fold (common to the gelsolin and cofilin families),
- the profilin structure (overall similar to the gelsolin fold but based on a different topology),
- the calponin homology domain,
- the myosin head domain,

- the villin headpiece F-actin binding module, (extensively described in chapter 1.5)
- the scruin β-propeller fold,
- the hisactophilin fold (a β-barrel configuration).

1.2.1.1 The gelsolin fold and profilin structure

The gelsolin fold is commonly found in the gelsolin and cofilin families. The proteins belonged to both these families promote the depolymerization of actin filaments but with a different mechanism of action and triggered by different signals.

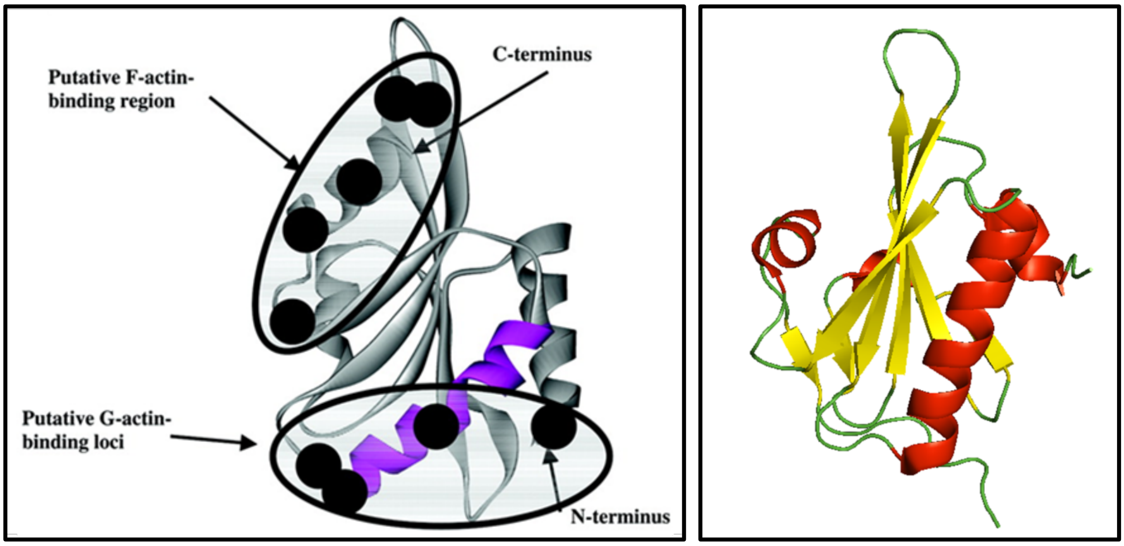

Figure 1.12 Left panel) Structure of gelsolin fold in yeast cofilin solved at 1.8 Å. The putative sites that are involved in the binding to actin are reported on the structure [16]. Right panel) Structure of gelsolin fragment G1 from Equus caballus solved at 3Å. The model was generated using PyMol software [17] (PDB:1RGI).

Cofilin (Figure 1.12, left panel) was initially classified as a protein that severed and depolymerized the filaments of actin, but it is now acknowledged that cofilin is involved in the regulation the assembly of cellular actin pool, including the formation of stable actin-cofilin rods that are associated with neurodegeneration [18]. Cofilin can bind both G-actin or F-actin but it shows the highest affinity to ADP-F.actin. It acts preferentially at the pointed end of filaments where the ADP-F.actin are located promoting the disassemblement of actin subunits.

Differently, gelsolin (Figure 1.12, right panel) responds to the concentration of Ca^{2+} in the cell. Structural models of gelsolin bound to actin filaments suggest a role for gelsolin in the capping of the barbed end preventing the elongations of filaments [16] and in the severing of the filaments [19]. Gelsolin can be divided into six domains (G1-G6) where the three N-terminus domains (G1-G3) are involved in the binding to actin while G6 is the domain that responds to Ca^{2+} concentration modulating the interaction to the actin filaments [19].

Structural models of actin filaments bound to cofilin or gelsolin revealed that these proteins share the same binding region on filaments (Figure 1.13). This region coincides also with the region that is involved in the interaction with tropomyosin defining a competitive binding to filaments in which the binding of tropomyosin completely exclude the binding by cofilin and gelsolin and vice versa [16].

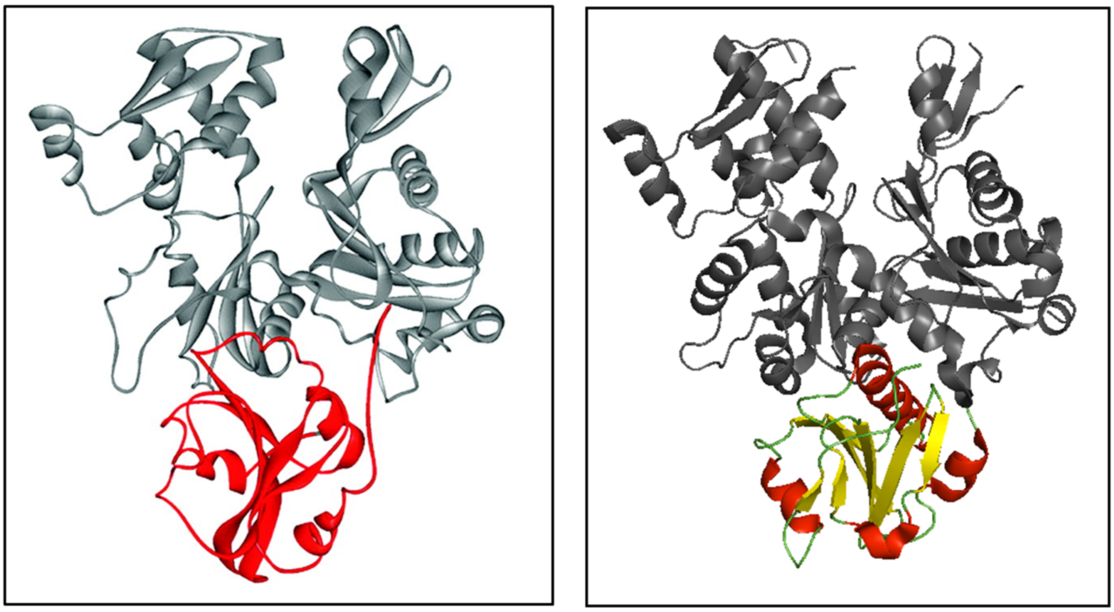

Figure 1.13 The left panel shows the crystal structure of yeast cofilin bound to a monomer of actin ([16]) while in the right one is presented the structure of gelsolin fragment G1 (PDB:1RGI) bound to actin filaments from Equus caballus (solved at 3Å). The model was generated using PyMol software.

Differently from gelsolin and cofilin families, profilin promotes the polymerization of G-actin into filaments decreasing the hydrolysis of ATP bound to actin and maintaining the actin subunits in a state where they have a high affinity for the growing barbed end of filaments. Similarly to cofilin and gelsolin, profilin binds near the cleft region but it occupies the back of the cleft (Figure 1.14) [6].

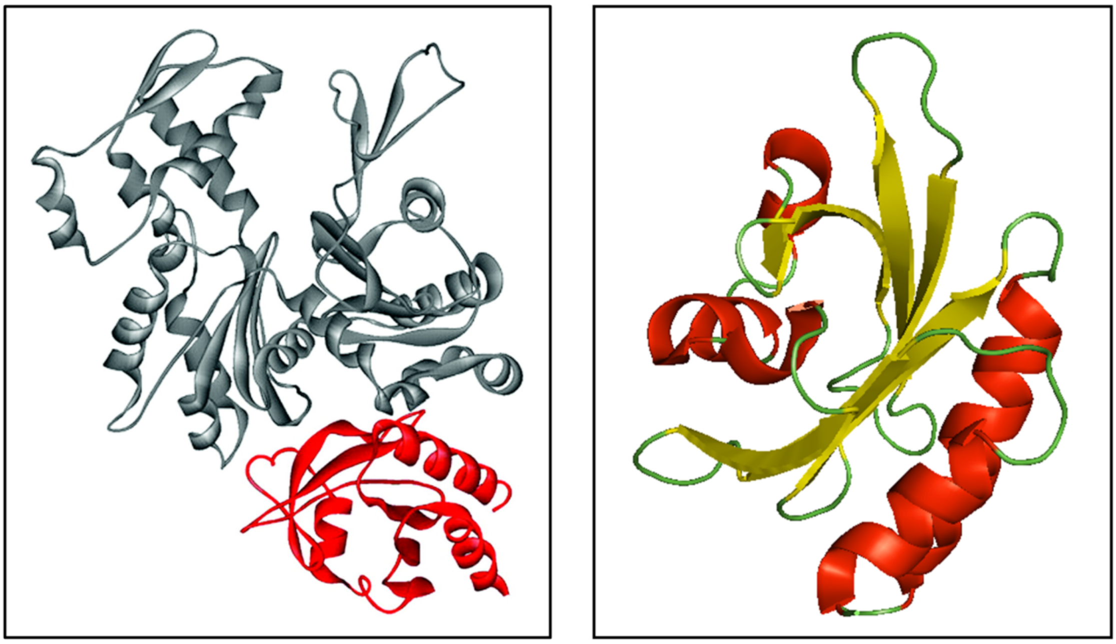

Figure 1.14 The left panel shows the crystal structure of bovine profilin (PDB: 2BFT) while in the right panel is presented the structure of bovine profilin bound to β-actin (PDB: 2BFT) [20]. The structure is overall similar to the structure in gelsolin structure module but profilin-bound actin filaments near the cleft region occupying the back of the cleft promoting actin polymerization. The models were generated using PyMol software.

The structure of profilin bound to filaments showed that the binding occurs to a site on actin that is inaccessible in the Holmes model of the filament, suggesting that after delivering a monomer to the growing end of the filament, profilin has to either move to a new site that does not block assembly or completely dissociate from the filaments [16].

Despite the families contained in this group sharing the same structural module and the same binding site on the filaments, they present a variety of different functions. It has been suggested that all these proteins could have been originated from a common ancient structural module and during their evolution they could have developed a characteristic and different specific function. The same hypothesis can be extended to all the actin binding modules, when the rather limited extension of actin surface available for the binding of an ABP is taken into consideration. Hence, the different modules could derive from a common ancestor and rearrangement in its amino acid sequence (point mutations, duplications, deletions, etc.) during their evolution could have generated the different modules with different functions [15].

1.2.1.2 The calponin homology domain

Calponin is an actin- and calmodulin-binding protein likely involved in the regulation of actin functions. Calponin consists in four different domains: a calponin homology (CH) domain at the N-terminus that is responsible for the binding to actin and three repeating domains called calponin-like repeats (CLR) that include the C-terminus [21]. The tertiary structure of CH domain is compact and globular and it is based on a core of four α-helices (I, III, IV and VI) connected by long loops, with two short α-helices (II and V) (Figure 1.15) [22]. Calponin binds actin through two contiguous but separate actin binding sites and binding to F-actin induce large conformational changes in it and to calponin [23]. Tandems of CH domains were found in several actin binding proteins such as α-actinin, filamin, spectrin etc. [24] acting as their actin binding domain.

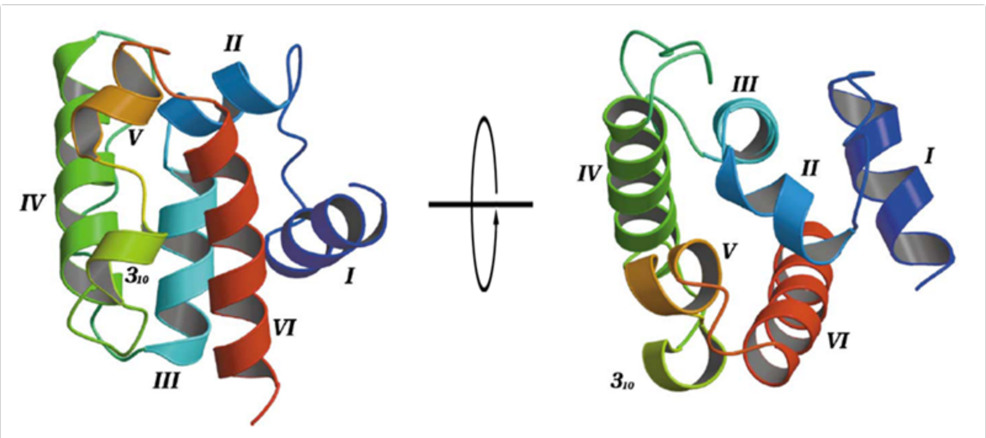

Figure 1.15 Structure of the CH domain of chicken calponin. The roman number report the enumeration of the α-helices in the structure [22].

One of the first models of calponin CH domain bound to F-actin was proposed by Bramham and coworkers fitting the NMR structures of the chicken calponin CH domain they solved into the electron density map obtained by electron microscopy. Nevertheless, the resolution of their model was not reported and two different orientations of the CH domain equally valid were presented [22]. Nowadays, the improvements in EM technique have made possible the generation of several structural models at a better resolution that suggests how the CH domain of different ABPs interacts with the filaments [25, 26]. The model reported in Figure 1.16 is an example that shows the possible structure of the tandem CH domain from α-actinin bound to actin filaments at a resolution of 16Å [27].

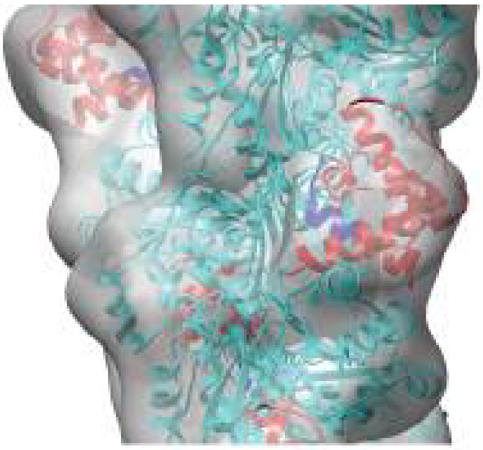

Figure 1.16 Structure of actin filaments decorated with CH tandem domain of α-actinin at 16 Å resolution [27].

1.2.1.3 The myosin motor domain and its regulation by tropomyosin

Myosin is the main protein involved in the muscle contraction and has the ability to transform the hydrolysis of ATP (energy) in movement along the filaments. Every myosin protein is composed of three domains: head, neck and tail chains (Figure 1.17). The globular head domain contains the actin- and ATP-binding sites and it is the one responsible for generating force. The neck acts as a linker between the head and the tail chains that are deputed to regulate the activity of the head domain and determine the specific function of the myosin isoforms [28].

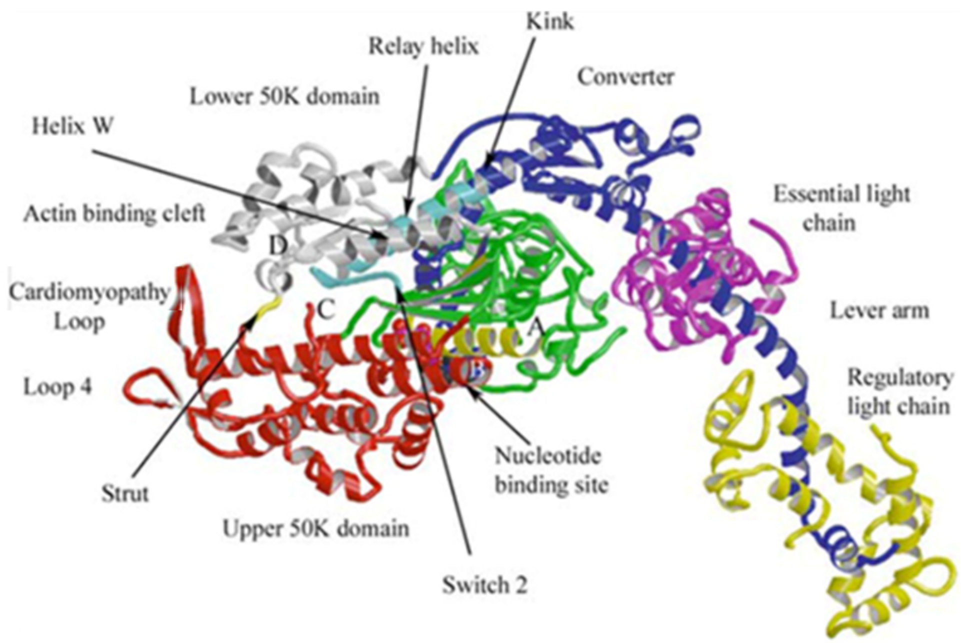

Figure 1.17 Ribbon representation of head domain S1 of a myosin molecule. The upper portion of the motor domain is separated by a large cleft (actin-binding cleft), the opening and closing of which modulates actin affinity [29].

A model at a resolution of 7.7Å of the actin-myosin complex at rigor was solved by cryoEM and published in 2012. The model showed that myosin interacts with two adjacent actin (subunits *n* and *n-2*) molecules through several loops forming a large contact surface (Figure 1.18) [30]. It is possible to think the binding site of myosin-like a pincer that clamps on a subunit of actin and at the same time take contact with the adjacent subunit creating a large contact surface.

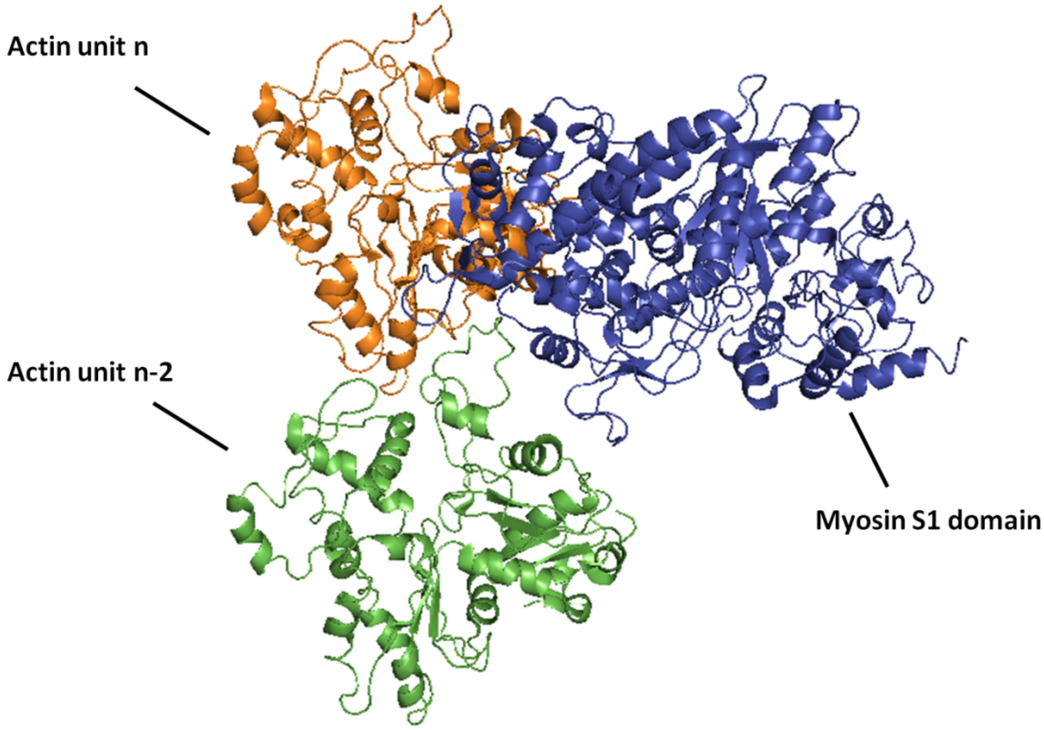

Figure 1.18 Ribbon representation of head domain S1 of a myosin molecule in rigor state (blue) bound to two adjacent subunits of actin (green and orange) n and n-2 (PDB: 4A7F) and solved at a resolution of 7.7Å. The model was generated using PyMol software.

In striated muscles the binding of myosin motors is mainly regulated by tropomyosin and troponin. Tropomyosin also binds the F-actin in smooth and in non-muscle cells and stabilize and regulate the filaments in absence of troponin [31]. Tropomyosin is a double strand of two parallel helices containing two sets of seven alternating actin binding sites arranged in a coiled-coil motif (Figure 1.19)[32].

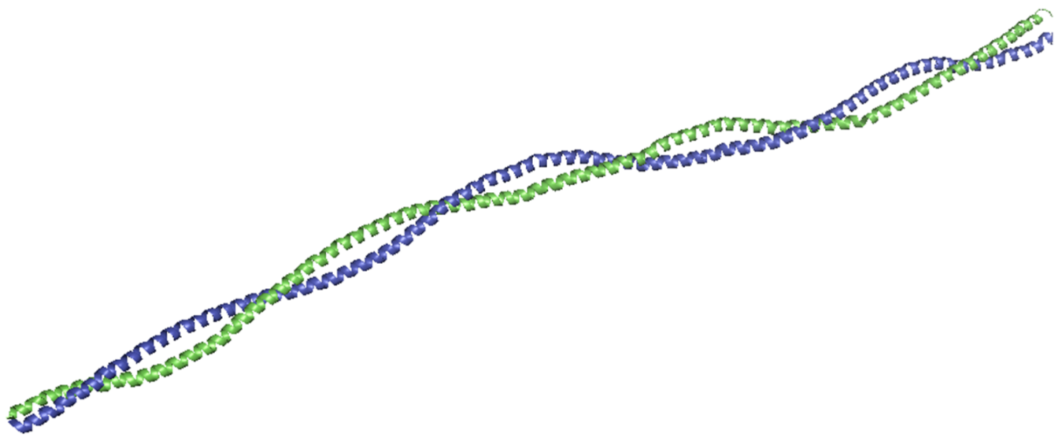

Figure 1.19 Ribbon representation of tropomyosin at 7Å resolution in the spermine-induced crystal form (PDB: 1C1G). The model was generated using PyMol software.

The model structure proposed for the tropomyosin-F-actin complex (Figure 1.20) showed that the mainly negatively charged surface of tropomyosin interacts with a positive groove on F-actin, and in particular it was suggested that lysine 326 and 328 (K326 and K328) on filaments strongly interact with the different pseudo-repeats of tropomyosin (Figure 1.21)[31].

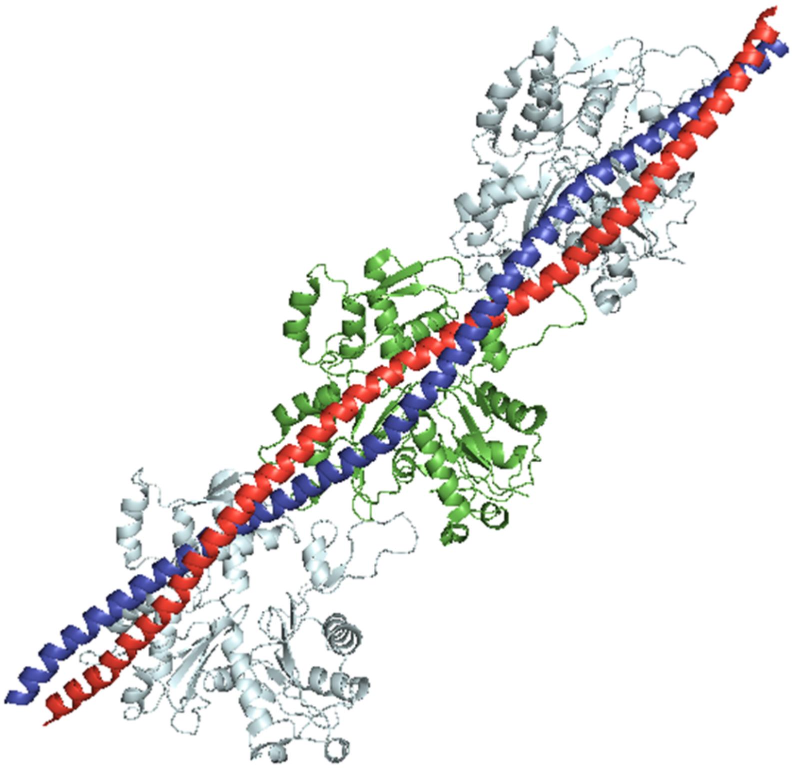

Figure 1.20 Ribbon representation of tropomyosin bound to F-actin at a resolution of 3.7Å solved by electron cryomicroscopy (PDB: 3J8A). The model was generated using PyMol software.

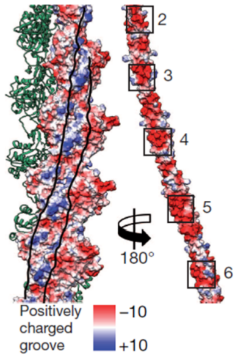

Figure 1.21 Surface of F-actin and tropomyosin (pseudo-repeats 2-6) showing their electrostatic charge (red, white, blue: negatively charged, positively charged and neutral) at pH7.5. Tropomyosin was rotated by 180° in order to show its negatively charged surface that it is involved in the binding to the positively charged patch in actin filaments [31].

The structural model for the complex of tropomyosin-myosin-F.actin was also solved at a resolution of 7.7Å (Figure 1.22)(PDB: 4A7F) [30].

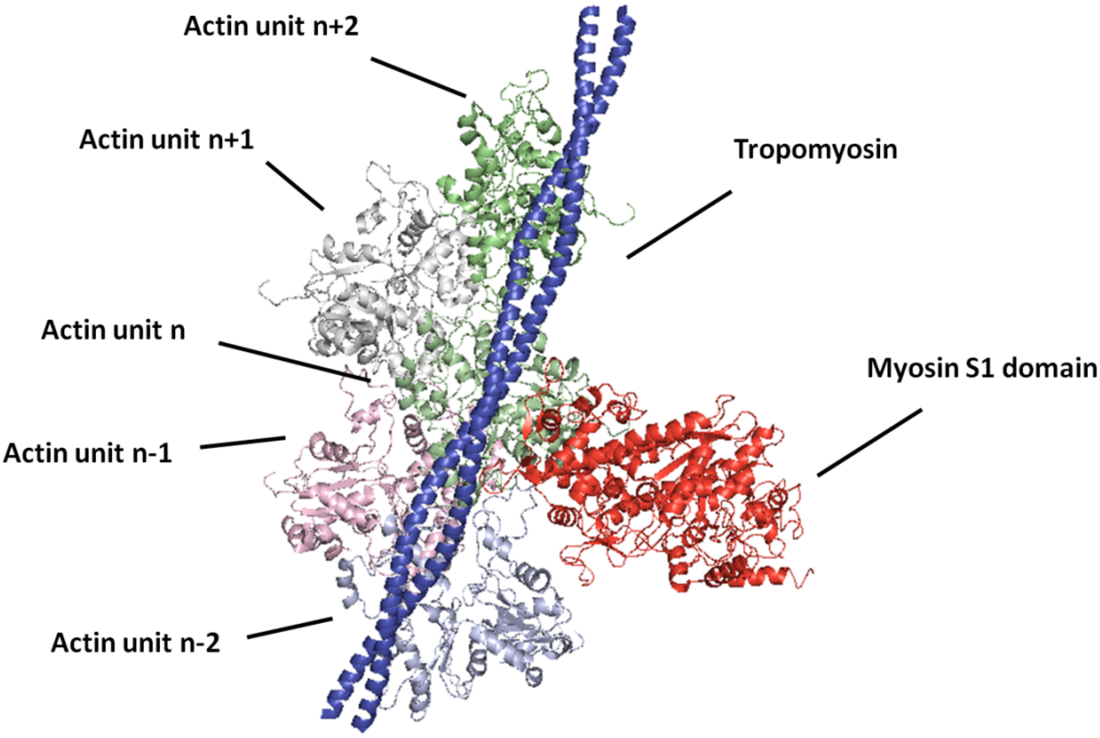

Figure 1.22 Ribbon representation of tropomyosin-myosin-F-actin complex solved at 7.7Å. In red is highlighted the myosin S1 domain while in blue the tropomyosin pseudo-repeats 2-6. The five actin subunit is referred as n, n+1, n+2, n-1 and n-2 (PDB: 4A7F). The model was generated using PyMol software.

1.2.2 Effect of phalloidin, cucurbitacin and ADP-BeF_x to the actin filaments

More than 30 compounds, among them toxins and drugs, can interact with actin filaments. Some of these molecules promote the dissociation of the filaments, other help their stability and in many cases they act through the modification of the filament plasticity and the reduction of the critical concentration for polymerization. Gelsolin, phalloidin, jasplakinolide, cucurbitacin E and ADP-BeF_x or ADP-alF4 are some examples of compounds able to stabilize the actin filaments.

The complex made of beryllium (Be) or aluminum (Al) with fluoride (F_x) is a good structural analogous of a phosphate group (Pi) that can be used to replace the third phosphate in nucleotides blocking the transition from ATP to ADP. The presence of ADP-BeF_x complex inside the cleft of actin subunit in filaments stabilizes strongly the actin filaments by decreasing the rate of subunit dissociation and the critical concentration for polymerization. More specifically it seems that this complex stabilizes the structure of the subdomain 2, as indicated by strong and cooperative inhibition of its cleavage by subtilisin (in the DNAse I binding-loop (D-loop)) and trypsin (in the 60–69 loop) [33].

Phallotoxins are a group of bicyclic heptapeptides from poisonous mushrooms. The major representative of this group, phalloidin (Figure 1.23), binds to actin filaments much more tightly than to actin monomers and shifts the equilibrium between filaments and monomers toward filaments [34]. Phalloidin stabilizes the filaments decreasing the critical concentration of actin polymerization, reducing the rate of monomer dissociation from both filament ends and inhibiting the phosphate release from the nucleotide binding cleft after ATP hydrolysis [35]. Phalloidin is known to bind at the interface of three actin monomers and stabilizes lateral interactions between the two filament strands [33]. A molecule of phalloidin bound to a filament can stabilize seven neighboring subunits [35].

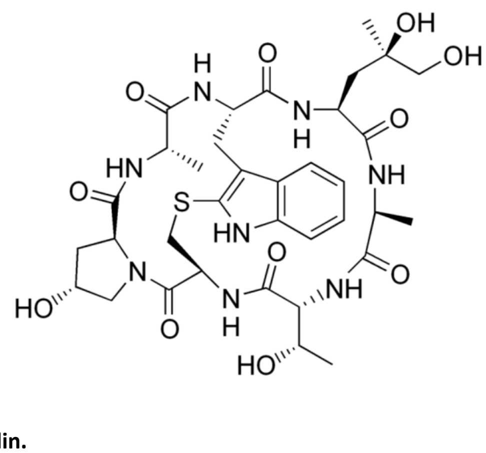

Figure 1.23 Structure of phalloidin.

Cucurbitacins are a class of compound produces by many plants member of the family of the *Cucurbitaceae* as a defensive mechanism against herbivore animals. Cucurbitacins are chemically classified as steroids, formally derived from the cucurbitane, a triterpene hydrocarbon. All cucurbitacins share the same tetracyclic scaffold but have varying substituents (cucurbitacin A−T) and are also often glycosylated (Figure 1.24). Although they are toxic, cucurbitacins have been used as traditional medicines, and more recently, they have been reported to be antitumor agents.

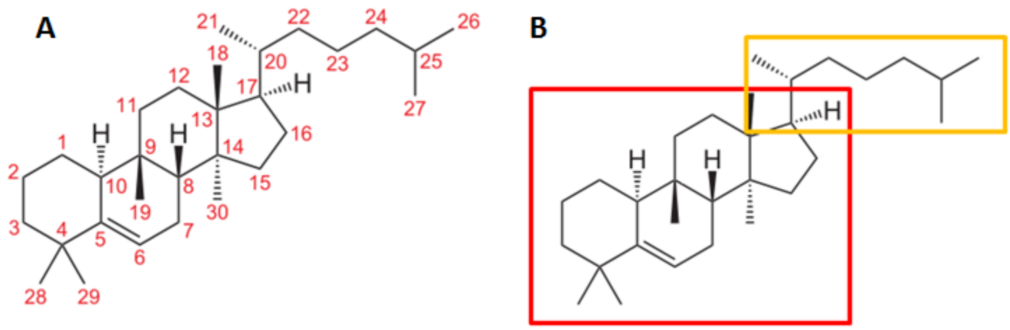

Figure 1.24 The structure of the precursor cucurbitane (or 19-(10→9β)-abeo-10α-lanost-5-ene). In panel A) is shown the standard carbon numbering. In panel B) the common tetracyclic scaffold is surrounded by a red square while in yellow is highlighted the region containing the substitution which characterizes the different cucurbitacins.

It was determined that cucurbitacin E is able to stabilize the filaments acting on their depolymerization without affecting their polymerization [36]. In fact, cucurbitacin E specifically binds only actin filaments forming a covalent bond at residue Cys257 (in rabbit skeletal muscle actin isoform), but does not interact with monomeric actin. This is due to the electrophilic Michael acceptor group (colored red in Figure 1.25), which can form a covalent bond with a nucleophile (for actin proteins this means their cysteine residues). Cucurbitacin E can inhibit the actin filaments depolymerization at sub-stoichiometric concentrations up to 1:6 cucurbitacin E:actin.

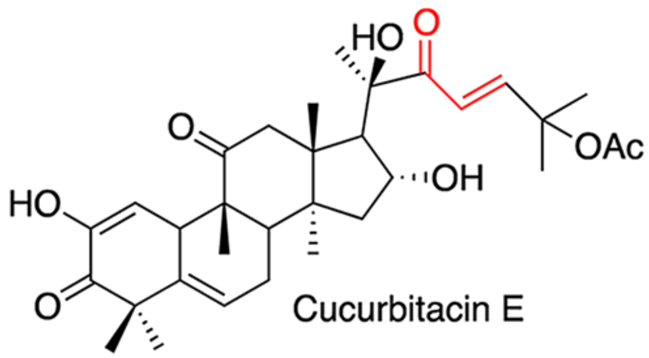

Figure 1.25 Structure of Cucurbitacin E.

1.3 Mutations in human actin and their pathologies

Minor changes in the highly conservative amino-acid composition of actin can have a deep impact on the structure of actin, its function and interactions with its partner molecules (e.g., myosin, tropomyosin). Even if mutations affect all the different isoforms of actin, the skeletal muscle α-actin (*ACTA1*) and cardiac α-actin (*ACTC1*) gene are the ones more affected [37]. Mutations in the actin-encoding genes, which are dominant missense mutations in most of the cases, lead to severe dysfunction of the related actin structures and diseases. Mutations in actin are frequently manifested in the form of skeletal and cardiac myopathies [5, 38].

Single amino acid mutations on *ACTA1* (Figure 1.26) can cause both structural and functional defects. For example mutations of L94P and E259V result in impaired folding while the I357L mutant exhibits a less compact protein conformation. The I64N, Q263L, G268C, G268R and N280K mutants have a lower capacity to copolymerize with wild type actin. The R183G nemaline mutant actin has reduced polymerization capabilities. In the case of the familial hypertrophic cardiomyopathy some mutant actins (Q99K, P164K, M305L) presented slower folding in vitro [5, 37, 38]. For an exhaustive list of all the mutation that affect *ACTA1* it is possible to refer to the supplementary table S1 attached to [37]. Besides mutations in actin gene itself, mutations in genes encoding actin-associated proteins also lead to genetic conditions. For example mutations in the dystrophin gene cause Becker and Duchenne muscular dystrophy and dilated cardiomyopathy characterized by the rapid progression of muscle degeneration and associated defects in the elasticity and integrity of the sarcolemma [5].

These data reported are only a few examples of how the integrity of actin filaments and all the machinery related to them is critical for the regular function of a cell. The understanding of all the processes behind this central role of actin filaments can be improved if structures (and no model) at high resolution will be available. The possibility to have available this kind of structure can also help in future studies focused on finding cures for actin-related diseases.

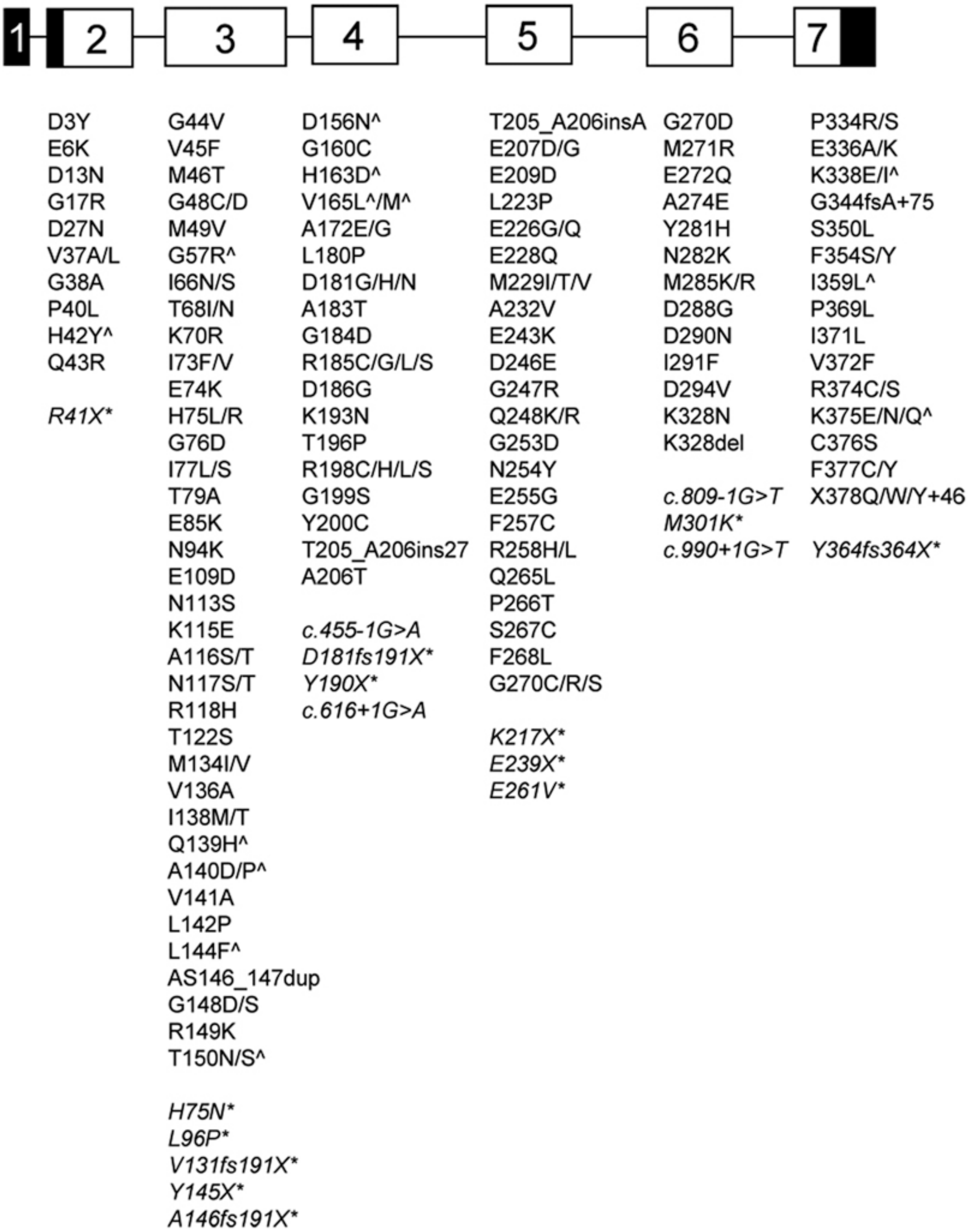

Figure 1.26 Linear diagram of the *ACTA1* gene showing the six coding exons and the location of all mutations. The dominant mutations are in normal text, the recessive mutations are italicized and at the bottom of the list for each exon. The open boxes represent translated regions of each exon, the filled boxes the 5’ and 3’ untranslated regions [37].

1.4 Approaches used to solve the structure of actin filament complexes

To solve the structure of macromolecule it is possible to implement different methods such as protein crystallography, solution NMR or electron cryomicroscopy. Nevertheless, every technique has some limitations that affect their application to address specific biological problems. It is also important to consider that, till a few years ago, only NMR and protein crystallography could generate information at atomic resolution but nowadays cryomicroscopy is reaching a similar resolution in the order of angstroms. In structure calculation the resolution is the most important parameter to consider because it determines the smallest features that can be distinguished in the structure. As reported in RCSB PDB database [39], the resolution is a measure of the level of detail present in the diffraction pattern. High-resolution structures show resolution values of near 1.2Å. Structures with a resolution between 2-3Å are still considered to have a good resolution while structures with a resolution of 3Å or higher are considered low resolution structure.

Protein crystallography is the technique which allows generating structure at the highest resolution. On the other hand, this approach requires the diffraction of a high ordered crystal of the sample and in many cases this is the bottleneck of the entire process. A protein or a protein-protein complex can precipitate neatly and generate a crystal in the order of minutes or hours. Nevertheless, in this case, the high velocity of clustering can result in a crystal with a low degree of order. On the other hand, a crystal can take days or months to grow and in the worst case it could never grow. The flexibility and heterogeneity of actin filaments avoid the generation of ordered structures during the precipitation that the crystallization solution promote. This makes impossible to grow crystals of actin filaments. On the other hand, neither solution NMR can be useful in solving the structure of actin filaments because this technique is limited by the size of the molecule. Thus, yet solving the structure of proteins with molecular weight higher than 20kDa presents substantial challenges using this technique. A detailed explanation of how the size of a molecule affects the solution NMR technique will be described in the next chapter. For these reasons other techniques such as x-ray scattering of actin filament sols or Electron Microscopy (EM) were used to try to solve this kind of structure.

The x-ray diffraction method, using well oriented filament sols, is a powerful tool for high resolution structure analysis of actin fibers. The success of this technique is restricted only by how well the layer-line reflections are separated from one another, which depends on the quality of their alignment in the filament sols. F-actin forms mainly two ordered phases of aligned filaments in solution. One is paracrystalline bundles, which are formed by adding polycations, or polymers or in solutions at pH below 5.2. The other is liquid crystalline phases, which are formed at high filament concentrations [5]. The optimization of the conditions to obtain well aligned filaments in liquid crystalline phase allowed to reach the model proposed by Oda in 2009 (Figure 1.10)[2]. On the other hand, the developments in EM technique achieved in the last few years have allowed the solution of several models at a high resolution of actin filaments complexed with several ABPs [18, 27, 30, 31] etc. A classic EM approach involves the acquisition of several EM pictures that are analysed and clustered. The electronic density map is created from the clustered images and the model is generated by the fitting of deposited structure and the density map generated. An example is the structure model of the complex of Actin-Depolymerization Factor (ADF) and F-actin characterized by a resolution of 9Å (Figure 1.27) [18].

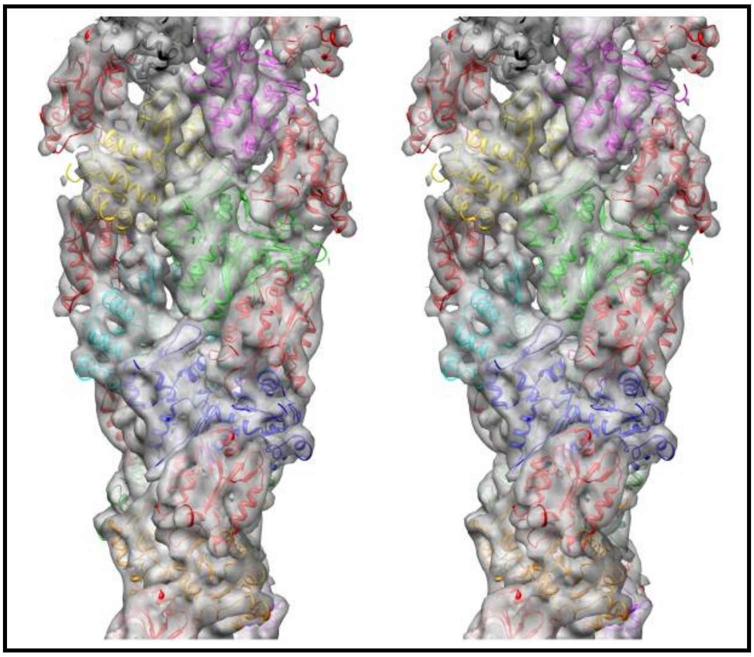

Figure 1.27 Stereo view of the 3D reconstruction of F-actin decorated with cofilin-2 (transparent surface) is shown with the corresponding pseudoatomic model of the complex (ribbons). Cofilin molecules are in red [18].

These models like almost all the models solved by EM or cryo-EM are only optimizations of the actin filament model suggested by x-ray fiber diffraction, meaning that data at atomic resolution were not available for any of this model. Considering this, the detailed descriptions of small conformational changes in actin filaments or in proteins bound to actin filaments listed for these structures has to be assumed as speculations based only on the best model which fitted their data till they will be confirmed by physics data.

In the last few years another technique emerged as new the frontier of structural biology: solid state NMR spectroscopy. As explained in detail in the next chapter, ssNMR maintains the best features of solution NMR but it is not affected by the limitations related to the size of the molecules. On the other hand, this is an approach in continuous development and in many cases there are not yet the tools able to address specific biological problems. This explains the reasons why there are only a few references available about the attempt to study actin filaments using this technique. The first actin study using ssNMR was published in 1991 and reported the first ^{13}C CP spectrum acquired on filaments at natural abundance (Figure 1.28) [40]. The spectrum was characterized by a very poor resolution due to the acquisition of the spectrum without the assistance of the MAS technique, but it was still possible to recognize the three regions which characterize the carbonyls, the Cα and the other aliphatic carbons. At that time with this resolution, an investigation in the structure of actin filaments or F-actin complexes was impossible to even think.

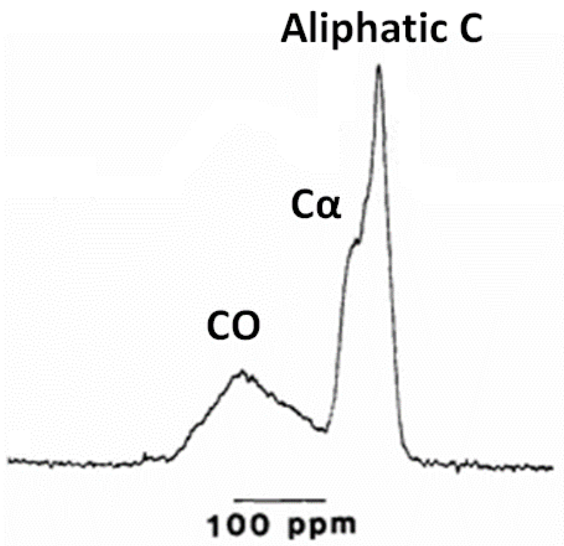

Figure 1.28 ^{13}C CP NMR spectrum of a hydrated pellet of F-actin after 28000 scans acquired at 283K at 300MHz, processed with a line broadening of 50Hz [40].

Nearly 20 years later a combined ssNMR and FTIR study on a complex between F-actin and the ^{13}C-^{15}N Myelin Basic Protein (MBP) was published [41]. In this study they characterized a secondary structure in the intrinsically unfolded MBP induced by the binding to the F-actin. The high resolution in the spectra they acquired (Figure 1.29) was achieved by the introduction of the MAS technique (an exhaustive explanation of this technique will be reported later) and the availability of magnets at higher magnetic field. These last encouraging data and the conviction that the ssNMR technique will be even improved in the next years were the basis on which my project was conceived.

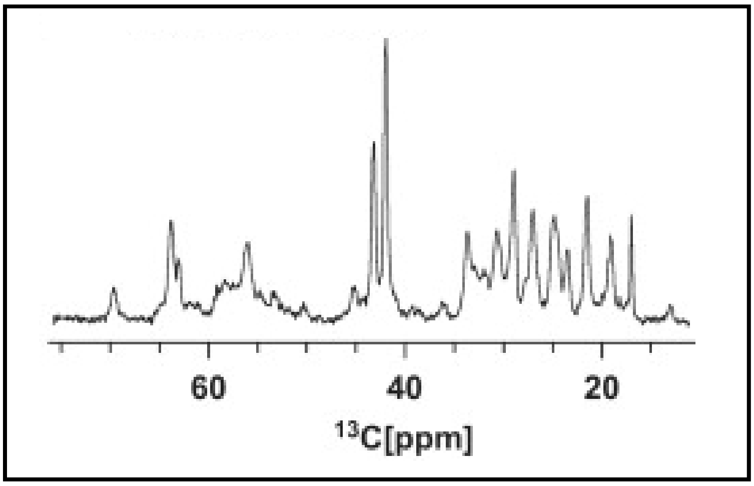

Figure 1.29 Aliphatic ^{13}C INEPT-MAS spectrum of uniformly ^{13}C,^{15}N-labelled 18.5 kDa rmMBP in rmMBP-actin complex acquired at 12kHz spinning speed, 290K at 800MHz and processed with 10 Hz exponential line-broadening before Fourier transformation [41].

1.5 Villin Headpiece Domain from ABLIM2

The headpiece is a modular F-actin motif contained in the C-terminus of several larger ABPs. There are more than 25 different headpiece domains identified from animals and plants [42], and the sequences show 35-40% homology [43]. The ABPs that contain the headpiece can be grouped into six different families in regarding the structure of the core domain that they contain (Figure 1.30). Villin headpiece was just the first headpiece discovered and characterized.

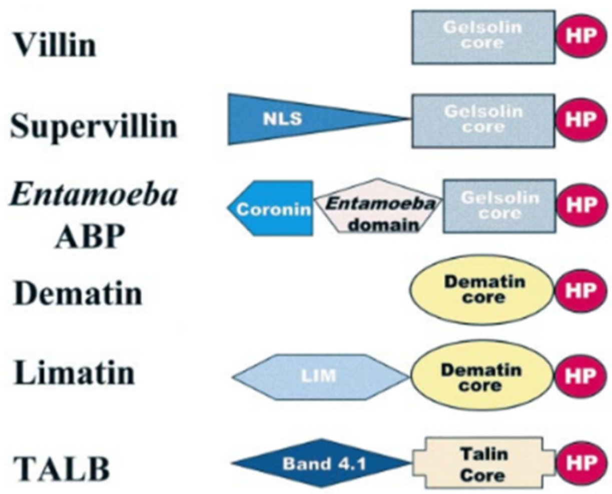

Figure 1.30 Six different families of proteins that contain the headpiece domain (HP) classified in relation to the structure of the core domain [44].

Originally the Headpiece domain was found by proteolytic digestion of the chicken villin protein and consists of 76 C-terminal residues. It was later discovered that the first nine residues were not necessary to maintain the high-affinity actin binding function. The resulting construct is normally denoted as HP67. Its structure is really compact and it is generated around an hydrophobic core (Figure 1.31) [44].

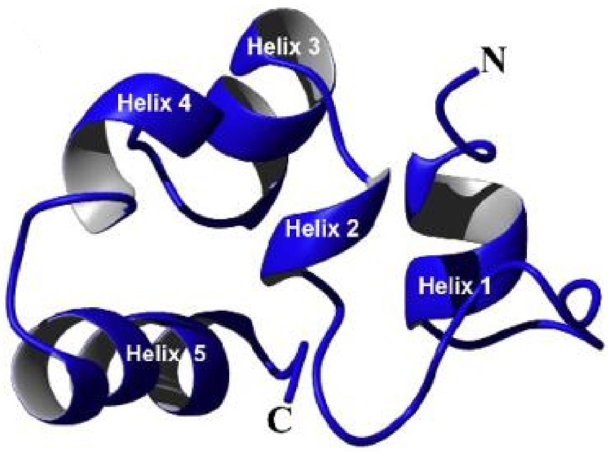

Figure 1.31 Ribbon structure of HP67 obtained using NMR in solution. The helices are labelled as H1-H4 [44] (PDB file: 1QQV, Assignment file deposited in BioMagResBank: 4428).

They proposed three regions in the VHD structure that are critical for the binding of F-actin: a hydrophobic "cap" formed by residues L63 and W64, an alternating charged "crown" below the cap, composed of the chains of K65, E72, K71, and R37 and the C-terminal carboxylate of F76, and a "positive patch" below the crown and cap that is composed of residues K38 and K73 (Figure 1.32)[43]. H32 is also important because it acts as a pH-sensitive switch for the N-terminal folding while the C-terminus can autonomously fold in a thermostable structure even when it is proteolytically cleaved from the N-terminus [44].

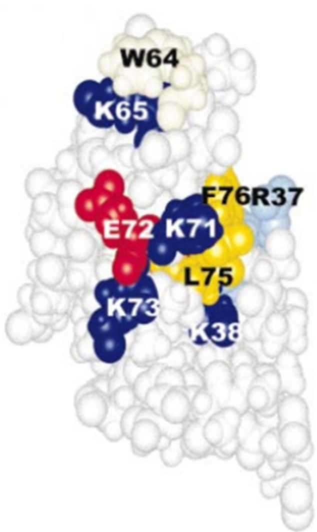

Figure 1.32 Space-filling representation of HP67. The residues that are implicated in the binding to F-actin are reported on the structure. Red color indicates negatively charged residues while blue positively and yellow neutral residues [44].

The comparison of the related charge distribution between headpiece domain with high affinity against low or nonspecific binding to actin filaments revealed as the charge on the surface, rather than the conserved three-dimensional structure, determine the affinity of VHD to bind F-actin [43]. As expected, the chicken villin headpiece (HP67), human villin headpiece (HVHP), dematin headpiece (DHP) and limatin headpiece (LHP), all headpiece domains that show high affinity to actin filaments, present a neutral hydrophobic cap region, a clear alternating pattern of positive and negative residues in the crown region and a region rich in positive residues below the crown (Figure 1.33) [43]. On the other hand, the domains that show low-affinity, protovillin headpiece (PV) and its mutated construct PV_{KKEK}) with residues 953–956 (RVDN) mutated to KKEK, show a charged patch instead of the hydrophobic region. The presence of the crown and the positively charged region below it maintain the binding to actin filaments even if with low affinity. The mutated protovillin presents an increased positive region and as consequence it shows a higher affinity (k_D 39.9 ± 34µM) than the wild type protovillin (k_D 54.6 ± 15µM). The two domains, supervillain headpiece (SVHP) and villidin headpiece (VD), miss completely of the positively charged region below the crown that result in the loss of the ability to specific bind actin filaments (Figure 1.34)[43].

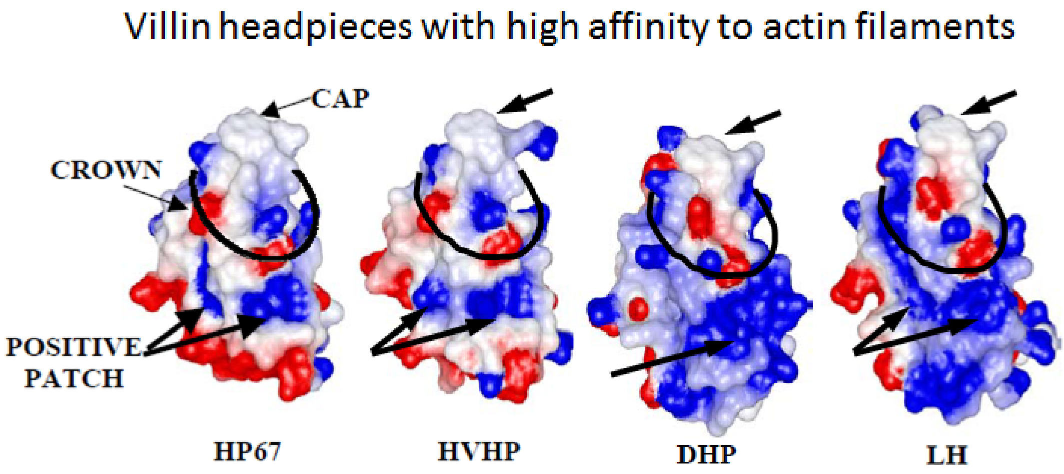

Figure 1.33 Surface charge studies for different headpiece domains that show high affinity to actin filaments. All of them present a hydrophobic region, an alternate positive and negatively charged patch called crown and a highly positive region below the crown. HVHP: human villin headpiece, DHP: dematin headpiece, LH: limatin headpiece. Red, blue, white: Negative, positive, and neutral charges, respectively [43].

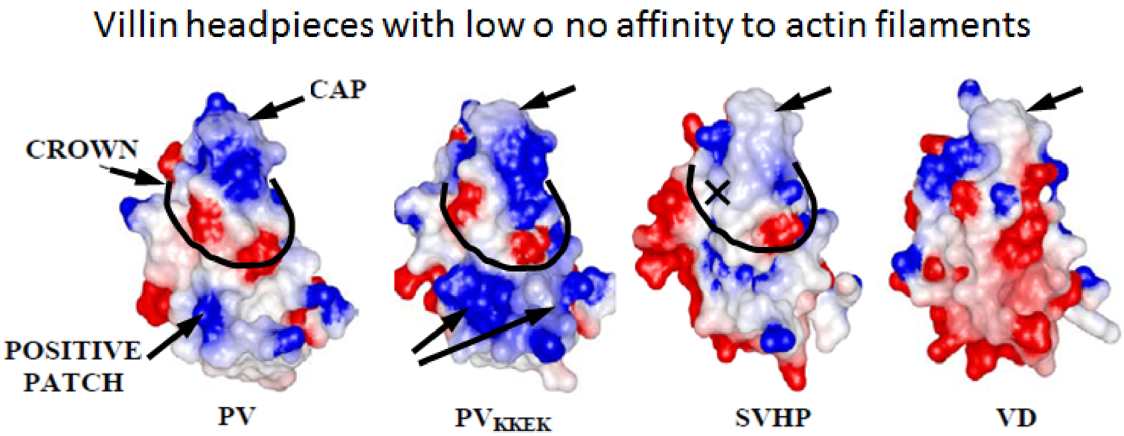

Figure 1.34 Surface charge studies for different headpiece domains that show low affinity or nonspecific binding to actin filaments. Protovillin (PV) and its mutated version PV_{KKKEK}, show a defined crown but the hydrophobic region is not present anymore. Nevertheless, the presence of a positively charged region below the crown maintains a low affinity to actin filaments. The larger positive region in the mutated PV results in a higher affinity compared to the wild type. Supervillain headpiece (SVHP) and villidin headpiece (VD) miss of the positive patch below the crown resulting in the inability to bind actin filaments. In addition, in the SVHP, the alternating charge crown is also less evident. Red, blue, white: Negative, positive, and neutral charges, respectively [43].

Actin-binding LIM2 (ABLIM2) is a 67.8kDa (611aa) actin binding protein composed of four LIM domains, followed by a linker region and then a Villin Headpiece Domain (VHD) at C-terminus (Figure 1.35) [45]. ABLIM2 can interact with a striated muscle activator called both STARS (Striated Muscle Activator of Rho Signaling) or MS1 (Myocyte Stress 1) and it was discovered that this complex is critical in the inducing of left ventricular hypertrophy [46]. The possibility to study the mechanism of interaction between this complex and actin filaments could provide the necessary information to find a clinical approach in the solving left ventricular hypertrophy.

In this work, it is presented a new approach based on ssNMR data acquisition for the characterization of the complex that occurs between actin filaments and the small VHD domain from ABLIM2 making the first step in the understanding how the ABLIM2-MS1 interact with the actin filaments.

Figure 1.35 Domains organization of ABLIM2

The alignment between the sequence of the chicken VHD (HP67) and the human VHD from ABLIM2 showed that the most important residues supposed to be involved in the binding with actin are almost conserved (Figure 1.36). Thus, the alternate surface charge is also conserved suggesting a high affinity to F-actin for human VHD from ABLIM2 (Figure 1.37).

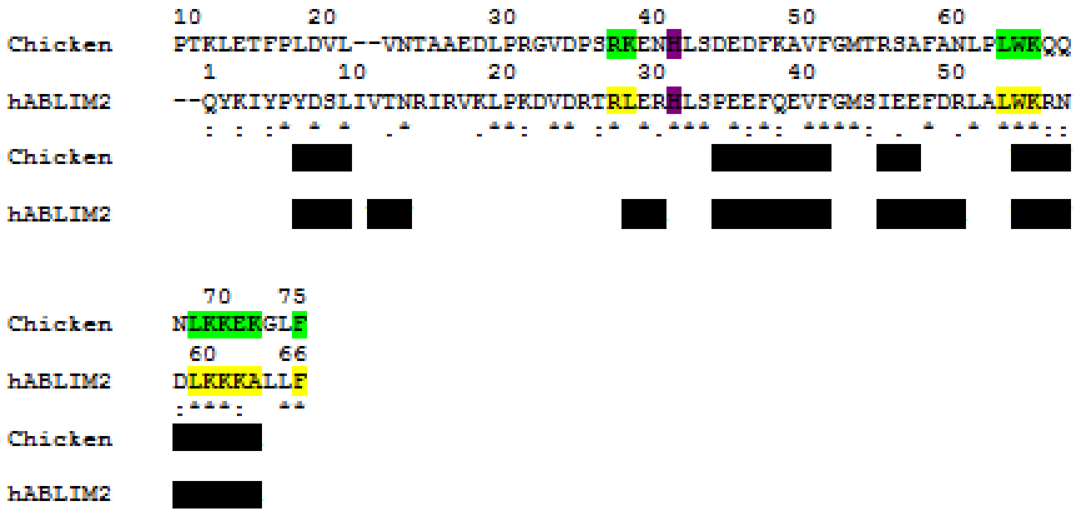

Figure 1.36 Sequence alignment between the sequence of the chicken VHD and the human VHD from ABLM2. In the alignment "*" means identical residues, ":" means conserved substitutions (residues in the same group) and "." means semi-conserved substitution (residues with similar shapes). The black barrels indicate the helix motifs in the VHD structure. The residues that will create the cap region (63-65 in the HP67sequence), the crown (K65, E72, K71, R37 in the HP67sequence) and the positive patch (K38 and K73) are highlighted in green (HP67) and yellow (human VHD). The histidine 32 in the HP67 sequence is highlighted in purple.

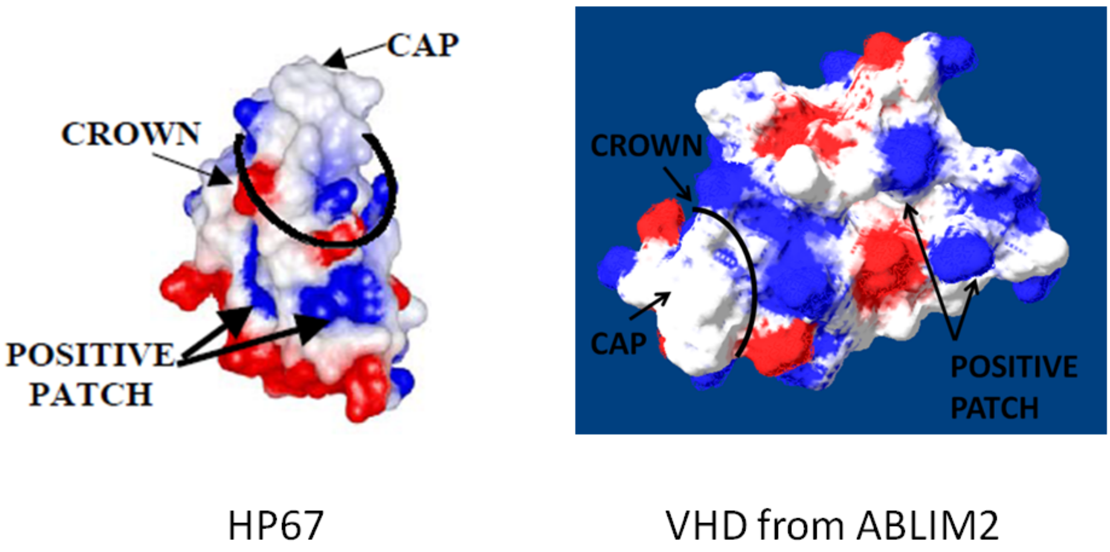

Figure 1.37 Electrostatic potential map of VHD surface probably involved in the binding with actin for HP67 and VHDF from ABLIM2 isoforms. The blue pattern indicates the positively charged residues while in red are indicates the negatively charged residues.

The structure of human VHD from ABLM2 was already solved by NMR in solution and deposited (Figure 1.38) (RBMB: and PDB: 2L3X). For the complete assignment made by NMR on a uniformly labelled ^{13}C-^{15}N VHD in solution refers to APPENDIX D.

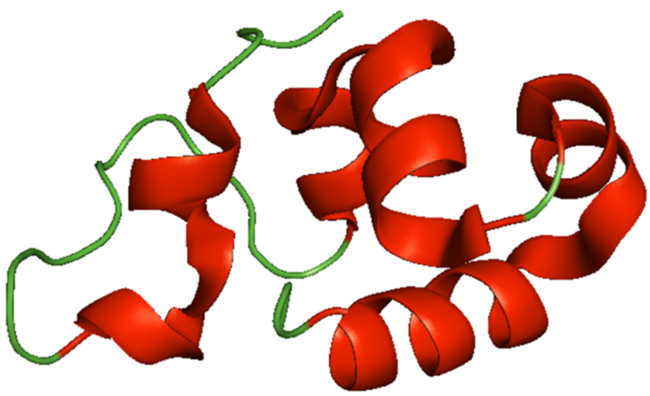

Figure 1.38 Ribbon structure of VHD from ABLIM2 solved by solution NMR (PDB: 2L3X).

2 solid state Nuclear Magnetic Resonance Spectroscopy

2.1 An introduction to the NMR spectroscopy

NMR is a spectroscopic technique able to produce information at atomic level about nuclei with non-zero spin quantum number *I*. In macromolecular studies, hydrogen (^{1}H) is the most commonly investigated nucleus by NMR due to its high natural abundance (near 99.98% of the total hydrogen) and intrinsic high sensitivity. Furthermore, ^{1}H monitoring allows the performance of simple and fast experiments that provide information about the purity of samples, the folding of proteins and a crude evaluation of the elements of secondary structure in a macromolecule. Other relevant nuclei in macromolecular studies are nitrogen (^{15}N isotope), carbon (^{13}C isotope) and phosphorus (^{31}P) which all have a natural abundance of 0.4%, 1.1% and 100% respectively (Table 2.1).

Nucleus	Spin	Gyromagnetic ratio (10^{7} rad T^{-1} s^{-1})	Natural Abundance (%)	Absolute Sensitivity
Hydrogen ^{1}H	$^{1}/_{2}$	26.75	99.98	1.0
Deuterium ^{2}H	1	4.10	0.015	$1.45{\cdot}10^{-6}$
Carbon ^{13}C	$^{1}/_{2}$	6.72	1.108	0.000176
Nitrogen ^{15}N	$^{1}/_{2}$	-2.71	0.37	$3.85{\cdot}10^{-6}$
Fluorine ^{19}F	$^{1}/_{2}$	25.18	100	0.83
Phosphorous ^{31}P	$^{1}/_{2}$	10.84	100	0.0663

Table 2.1 Value of spin, natural abundance and absolute sensitivity for the most relevant nuclei analysed in the investigation of biological macromolecules. Absolute sensitivity of a nucleus is calculated as its relative sensitivity multiplied for its natural abundance ($\gamma^{3} \cdot C \cdot I(I+1)$ where γ represent the nuclei gyromagnetic ratio while C and I represent, respectively, its natural abundance and spin number). Absolute sensitivity represents the relative receptivity of a nucleus compared with the hydrogen and it is used to understand the nuclear response of nuclei in natural abundance.

NMR spectroscopy, similarly to other spectroscopic techniques, measures the energy emitted by molecules during the relaxation from an excited state to the ground state. In NMR spectroscopy the excitement of molecules involves transitions between nuclear spin levels. In this spectroscopy the presence of an external magnetic field is required in order to create a ground state in which the energy levels associated with the spins system are not degenerated. The ground state corresponds to the equilibrium condition of the entire system [47].

In quantum mechanics, the spin is a fundamental and intrinsic property of particles such as charge and molecular mass. As the name suggests, spin was originally conceived as the rotation of a particle around its own axis. Spins obey the laws of quantized angular moments and in addition they are associated with a nuclear magnetic moment (μ_n). The nuclear magnetic moment (μ_n) is related to the strength of the magnetic field produced by nuclear spins. In the absence of an external magnetic field a collection of nuclear spins (and as consequence their related μ_n) can adopt all possible spatial orientations. When placed in a magnetic field B_0, the μ_n of NMR active nuclei with $I = {}^1/_2$ can assume two orientations, same or opposite direction in respect of the external magnetic field. Nevertheless, the same direction of magnetic field is energetically favored, meaning that, at thermal equilibrium, the nuclear magnetic dipole moments are asymmetrically distributed defining a Boltzmann distribution. As a consequence, the vectorial sum of all the magnetic moments will produce a net magnetic field along the direction of the applied field. This is called bulk magnetization of the sample and can be represented by a vector, called magnetization vector. When a magnetic dipole moment is under the influence of an external magnetic field B_0, it experiences a torque moment that tilts its direction of an angle ϕ in respect B_0 and induces the precession of the magnetic moment around the direction of B_0. This precession of a spin around B_0 is called Larmor precession and its frequency is defined as:

$$\omega_0 = -\gamma B_0 \text{ in rad s}^{-1}$$
$$\omega_0 = \frac{-\gamma B_0}{2\pi} \text{ in Hz} \qquad (2.1)$$

where γ represent the magnetogyric ratio, a constant specific for a given type of nucleus. To perturb the equilibrium state of the magnetization vector, an additional magnetic field B_1 is applied perpendicularly to B_0, at or near its Larmor frequency (ω_0). As a consequence, the magnetization vector is forced to move from the *z-axis* (the direction aligned to B_0) to the *xy-plane* where it continues to precess at its Larmor frequency. If the magnetization vector is placed inside a coil, its precession in the *xy-plane* will induces a current that can be measured that is called Free Induction Decay signal (FID). The terms decay derives from the exponential decay during the time of the induced current originated by the return of the magnetization vector to the equilibrium state. As a consequence, the signal is recorded in function of time. The time-domain signal is then converted into the frequency-domain representation by Fourier Transform that generates an output in which the data are shown as a function of frequency [47].

2.2 An insight into the phenomenon of relaxation

In NMR, with the term relaxation we refer to the processes by which spins return to the equilibrium state after being perturbed. The relaxation is achieved by two different processes. The return of the z-magnetization from the *xy-plane* to its equilibrium value is called *longitudinal relaxation* or *spin-lattice relaxation* (T_1). Such relaxation is brought about by local magnetic fields that are oscillating at the Larmor frequency promoted by molecular motions that lead to reorientation of interacting spins with respect to each other and the external magnetic field. The process by which transverse magnetization decays away to its equilibrium value of zero is called *transverse relaxation* or *spin-spin relaxation* (T_2) [47].

In solution, random collisions among molecules induce a random motion in a molecule that is defined as rotational diffusion. Due to this rotational diffusion it is important to introduce the notion of rotational correlation time (τ_c) which is the average time that it takes for a molecule to end up at an orientation about 1 radian from its starting position. For small molecules τ_c is around 10ps while for proteins could reach 10ns [47]. The overall rotation characterized by the correlation time represent the lead molecular motion causing the reorientation in the interaction spins that is behind the phenomenon of relaxation. The plot of T_1 and T_2 versus τ_c (Figure 2.1) well summarize the general features of the relaxation dependence on the correlation time.

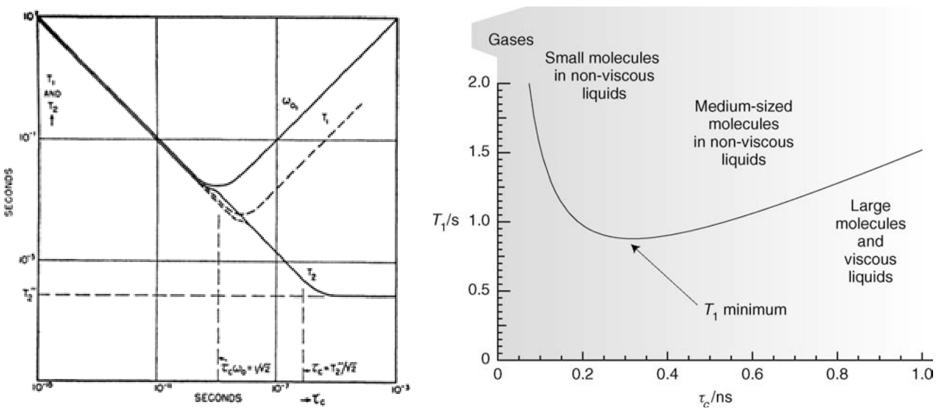

Figure 2.1 Left Panel) Dependence of T_1 and T_2 upon τ_c, according to the simplified theory in which all interaction are assumed to have the same correlation time [48]. Right panel) The spin–lattice relaxation time constant as a function of correlation time for random field fluctuations. Typical ranges of correlation time are shown [49].

To better understand the implications that this graph involve, it is important to remember that the value of τ_c is directly dependent on the size of a molecule and the viscosity of a solution. When the correlation time is short (small molecules), T_1 and T_2 are equal and this is called extreme narrowing limit. Analyzing the trend of T_1 in function of τ_c it is possible to observe that, after an initial decreasing, T_1 goes through a minimum and then increases with increasing τ_c. On the other hand, T_2 only decreases with increasing τ_c. The importance of this behavior is explained when the length of the relaxation parameters $T_1$and T_2 are considered in relation to the linewidth of an NMR signal. In NMR discussions it is usually assumed that it is possible to define T_2 as a measure of the inverse of the linewidth of a signal. The FT applied during the acquisition of an NMR experiment generates a function $S(\omega)$ called absorption Lorentzian which identifies a signal in a NMR spectrum:

$$S(\omega) = \frac{\lambda}{\lambda^2 + (\omega - \omega_0)^2} \tag{22}$$

The parameter λ is called the coherence decay rate constant, and is approximation is equal to the inverse of the transverse relaxation time constant T_2:

$$\lambda = \frac{1}{T_2} \tag{2.3}$$

Therefore, the linewidth at half-height of a Lorentzian peak $lw_{1/2}$, measured in Hz, can be defined as:

$$lw_{1/2} = \frac{1}{\pi T_2} \tag{2.4}$$

It is easy to understand how increasing the value of T_2 the value of $lw_{1/2}$decreases [50]. Remembering that the value of T_2 decreases when τ_c increases (Figure 2.1, left panel), NMR peaks get progressively broader as the molecular mass increase. This behavior represents the fundamental limit on the study of macro-complexes by solution NMR. Their big size means very long τ_c and hence very short T_2 which results in broad signal with a very low signal to noise ratio. On the other hand, in solid state NMR, the motion of the molecules are completely avoided and the concept of τ_c does not have any meaning anymore. This means that the size of a molecule does not matter anymore in terms of relaxation allowing the potential investigation of any macromolecule independently from its dimension. Nevertheless, in ssNMR the relaxation is caused by different mechanisms that contribute to the broadening of a signal in a different significance. Chemical shielding, dipole coupling and quadrupole coupling are the principal interactions in a sample that define the broadening of a signal. To be precise, the same interactions affect the spins also in solution NMR but, in this case, the tumbling of the molecule average to zero their contribution making them negligible.

2.3 solid state NMR spectroscopy: a brief introduction

2.3.1 Hamiltonian operator and its meaning

In quantum mechanics, the state of a system, such as a nuclear spin or a collection of spins immerse in a specific environment, is described by a wavefunction denoted by the Greek letter ψ or Ψ [51]. If the wavefunction of a system is known it would be possible to deduce anything from that system. In order to extrapolate these information specific operator has to be involved. An operator is something that acts on a function to produce a new function [47]. The solution of the new function generate specific operator describes the corresponding observable physical information for the system described by Ψ [51]. The total energy of a system is described by a particular operator that is called the *Hamiltonian operator* and it is defined as:

$$\hat{\mathcal{H}} = \hat{V} + \hat{K} \tag{2.5}$$

where $\hat{V}$ represent the potential energy operator and $\hat{K}$ is the kinetic energy operator [50].

2.3.2 Powder spectrum, when the molecular interactions matters

Generally in solid-state NMR the samples are represented, for the majority, by a powder consisting of many crystallites with random orientations. All the molecular interactions mentioned above, chemical shielding, dipole-dipole interaction and quadrupole coupling, are dependent on the crystallite orientation in respect of the external magnetic field and for this reason they are defined as anisotropic. In static ssNMR, this dependence on the orientation of the molecular interactions contributes to widening the linewidth of a signal resulting in a spectrum called powder spectrum (Figure 2.2) [51].

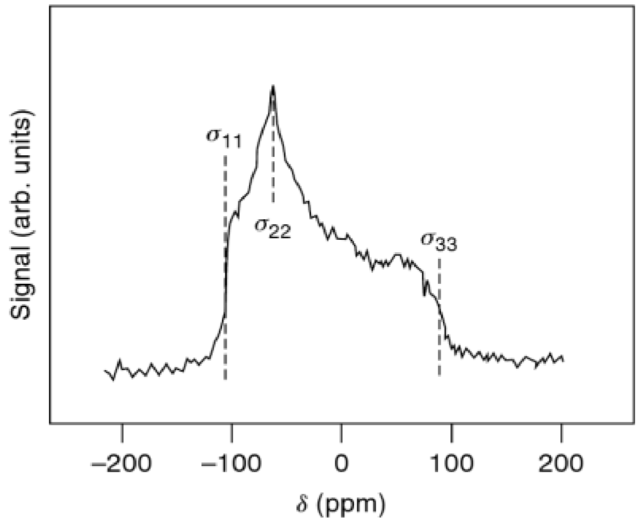

Figure 2.2 Experimental ^{19}F powder spectrum of fluoranil ($C_6F_4O_2$ at 300K) [52].

To explain the reasons of this broadening of the signals with dependence to the orientation it is necessary to consider all the interactions that can affect a spin. The expression for the total Hamiltonian $\widehat{\mathcal{H}}$ for a spin system takes the following form:

$$\widehat{\mathcal{H}} = \widehat{\mathcal{H}}_{ext} + \widehat{\mathcal{H}}_{int} \tag{2.6}$$

where $\widehat{\mathcal{H}}_{ext}$ take into consideration the external magnetic field B_0 and $\widehat{\mathcal{H}}_{int}$ represent the internal molecular interactions and it can be represented as the sum of them:

$$\widehat{\mathcal{H}}_{int} = \widehat{\mathcal{H}}^{CS} + \widehat{\mathcal{H}}^{Q} + \widehat{\mathcal{H}}^{II} + \widehat{\mathcal{H}}^{IS} + \widehat{\mathcal{H}}^{SS} \tag{2.7}$$

where the first term represents the shielding contributions, the second term the quadrupolar contributions and the last three summarize all the direct and indirect spin-spin interactions between two different species of spin (*I* and *S*)[53]. It becomes evident that, in an NMR experiment, a spin system does not interact only with the external magnetic field B_0, but small local magnetic fields (B_{loc}) arising from other nuclear magnetic dipoles and electron shielding can affect the spin system as well. In solution NMR the effect of these B_{loc} is averaged to zero by the tumbling of the molecule. On the other hand, in ssNMR the tumbling of the molecule is not allowed meaning that a set of similar spins under the influence of an external magnetic field can differently experience the surrounding B_{loc} if not perfectly aligned as it happens in highly ordered system such as crystals. This implication introduces two related concepts that are fundamental in ssNMR spectroscopy: the orientation dependence of the spin interactions (discussed later in the chapter) and the idea of sample homogeneity. Homogeneous samples are intended as ordered samples and, as consequence, it is easy to understand that homogeneity and contribution from spin interaction are indirectly related. A homogeneous sample implicates an ordered sample in which the contribution from the spin interactions to the broadening of a signal will be small. Unfortunately, in most cases the samples for ssNMR consist of crystallites, powder or gel-like pellets characterized by a low internal order. Even if there are techniques (described in detail later in this chapter) that can help to narrow the signals, in some case these are not sufficient to average to zero the contribution from these orientation dependent interactions and an improvement in the homogeneity of the sample is necessary to improve the resolution.

The quadrupolar interaction will not be discussed because its contribution is averaged to zero when nuclei with spin $1/2$ such as ^{13}C, ^{15}N, ^{1}H, ^{31}P or ^{19}F, (the nuclei mostly studied in biologic characterizations) are taken into consideration.

2.3.3 Shielding interaction and chemical shift

The electrons surrounding a nucleus when immersed in a magnetic field interact with the field inducing currents in the electronic clouds. These currents generate a secondary magnetic field (B_{loc}) that contributes to the total field that affects the nucleus changing its resonance frequency. The interaction of this secondary field produced by the electrons with a close nucleus is called *shielding interaction* (σ). Performing an NMR experiment, it is impossible to measure absolute frequencies, so a reference compound is added to a sample. The frequency of any signal in a NMR spectrum is measured as difference in frequency with the reference substance and it is quoted as *chemical shifts* with respect to that substance. As previously mentioned, the chemical shift depends on the orientation of a molecule in respect of the external magnetic field B_0 and the surrounding nuclei (Figure 2.3) so it cannot be treated as a scalar number like in solution NMR but like a tensor. This tensor is called chemical shift tensor σ [49, 51].

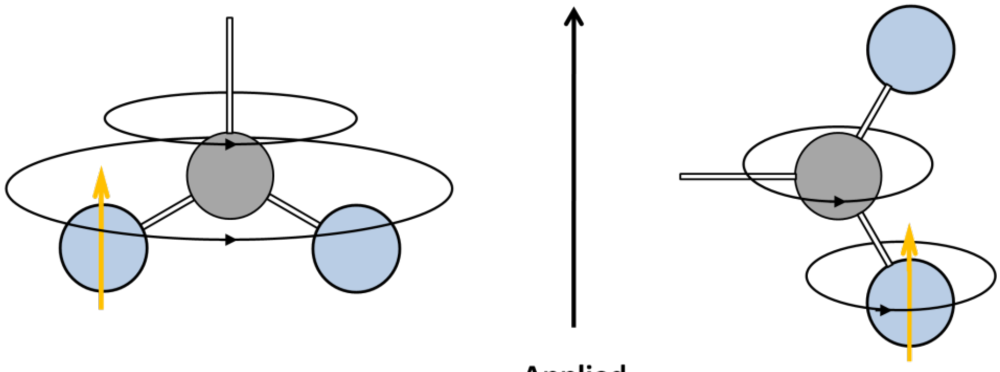

Figure 2.3 Illustration of the orientation dependence of the shielding interaction. The size and the direction of the shielding field experienced by the nuclear spin (yellow arrow) depend on the orientation of the electron density with respect to the applied magnetic field [51].

The Hamiltonian equation associated to the shielding effect by a spin I is defined as:

$$\mathcal{H}^{CS} = -\gamma I \cdot \sigma_{lab}^{xyz} \cdot B_0 \tag{2.8}$$

where γI identified the magnetic moment, B_0 is the external magnetic field and the chemical shield tensor σ is characterized by its orientation in the given reference frame (the simplest is the Cartesian frame x, y and z called laboratory frame)[51]. The mathematical development of the chemical shielding Hamiltonian will not be discussed here. Nevertheless, it is important to highlight that the contribution to the frequency of an observed nucleus from the chemical shielding (with axial symmetry) is dependent on $(3\cos^2\theta - 1)$ where θ is defined as the angle between B_0 and the orientation of σ [51].

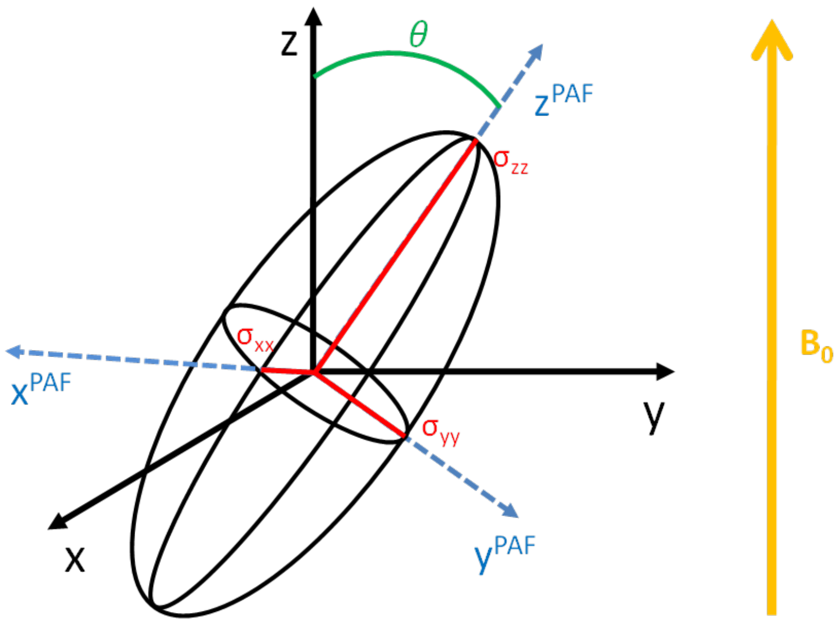

Figure 2.4 Relation between the Principal Axis Frame (blue dotted lines) and the laboratory frame (black lines). The component for the chemical shift shielding is reported as red lines. θ is defined as the angle between B_0 and the orientation of σ [51].

To explain what the orientation dependence of chemical shift implies we can use a carboxyl group under the influence of an oriented external magnetic field as a model (see Figure 2.5). As shown in the picture the carboxyl group could be randomly oriented, so all its possible orientations are present with a random distribution. Powder patterns arise because each different molecular orientation with respect to B_0 has its own spectral frequency. Each different orientation thus gives rise to its own (sharp) spectral line.

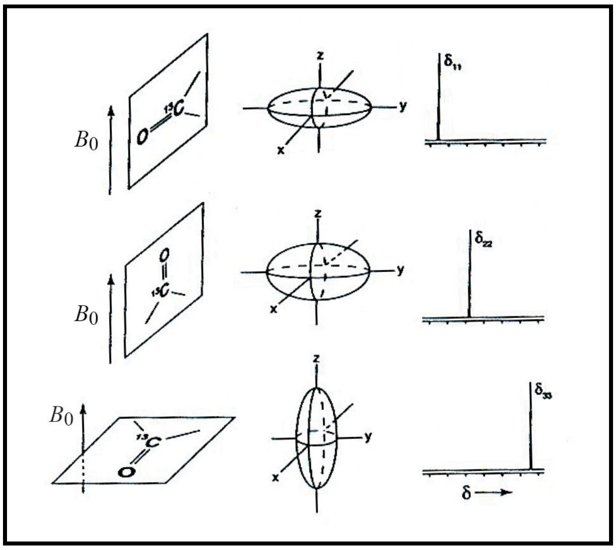

Figure 2.5 The dependence of chemical shift upon orientation for the ^{13}C nucleus of a carboxyl group [54].

The lines from different orientations overlap continuously giving rise to the observed powder pattern. Depending in the symmetry of the σ tensor contributions in the sample the powder spectra assume typical patterns as shown in Figure 2.6 [49, 51].

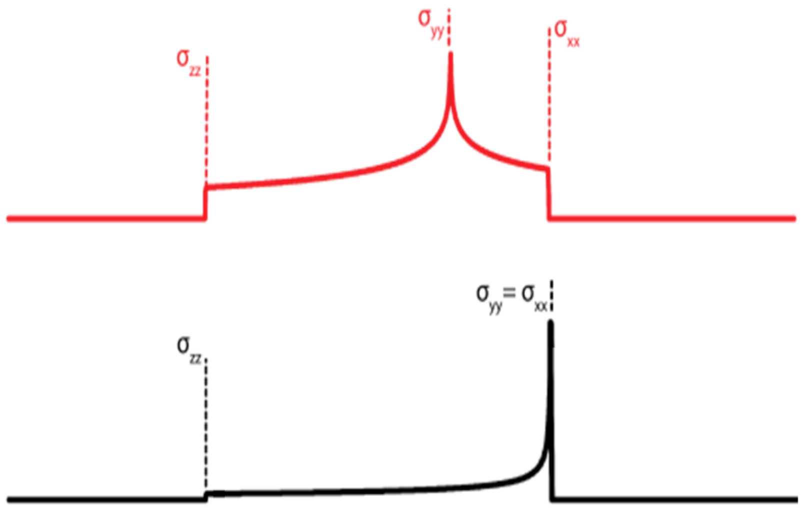

Figure 2.6 Chemical shift anisotropy powder pattern calculated for sample with no axial symmetric tensor contribution (red spectrum) with $\sigma_{zz} \neq \sigma_{yy} \neq \sigma_{xx}$ and with axial symmetry $\sigma_{zz} \neq \sigma_{yy} = \sigma_{xx}$.

2.3.4 Dipolar coupling

As previously mentioned, in quantum mechanics every spin is associated with a magnetic moment. This means that they could create a local magnetic field that is able to interact with other spins in the neighborhood. This kind of interaction through space is called dipole-dipole (or dipolar) coupling (Figure 2.7).

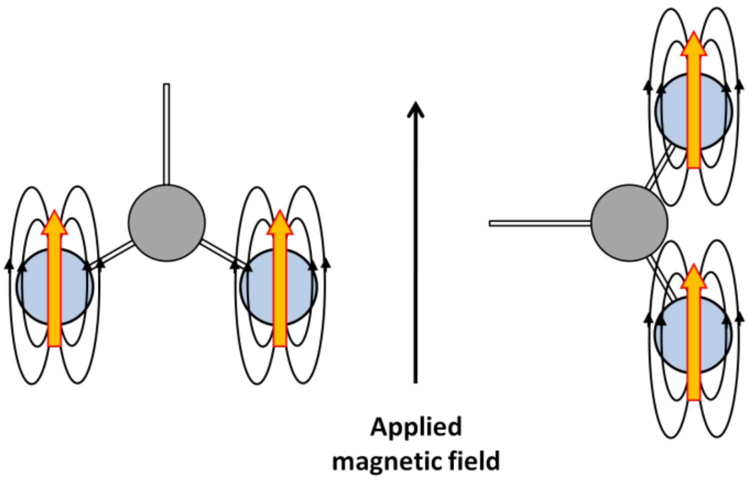

Figure 2.7 Illustration of the orientation dependence of the dipolar coupling between two nuclear spins (orange arrows). The interactions between these local fields depend on the relative position in space of the two spins with respect to the applied magnetic field [51].

The interaction Hamiltonian for dipolar coupling between two spins *I* and *S* in angular frequency units (rad s^{-1}) is defined as:

$$\mathcal{H}^{DD} = -\left(\frac{\mu_0}{4\pi}\right)\gamma_I\gamma_S\hbar\left(\frac{I\cdot S}{r^3} - 3\,\frac{(I\cdot r)(S\cdot r)}{r^5}\right) \tag{2.9}$$

where $\left(\frac{\mu_0}{4\pi}\right)\gamma_I\gamma_S\hbar$ is called dipolar-coupling constant (in rad s^{-1}), $\frac{I\cdot S}{r^3}$ represent the internuclear contribution and $\frac{(I\cdot r)(S\cdot r)}{r^5}$ the molecular orientation. The development of the Hamiltonian to obtain the operator for $\hat{\mathcal{H}}^{DD}_{homo}$ and $\hat{\mathcal{H}}^{DD}_{hetero}$ will not be discussed but it is important to highlight that for both the dipolar coupling is dependent on the orientation in the form of $(3\cos^2\theta - 1)$. The strength of the interaction for the dipolar coupling depends principally on two factors: the internuclear distance (with dependence of $1/_{r^3}$ where r represent the distance) and the molecular orientation.

It is important to distinguish between two types of dipolar coupling: homonuclear and heteronuclear dipolar coupling. Even if they are generated in the same way their effect is different. The effect of the homonuclear dipolar coupling ($\hat{\mathcal{H}}^{DD}_{homo}$) is to widely broaden the linewidth of signals. If the system of coupled spins is large enough, the lineshape of the resulting signal approximates a gaussian. For this reason, the strong dipolar coupling among ^1H determines linewidth in macromolecules usually in the order of hundreds of kHz (Figure 2.8). The effect of the heteronuclear dipolar coupling ($\hat{\mathcal{H}}_{hetero}^{DD}$) on a spin system is similar to the effect produced by the scalar coupling. In a system of two spins *I* and *S* (both with spin $^1/_2$) the effect of $\hat{\mathcal{H}}_{hetero}^{DD}$ results in the splitting of the signal as a doublet (Figure 2.9) [51].

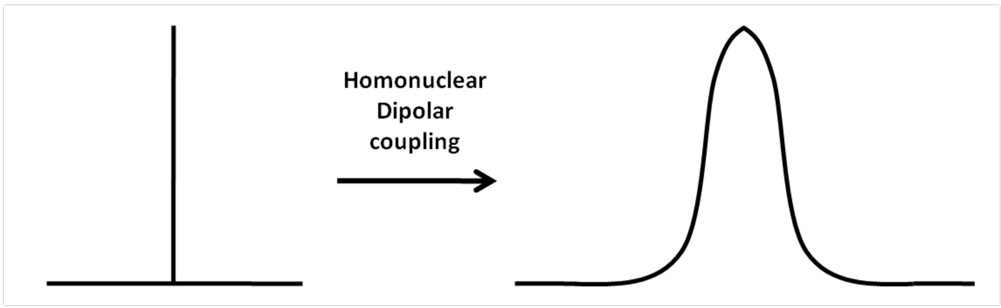

Figure 2.8 Homonuclear dipolar coupling contributes to the broadening of a resonance line giving the typical shape of a Gaussian to the signals.

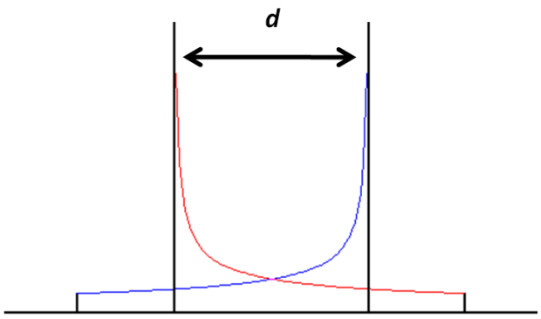

Figure 2.9 The splitting of the powder spectrum of a spin *I* due to the effect of heteronuclear dipolar coupling on a two-spin system *I* and *S*. The distance in Hz is equal to the coupling constant *d*.

When the nuclear coupling is discussed, it is important to distinguish the dipolar coupling from the scalar (J) coupling, that is an indirect coupling of the nuclear spins mediated by the electrons involved in the binding between the nuclei. In solution, the dipolar coupling is averaged to zero by the tumbling of the molecule while the scalar coupling survives because this is an interaction independent of molecular orientation. Consider a system in which two nuclei are bound. The electrons involved in the binding are in a degenerate state as the Pauli principle states. Nevertheless, when the nuclei are taken into consideration their polarization can generate different states depending on their orientation (up or down) respect each other generating an isotropic component that is not averaged by the tumbling (Figure 2.10). The presence of J-coupling leads to a splitting of the line of a spin resonance that gives information about the binding framework in which the spin is located.

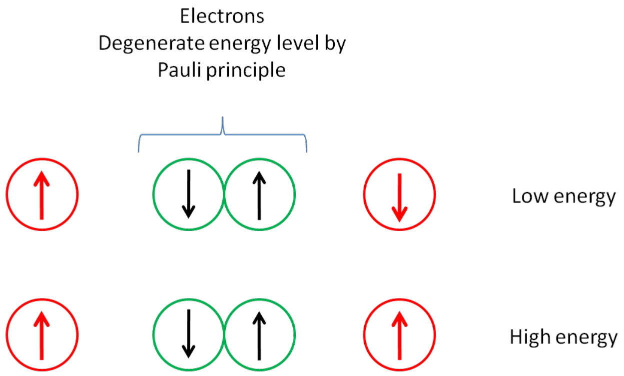

Figure 2.10 Scalar coupling mechanism. The energy levels related to the electrons involved in the binding are degenerated as enunciated by the Pauli principle while it is the orientation of the polarization of the nuclei bound that generates this small magnetic component that is orientation independent ("scalar").

Scalar coupling affects two nuclei bound to each other also in ssNMR spectroscopy but in this case its contribution compared to the dipole-dipole coupling is small enough to be ignored. In Table 2.2 is reported the relative magnitude (in Hz) of the major interactions that affect a spin in ssNMR when under the influence of an external magnetic field B_0. The contribution from quadrupole coupling is zero for nuclei with spin $^1/_2$. On the other hand, chemical shift and dipolar coupling relative magnitude results to be a thousand time higher than scalar coupling effect making this contribution negligible.

Interaction	Magnitude [Hz]
Quadrupole coupling	10^6
Dipolar coupling	10^4
Chemical shift	10^3
Scalar coupling	10

Table 2.2 Relative magnitude of the major interactions that affect a nucleus under the influence of an external magnetic field B_0 [55] [50].

2.4 Techniques used to reach high-resolution in ssNMR spectra

Usually, in solid state, the samples consist of molecules with random orientations such as crystallites or powder. As previously described, all the nuclear interactions which affect a spin system depend on the orientation in which they work, and their effects result in a powder spectrum which contains broad lines. Hence, it is necessary to minimize these effects to achieve high resolution in the spectra. Two techniques are routinely applied in ssNMR spectroscopy to achieve a resolution similar to that it is usually reached in solution NMR: Magic-angle spinning (MAS) and dipolar decoupling pulse sequences (Figure 2.11). It is useful to report that the dependence on the orientation of the molecular interactions takes the forms reported in Table 2.3 [51].

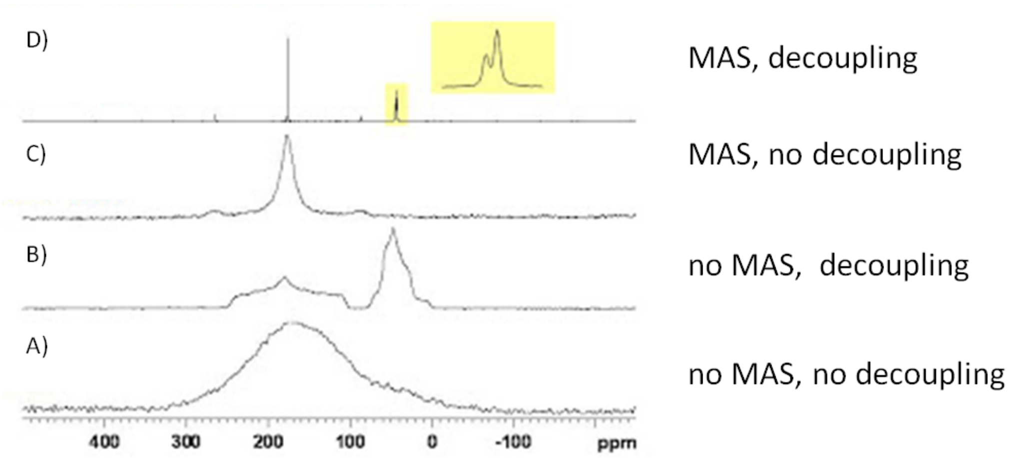

Figure 2.11 Effects of the implementation of MAS technique or high power ^1H decoupling on ^{13}C CP spectra of glycine acquired at 4.7T. In row a) is reported the spectrum of glycine recorded with neither MAS nor decoupling. In line b and c are reported the spectra when, respectively, decoupling and MAS were applied and an improvement in the resolution is observable. In row d) both the technique were applied simultaneously and the effect of the combination is clearly noticeable [56].

Interaction	Term for the dependence on the orientation
Dipolar coupling	$(3\cos^2\theta - 1)$
Chemical shift anisotropy	$(3\cos^2\theta - 1)$
Quadrupolar interaction	$(3\cos^2\theta - 1) - \eta_Q \sin^2\theta \cos\phi$

Table 2.3 Dependence of the major nuclear interactions to the orientation. The angles θ is defined as the angle between B_0 and the orientation of spin interaction tensor observed.

2.4.1 Magic-angle spinning (MAS)

Magic-angle spinning allows achieving an effect similar to the isotropic tumbling of the molecules in a solution. Consider the experimental setup described in Figure 2.12. As discussed previously, the orientation dependence is in the form of $(3\cos^2\theta - 1)$ where θ is the angle between the applied magnetic field and the orientation of the spin interaction tensor (the shielding tensor for the chemical shift, the dipolar tensor for the dipolar coupling, etc.).

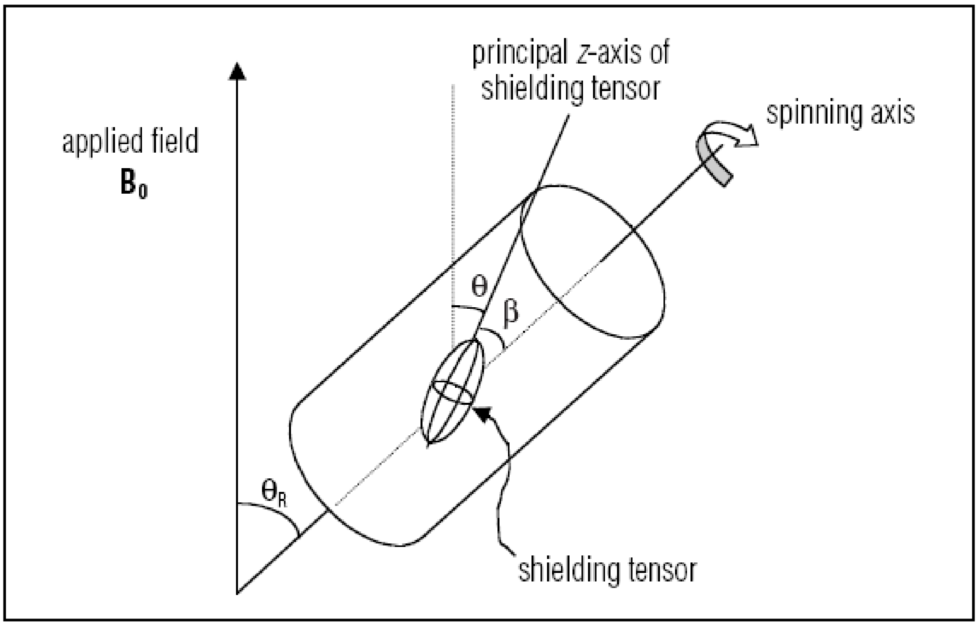

Figure 2.12 The setup for a MAS experiment. The rotor in which is contained the sample is spun at high speed about the spinning axis which orientation is set to θ_R (the angle between the spinning axis and the applied magnetic field B_0). When θ_R is set to 54.74° (the magic-angle value) MAS removes the effects of chemical shielding anisotropy and heteronuclear dipolar coupling [51].

In a powder sample, the angle θ can take all the possible values because all molecular orientations are allowed. As a consequence, the spin interaction tensors have a different value for each orientation contributing to broaden the linewidth of a signal as briefly described in the previous paragraphs. However, if we spin the sample about an axis inclined at an angle θ_R from the applied magnetic field, then θ varies in relation of the rotation of the molecule. The average of the orientation dependence of the nuclear spin interactions under this experimental design becomes:

$$\langle 3\cos^2\theta - 1\rangle = \frac{1}{2}(3\cos^2\theta_R - 1)(3\cos^2\beta - 1) \tag{2.10}$$

where the angles β and θ_R are defined in Figure 2.12. The angle β similar to the angle θ can take on all possible values for a powder sample. On the other hand, the angle θ_R is decided by the user and if it is set to 54.74° then the contribute $(3\cos^2\theta_R - 1)$ became zero as became zero also the average $\langle 3\cos^2\theta - 1\rangle$. In order to efficiently average to zero the anisotropy, the sample has to be spun at a rate that is 3-4 times greater than the contribution of the interaction [51]. This explain why, till recent, it was not possible to acquire experiments directly on proton dimension: the available probes were not able to reach spinning rate sufficiently high to average the contribution from the ^1H homonuclear dipolar coupling. Thus, a spinning rate slower than the anisotropy produces a set of spinning sidebands in addition to the line due to the isotropic chemical shift. The result of this approach is a considerable improvement in the resolution of a ssNMR spectrum as shown in Figure 2.13.

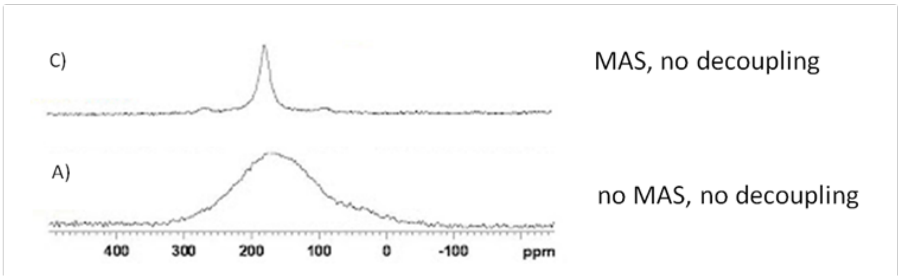

Figure 2.13 Effect of the Magic-Angle Spinning in the study of glycine. The increase in the resolution due to the erase of the orientation dependence of nuclear interaction is noticeable even if the resolution achieved is not enough to distinguish the different signals.

2.4.1.1 Magic-angle spinning for homonuclear dipolar couplings: Ultrafast spinning MAS

The dipolar coupling Hamiltonian for a homonuclear-coupled spin pair, *I* and *S*, is

$$\mathcal{H}_{homo}^{dd} = -d\frac{1}{2}(3\cos^2\theta_R - 1)\left[3\hat{I}_z\hat{S}_z - \hat{I}\cdot\hat{S}\right] \tag{2.11}$$

where *d* is called dipolar coupling constant $\left(\frac{\mu_0}{4\pi}\right)\frac{\gamma_I\gamma_S\hbar}{r^3}$. As explained in 2.4.1 the MAS technique can average to zero this Hamiltonian, providing the rate of spinning is fast compared to the homonuclear dipolar-coupling linewidth. Ultrafast spinning rates in the range of 70-100kHz are now available in several probes and they are fast enough to average the homonuclear proton coupling and produce spectra at high resolution for ^1H. The averaging of $\mathcal{H}_{homo}^{dd}$ to zero allows to record experiments in indirect acquisition rendering experiments like 2D ^1H-^{15}N correlation spectra suitable also for ssNMR with all the benefit that derives from their application in the investigation of biological samples [49].

2.4.2 Heteronuclear decoupling

The most effective and simplest technique able to averages to zero the effect of heteronuclear dipolar coupling ($\mathcal{H}_{hetero}^{dd}$) is high-power decoupling. It consists in the application of a continuous irradiation of very high power at the frequency of the atom (interested in the decoupling) resonance. Usually for biological samples, these kinds of pulses are applied on protons which are the most abundant nucleus in the sample. The gain in resolution of a ^{13}C spectrum when protons are decoupled is considerable as shown in Figure 2.14 [51].

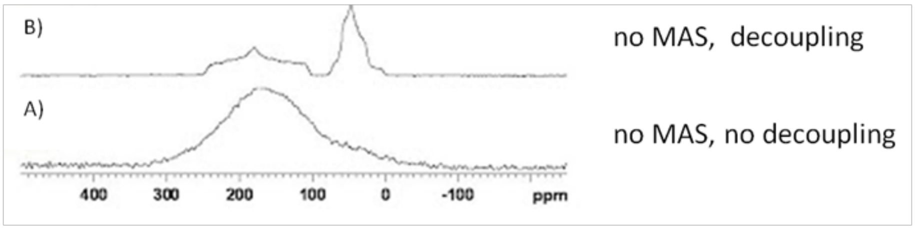

Figure 2.14 Effect of the proton decoupling in the study of glycine. The increase in the resolution due to the erase of the dipolar coupling between proton and carbon is noticeable even if the resolution achieved is not enough to distinguish the different signals.

The required pulse sequence for the acquisition of the other nucleus/i is simultaneously applied and the FID is measured while the high-power decoupling is working (see Figure 2.15). The effect of this rf pulse close to Larmor frequency is to cause a spin system to undergo repeated transition $(\alpha \leftrightarrow \beta)$ at a rate determined by the amplitude of the irradiation [51]. To work efficiently, the rf amplitude for the decoupling should be at least three time greater than the largest $\mathcal{H}_{hetero}^{dd}$. On the other hand, the application of high power during the acquisition means that high power is acting on the probe. This level of power could be a serious source of damage for the probe if not well calibrated. Thus, it is very important that the probe is very well tuned for both the decoupled and the observed frequencies in order to avoid electrical arcing which occurs when high-power decoupling is used in a poorly tuned instrument. The damages produced by the electrical arcing could require a repair or replacement of the probe [49, 51].

When heteronuclear decoupling is applied at the same time of MAS technique it is important to remember that if the decoupling amplitude is similar to the spinning rate the two techniques interfere with each other. When low speed spinning (5-20kHz) and high power decoupling (>60kHz) is used, no problems arise. On the other hand, for the ultrafast spinning MAS experiments (>50kHZ) it can be more effective to use low-power decoupling to avoid interference between the two process [57],[58].

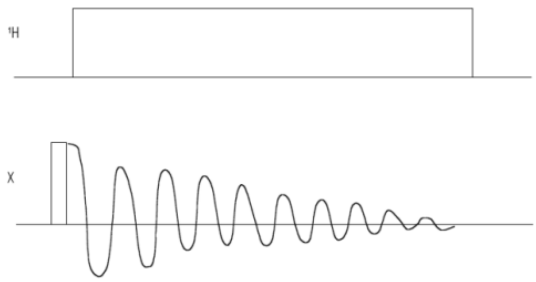

Figure 2.15 Classic example of decoupling on the proton channel during the acquisition of another nucleus X.

2.5 Cross-polarization (CP)

Cross-polarization (CP) is a technique usually applied in the study of spins at low abundance, although it can be used to perform spectral editing. CP is a pulse sequence (Figure 2.16) able to move the magnetization from a collection of spins I_j at high concentration and characterized by high γ (usually protons) to a pool of close (experiencing a dipolar coupling between them) diluted spins I_k with lower γ (for example nitrogen, carbon, phosphorus, etc.). The overall effect is to enhance the signal to noise ratio of the diluted spins potentially by a factor of $\frac{\gamma_j}{\gamma_k}$ [51].

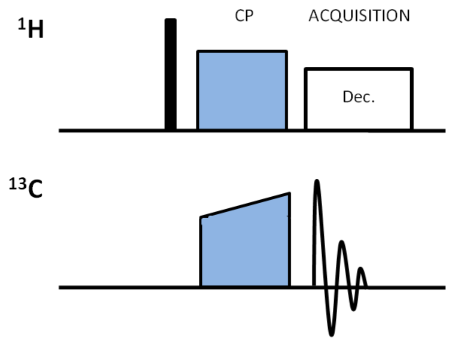

Figure 2.16 Scheme for the ^1H-^{13}C CP pulse sequence. It is easy to recognize the CP element composed by a first 90° pulse on the ^1H channel and then the contact pulses. The decoupler after the CP element is left switched on during the ^{13}C data acquisition in order to provide ^1H decoupling.

The transfer of magnetization occurs during the contact time mediated by the dipolar interaction between ^{1}H and X spins. It is important to mention that this transfer is allowed only when the two contact pulses in the cross-polarization experiment have been set to achieve the Hartmann-Hahn matching condition:

$$\gamma_H B_1(\,^1H) = \gamma_X B_1(X) \tag{2.12}$$

(if we move the magnetization from protons to another nucleus X). The equation states that the magnetization transfer is allowed only when the nutation frequencies of the two nuclei, determined by the pulse width of the spin locks (B_1), are on resonance. When the Hartmann-Hahn condition is met, the energy gaps between the two spin system ^{1}H and X are equal, so a transition absorbing energy on a ^{1}H spin can be exactly compensated by a transition on spin X that releases energy. Because every transition on ^{1}H is compensated for an opposite transition in the opposite direction on an X spin, the net spin magnetization is also preserved [51].

The dynamics of a molecule is an important aspect to take into consideration when the magnetization is transferred using cross polarization. It has been discussed in the literature [59] that during CP two distinct events happen simultaneously. While the influence of the relaxation of protons has been defined as the main event that is behind the transfer of magnetization it has been also speculated that there are two distinct relaxation mechanisms ^{1}H-X distance related that affect the magnetization transfer during CP. There is a fast transfer driven by directly bound ^{1}H-X and a slow transfer mediated by local dynamic portions of molecule [59]. Practically, this results in a complicated cross polarization pattern. This means that for the same molecule the optimal contact time for the cross polarization is not unique and dynamic nuclei can show a longer contact time. Therefore, this peculiar property of the CP transfer is often used to study the dynamic portions of a molecule [59].

The CP pulse scheme is a standard technique used to start or build up more complicated ssNMR pulse sequences such as NC_O or NC_α sequences (Figure 2.17) in which two CP events are used. Moreover, exciting the fast relaxing protons, and then using a CP element to transfer the polarization to another desired nucleus, the time between scans can also be decreased considerably, since it is the small T_1 of the protons that determines the recycle delay necessary.

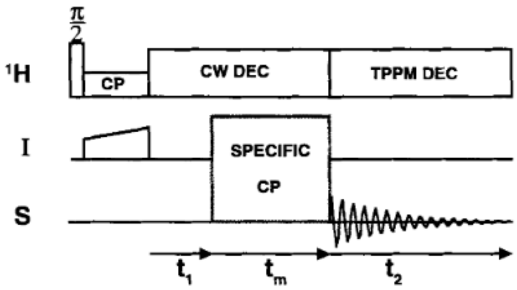

Figure 2.17 Experimental setup for applications of the SPECIFIC CP experiment in the context of triple-resonance solid state NMR experiments. After an initial CP step from protons to the nuclei I (in our application ^{15}N) SPECIFIC transfer to the nucleus S (usually ^{13}C) is applied. The decoupler after the second CP element is left switched on during the acquisition of data on ^{13}C channel [60].

In the characterization of the three-dimensional structure of biological macromolecules such as proteins it is crucial to study the correlation between carbon and nitrogen in their backbone to allow their sequence specific assignment. To solve this problem, pulse sequences including two CP events, called double cross polarization sequences (DCP), were developed. In a DCP experiment, the magnetization is usually transferred to ^{15}N from ^{1}H by the first CP and then moved to ^{13}C in the second CP event. While the first CP between a nucleus with high γ ratio (proton) and a nucleus with low γ ratio (^{15}N) is easy to set up and lead to an efficient transfer of the magnetization, the CP between two low γ ratio nuclei results in a poor efficiency of transfer. For this reason, the second CP event is carried out as a "SPECIFIC CP" sequence with a selective polarization pathway from ^{15}N to $^{13}C_O$ or ^{15}N to $^{13}C_\alpha$ generating two sets of experiments called C_ON and $C_\alpha N$ [61]. The efficiency for these SPECIFIC CP experiments is near 30-40% if compared to ^{13}C CP recorded with the same number of scans (Figure 2.18 and Figure 2.19).

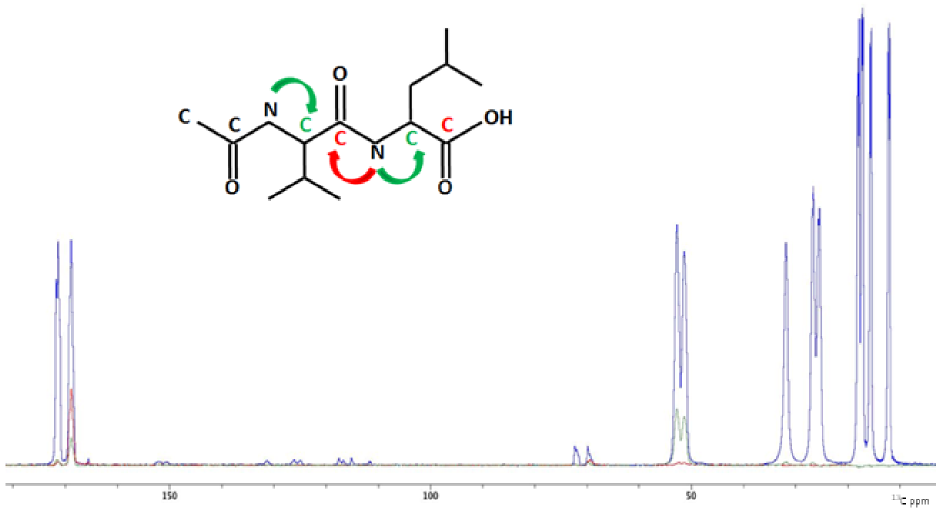

Figure 2.18 Double cross polarized ^{13}C spectra using N→Cα (green spectrum) and N→CO (red spectrum) as polarization conditions, normalized with the spectrum of the direct $^{1}H \rightarrow ^{13}C$ CP (blue spectrum) to illustrate their polarization efficiency for an Acetate Val-Leu dipeptide. Only the carbons highlighted in green and red were ^{13}C isotope while both the nitrogen were ^{15}N isotope. The maximal efficiency for these SPECIFIC CP experiments was 40% for the carbonyl (NCO) and 35% for the aliphatic (NCα) region.

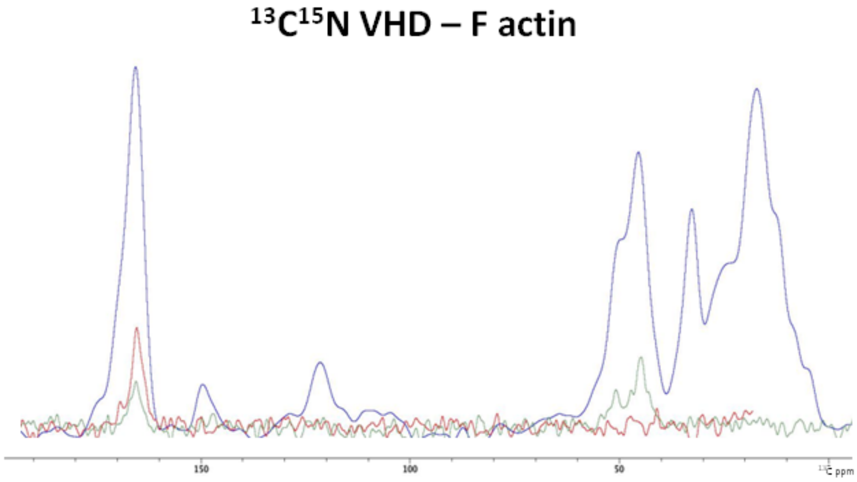

Figure 2.19 Double cross polarized ^{13}C spectra using N→Cα (green spectrum) and N→CO (red spectrum) as polarization conditions, normalized with the spectrum of the direct ^{1}H→^{13}C CP (blue spectrum) for the uniformly isotopic labelled VHD bound to actin filaments. The maximal efficiency for these SPECIFIC CP experiments was 28% for the carbonyl (NCO) and 18% for the aliphatic (NCα) region.

2.6 Homonuclear Recoupling Techniques

As previously described, the application of the MAS technique to achieve high resolution averages to zero the nuclear magnetic dipolar coupling and all the related information. Several techniques were designed to reintroduce the homonuclear dipolar coupling in synchrony with MAS. Dipolar techniques are commonly used because they allow quantitative measurements of internuclear distances and they can be applied during the mixing periods of multi-dimensional pulse sequences to produce cross-peak signals.

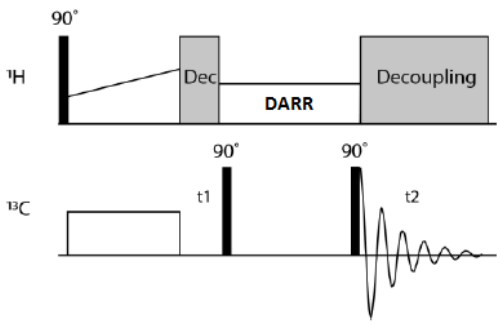

Figure 2.20 Scheme for the ^{13}C-^{13}C DARR pulse sequence.

The *Dipolar-Assisted Rotational Resonance* (DARR) experiment [62] is the common experiment used in the study of biological compounds which allows the transfer of polarization among similar nuclei closed in space. The scheme of a ^{13}C-^{13}C DARR pulse sequence is shown in **Error! Reference source not found.**. The first CP element is followed by the so-called DARR element which consists of a pair of oppositely phased 90° pulses on the carbon channel which brackets a time delay, known as mixing time, directly chosen by the operator. At the same time an irradiation on the proton channel is performed in order to re-establish the dipolar interaction between ^{1}H and ^{13}C which lead the rebuilding of the ^{13}C-^{13}C dipolar interaction and so allow the polarization transfer among the carbons.

The pathway of the magnetization transfer during a ^{13}C-^{13}C DARR experiment is shown in Figure 2.21. During the CP element the magnetization move from the protons to the carbons and then during the DARR element spread among all the carbons. The choice of the mixing time characterized how far the magnetization can move from a nucleus. If the mixing time is short the magnetization will be transferred only to the neighborhood atoms, while a long mixing time allows a long range magnetization transfer.

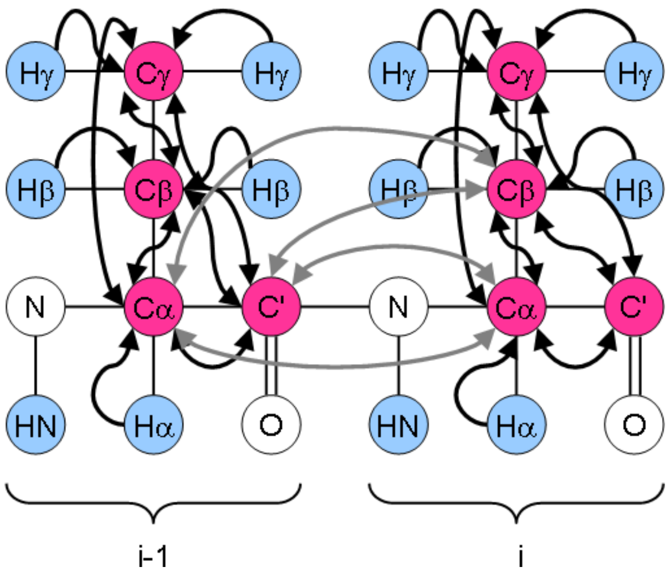

Figure 2.21 Scheme of the magnetization transfer during a ^{13}C-^{13}C DARR experiment. In pink are represented the atoms which are observed while in blue are reported the atoms through which magnetization flows. The gray arrows indicate magnetization transfers which are usually only observed when longer mixing times are used [63].

The output of the DARR experiment for a glycyl-isoleucine with a mixing time of 3ms is shown in Figure 2.22. The diagonal of the spectra represent the nucleus from which the magnetization starts (practically correspond to a CP ^{13}C experiment) while the cross peaks represent the correlation between two carbon atoms. Due to a very short mixing time only the cross-peaks between directly bound CO and C_{α} are appreciable [62]. Longer mixing times will lead to additional cross-peaks arising in the spectrum.

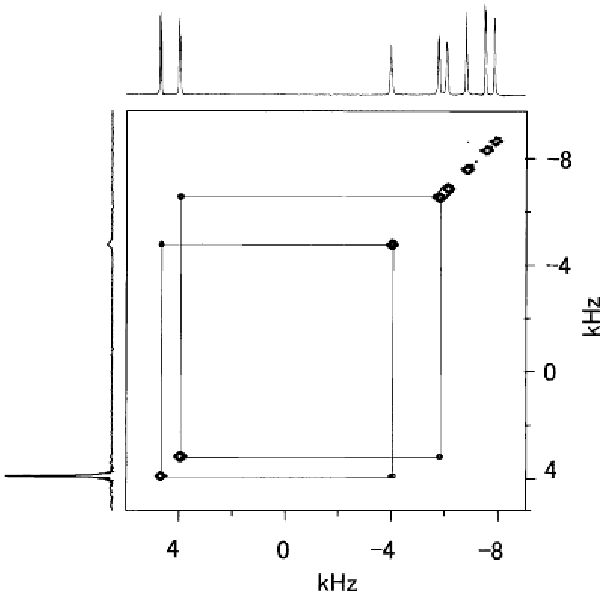

Figure 2.22 ^{13}C-^{13}C DARR spectrum of glycyl-isoleucine acquired at 15kHz spinning speed, room temperature and a mixing time of 3ms [62].

2.7 Double-quantum (DQ) ssNMR spectroscopy

Assuming the theory of the quantization of energy, a single spin $^1/_2$ when under the influence of an external magnetic field can have only two degenerate energy levels $(2I + 1)$ that can be represented as ↑ and ↓. When two coupled spins are taken into consideration more than one transition is permitted as shown in Figure 2.23. The transition of only one of the two spins (↑↑ to ↑↓) is called single quantum transition (SQ) while the transition of both the two spin (↑↑ to ↓↓) double quantum transition (DQ). The transition ↑↓ to ↓↑ is called zero quantum transition (ZQ) [49, 51].

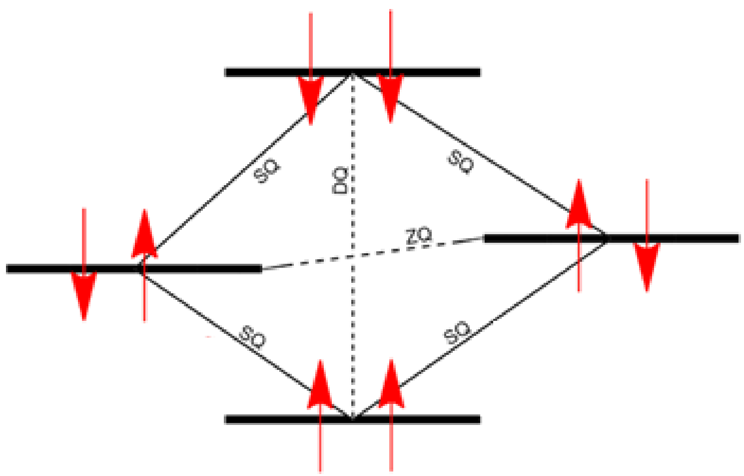

Figure 2.23 Energy levels of a coupled two spin system. The energy level is indicated as ↑↑, ↑↓, ↓↑, ↓↓ and single quantum (SQ), zero quantum (ZQ) and double quantum (DQ) transition are reported.

In NMR only the SQ transition (or coherence) can be directly observed during the acquisition time because it is the only one that can generate transverse magnetization. Nevertheless, important information can be obtained observing multi-quantum (MQ) coherence. In particular, when DQ NMR spectroscopy is applied it is possible to suppress signals from isolated spins $^1/_2$ because only coupled spins $^1/_2$ can generate a DQ signal. The frequency of a double quantum signal is the sum of the frequencies of the two spins coupled (Figure 2.26) [49].

DQ coherence cannot be directly observed and this means that the DQ information generated has to be transformed into SQ coherence before the acquisition. Furthermore, considering that in ssNMR spectroscopy the experiments are recorded under the effect of MAS it is fundamental to reintroduce the dipolar coupling prior to generate DQ coherence. "Symmetry-Based Recoupling" (SBR) sequences are a group of pulse sequences developed to reintroduce the dipolar coupling and at the same time to select for the MQ coherence information desired. The basic scheme of an SBR sequence for detecting MQ coherence is illustrated in Figure 2.24 [49].

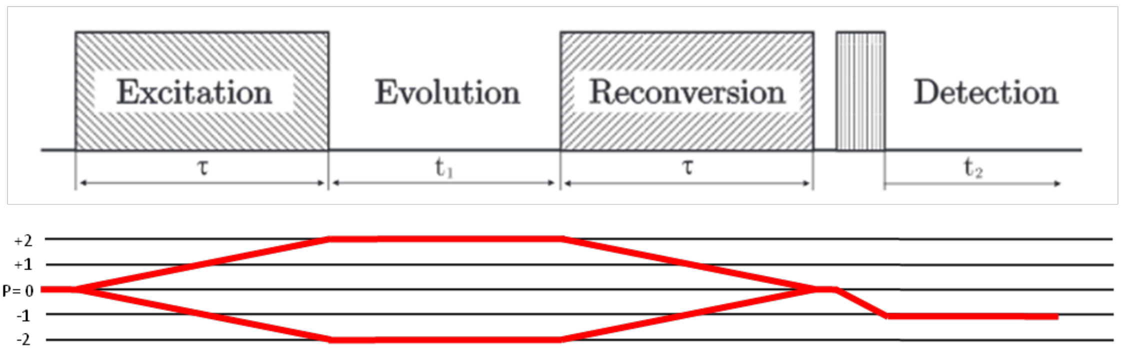

Figure 2.24 Simplified scheme of a "Symmetry-Based Recoupling" pulse sequence that allows observing double-quantum coherence and its coherence pathway. During the excitation train of pulses the double-quantum coherence is created. After an evolution time the double-quantum coherence is converted in single-quantum coherence. A final detection pulse is applied to allow the detection of the signal.

The MQ coherence is generated in the first train of pulses called excitation. There are two different schemes of a symmetric train of pulses that can reintroduce the dipolar coupling and select MQ coherence that are based on the different type of rotation of the nuclear spin that they induce: CN_n^ν and RN_n^ν pulse sequences. In CN_n^ν pulse sequences the idea is that n rotational periods of the sample are divided into N equal intervals (i.e. 7 for the C7 sequence and 5 for the C5). Each interval N contains a radio frequency pulse sequence (which is a cycle) that induces a rotation of the nuclear spin through an integer of 360° ($n2\pi$). The radio frequency phases of subsequent intervals are shifted with respect of each other by the angle $^{2\pi\nu}/_{N}$, causing a repeated incrementation of the phases during the sequence. The sample rotates bodily through n full rotations, in the same time that it takes the radio-frequency phases to advance through ν spin full rotations, in N equal steps. Independently from the number of N intervals chosen, the phase at the end of the N elements accomplishes a final rotation of 360°. Differently from CN_n^ν sequences, the general idea in a RN_n^ν symmetry is that at the end of the N elements the phase shift of 180° about the x axis. The look of a RN_n^ν pulse sequence is similar to a CN_n^ν schemes, with the differences that in a R_n^N scheme each element provides a 180° rotation, rather than a cycle, and that the radio frequency phase is alternated between two values ($R_\phi R_{-\phi}$, where ϕ is the overall phase shift, equal to $^{\pi\nu}/_{N}$ radians), rather than incremented. It becomes clear that the number of N elements has to be even in R_n^N symmetry elements [49].

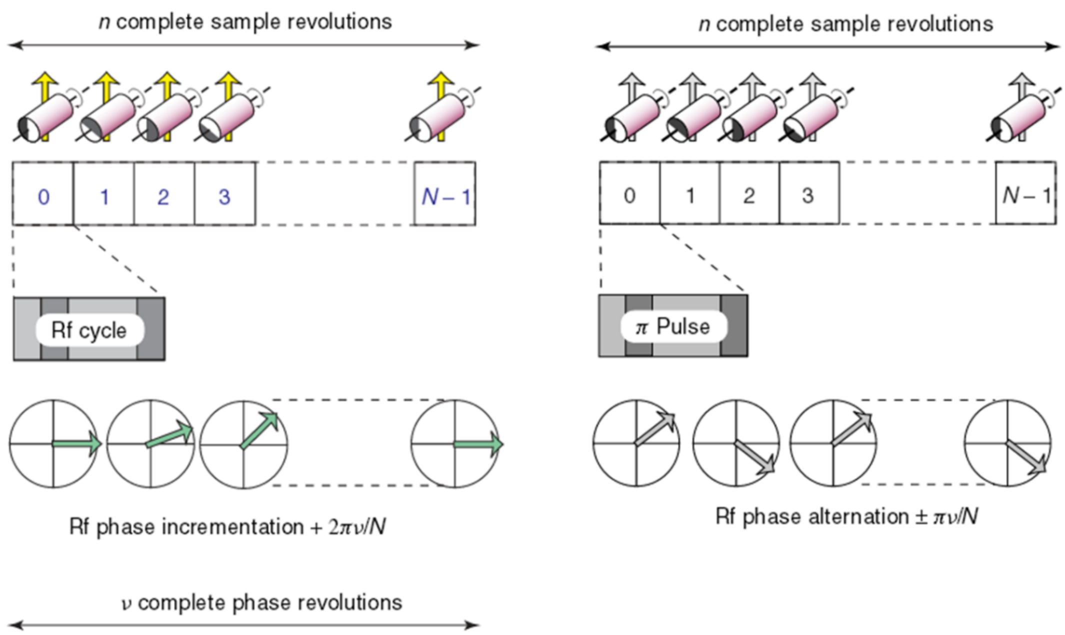

Figure 2.25 Left panel) Construction of a CN_n^ν sequence. Right panel) construction of a RN_n^ν sequence [64]. In CN_n^ν sequences the phase is increased in each *N* element in order to accomplish a rotation of 360° at the end of the *N* elements while in RN_n^ν sequences the phase change of 180° at the end of the *N* elements (in each element the phase is alternatively changed of 180° [64].

The MQ coherence generates can be left to evolve during the time t_1 under the influence of the external magnetic field and the local magnetic fields around the spin system or not, depending on the type of experiment that is recorded (respectively, 2D or 1D). The signal is finally reconverted in zero-quantum coherence during the reconversion train of pulses where the same pulse sequence used for the excitation, but with all pulses shifted by 90°, is implemented. After this step the magnetization is parallel to the external magnetic field so a final last detection pulse has to be added to create SQ coherence that can be revealed. The only condition that must be fulfilled is that the excitation time and the reconversion time must be equal [49].

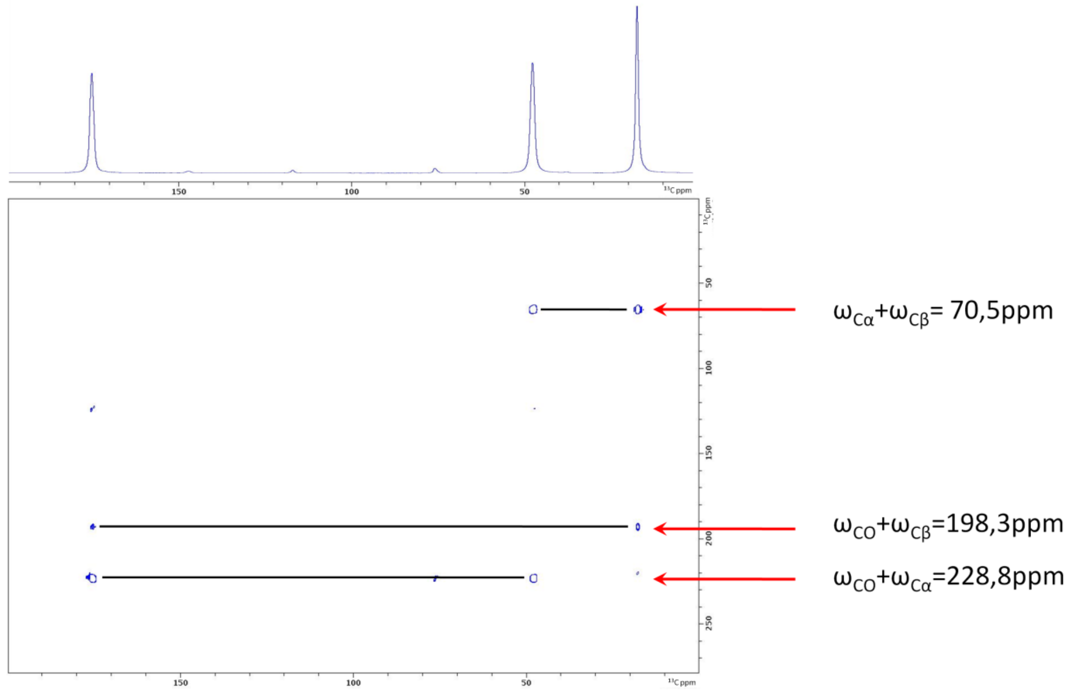

Figure 2.26 Alanine DQ-SQ ^{13}C-^{13}C correlation spectrum using a post-c7 train of pulses (n=14) for excitation and reconversion of DQ to SQ magnetization. The frequencies on DQ dimension results to be equal to the sum of the frequencies of the two spin coupled. In alanine powder the chemical shift for CO, Cα and Cβ are respectively 177,8ppm, 51,0ppm and 20,5ppm producing coupled signal at 228,8ppm ($\omega_{CO}+\omega_{C\alpha}$), 198,3ppm ($\omega_{CO}+\omega_{C\beta}$) and 70,5ppm ($\omega_{C\alpha}+\omega_{C\beta}$). The spectrum was acquired at room temperature, 10kHz spinning speed in a 400MHz Bruker magnet equipped with a double resonances CP probe.

3 Aim of the project

The project was focused on understanding the suitability of solid state NMR spectroscopy as new approach to solve the structure of thin filaments complexes. Due to several issues arose during the research, as well explained later in chapters 6 to 8, the structure of the complex studied is not available yet. The project was then primarily focused on the optimization of a platform of experiments that allow a systematic approach to the study of thin filament complexes by ssNMR. At the same time, it was also questioned and studied what can be the impact of the ssNMR technique on a sample, especially investigating how the loading in a ssNMR rotor and the acquisition of ssNMR experiments can affect the sample.

4 Materials and methods

The recipes for the buffers and media implemented in this study are reported in APPENDIX A.

4.1 Expression of Villin Headpiece Domain (VHD)

4.1.1 Preparation of competent cells

10ml of LB medium were inoculated with the chosen cell type and incubated in a shaker at 37°C overnight. 1ml of the overnight culture was transferred in 100ml of fresh LB medium and incubated in a shaker at 37°C until the OD at 600nm reached a value between 0.5-0.7. The cultures were centrifuged at 5000rpm for 15 minutes at 4°C. The supernatant was discharged, the pellet was gently resuspended in 15ml RbTXN salts (MP Biomedicals) and incubated on ice for 30 minutes. The cells were centrifuged at 3000rpm for 30 minutes at 4°C. The supernatant was discharged, the pellet was gently resuspended in 4ml RbTXN salts and incubated on ice for other 30 minutes. 1ml of a sterile 50% glycerol solution was added and the mixture was split in 50µl aliquots. The aliquots were flash frozen in liquid nitrogen and stored at -80°C.

4.1.2 Transformation of cells and preparation of glycerol stocks

An aliquot of competent cells was defrosted in ice for one hour. The plasmid containing the construct of interest was added to the cells and the mixture was left in ice for other 30 minutes. The cells were heat-shocked putting them 30 seconds at 42°C and then transferred in ice for 3-5 minutes before to add 250µl of pre-warmed LB medium and incubate the mixture for one hour at 37°C. The culture was plated in LB agar plates containing the appropriate antibiotic and incubated overnight at 37°C.

Glycerol stocks of transformed cells were prepared using a single colony from one of the plates, transferred in 10 ml of fresh LB medium with the appropriate antibiotic and incubate at 37°C in a shaker until the medium is turbid. 700µl of cells suspension was mixed with 300µl of a sterile 50% glycerol solution and split in aliquots. The aliquots were flash frozen in liquid nitrogen and stored at -80°C.

4.1.3 Expression of ^{15}N or ^{15}N and ^{13}C uniformly labelled protein [65]

A single colony was picked from one of the plates, transferred in 5 ml of fresh LB medium with the appropriate antibiotic (for simplicity all media are referred as containing the appropriate antibiotic if not specified) and incubated at 37°C during the day. Depending on the turbidity of the day culture, from one milliliter to the entire culture was transferred in 100ml of fresh LB medium and incubated overnight at 37°C. The overnight culture was used to inoculate 4 liters of LB medium (20-25ml of overnight culture for each liter of fresh LB medium) and incubated at 37°C in a shaker (200-230rpm) until the OD at 600nm reached a value between 0.8-1. The culture was centrifuged at 5000rpm for 5 minutes, the supernatant was discarded and the pellet was gently washed in 300ml of sterile M9 salts. The cells were centrifuged again at 5000rpm for 5 minutes and the pellet gently resuspended in sterile minimal M9 medium containing the appropriate isotope for single labeling or mixture of isotopes for multiple labeling. ^{15}N ammonium chloride salt (Sigma-Aldrich) was used as unique nitrogen source while ^{13}C-glucose (Sigma-Aldrich) was added as solo carbon source. After one hour in a shaker at 37°C the expression of the construct was induced by the addition of $1/_{1000}$ 0.75M IPTG. The cells were incubated in a shaker for 3-5 hours at 37°C and finally centrifuged at 8000rpm for 6 minutes. The pellet was resuspended in the appropriate lysis buffer or stored at -80°C.

4.1.4 Expression of ^{2}H, ^{15}N and ^{13}C uniformly labelled protein

To efficiently express a ^{2}H, ^{15}N and ^{13}C uniformly labelled protein it was fundamental to maintain the value of absorbance of the culture measured at 600nm under 0.6. For this purpose the culture was sampled every hour and monitored by measuring its OD_{600nm}.

A single transformed colony was picked from one of the plates, transferred in 5ml of fresh LB medium with the appropriate antibiotic and incubated at 37°C during the day. The OD_{600nm} was measured and used to calculate the maximum volume to dilute the culture to a value of OD_{600nm} of 0.01 or smaller. The proper volume of the day culture was transferred in 100ml of fresh sterile deuterated minimal M9 medium containing the appropriate mixture of isotope for proton ($^{2}H_2O$, Cortnect), nitrogen ($^{15}NH_4Cl$) and carbon (^{13}C-glucose) (the recipe for the deuterated minimal media will be the same if not specified) and incubated in a shaker at 37°C until the OD_{600nm} was near 0.6. The culture was centrifuged at 5000rpm for 5 minutes, the supernatant was discharged and the pellet was gently resuspended in 500ml of fresh sterile deuterated minimal M9 medium. The cells were incubated again at 37°C until the OD_{600nm} was near 0.6. The culture was centrifuged at 5000rpm for 5 minutes and the pellet was gently resuspended in 5ml of deuterated water and transferred in 1L of fresh sterile deuterated minimal M9 medium. The cells were incubated in a shaker at 37°C until the OD_{600nm} was near 0.6 and the expression of the construct was induced by the addition of $^{1}/_{1000}$ 0.75M IPTG. The cells were incubated for other 3-5 hours at 37°C and finally centrifuged at 8000rpm for 6 minutes. The pellet was resuspended in the appropriate lysis buffer or stored at -80°C. This protocol can lead to a near 95-6% deuteration of the protein due to the use of a non deuterated carbon source.

4.1.5 Expression of ^{15}N uniformly labelled and ^{13}C metabolic labelled protein

The protocol to selectively label a protein in ^{13}C is the same described in 4.1.3 but, instead of supplying the minimal medium with ^{13}C-glucose as the carbon source, two different varieties of ^{13}C labelled glycerol (1,3 ^{13}C-glycerol and 2 ^{13}C-glycerol, supplied by Cortnect) were added.

4.1.6 Expression of protein ^{15}N and ^{13}C ALA selective labelled

The protocol is similar to 4.1.3. After the washing of the cells in M9 salts solution and the following centrifugation, the pellet was resuspended in a non-labelled version of the M9 minimal medium and the culture was incubated in a shaker at 37°C for 1h. The cells were induced for the production of the construct with a solution $^{1}/_{1000}$0.75M IPTG and supplemented with 150mg/L of ^{15}N and ^{13}C labelled alanine (Cortecnet). The cells were incubated in a shaker for 4 hours at 37°C and then centrifuged at 8000rpm for 6 minutes. The pellet was resuspended in the appropriate lysis buffer or stored at -80°C.

4.2 Purification of Villin Headpiece Domain (VHD)

4.2.1 Cells lysis and affinity chromatography

Each cell pellet from the different expression conditions was resuspended in 50 ml of FF6 wash buffer and the cells were opened using a sonicator. An aliquot of the lysate (total fraction) was collected (5-10µl) while the rest was centrifuged at 18000rpm (SS34 Sorvall rotor) for 90 minutes at 4°C. An aliquot of the supernatant (soluble fraction) and of the pellet resuspended in urea 6M (insoluble fraction) were collected and analysed by SDS-PolyAcrylamide Gel Electrophoresis.

The soluble fraction was loaded in a syringe packed with 2ml of Nickel Sepharose 6 Fast Flow matrix (GE Healthcare). To promote the binding of the protein to the matrix the pH of the soluble fraction was adjusted to pH 7.5-8.0. The column was washed with 40ml of FF6 wash buffer to remove unspecifically bounded proteins. The protein of interest was eluted with 10ml of a 0.5M imidazole solution and DTT to a final concentration of 2mM was added to the eluate. An aliquot of flow through, wash and elution fractions were analysed by SDS-PAGE.

4.2.2 His-Tag cleavage

500µl of a 12mg/ml TEV solution was added to the elution fraction and the solution was incubated at room temperature for 2 hours. The efficiency of the cleavage was evaluated by SDS-PAGE. The solution was dialyzed against 3 liters of FF6 wash buffer (1L each time).

4.2.3 Second affinity chromatography and quantification

In order to eliminate the His-Tag, the TEV and the unspecific proteins eluted with the protein of interest another step of affinity chromatography was performed. Differently from before, in this step, the protein of interested missing of the His-Tag was collected in the flow through. The column was washed with FF6 buffer and the impurities were eluted increasing the concentration of imidazole to 0.5M. The matrix was regenerated as explained by the manufacturer's protocol.

DTT to a final concentration of 2mM was added to the fraction containing the protein. The solution was dialyzed against 3 liters (1L each time) of a buffer suitable for the further analysis (NMR, fluorescence or co-sedimentation assay, etc.).

The protein concentration was determined measuring the absorbance at 280nm by nanodrop. The extinction coefficient of the protein was calculated from its amino acid sequence using the protparam tool from expasy [66].

4.3 Expression of point mutants

The Q-5®Site-Direct Mutagenesis Kit (New England BioLabs) was used to insert single point mutations in the protein of interest. NEBaseChanger™ software was used to design the primers for the mutagenesis. A first exponential amplification step was followed by a Kinase, Ligase & DpnI (KLD) treatment (mix incubated 2h at room temperature) and the result of the reaction was used to transform high-efficiency NEB 5-alpha Competent *E. coli* cells provided in the kit. In the table below is reported the recipe to prepare the master mix for the amplification reaction:

Reagent	Final concentration
Q5 Hot Start High-Fidelity Master Mix	1x
Forward Primer	0.5µM
Reverse Primer	0.5µM
Template DNA	1-25ng
Nuclease-free water (up to 25µl)	-

Table 4.1 Mutagenesis PCR conditions set up.

Thermocycling was performed according to the following protocol:

Step		Temperature	Time
Initial Denaturation		98°C	30s
25 Cycles	**Denaturation**	98°C	10s
	Annealing	50-72°C	30s
	Extension	72°C	3m 45s
Final Extension		72°C	2m
Hold		4°C	-

Table 4.2Thermocycling conditions for mutagenesis PCR.

4.4 Actin filament preparation

4.4.1 Preparation of acetone powder from rabbit skeletal muscles

Skeletal muscles from rabbit were collected, washed from the blood with water and stored at -80°C. In every acetone powder preparation near 150g of rabbit skeletal muscle were used. After slowly thawing in ice, the muscles were minced and washed with 3 volume of extraction buffer 1 for 10 minutes while stirring. The solution was then centrifuged at 7000rpm for 20 minutes at 4°C and the supernatant was discharged. The pellet was resuspended by manual stirring in 10 volumes of ice water and the solution was filtered through a bandage (nylon or cotton) and squeezed in order to dry the particulate as much as possible. The wash with water was repeated twice. The particulate was then resuspended in a solution 0.4% $NaHCO_3$ and stirred for 45 minutes at room temperature. A longer extraction with $NaHCO_3$ should be avoided because it could cause appreciable extraction of actin. The solution was filtered and squeezed as previously described. The particulate was washed twice in a solution 1mM Tris-HCl pH 8.5 previously cooled at 4°C and it was filtered as described. The filtrate was resuspended in one liter of acetone and incubated 10 minutes. The solution was filtered as described before. This wash in acetone was repeated for a total of four times. The resulting wet powder was placed in a large glass dish under the fume hood until the acetone was completely evaporated. The acetone powder obtained is stable for months if properly stored at -20°C.

4.4.2 Extraction and purification of globular actin from acetone powder

A typical extraction of globular actin use 1.5g of acetone powder. The powder was soaked in 50 ml of G-actin buffer and incubated on ice for 30 minutes. Because actin is extracted under depolymerization conditions, it is desirable to keep the concentrations of Mg^{2+}, K^+, and Na^+ in the buffer as low as possible to avoid significant polymerization[67]. The solution was centrifuged at 18000rpm (Sorvall SS34 rotor) for 30 minutes at 4°C. The supernatant was filtered through a nylon filter and maintained on ice while the pellet was resuspended in 50 ml of G-actin buffer and incubated for a further 30 minutes on ice. The solution was centrifuged as previously described and the two supernatants were pooled.

4.4.3 Polymerization of globular actin in actin filaments

0.1 volumes of 10x KME buffer were added to the supernatant from 4.4.2. The mix was incubated at 30°C for 45 minutes to allow the polymerization of actin into filaments. Solid KCl was slowly added to a final concentration of 0.8M and incubated 5 minutes at 30°C in order to remove tropomyosin from the filaments. The solution was centrifuged at 50000rpm (Beckman 70Ti rotor) for 2 hours at 4°C and the pellet was soaked overnight in 4ml of G-actin buffer to promote the depolymerization of the filaments. The solution was diluted to a final concentration of 2mg/ml and dialyzed against 3 liters of G-actin buffer (1L each time). The dialyzed actin was centrifuged at 50000rpm (Beckman 70Ti rotor) for 1 hour at 4°C and the supernatant was collected. The globular actin was polymerized into filaments using the protocol previously described. After the ultracentrifugation step, the pellet was soaked overnight in 5 ml of Actin binding buffer. The day after the pellet was homogenized and it is stable for almost 15-20 days if properly stored in ice.

4.4.4 Polymerization of G-actin in actin filaments in presence of Phalloidin

In order to obtain actin filaments containing phalloidin, this toxin was added to a solution of actin in globular state respecting the stoichiometric reaction ratio between them of 1:1.

0.1 volumes of 10x KME buffer were added to the solution and the actin was incubate at 4°C overnight to promote the polymerization of actin. Solid KCl was slowly added as previously described and the mix was centrifuged at 50000rpm (Beckman 70Ti rotor) at 4°C for 2 hours to sediment the filaments. The pellet resuspended in the appropriate buffer and stored in ice.

4.4.5 Polymerization of G-actin in actin filaments in presence of Cucurbitacin E

Cucurbitacin E-actin filaments were prepared similarly to the protocol described by Sörensen et al. [68]. Cucurbitacin E was added to globular actin in substoichiometric amount and the mixture was incubated on ice for 2.5 hours. The filaments were polymerized as described above and they were finally sedimented at 50000rpm (Beckman 70Ti rotor) at 4°C for 2 hours. The pellet was resuspended in the appropriate buffer and stored in ice.

4.4.6 Polymerization of G-actin in actin filaments in presence of the ADP transient analogue ADP-BeF_x and ADP-AlF_4

ADP.BeF_x-actin filaments were prepared as described by Orban et al. [35]. 3mM $BeSO_4$and 10mM NaF were added to the actin in the globular state. The filaments were polymerized similarly as described but at room temperature for 3 hours. The reaction between $BeSO_4$ and NaF can produce both the species ADP.$BeF_2(OH)^-{\cdot}H_2O$ and ADP.BeF_3^- $\cdot H_2O$ so we referred to them as ADP.BeF_x. The filaments were sedimented at 50000rpm for 2 hours, the pellet resuspended in the appropriate buffer and stored in ice.

ADP.AlF_4-actin filaments were prepared as described for ADP.BeF_x except for the addition of 3mM $AlCl_3$ instead of $BeSO_4$.

4.4.7 Post polymerization modification of actin filaments: covalent addition of a spin label

In order to prepare MTSL-F.actin, actin filaments were added with a three folds excess of (1-oxy-2,2,5,5-tetramethyl-delta3-pyrroline-3-methyl) methanethiosulfonate (MTSL spin label, Figure 4.1) and left to react overnight at 4°C in the dark. The excess of the spin label was separated by sedimentation of the filaments at 50000rpm at 4°C for 1 hour. The supernatant containing the excess of the spin label was discarded and the pellet resuspended in the appropriate buffer and stored protected from sources of light. The methanethiosulfonate group in MTSL is able to react with the thiol group of cysteine and to form a disulfide covalent bond. In actin filaments, MTSL reacts prevalently with the thiol group contained in cysteine 374, the cysteine reported in the literature to be the most accessible on actin surface [69, 70]. The mechanism for this reaction is reported in Figure 4.1.

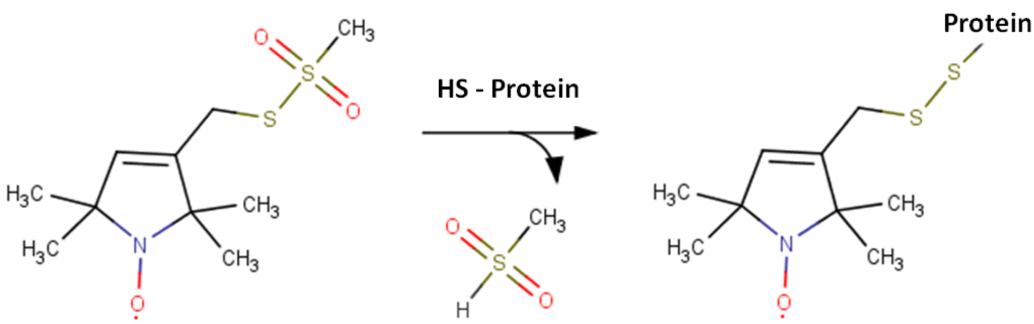

Figure 4.1 The reaction scheme of MTSL reacting with a thiol group of a cysteine in protein.

4.5 Actin binding assays

Two different approaches were used to study the affinity of the binding between the VHD and the actin filaments: a fluorimetric assay and a co-sedimentation assay.

4.5.1 Fluorimetric assay

This approach was based on the variation of intensity of a fluorophore bound to the actin filaments. Usually, the binding of a protein to F-actin promotes in the fluorophore an effect called photobleaching which determines a decrease in its total fluorescence intensity. In this way, the decreasing of the intensity is directly related to the amount of protein bound to the filaments and this allows calculating the value of k_D (dissociation constant) that characterize the binding. The actin filaments were modified with n-(1pyrene) iodoacetamide, a fluorophore able to react through its iodoacetamide group with the thiol group contained in a cysteine. In F-actin the iodoacetamide reacts specifically with cysteine 374 (Figure 4.2).

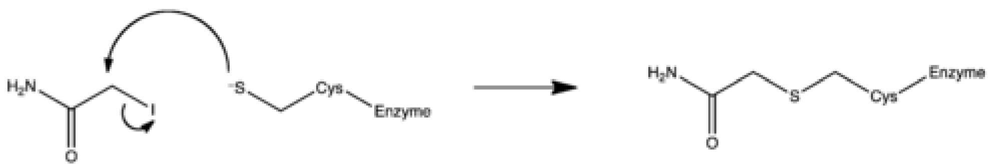

Figure 4.2 Mechanism of cysteine side chain alkylation using iodoacetamide.

Respectively in Figure 4.3 and Figure 4.4 are reported the characteristic excitation and emission spectra of pyrene attached to actin filaments.

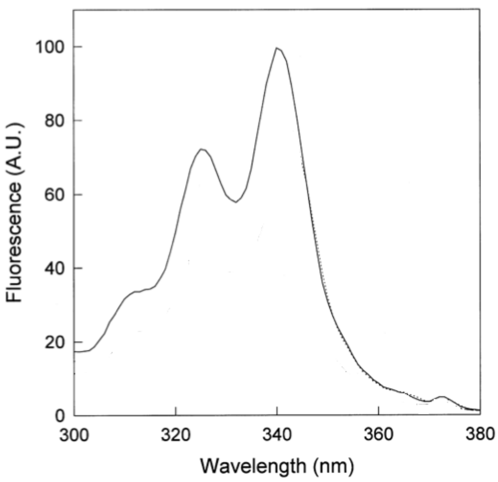

Figure 4.3 Excitation spectra of Cys-374 pyrene-labelled F-actin. The emission wavelength was set at 393 nm.

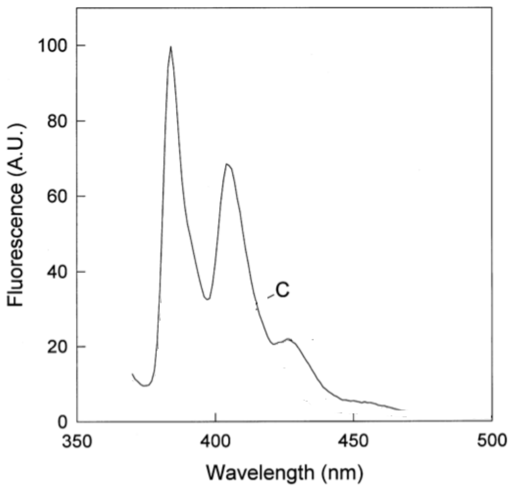

Figure 4.4 Emission spectra of Cys-374 pyrene-labelled F-actin. The excitation wavelength was set at 343 nm.

4.5.1.1 Preparation of pyrene-labelled actin filaments

The F-actin solution was centrifuged at 50000rpm (Beckman 70Ti rotor) at 4°C for one hour and the pellet was resuspended in 10-15ml of pyrene labeling buffer. N-(1pyrene) iodoacetamide resuspended in DMSO was slowly added to the F-actin solution while stirring to avoid the unfolding of actin and the mixture was incubated overnight at 4°C. From this step the solution has to be protected from the light to avoid the degradation of the pyrene. To separate the excess of fluorophore the solution was centrifuged at 10000rpm (SS34 Sorvall rotor) for 10 minutes at 4°C. The supernatant containing the modified filaments was collected and centrifuged at 50000rpm at 4°C for 2 hours to pellet the actin. The pellet was then resuspended in the appropriate buffer.

4.5.1.2 Acquisition of data and analysis

The pyrene-F.actin solution was diluted at different concentrations and each dilution was titrated with an increasing amount of protein. The pyrene was excited at 343nm with a 1nm slit in the entrance and the emission spectrum from 350nm to 450nm was recorded for each point of the titrations (from 0 to complete saturation of the filaments).

The values of the intensity of the peaks at 365nm for each spectrum acquired were listed and plotted against the respective concentration of protein added. The curves obtained were fitted using a script developed by Dr. Pfuhl for the statistic program R[71] that returns as output the value of k_D for the complex. The k_D of a complex is defined as:

$$P_1 + P_2 \overset{k_D}{\leftrightarrow} P_1P_2$$

$$k_D = \frac{[\mathrm{P_1}]_{\mathrm{eq}} * [\mathrm{P_2}]_{\mathrm{eq}}}{[P_1P_2]_{\mathrm{eq}}}$$

whereP_1 and P_2 identified the two proteins that interact. The script implemented for the k_D calculation of ABD-F.actin complex is reported in APPENDIX C and it uses a derivation of the previous equation:

$$[P_2] = \frac{([P_1] * k_D * C) - \sqrt{([P_1] * k_D * C)^2 - 4 * ([P_1] * C)}}{2 * C}$$

where $[P_2]$ indicates the amount of protein P_2 is saturated by the adding of $[P_1]$ while C represents the total amount of protein (saturated and non-saturated) P_2 present in solution.

4.5.2 Co-sedimentation assay

Similar to the previous binding assay, also in the co-sedimentation assay different dilutions of actin filaments were titrated with an increasing amount of an ABD. An F-actin solution at known concentration was divided into equal aliquots (500µl each) and was added with an increasing amount of the other protein (previously dialyzed in the same buffer of the actin filaments). Each mixture was incubated at room temperature for 5 minutes and then centrifuged at 25000rpm (Sorvall Fibrelite F50L) for one hour at 4°C. The supernatant of every aliquot was collected in a clean tube and the pellets were resuspended in a volume of buffer equal to the volume of supernatant collected.

An equal aliquot of every sample was taken, added with the same volume of SDS loading buffer, boiled for 2 minutes, centrifuged and finally checked by SDS-PAGE. The same volume from each aliquot was loaded onto the gel and to allow a quantitative approach four samples of VHD at different known concentrations were loaded as references to build a calibration curve. The different gels were stained with Instant Blue staining solution and they were scanned using a Biorad Imager. The volume of every band in the gel was quantified and the value was listed. The percentage of saturated filaments was calculated for each point of the titration as the ratio between the volume of the band from the protein in the complex and the volume for the band of the filaments without VHD. The percentage of saturated filaments was plotted against the respective concentration of ABP added and the k_D was calculated using the script written by Dr. Pfuhl for the statistic program R [71] described above.

4.6 Electron microscopy (EM)

The electron microscopy was used to help the interpretation of the data acquired by ssNMR spectroscopy. Negative staining of the actin filaments with uranyl acetate was performed and pictures were acquired using a TEM (FEI Tecnai T20 and FEI Tecnai T14 at the Center for Ultrastructural Imaging (CUI) at the King's College London). The advantage using uranyl acetate is that it can produce the highest electron density and image contrast and at the same time it can impart a fine grain to the image.

4.6.1 Sample preparation

30µl of F-actin solution was loaded into every spot of a formvar grid. Salty solutions should be sufficiently diluted to avoid breaking of the formvar grid. After 30 seconds the excess of solution was removed with a paper filter and the grid was incubated in a drop of uranyl acetate staining for one minute. Excess of stain was removed with a paper filter and the grid mounted into the TEM. It is particularly important to correctly dispose of the contaminated waste due to the mild level of radioactivity (0.37–0.51µCi) of uranyl acetate (it is harmful by ingestion or by skin contact).

4.7 Cloning and expression of Actin in *P.pastoris*

EasySelect™ *Pichia* Expression Kit (Invitrogen) was used to successfully clone the human skeletal actin gene in *P.pastoris* strain. Three different strains of *P.pastoris* were transformed (X-33, GS115 and KM71H) but only the X-33 strain gave positive results.

4.7.1 *P.pastoris* strain propagation and storing method

A single colony of P.pastoris was grown overnight in 5ml of YPD medium at 30°C in a shaker (230rpm) and centrifuged the day after at 6000rpm for 5 minutes. The cells were resuspended in YPD containing 15% glycerol at a final OD_{600nm} of 50-100 approximately. The cells were frozen in liquid nitrogen and stored at -80°C.

4.7.2 Amplification of gene of interest

The gene of interest was exponentially amplified by PCR and then purified from 1% agarose gel using Purelink® Quick Gel Extraction (Invitrogen). In Table 4.3 the set up for the PCR is reported:

Reagent	Final concentration
GoTaq® Green Master Mix	1x
Go Taq® Polymerase	1.5u/50µl
Forward Primer	1µM
Reverse Primer	1µM
Template DNA	1-25ng
Nuclease-free water (up to 50µl)	-

Table 4.3 PCR conditions set up.

Thermocycling was performed according to the following protocol:

Step		Temperature	Time
Initial Denaturation		95°C	2m
25 Cycles	**Denaturation**	95°C	1m
	Annealing	62°C	30s
	Extension	72°C	3m
Final Extension		72°C	5m
Hold		4°C	-

Table 4.4Thermocycling condition for PCR.

4.7.3 Insert and plasmid preparation

The purified PCR product was double digest with the two restriction enzymes KpnI and ApaI. Table 4.5 shows the conditions used for the digestion.

Reagent	Final concentration
PCR product	1µg
Buffer J (Promega)	1x
Acetylated BSA	0.1µg/µl
KpnI	10u
ApaI	20u
Nuclease-free water (up to 20µl)	-

Table 4.5 PCR product double digestion conditions set up.

The mix was incubated at 37°C for 4h and the enzymes were inactivated by heating at 65°C for 20 minutes. In the same way, the pPICZ plasmid was prepared by double digestion with the same two restriction enzymes KpnI and ApaI. Table 4.6 shows the conditions used for the digestion.

Reagent	Final concentration
pPICZ plasmid	1µg
Buffer J (Promega)	1x
Acetylated BSA	0.1µg/µl
KpnI	10u
ApaI	20u
Nuclease-free water (up to 20µl)	-

Table 4.6pPICZ plasmid double digestion conditions set up.

The reaction was performed as described for the insert and after the inactivation of the enzymes an aliquot of the reaction was analysed by agarose gel to confirm that all the vectors were efficiently digested.

4.7.4 Ligation

The ligation reaction between plasmid and insert was performed using the T4 ligase enzyme (Promega). The following table shows the conditions used for the ligation.

Reagent	Final concentration
PCR product	240µg
pPICZ plasmid	100µg
T4 ligase buffer	1x
T4 ligase	1u
Nuclease-free water (up to 20µl)	-

Table 4.7 T4 Ligase reaction conditions set up.

A 7:1 molar ratio of insert to plasmid was used to perform the reaction. The conversion of molar ratios to mass ratios was carried out using the following equation:

$$\frac{ng \text{ of plasmid} \cdot kb \text{ size of insert}}{kb \text{ size of plasmid}} \cdot \text{molar ratio of } \frac{\text{insert}}{\text{plasmid}} = ng \text{ of insert}$$

The reaction was incubated for 3h at room temperature, then the T4 ligase was inactivated by heating to 70°C for 10 minutes.

4.7.5 Transformation of TOP10 *E.coli* cells and zeocin screening

The transformation of TOP10 *E.coli* cells was performed as described in 4.1.2. For Zeocin™ selection the salt concentration has to remain low and the pH must be 7.5. A version of Low Salt LB medium was used instead of the classic LB medium. After the transformation, the cells were spread on Low Salt LB agar plates containing 25µg/ml Zeocin™ and incubated overnight at 37°C for the selection of transformed colonies. Several colonies from the plates were picked and colony PCR was run in order to discriminate false positives from the colonies containing the plasmid with the insert. Primers designed to anneal to the *AOX1* regions on the plasmid that flanks the inserts were used. Every PCR reaction was analysed by electrophoresis on a 0.8% agarose gel.

False positive colonies which contained the plasmid without the insert showed a band at 320bp while the one containing the gene of interest showed a band at near 1.2kbp. In the tables below the set up for the PCR is reported:

Reagent	Final concentration
Go Taq® Green Master Mix	1x
Go Taq® Polymerase	1.5u/50µl
Forward AOX1 Primer	1µM
Reverse AOX1 Primer	1µM
DNA from colonies	1-25ng
Nuclease-free water (up to 50µl)	-

Table 4.8 Colony PCR set up conditions.

Thermocycling was performed according to the following protocol:

Step		Temperature	Time
Initial Denaturation		94°C	2m
	Denaturation	94°C	1m
25 Cycles	Annealing	55°C	1m
	Extension	72°C	1m
Final Extension		72°C	7m
Hold		4°C	-

Table 4.9Thermocycling conditions for colony PCR.

Positive colonies were growth in 5ml of selective Low Salt LB medium and then used to make glycerol stock as described in 4.1.2.

4.7.6 Preparation of transforming DNA

Prior to transforming *Pichia*, 5-10µg of transforming DNA had to be linearized in order to promote the homology recombination into the genome of *Pichia*.

5-10µg of plasmid DNA were digested with the restriction enzyme SacI that cuts the plasmid one time in the 5' *AOX1* region at base 209. Below are reported the conditions for the digestion:

Reagent	Final concentration
pPICZ + insert	1µg
Multicore™ buffer (Promega)	1x
Acetylated BSA	0.1µg/µl
SacI	10u
Nuclease-free water (up to 20µl)	-

Table 4.10pPICZ linearization conditions

The mix was incubated at 37°C for 4h and the enzyme was inactivated by heating at 65°C for 20 minutes. The linearized DNA was purified by ethanol/chloroform extraction and ethanol precipitation using 1/10 volume 3M sodium acetate and 2.5 volumes of 100% ethanol. The DNA was centrifuged to pellet it and then resuspended in 20µl sterile water.

4.7.7 Electroporation of *P.pastoris*

P.pastoris strains were grown in 5ml of YPD medium at 30°C overnight. 500ml of fresh YPD in a 2L flask was inoculated with 0.1-0.5ml of the overnight culture and left to grow until the OD_{600nm} is 1.3. The culture was centrifuged at 1500g for 5minutes at 4°C and then resuspended in 500ml of ice-cold, sterile water. The cells were centrifuged again as described before and resuspended in 250ml of ice-cold, sterile water. Another step of centrifugation was performed and the cells resuspended in 20ml of a solution 1M sorbitol. The cells were centrifuged one last time and the pellet resuspended with sorbitol at a final volume of approximately 1.5ml.

80µl of cells were mixed with 5-10µg of linearized transforming DNA and transferred to an ice-cold 0.2cm electroporation cuvette. The cuvette was incubated on ice for 5 minutes and then pulsed at 1800V for 5ms. 1ml of a sterile solution of 1M sorbitol was immediately added to the cuvette and the content was then transferred into a 15ml falcon tube and incubated at 30°C without shaking for 2h. Different amounts of transformed cells were spread on YPDS plates containing 100µg/ml Zeocin™ and the plates were incubated at 30°C for 3-10 days. Several colonies from the plates were picked and colony PCR was run in order to confirm the presence of the insert in the genome of *P.pastoris*. The same setup described in Table 4.8 and Table 4.9 was used.

4.7.8 Determining the Mut^+ phenotype

Two different phenotypic classes of recombinant *P.pastoris* strains can be generated after the transformation: Mut^+ and Mut^S and they refer to the rate of methanol utilization. Mut^S refers to a "Methanol Utilization slow" strain that it is created by the loss of alcohol oxidase activity encoded by the *AOX1* gene. Different Mut phenotypes could aid the expression of the insert and for this reason several recombinants per phenotype should be tested. Transformation of X-33 and GS115 with DNA linearized in the 5' *AOX1* region will hold to Mut^+ phenotype while KM71H to Mut^S.

Using a sterile toothpick, a single colony was picked from the Zeo^R plate from 4.7.7 and streaked in a regular pattern on both an MM plate (methanol medium) and MD plate (minimal dextrose) making sure to streak the MM first. Two differentiated phenotypes GS115/Mut^S Albumin and GS115/pPICz/*lacZ* Mut^+ were used as control and streaked in both MM and MD plates. The plates were incubated at 30°C for 2 days. The Mut^+ strain will grow normally in both MM and MD plates while the Mut^S strains will grow normally in MD plates but they will show little or no growth in MM plates.

4.7.9 Intracellular expression of protein in X-33 Mut^+ *P.pastoris* strain

The most important parameter to consider during an expression using *P.pastoris* as expression system is the concentration of available oxygen in the medium to the cells for their metabolism. The oxygen concentration is not critical during the biomass production but it becomes the limiting reagent after the induction with methanol and during the insert expression. In fact, the first step in methanol metabolism is the oxidation of methanol to formaldehyde using molecular oxygen by the enzyme alcohol oxidase. For this purpose, a general rule of filling any baffled flask not more than 10-30% of their total volume was applied in any expression trial.

A single colony was used to inoculate 50ml of MGY, BMG, or BMGY medium and incubated at 30°C in a shaking incubator at 250rpm until the culture reaches an OD_{600nm} of 2-6 that corresponds to log-phase growth. The culture was centrifuged at 1500g for 5 minutes at room temperature and the pellet resuspended in the proper volume of MM, BMM or BMMY medium to dilute the cells to an OD_{600nm} of near 1 to induce the expression of the protein of interest. The baffled flask was covered using cheesecloth to help the aeration of the medium and incubated at 30°C in the shaking incubator at 250rpm. Every 24 hours for the next 3 days 100% methanol was added to a final concentration of 0.5% to the culture to maintain the expression. After the induction, every 6 hours an aliquot of cells was collected to analyse the expression level and determine the optimal time post-induction to harvest the cells. The culture was centrifuged at 1500g for 15 minutes at room temperature and the pellet freeze-dried using liquid nitrogen and stored at -80°C. An aliquot of the cells lysate was analysed by SDS-PAGE and Western Blot to confirm the properly expression of the protein of interest.

4.8 List of ssNMR experiments used

4.8.1 Calibration of ssNMR experiments

Potassium bromide powder was used to calibrate the magic angle before every session of experiments. ^{79}Br is an abundant half-integer (I=3/2) spin with small quadrupolar coupling contribution (that became 0 when in form of KBr salt due to its symmetric structure) and high sensitivity. The magic angle is calibrated maximizing the amplitude of the sidebands generated by the ^{79}Br. Furthermore, the dataset acquired can be stored and used each time to adjust and compensate any drift on the magnetic field [72]. Adamantane and alanine at natural abundance were used as reference for the ^{13}C experiments and for the optimization of the shims. ^{31}P-sodium phosphate was used for the calibration of ^{31}Pexperiments and ^{15}N-ammonium chloride for ^{15}N experiments.

4.8.2 Cross Polarization experiments: 1D spectrum of carbon, nitrogen, phosphorus

In CP experiments the time and spin-lock power level to satisfy the HH condition and the decoupling of protons during the acquisition were the parameters to set up. Usually, the optimal time for the magnetization transfer is between 900µs and 5000µs. During the acquisition, the decoupling power level on protons was set around 90kHz and SPINAL64 was always applied as decoupling sequence. For ^{15}N and ^{13}C experiments a 2s delay was set at the end of the sequence to allow the complete relaxation of the nuclei. A longer delay of 5s was applied for ^{31}P experiment due to the slower relaxation of this nucleus. In all the CP based sequences the setup of the magnetization transfer was performed as described above.

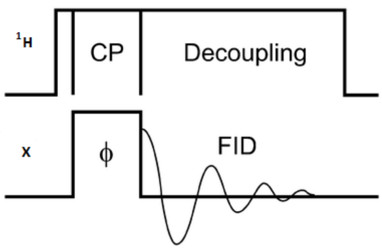

Figure 4.5 Scheme for a CP MAS experiments

It is important to mention that the contact time used in every CP calibration was chosen not taking into consideration the difference in length that can arise between the contact time of rigid and dynamic portions of the protein. The contact time was calculated looking at the optimal time in which it the highest signal intensity was achievable. This could have resulted in the loss of resonances of dynamic nuclei in the background noise.

4.8.3 Dipolar assisted rotational resonance (DARR) experiments[62]

The setup of the recoupling step on a DARR pulse sequence requires measuring of the parameters (length and power level) for the 90° pulse on the X channel and the calculation of the irradiation on the proton channel that promotes the recoupling of X nuclei. The irradiation power level in Hz has to be set in accordance with the spinning speed used (e.i. if the speed is set to 10kHz the power level on proton has to be 10kHz).

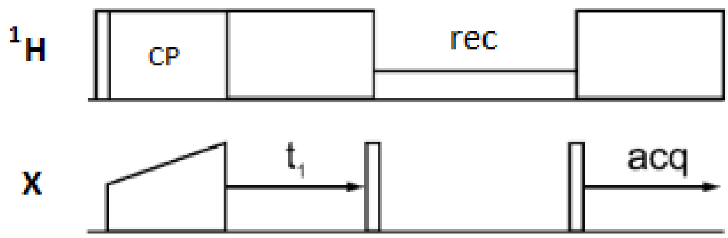

Figure 4.6 Scheme for a DARR experiment. Magnetization is transferred to the z-axis and then moved to the X nuclei. During the DARR mixing period, the ^{1}H RF field strength is set to the rotational resonance condition.

List of critical parameters optimized:

- ^{1}H 90° pulse
- ^{13}C 90° pulse
- ^{1}H and ^{13}C RF during CP
- Time for the DARR block: 20ms, 100ms and 250ms
- ^{1}H RF used during the DARR block
- Decoupling during acquisition: 91kHz

4.8.4 Double CP based experiments [61]

Ina DCP experiments the second CP is the crucial step to set up. The second CP event was optimized as specific CP sequence (Figure 4.8) with a selective polarization pathway from ^{15}N to $^{13}C_O$ and ^{15}N to $^{13}C_\alpha$ generating two sets of experiments called C_ON and C_αN. The setup of the second CP has to be optimized in the same way of the first CP. On the other hand, the range of values that matches the HH condition for two nuclei with low $\gamma$is very narrow (Figure 4.7) making difficult their optimization. The mixing time for the second CP was set between 2ms and 6ms depending on the sample analysed.

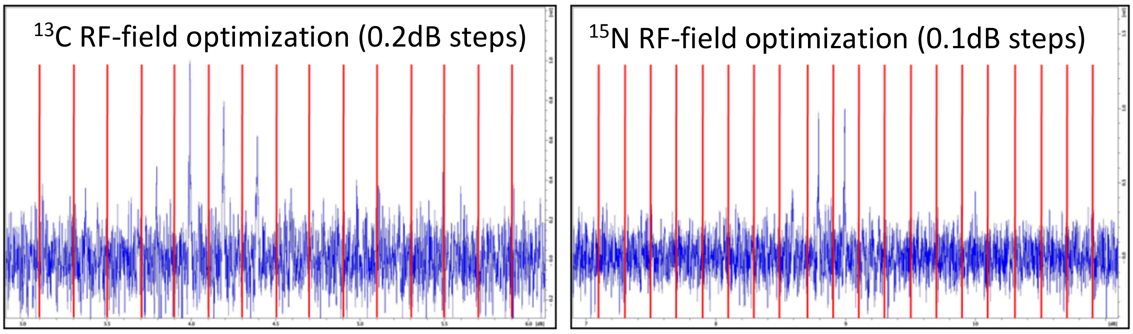

Figure 4.7 Optimization of ^{13}C and ^{15}N power level for the pulses in the second CP. The range of values of RF for the two nuclei that matched the HH conditions for the second CP was very narrow and contained in less than 1dB for carbon and 0.3dB for nitrogen.

The decoupling during the second CP is extremely important in order to avoid any unspecific transfer of magnetization from proton to carbon by the undesired matching of HH condition between them. The SPINAL-64 sequence with an amplitude of90-93kHzwas applied during t1 and the acquisition time on proton channel, while an 85-90kHz CW decoupling was used during the ^{15}N–^{13}C contact time (Figure 4.8).

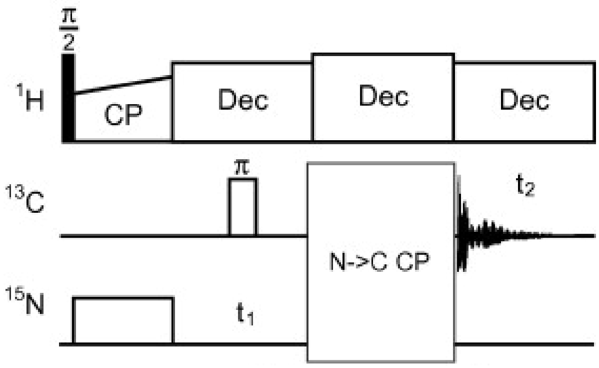

Figure 4.8 Pulse sequences used in 2D $^{15}N^{13}C$ heteronuclear correlation experiments in solid-state MAS NMR [61].

List of critical parameters optimized

- ^{1}H 90° pulse
- ^{13}C 90° pulse
- ^{15}N 90° pulse
- ^{1}H and ^{15}N RF applied during first CP
- ^{15}N and ^{13}C RF applied during second CP
- ^{1}H RF used during second CP event
- Decoupling during acquisition

4.8.5 2D ^{1}H-^{15}N correlation experiments based on CP or INEPT recorded implementing ultrafast MAS

In solution NMR, the ^{1}H-^{15}N HSQC experiment could be considered as the entry point to understand what quality of spectra it is possible to achieve from a sample. The 2D ^{1}H-^{15}N correlation experiment implemented in ssNMR can be intended as a similar experiment.

In a 2D ^{1}H-^{15}N correlation experiment, a 90° pulse on resonance with the proton frequency is applied to move the magnetization to the plane. Independently from the magnetization transfer methods used (CP or INEPT), the magnetization is transferred to the heteronuclear (usually ^{15}N or ^{13}C) and allowed to evolve in this dimension. The magnetization is transferred again on the proton and the signal is acquired. In ssNMR the dipolar coupling between ^{1}H-^{1}H is too large to be erased at spinning rate lower than 40kHz at least. This means that only using probes that allow spinning at 60kHz or more allow the acquisition of proton at high resolution.

The transfer of the magnetization could be carried out both using double CP (INVerted CP) and double INEPT block of pulses with the only difference that the former moves the magnetization in a rigid spin system while the latter in a dynamic spin system. In both the versions of this sequence it is very important to optimize the decoupling sequences on proton channel during the evolution of the signal in the heteronuclear dimension. It is important to remember that if the decoupling amplitude is similar to the spinning rate the two techniques interfere with one another.

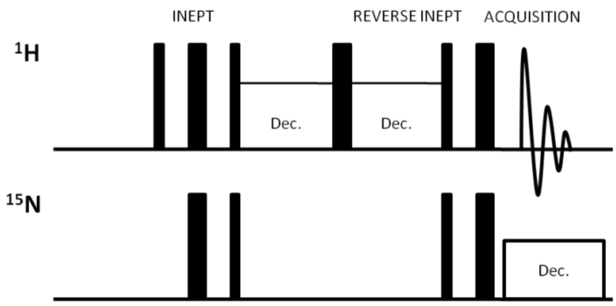

Figure 4.9 2D ^{1}H-^{15}N correlation experiments pulse sequence scheme using double INEPT to transfer the magnetization.

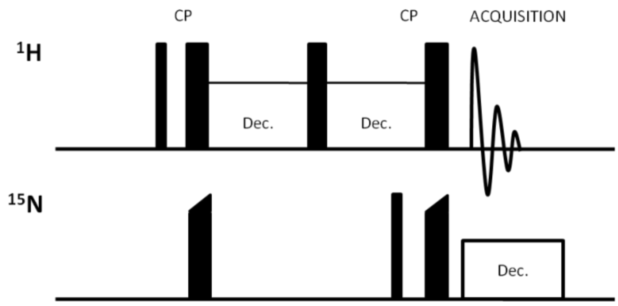

Figure 4.10 2D ^1H-^{15}N correlation experiments pulse sequence scheme using two CP to transfer the magnetization (INVCP).

It is important to make some more considerations when ultrafast MAS is implemented. The friction against the surrounding atmosphere experienced by the rotor during spinning at a rate higher than 40kHz can generate enough heat to unfold a protein sample. Increases in temperaturef to about 47°C for a sample spinning at 28kHz in a 2.5mm rotor, to 66°C when spinning at 50kHz in a 2mm rotor or to 34°C when spinning at 40kHz in a 1.8mm rotor have been reported in the literature [73]. As a consequence, the implementation of a very efficient VT system is crucial to avoid the unfolding of the sample when spinning at these rates. Zhou and coworkers reported that when an efficient VT unit has been implemented the increase in the temperature was no higher than 16°C for a 1.6mm rotor spinning at 40kHz. The calibration curve they built using a flow of 75 scfh cooling gas regulated at -5°C fit a quadratic function of the spinning rate [73]. To establish the temperature during the acquisition of experiments at spinning rate of 60kHz, two drops of a 5mM deuterated solution of DSS was added in each 1.8mm rotor filled. The single ^1H sharp signal generated by the DSS was used to reference the spectrum to zero ppm. The temperature was estimated running a macro optimized by Dr. Lewandowski where the changes in chemical shift for the water signal from the reference at 25°C were calculated as changes in temperature to sum or subtract to the reference temperature.

The solvent suppression is crucial when hydrate samples are analysed. All the pulse sequences for 2D ^1H-^{15}N correlation experiments were optimized adding a solvent suppression scheme based on the saturation of water signal.

In ultrafast spinning ssNMR, ^1H diluted samples are used to improve the resolution decreasing the amount of ^1H-^1H dipolar coupling interactions in the sample. For this purpose, perdeuterated proteins back-exchanged with H_2O are usually prepared. On the other hand, the reintroduction of ^{1}H and its detection means that the delay at the end of the acquisition in a pulse sequence is subject to the slow T_1 of ^{1}H. Nevertheless, when the sample is doped with a paramagnetic reagent the T_1 drastically decreases. For example, the addition of 10mM $Cu(II)Na_2EDTA$ to a sample containing ubiquitin or lysozyme, can improve the sensitivity by decreasing the proton T_1 from of about 0.4-0.8s to 60-70ms[73].

List of critical parameters optimized

- ^{1}H 90° pulse
- ^{15}N 90° pulse
- ^{1}H and ^{15}N RF applied during CP
- Decoupling during acquisition

4.8.6 Double quantum coherence ssNMR spectroscopy: spc5 and post-C7

"Symmetry-Based Recoupling (SBR)" sequences are pulse sequences that can recouple specific spin interactions, using cyclic sequences composed of N phase-shifted repetitions of either 2π (CN_n^{ν}symmetry sequences) or π (RN_n^{ν}symmetry sequences) rotation elements. Which interaction(s) are recoupled by a given sequence is determined by the relationship between the sample rotation rate, the spin rotation rate, and the rate of phase shift between the elements. To understand how the selection rules for a symmetry sequence work it would be easier to think about these sequences as a wall with holes regularly disposed at distances $\pm N$. The only coherence information that can be generated is the coherence that goes through these holes. Both spc5 and post-C7 are CN_n^{ν} symmetry sequences can select Double Quantum coherence. Post-C7 symmetry element is a $C7_2^1$ that include the "POST" element ($C = 270_0 180_{180} 90_0$ where ξ_ϕ indicates a rectangular, resonant radio frequency pulse with flip angle ξ (the angle are written in degree) and phase ϕ) that minimizes the contribution from the chemical shift isotropy that in a $C7_2^1$ is not zero. Based on the selection rules, post-C7 based sequences can generate only DQ coherence. On the other hand, a $C5_2^1$ symmetry based sequences can generate DQ coherence but at the same time it allows the generation of CSA contribution and SQ coherence. To average to zero these undesirable elements using a $C5_2^1$ symmetry, a 180° phase shift supercycle was implemented in the form of a $C5_2^1$ element ($[C5_2^1]_0$) followed by the same block of pulses shifted by 180° ($[C5_2^1]_{180}$). The resulting sequence was called spc5. In this form spc5 has the same selection rules of the post-C7 and DQ coherence can be efficiently selected[64].

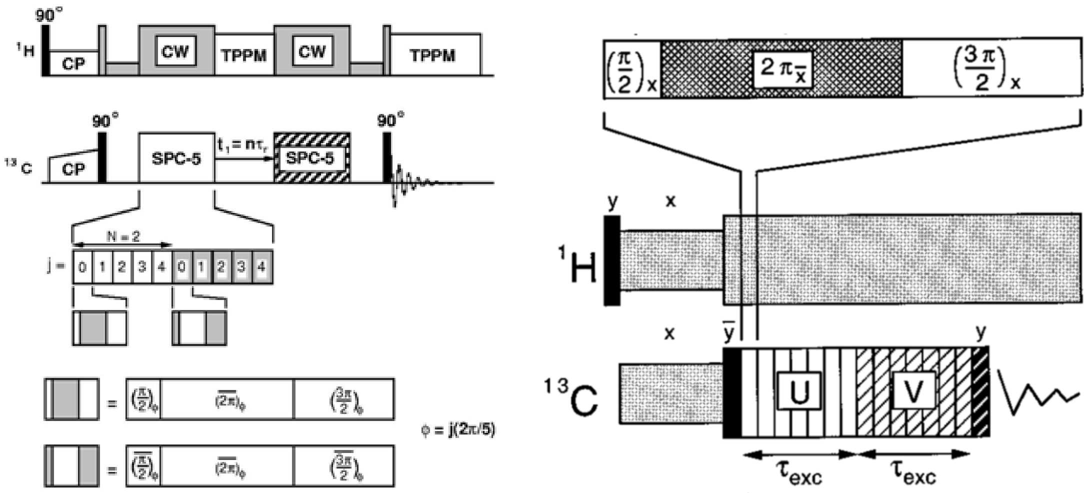

Figure 4.11 Panel A) Pulse scheme for a $C5_2^1$SBR implementing a supercycle. After the CP element, longitudinal sum polarization is created by a 90° pulse, which is followed by a z-filter for one rotor period. Subsequently, the spc5 sequence is initiated. It is easy to recognize the implementation of a 180° phase shift supercycle in which the 5 elements from the $C5_2^1$ (white numbered bars) are followed by the same 5 elements with phases shifted by 180° (gray numbered bars).Isotropic chemical shift evolution during t_1 is followed by a DQ reconversion step. Another z-filter period followed by a 90° pulse creates detectable transverse magnetization[74].
Panel B) Pulse scheme for a $C7_2^1$SBR implementing "POST" element. After a CP element, the DQ coherence is generated during the excitation step (marked with U) and then reconverted in zero-quantum during the reconversion step (marked with V). The SQ coherence that can be acquired is finally generated by the application of a 90° pulse. Seven rf cycles are implemented to cover two rotational periods. Black filled bars indicates 90° pulses while the white bars indicates the "POST" elements [75].

In the setup of an "SBR" sequence is important to optimize the number of loops during the excitation and reconversion of the double quantum signal. It has to be a multiple of 5 for the SPC5 and 7 for the post-C7. It is crucial that the proper number of loops to achieve the best DQ transfer efficiency is properly calculated. The decoupling on proton and the optimal calibration of the 90° pulse for the X nucleus are the crucial parameters in the setup of these sequences. During the excitation and reconversion of the DQ signal the implementation of CWLG decoupling sequence is the standard. The CW sequence is a continuous-wave on-resonance irradiation that decouples heteronuclear dipolar interactions while LG (Lee-Goldburg) is an off-resonance irradiation scheme that decouples homonuclear dipolar interactions efficiently while chemical shifts and heteronuclear couplings remain. TTPM or SPINAL64 are used during the evolution of the DQ signal and during the acquisition of the signal. Efficient decoupling during the DQ trains of pulses completely erases any residual matching of the HH conditions that can

reintroduce signal that will be mixed with the signal from the reconversion of the DQ signal. The power level in Hz for the single pulses that build each element of the excitation and reconversion has to be calculated as the product of the spinning speed in Hz multiplied by the number of elements in the sequence (i.e. if spinning at 1000Hz, for post-c7 is calculated as $1000 \cdot 7 = 7000Hz$ while for the SPC5 as $1000 \cdot 5 = 5000Hz$).
List of critical parameters optimized

- ^{1}H 90° pulse
- ^{13}C 90° pulse
- ^{1}H and ^{13}C RF applied during CP
- Time for the evolution of signal between excitation and reconversion
- Decoupling during acquisition

4.9 List of solution NMR experiments used

Classic experiments, such as the 1D proton and ^{1}H-^{15}N HSQC experiments, were used to routinely check the proper folding of VHD expressed in different conditions, and to confirm the patterns of the different enrichments expressed (chapter 4). 3D HCCH-TOCSY and $HNC_{O/\alpha}$ correlation experiments have been recorded and their CC and CN projections have been both calculated and used as references for the ssNMR experiments as explained in chapter 9. For the development of an efficient protocol for the assignment of positively charged regions of arginines and lysines (chapter 8) modified CxN pulse sequences were used. The solution NMR experiments used are listed below.

- ^{1}H direct acquisition using single 90° square pulse.
- ^{1}H-^{15}N HSQC.
- ^{1}H-^{13}C HSQC.
- CC projection calculated from HCCH TOCSY experiment used as reference for the apo protein to compare to CC correlation spectra acquired by ssNMR on the holo version of the protein.
- NC_O projection calculated from an HNC_O experiment used as reference for the apo protein to compare to CC correlation spectra acquired by ssNMR on the holo version of the protein.

- NC_α projection calculated from an HNC_α experiment used as reference for the apo protein to compare to CC correlation spectra acquired by ssNMR on the holo version of the protein.
- C_ON optimized pulse sequences for the revelation of $C_\zeta N_\varepsilon$ and $C_\zeta N_\eta$ correlation on guanidine group of arginines.
- $C_\alpha N$ optimized pulse sequences for the revelation of $C_\delta N_\varepsilon$ correlation on guanidine group of arginines and $C_\varepsilon N_\zeta$ correlation on amine group of lysines.

All the spectra acquired were processed using TopSpin software by Bruker while the software CCPN [76] was used to perform the assignment.

4.10 List of magnets used

- 500MHz (Bruker) equipped with a triple resonance cryo-probe for solution NMR.
- 700MHz (Bruker) equipped with a triple resonance cryo-probe for solution NMR.
- 500MHz (Bruker) equipped with a triple resonance 4mm efree probe (Bruker) for ssNMR (University of Warwick, Department of Physics).
- 400MHz (Bruker) equipped with a double resonance 4mm CP MAS probe.
- 600MHz (Bruker) equipped with a triple resonance 1.3 mm ultrafast spinning probe (University of Warwick, Department of Physics).
- 600MHz (Bruker) equipped with a double resonance 4mm CP MAS probe (University of Warwick, Department of Physics).
- 850MHz (Bruker) equipped with a triple resonance 1.3mm ultrafast spinning probe (University of Warwick, Department of Physics).
- 850MHz (Bruker) equipped with a triple resonance 4mm CP MAS probe (University of Warwick, Department of Physics).

All spectrometers for ssNMR spectroscopy were equipped with a cooling system to run the experiment at 278K. All the instruments were controlled by the software TopSpin developed by Bruker Corporation.

4.11 Peak fitting protocol

The calculation of the linewidth of isolated peaks is the best approach in order to recognize improvements in the resolution in a series of spectra acquired with different conditions. Nevertheless, it happens that sometimes signals are overlapped making it impossible to determine the linewidth of the peaks. A deconvolution is usually applied in order to resolve these peaks and calculate the linewidth of each signal that contributes to create them (Figure 4.12). The peak fitting protocol validation is reported in APPENDIX B.

The peak fitting was performed using the suite called "line fitting" contained in ACD/Lab [77] or MestReNova [78] software. A FID is processed, the phase was corrected and the baseline flattered. The peaks were identified and picked using the dedicated tool. Remembering that an NMR peak has a Lorentzian shape (at least theoretically) and the field inhomogeneity can give a more Gaussian lineshape, when the fitting was performed a Lorentzian plus Gaussian algorithm was applied. The number of iterations was set at least to 1000 (or higher if required) to find the best fit, the maximum linewidth was increased until it is not a restriction in the calculation while the tolerance was set to the minimum to optimize the fitting. After the calculation both the software return a summary of the fitting which reports the actual number of iterations made, the residual sum of squares, the time used and the goodness-of-fit of the model. The visual output for ACD/LAB is reported in Figure 4.12 and shows the peaks fitted (cyan peaks), the sum of the fitted peaks (orange line), the starting spectrum (black line) and the difference between the starting spectrum and the sum of the fitted peaks (red line). The better the overlap between the original spectrum and the sum of the fitted peaks, the better will be the fit which will be confirmed quantitatively by a goodness-of-fit value close to zero. The table of peaks is automatically updated after the fit adding to the chemical shift value of each peak, also area, linewidth and the function used to fit each peak.

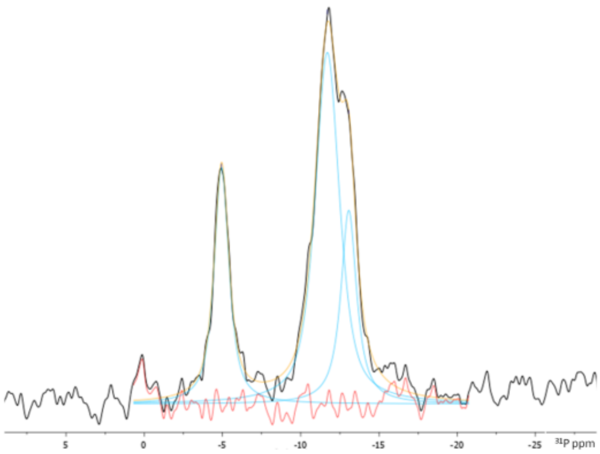

Figure 4.12 Example of a deconvolution output for two overlapped peaks returned by ACD/Lab. The black line indicates the original spectrum, the cyan line the fitted peaks and the orange line the sum of the fitted peak. The better the overlapping between the black and the orange lines, the better will be the fit.

5 Expression of isotopic labelled Villin Headpiece Domain

5.1 Transformation and expression of VHD

An aliquot of ONE SHOT® BL21 (DE3) competent cells (Invitrogen™) was transformed as described in 4.1.2 with 5µl of 50ng/µl pLeics07 plasmid (Figure 5.1) already containing the sequence for the expression of the VHD provided by Dr. Pfuhl. The gene that encodes for the resistance to kanamycin and the His-tag (a sequence of six repeated histidine residues) placed at the N-terminus of the insert that allows an easy first step purification by affinity chromatography are the two most peculiar features of the pLeics07 plasmid. Six residues encoding for the recognition site by TEV protease (usually ENLYFQ\S) are inserted between the His-tag and the sequence of the protein of interest for a fast cleavage of the tag after the purification protocol.

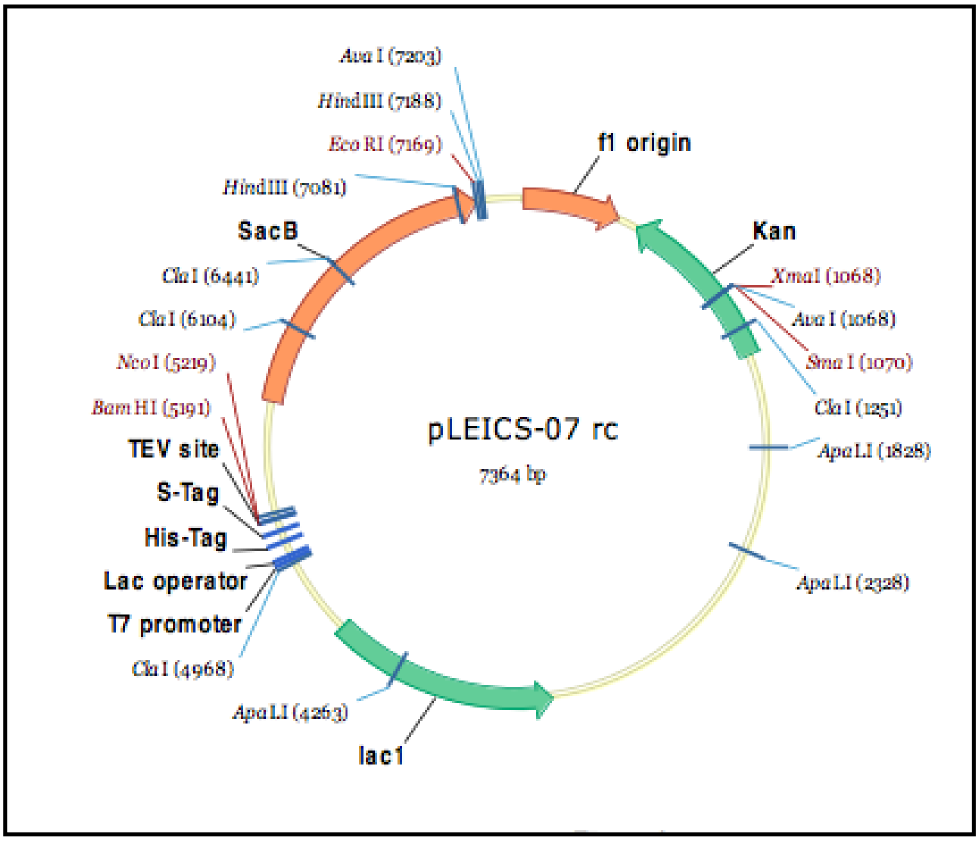

Figure 5.1 Map of an empty pLeics07 plasmid.

A transformed colony was picked, transferred to 5ml of fresh LB medium (if not specified the medium contains the required antibiotics kanamycin) and incubated overnight at 37°C in a shaker. The day after, the overnight culture was used as starter culture for the expression of VHD as described in 4.1.3. After the harvesting of the cells the pellet was resuspended and the cells were lysate. Figure 5.2 shows the result of this step.

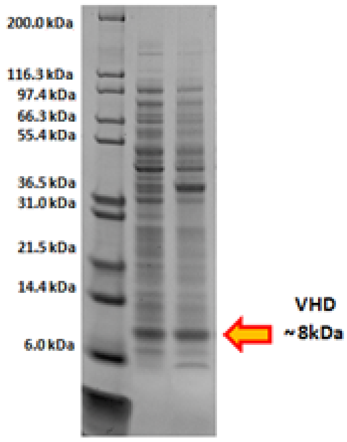

Figure 5.2 SDS-PAGE of after cellular lysis. The first column corresponds to the marker while the second and the third correspond (respectively) to the total lysate and soluble fraction. The band corresponding to the VHD (~ 8kDa) is highlighted by the orange arrow.

The subsequent application of two steps of affinity chromatography, intercalated by the cleavage of the histidine tag, as shown in Figure 5.3, proved to be sufficient to produce a clean protein sample as demonstrated in the FT line in Figure 5.3 where only the band from the VHD is present.

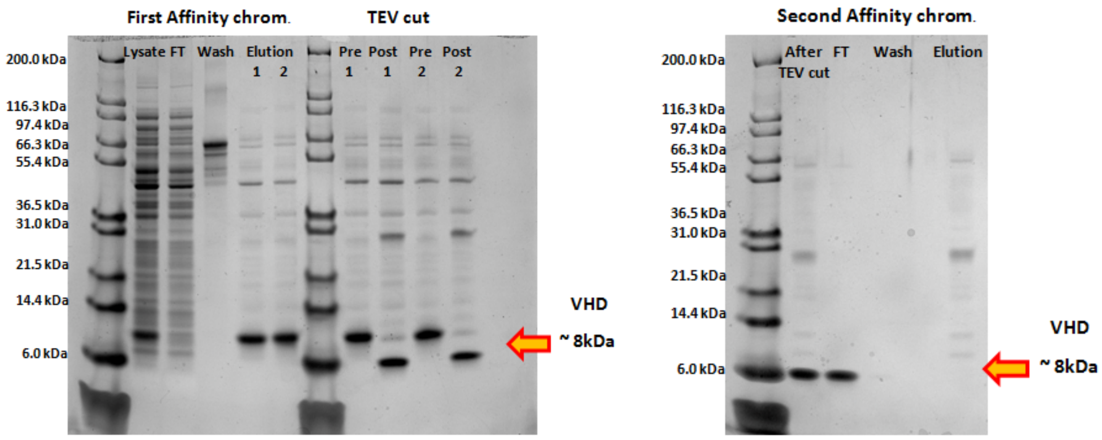

Figure 5.3 In the left panel is shown the SDS-PAGE of the first step of affinity chromatography and the efficiency of the TEV cleavage. The lysate solution was loaded in two different columns (1 and 2). FT indicates the flow through fraction. In the right panel is reported the SDS-PAGE of the second step of affinity chromatography. After the TEV cut the two aliquots were mixed and loaded into one column.

Every preparation was analysed by NMR to check the proper folding of the protein and to confirm the desired labelling. Simple one-dimensional ^{1}H spectra were used to define the folding of VHD by the analysis of the region between 0ppm and -1ppm, while ^{1}H-^{15}N and ^{1}H-^{13}C HSQC spectra were acquired to confirm the goodness of the desired labelling.

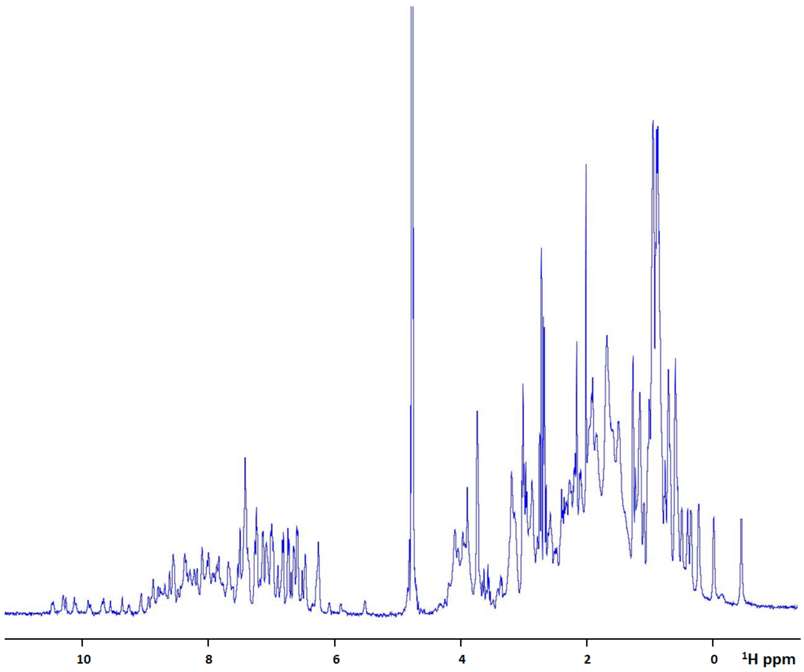

Figure 5.4 1D ^{1}H spectra were used to define the folding of VHD by the analysis of their region between 0ppm and -1ppm. The spectrum was recorded at room temperature using a 500MHz Bruker magnet equipped with a triple resonances cryoprobe.

5.2 Isotopic labeling of VHD

In NMR only the nuclei with spin $1/2$ can be easily detected since they are not affected by the quadrupolar interaction that arises in nuclei with a different spin number. Unfortunately, the principal nuclei that constitute an amino acid, carbon and nitrogen with the exception of protons, have spin numbers different from $1/2$ in natural abundance. Therefore, isotopic labeling of a protein is required in order to increase the sensitivity and resolution and to simplify the complexities of spectra. The most common strategy involves the uniform and extensive labeling of the protein with ^{13}C-glucose and ^{15}N-ammonium salt [79].

In a cell, the glucose is metabolized in two molecules of pyruvate and energy (ATP and electron acceptors) at the end of glycolysis. The pyruvate produced is then converted in Acetyl-CoA and enters the citric acid cycle. The principal function of this cycle is to create energy through the oxidation of acetate (GTP and electron acceptors) and, in addition, the citric acid cycle provides the precursors for most of the amino acids. The schematic pathway for the biosynthesis of all the amino acids in *E.coli* is illustrated below.

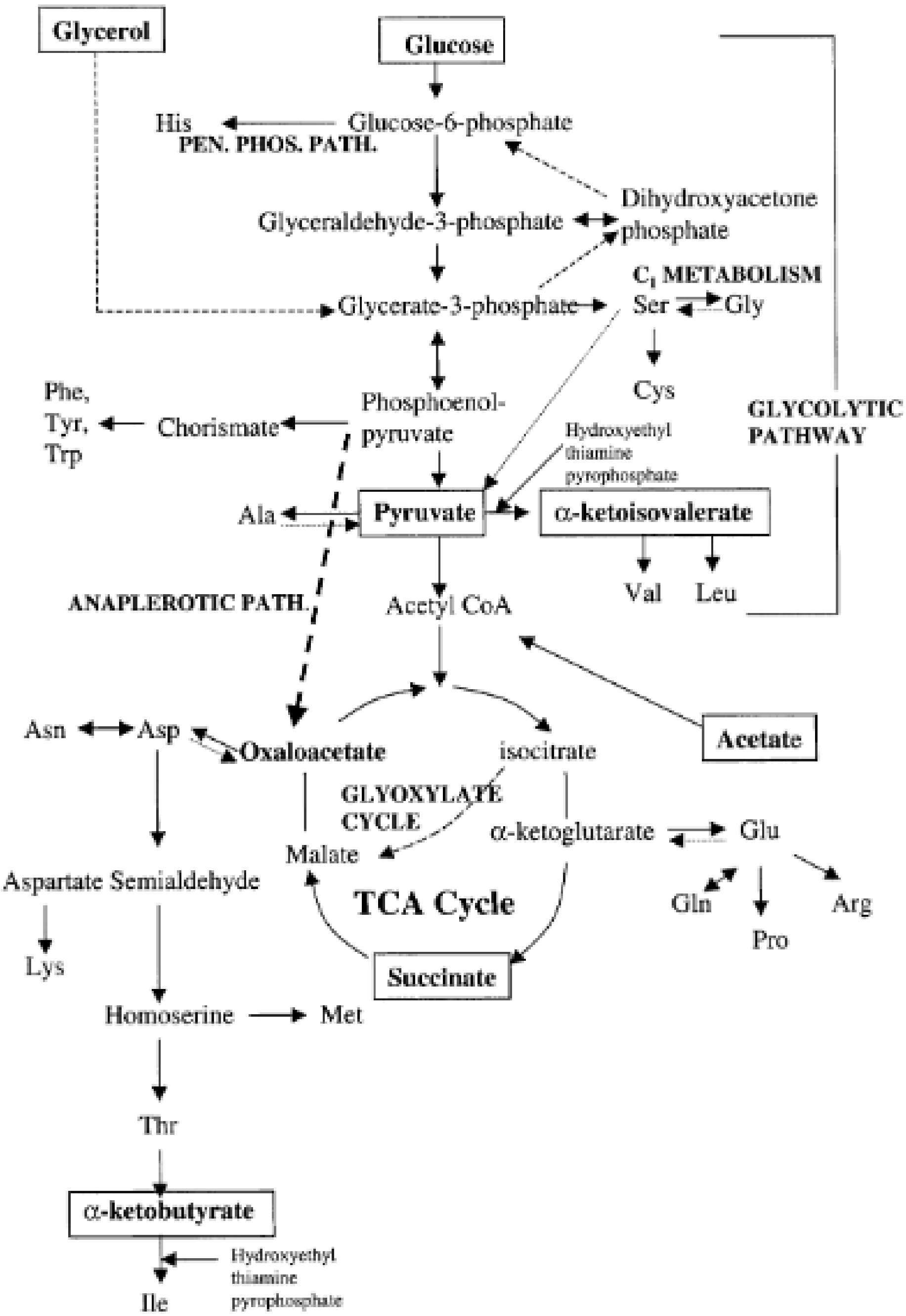

Figure 5.5 Schematic of amino acid biosynthesis in *E. coli*. The reaction scheme illustrates how isotopically labelled carbon sources (bold and boxed) are incorporated into amino acids; the pathways shown are the Glycolytic and Pentose Phosphate Pathways, C1 metabolism, the Tricarboxylic Acid Cycle including the Glyoxylate Shunt, and the Anaplerotic pathway [79].

On the other hand, it is reported in the literature that, when cells are supplied with a different source of carbon than ^{13}C-glucose, it is possible to create different and selective schemes of isotope labeling. These new selective schemes are an important tool that helps dilute the resonances when large molecules are observed [80] helping their complete assignment. Under aerobic conditions, bacteria can utilize glucose, pyruvate, acetate, succinate and glycerol as sole carbon source, and ammonium salts as the sole nitrogen source to synthesize all the amino acids [79]. Nowadays, different isotopic labeling of these precursors are commercially available (Figure 5.6) and new exotic selective labeling schemes are therefore possible.

Labelling agent	Chemical formula	Incorporation sites
[$^{13}C_6$]-Glucose	$^{13}C_6H_7(OH)_5O$	Uniform ^{13}C
[1-^{13}C]-Glucose	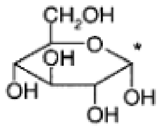	$^{12}C-^{13}C-^{12}C^{c}$
[$^{13}C_6$,d_7]-Glucose	$^{13}C_6D_7(OH)_5O$	Uniform ^{13}C and perdeuteration
Acetate d_4	CD_3CO_2D	Perdeuteration
$^{13}C_2$ Acetate	$^{13}CH^{13}CO_2H$	Uniform ^{13}C
[4,4′-^{13}C]-α-ketoisovalerate	$(^{13}CH_3)_2CHCOCO_2H$ in H_2O	(^{13}C-δ-Me) Leu (^{13}C-γ-Me) Val
[3,^{2}H]-^{13}Cα-ketoisovalerate	$(CH_3)_2CDCOCO_2H^{d}$ in D_2O	($^{13}C^1H$-δ-Me) Leu ($^{13}C^1H$-γ-Me) Val Selective methyl protonation
[4-^{13}C]-α-ketobutyrate	$^{13}CH_3CH_2COCO_2H$ in H_2O	(^{13}C-δ1-Me) Ile
[3,3′-$^2H_2$]-^{13}Cα-ketobutyrate	$CH_3CD_2COCOH_2^{d}$ in D_2O	($^{13}C^1H$-δ_1-Me) Ile Selective methyl protonation
[2-^{13}C]-glycerol	$CH_2(OH)^{13}CH(OH)CH_2(OH$	$^{12}C-^{13}C-^{12}C$
[1,3-$^{13}C_2$]-glycerol	$^{13}CH_2(OH)CH(OH)^{13}CH_2(OH$	$^{12}C-^{13}C-^{12}C$
Glycerol $^2H_8$	$CD_2(OD)CD(OD)CD_2(OD)$	Perdeuteration
$^{13}C_3$ Pyruvate	$^{13}CH_3{}^{13}CO^{13}CO_2H$ in D_2O	(^{1}H-δ-methyl) leu (^{1}H-γ-methyl) val (^{1}H-γ2-methyl) ilel (^{1}H-β-methyl) ala Uniform ^{13}C-labelling
[3-^{13}C]-Pyruvate	$^{13}CH_3COCO_2H$ in H_2O or D_2O	(^{13}C-δ-methyl) leu (^{13}C-γ-methyl) val (^{13}C-γ2-methyl) ilel (^{13}C-β-methyl) ala
Succinate d_6	$DO_2C(CD_2)_2CO_2D$	Perdeuteration

Figure 5.6 Precursors and metabolites used in uniform and selective isotope labeling strategies [79].

The amount of VHD expressed in *E.coli*, meant as the yield of VHD in mg from one liter of minimal medium, was very different when the cells were supplied with different sources of ^{13}C. When the expression was induced directly in LB medium it was possible to obtain near 25-30mg of non-labelled VHD from one liter of media. The yield dramatically decreased when the cells were moved into minimal medium. E.g. when *E.coli* was supplied with ^{15}N-ammonium chloride and glucose the final yield was just 20-22mg while when supplied with ^{15}N-ammonium chloride and ^{13}C-glucose the yield dropped to just 15-18mg. In Table 5.1 is reported the yield of protein in mg from one liter of minimal medium for the different media used to achieve the several isotopic labelling schemes attempted. It is interesting to notice how the increase in the complexity of the isotopic hydrogen, nitrogen and carbon sources coincides with a decrease in the yield of VHD expressed.

Nitrogen and carbon source	Yield in mg from L of minimal medium
LB medium	25-30mg/L
$^{15}NH_4Cl$ and glucose	20-22mg/L
$^{15}NH_4Cl$ and ^{13}C glucose	15-18mg/L
^{2}D, $^{15}NH_4Cl$ and ^{13}C glucose	10mg/L
$^{15}NH_4Cl$ and 1,3-^{13}C-glycerol	12-14mg/L
$^{15}NH_4Cl$ and 2-^{13}C-glycerol	10-12mg/L
^{15}N, ^{13}C Alanine, NH_4Cl and glucose	6-8mg/L

Table 5.1 VHD yield in mg from one liter of minimal medium for the different media employed. Increasing the complexity of the nitrogen, carbon and hydrogen sources supplied to the bacteria resulted in a decreasing of the yield of protein expressed.

5.2.1 Expression of uniformly labelled VHD: ^{15}N, ^{15}N and ^{13}C and perdeuterated ^{15}N and ^{13}C labeling

As just mentioned the yield in mg of VHD when the bacteria were supplied with a different isotopic version of the atoms differs in each condition. When the expression was performed only for ^{15}N labeling, after the purification, the amount of VHD obtained was usually close to 20-22mg while the amount decreased to 15-18mg when the double labelled version of VHD was expressed. The production of a perdeuterated version of ^{15}N and ^{13}C VHD resulted in an even more severe lowering of the yield to 10-12mg of protein from a liter of deuterated minimal medium.

The incorporation of isotopic atoms in the VHD was higher than 95% both when supplied with ^{15}N-ammonium salt and with ^{13}C-glucose and ^{15}N-ammonium salt (respectively, Figure 5.7 and Figure 5.8, Figure 5.9 and Figure 5.10). Analysis of the intensity of the signals from the splitting of the peak at -0.45ppm and 0.05ppm were used to estimate the rate of incorporation of ^{13}C (Figure 5.10).

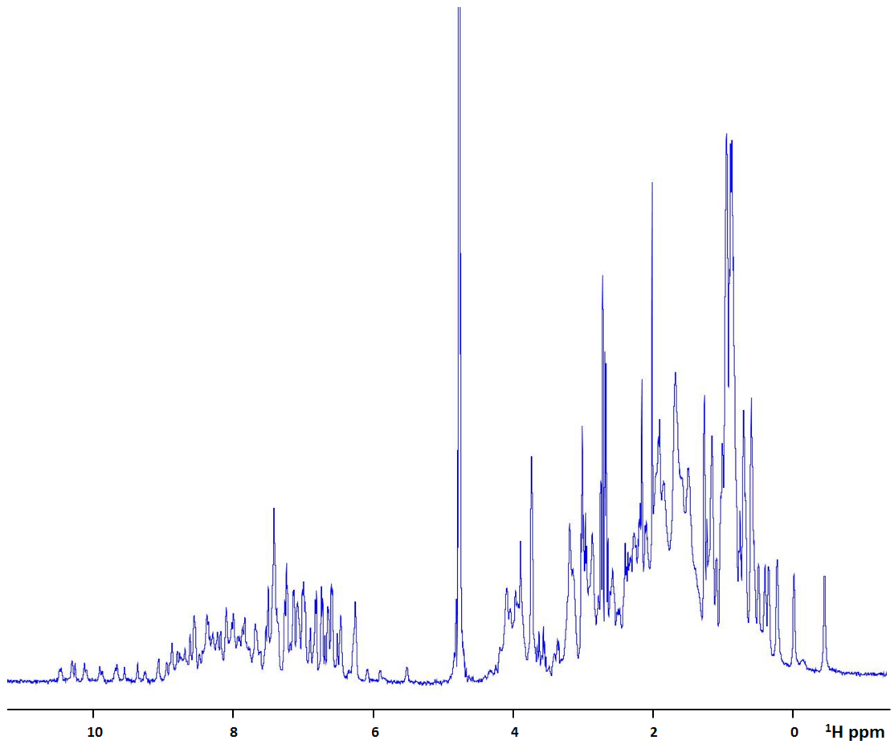

Figure 5.7 1D ^{1}H spectrum of uniformly labelled ^{15}N-VHD. The peaks around 10ppm confirmed the good incorporation of the isotopic version of nitrogen. The peaks at -0.45ppm and 0.05ppm showed that the VHD was folded. The spectrum was recorded at room temperature using a 500MHz Bruker magnet equipped with a triple resonance cryoprobe.

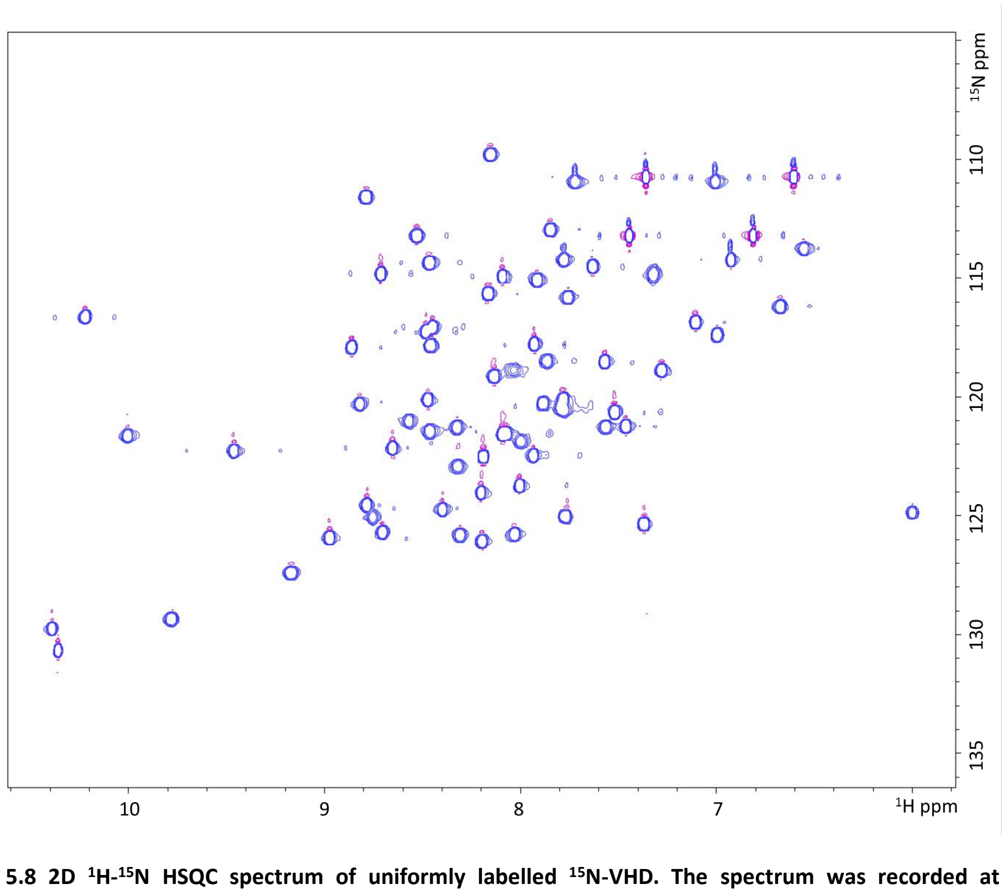

Figure 5.8 2D ^{1}H-^{15}N HSQC spectrum of uniformly labelled ^{15}N-VHD. The spectrum was recorded at room temperature using a 500MHz Bruker magnet equipped with a triple resonance cryoprobe.

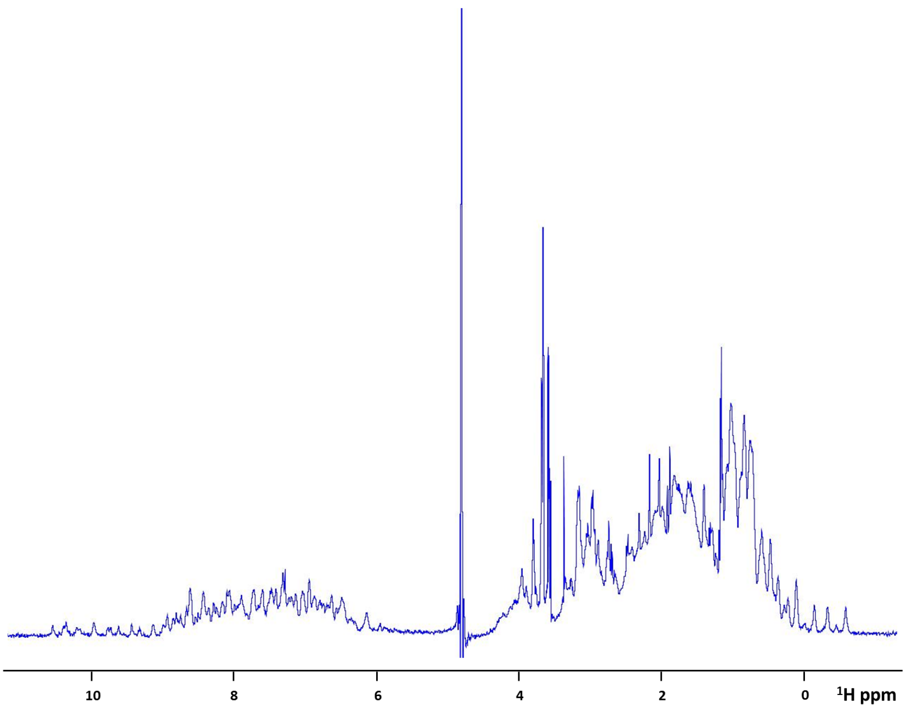

Figure 5.9 1D ^{1}H spectrum of uniformly labelled ^{15}N-^{13}C VHD. The peaks at 10ppm confirmed the incorporation of ^{15}N while the splitting into a doublet of the signal at -0.45ppm the incorporation of ^{13}C carbon. The rate of incorporation is higher than the 90% of the total as residual peaks at -0.45ppm and 0.05 were still recognizable and they counted for less of 10% for their integral. The spectrum was recorded at room temperature using a 500MHz Bruker magnet equipped with a triple resonance cryoprobe.

Figure 5.10 2D ^{1}H-^{13}C HSQC spectrum in D_2O of uniformly labelled ^{15}N-^{13}C VHD. This experiment was used as reference to confirm the quality of the different selective labeling in the ^{13}C that were performed. The spectrum was recorded at room temperature using an 800MHz Bruker magnet equipped with a triple resonance cryoprobe.

The crucial point for the incorporation of isotopic atoms was the wash of the pellets with the M9 salts before to transfer the resuspended cells in minimal medium. It was observed that a hurried and inaccurate wash can lower the incorporation of ^{13}C until 50-60% (Figure 5.11).

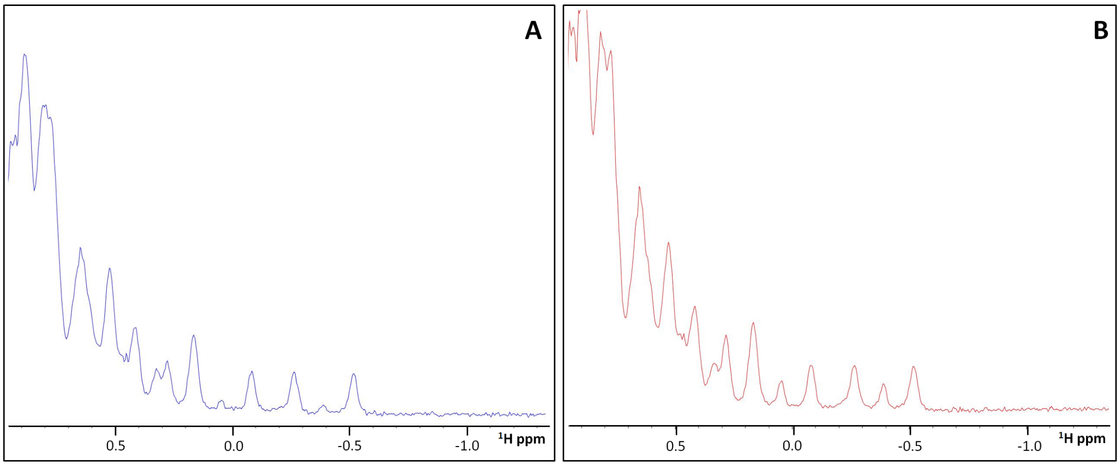

Figure 5.11 1D ^{1}H spectra of the region close to 0ppm of uniformly labelled ^{15}N-^{13}C VHD when an inaccurate wash of the cells with M9 diluted salt solution is performed. Panel A (blue spectrum) showed the spectrum originated from of an accurate wash. The doublet highlighted derived from the splitting of the resonance of a methyl group due to the presence of the J-coupling between the ^{1}H and the ^{13}C in it. When the wash is not accurately performed in the minimal medium part of the non-isotopic carbon from the LB medium will be still present. This will interfere with a correct incorporation of the ^{13}C supplied maintaining a pool of the protein expressed containing the unlabelled carbon. In this case, (Panel B, red spectrum), taking into account the methyl described above, the spectrum originated will show the doublet due to the J-coupling between the ^{1}H and the ^{13}C in the labelled protein and the signal not split from the methyl group in the unlabelled protein. The integral over the three signals was count as 1 and the three components were calculated. The not-split signal from the unlabelled protein counted for less than 5% in the blue spectrum but near the 40% for the red spectrum indicating an incorporation of the isotopic carbon of, respectively, ~95% and ~60%.

The incorporation of ^{2}H was not 100% as shown in the proton spectrum in Figure 5.12. Its incorporation was limited only to the positions of amino acids that cannot exchange with the solvent (Figure 5.12) due to the fact that during the protein purification non-deuterated buffers were used. The back-exchange of ^{1}H in the backbone positions using 100% H_2O buffer is called fractional protein deuteration [81] and it has been done on purpose (Figure 5.13) in order to maintain a pool of ^{1}H fundamental for running a ^{13}C CP experiment. On the other hand, the presence of ^{2}H in the side chains can significantly enhance the resolution of proton spectra by diluting the proton-proton dipolar coupled network [82].

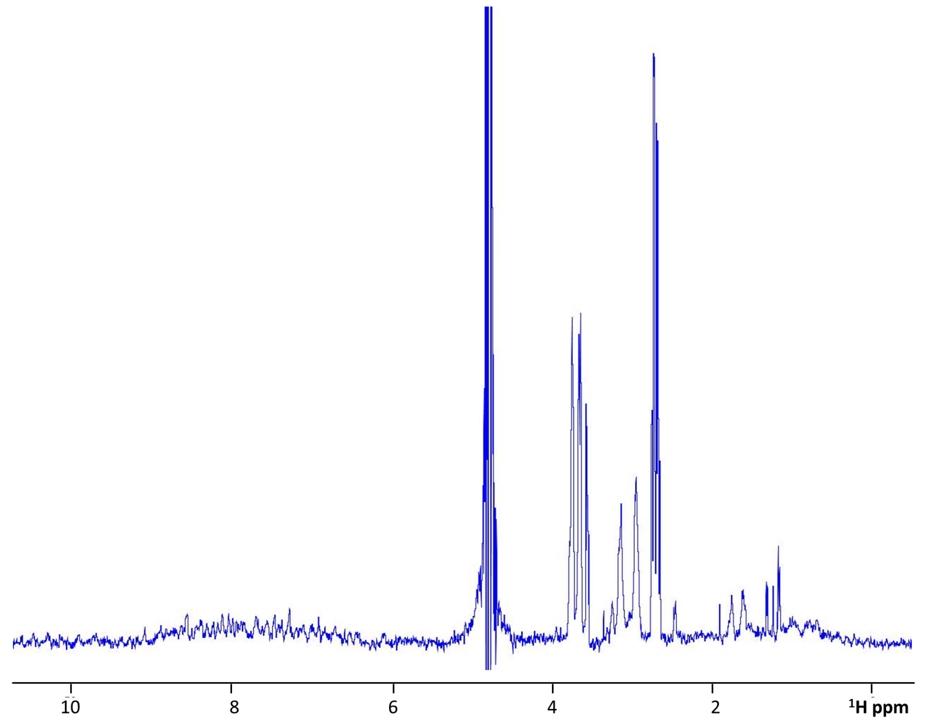

Figure 5.12 1D ^{1}H spectrum of uniformly labelled ^{2}H-^{15}N-^{13}C VHD. Only the region between 6 to 10ppm showed signals from proton indicating the incorporation of ^{2}H into the side chains. The signals at high field arise from contaminants such as glycerol and DTT. The spectrum was recorded at room temperature using a 500MHz Bruker magnet equipped with a triple resonances cryoprobe.

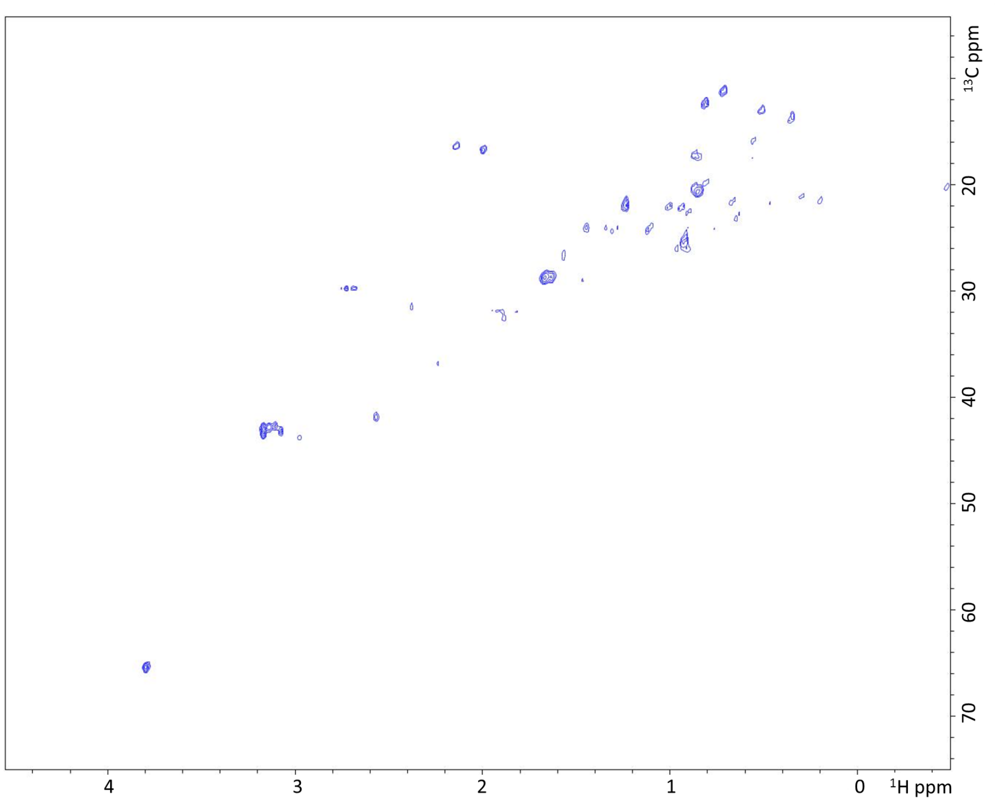

Figure 5.13 2D ^{1}H-^{13}C HSQC spectrum of uniformly labelled ^{2}H-^{15}N-^{13}C VHD. The absence of most of the resonances confirmed the incorporation of the ^{2}H into the side chains. The resonances still present arose from a small portion of proteins that did not incorporate the deuterium. The spectrum was recorded at room temperature using a 500MHz Bruker magnet equipped with a triple resonance cryoprobe.

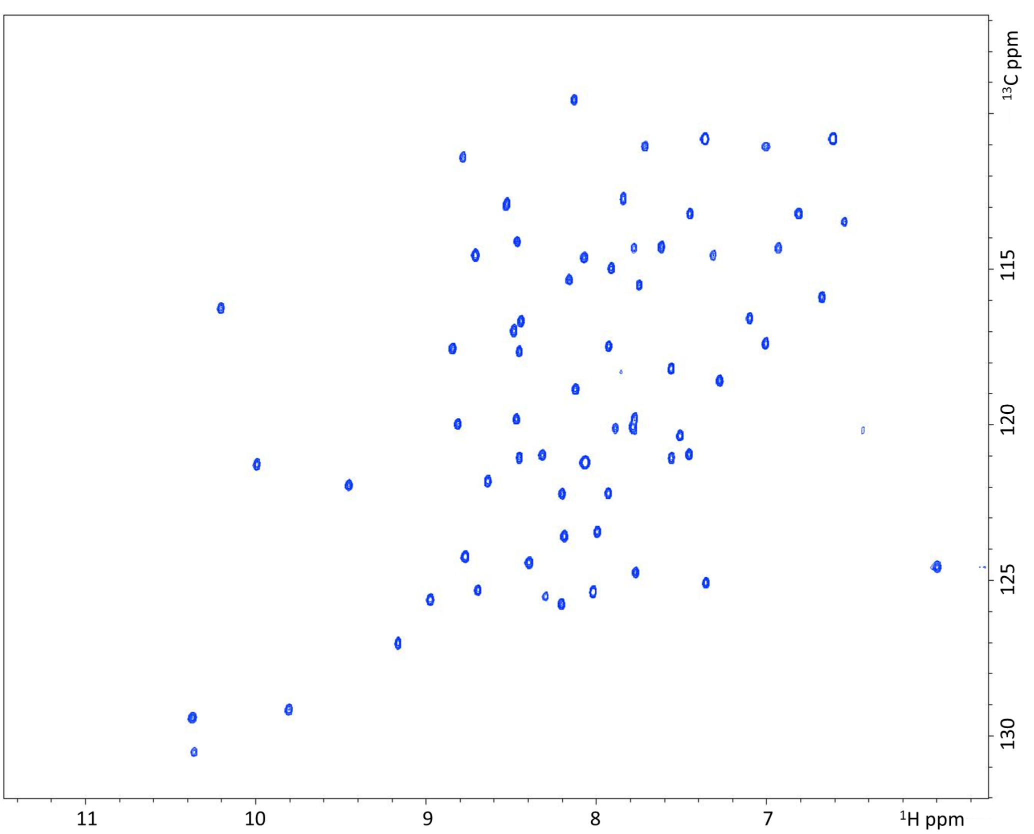

Figure 5.142D ^{1}H-^{15}N HSQC spectrum of uniformly labelled ^{2}H-^{15}N-^{13}C VHD back-protonated using 100% H_2O. The ^{2}H in the backbone that could exchange with the solvent were changed with protons from non-deuterated buffer implemented during the purification of the protein. The spectrum was recorded at room temperature using a 500MHz Bruker magnet equipped with a triple resonances cryoprobe.

5.2.2 Expression of ^{15}N uniformly labelled and ^{13}C selective labelled VHD

Two original selective schemes based on the addition to minimal medium of one between 1,3-^{13}C-glycerol and 2-^{13}C-glycerol are now of common use [83-86]. When these forms of glycerol were supplied to *E.coli*, the amino acids that derived from the glycolytic and pentose phosphate pathways (alanine, cysteine, glycine, histidine, leucine, phenylalanine, serine, tryptophan, tyrosine and valine) have all sites either ^{13}C or ^{12}C labelled in almost 100% of the cases [80]. All the amino acids that are synthesized from precursors from the citric acid cycle result in an almost random carbon labeling. If an unlabelled version of these amino acids is added to the medium their synthesis can be blocked (

Figure 5.15).

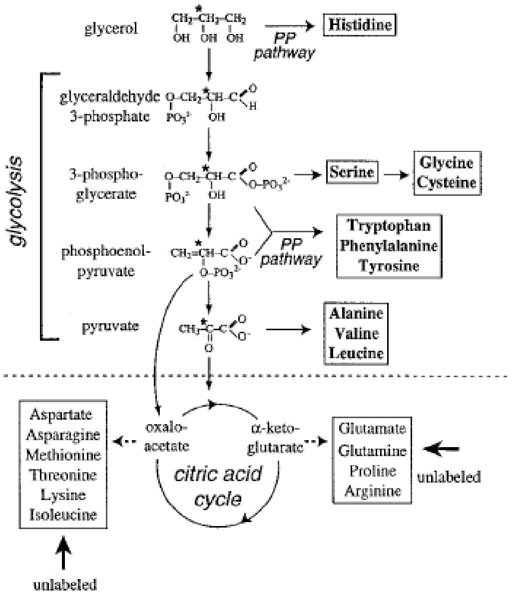

Figure 5.15 Amino acid biosynthetic pathways in bacteria, utilizing glycerol as the main carbon source. To achieve selective 13C labeling of hydrophobic amino acids, which are largely produced from the glycolytic and the pentose phosphate (PP) pathways, the growth media is supplemented with unlabelled amino acid products of the citric acid cycle [85].

A schematic table illustrating the two patterns of labeling arising adding these two forms of glycerol is reported in the Figure 5.16.

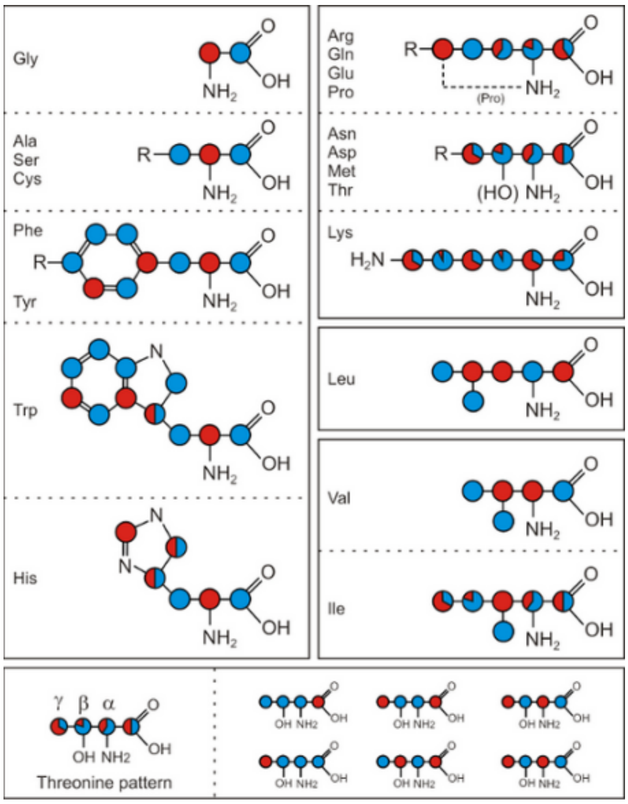

Figure 5.16 Schematic representation of the effective ^{13}C enrichment for the indicated residues, as obtained by protein expression in *E. coli* BL21 (DE3). The blue color corresponds to the degree of ^{13}C labeling pattern obtained by growth on [1,3-^{13}C]glycerol; the opposite labeling pattern, obtained by growth on [2-^{13}C]glycerol, is represented in red. In cases with mixed labeling, the percentage label from [2-^{13}C]glycerol and [1,3-^{13}C]glycerol for a particular atom is represented using relative red/blue coloring [84].

The yield of selective labelled VHD using 1,3-^{13}C-glycerol ([1,3-^{13}C]-^{15}N VHD) was around 12-14mg of protein from one liter of minimal medium but, when supplied with 2-^{13}C-

glycerol ([2-^{13}C]-^{15}N VHD), the yield was 10-12mg, always slightly lower in respect of the other isotope of glycerol. No unlabelled amino acids were added in order to block the synthesis of residues with mix isotope labeling. The ^{1}H-^{13}C HSQC spectrum in Figure 5.18 (blue spectrum in panel C) represents the labeling arising from 1,3-^{13}C-glycerol while the spectrum in Figure 5.19 (red spectrum in panel C) the labeling from 2-^{13}C-glycerol. Both were overlapped to the ^{1}H-^{13}C HSQC of a ^{13}C uniformly enriched VHD acquired in D_2O (Figure 5.17) showing a clear dilution in the number of their resonances (Panel D of both Figure 5.18 and Figure 5.19).

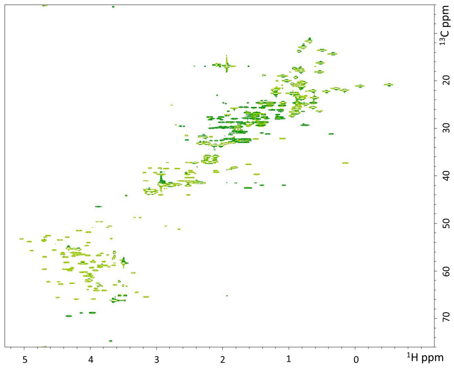

Figure 5.17 ^{1}H-^{13}C HSQC spectrum in D_2O of uniformly labelled ^{15}N-^{13}C VHD used as reference to estimate the quality of the selective ^{13}C labeling performed. The spectrum was recorded at room temperature using an 800MHz Bruker magnet equipped with a triple resonance cryoprobe.

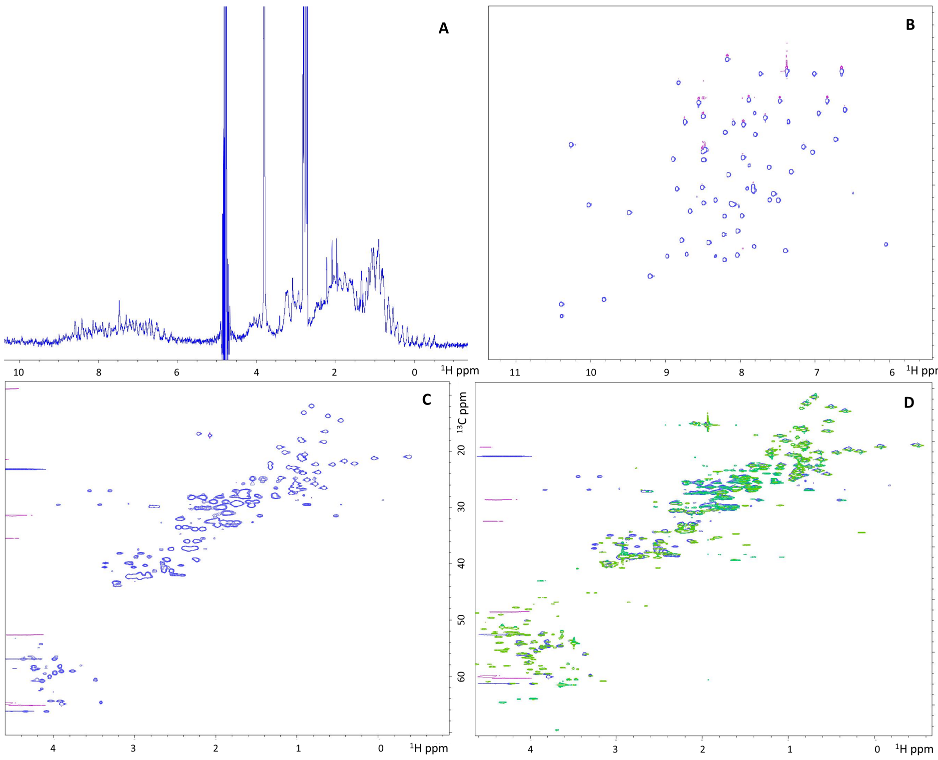

Figure 5.18 Characterization of [1,3-^{13}C]-^{15}N VHD (blue spectra). Panel A shows the 1D ^{1}H spectrum while panel B the ^{1}H-^{15}N HSQC. The ^{1}H-^{13}C HSQC reported in panel C was then overlapped (panel D) to the reference ^{1}H-^{13}C HSQC (green spectrum). The assignment of the resonances confirmed the expected pattern of resonances that should arise using 1,3-^{13}C-glycerol as only isotopic carbon source. The spectra were recorded at room temperature using a 500MHz Bruker magnet equipped with a triple resonances cryoprobe.

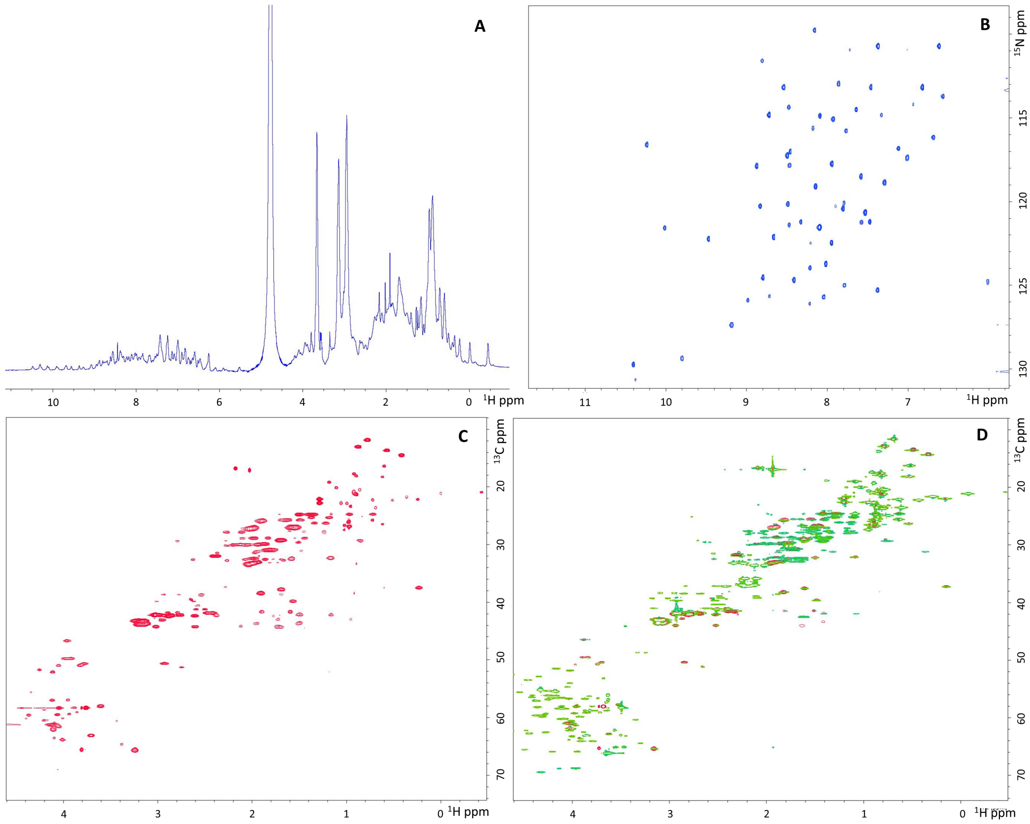

Figure 5.19 Characterization of [2-^{13}C]-^{15}N VHD (red spectra). Panel A shows the 1D ^{1}H spectrum while panel B the ^{1}H-^{15}N HSQC. The ^{1}H-^{13}C HSQC in panel C was then overlapped (panel D) to the reference ^{1}H-^{13}C HSQC (green spectrum). The resonances assignment confirmed the pattern of signals arising using 2-^{13}C-glycerol as only isotopic carbon source. The spectra were recorded at room temperature using a 500MHz Bruker magnet equipped with a triple resonance cryoprobe.

5.2.3 Expression of protein ^{15}N and ^{13}C ALA selective labelled

In order to achieve the simplest spectrum possible a single isotopic labelled incorporation strategy was implemented. As reported in the literature [87, 88] for some of the amino acids (alanine, leucine, isoleucine, lysine, methionine, cysteine and histidine), when the isotopically labelled version is supplied, the spectra show strong signals that correspond only to the amino acid added. Instead, the other amino acids that are not at the end of a metabolic pathway show a considerable label scrambling to other residues. E.g. glycine shows a significant label scrambling to serine [87, 88].

The VHD amino acidic sequence showed the presence of only two alanine residues and it was selected as a candidate for this protocol. As shown in Figure 5.20 only the signals from alanine residues arose confirming the selectivity of the labelling for this residue.

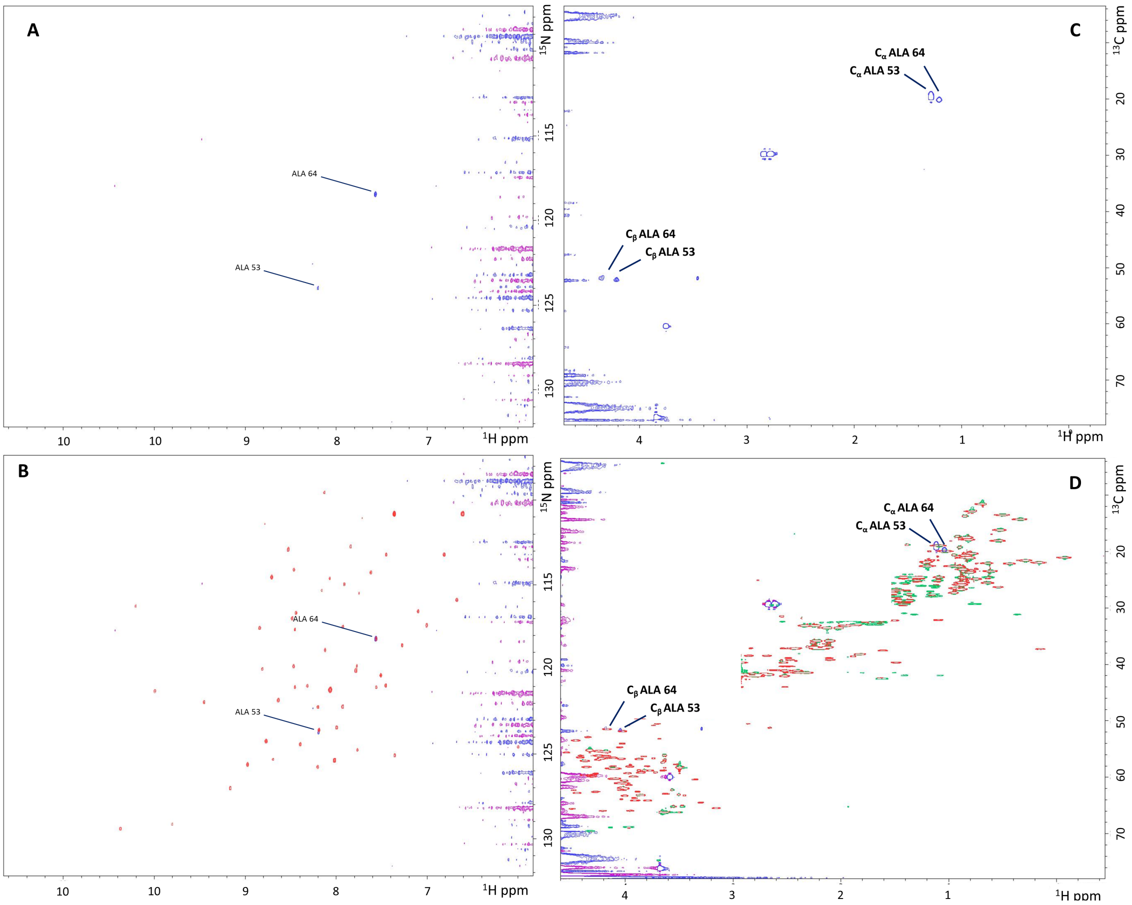

Figure 5.20 Characterization of ^{15}N, ^{13}C Alanine selective labeling. In panel A is reported the ^{1}H-^{15}N HSQC and in panel B the overlapping to the 15N uniformly labelled VHD. In Panel C was reported the ^{1}H-^{13}C HSQC that was then overlapped (panel D) to the reference ^{1}H-^{13}C HSQC of a uniformly labelled ^{15}N-^{13}C VHD. In both nitrogen and carbon spectra no signs of scrambling are recognizable. The spectrum was recorded at room temperature using a 750MHz Bruker magnet equipped with a triple resonance cryoprobe.

The yield in mg from a liter of minimal medium supplied with ^{15}N-^{13}C alanine and glucose was never higher than 6-8mg. Nevertheless, the actual rate of incorporation of enriched alanine is not available and a method to measure it is under investigation.

6 Optimization of the conditions to prepare VHD-actin filament complex suitable for ssNMR

6.1 Actin filament preparation

Starting from near 150g of skeletal rabbit muscles more than 20g of acetone powder were obtained using the protocol described in 4.4.2. Each extraction and subsequently purification of actin was performed using 1.5g of powder each time resulting in near 90-100mg of protein each extraction. As illustrated in Figure 6.1, after the first polymerization of monomeric actin into filaments, the SDS-PAGE showed in the pellet the presence of several actin binding proteins that were easily removed by the second round of depolymerization and polymerization in filaments (line 4 and 5 of SDS-PAGE in Figure 6.1).

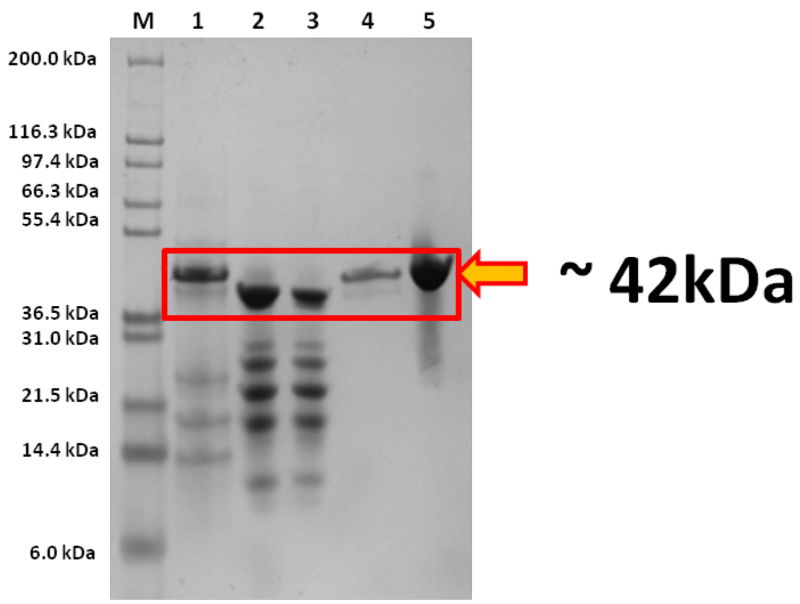

Figure 6.1 SDS-PAGE of actin filaments preparation. In line 1 the pellet resuspended after the first run of ultracentrifuge showed the presence of several actin binding proteins; in line 2 was loaded the actin solution after dialysis while in line 3 was loaded the supernatant from the second ultracentrifuge; the supernatant and the pellet from the last ultracentrifuge of the protocol were loaded respectively in line 4 and 5. No presence of contaminants is noticeable. The different position of actin bands is due to the sensitivity of SDS-PAGE to the different salt concentration.

6.2 Binding affinity determination

To measure the affinity between the VHD and the actin filaments two different approaches were used, a fluorimetric assay and a co-sedimentation assay. These two approaches allowed to work with a dilute solution of actin filaments (around 15µM for each repetition) thus avoiding the tendency of actin filaments to aggregate, creating bundles. For this reason, the more common ITC technique or the newer MST technique which can give false results in these conditions were not applied. Both assays were performed in triplicate, the concentration of actin maintained around 15µM for each assay. The data collected were analysed in order to plot the percentage of saturated sites in the actin filaments against the increasing concentration of VHD added. Even if the stoichiometry of the binding was unknown a 1:1 VHD to actin monomer was assumed when the data was processed. Nevertheless, a different ratio cannot be excluded and structural data are required to clarify it. The measured kD was in the around of 2.7µM for both the techniques as shown in Figure 6.2.

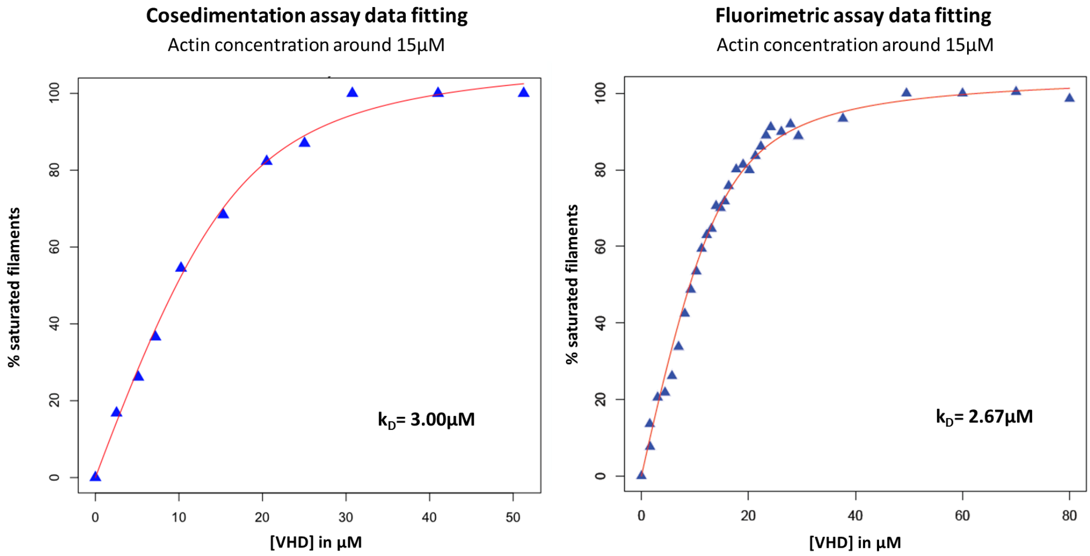

Figure 6.2 Fitting of the data from binding affinity assays performed using R software. The left panel shows the fitting performed on the data from the fluorimetric assay, while the right panel from the cosedimentation assay. In both the biological assays performed, the affinity calculated was in the order of 2.7µM.

This means that to complete saturate the filaments, the amount of VHD had to be at least seven times the amount of actin used. This was considered unachievable when any isotopically labelled version of VHD was used for experiments employing a 4mm rotor. On the other end, it was estimated that 5-7mg of labelled protein should be enough to successfully run ssNMR experiments in 4mm rotors. For this purpose, 10-15mg of labelled VHD was added to 35-40mg of actin filaments which were sufficient to prepare a sample in which near 5-6mg of labelled protein were bound to the filaments.

6.3 Actin filaments precipitation

Usually, in ssNMR, the sample consists of powder or crystallites. Unfortunately, it is not possible to achieve crystallites containing actin filaments or dry to powder the actin filaments without affecting their structure. On the other hand, actin when in the filamentous state can easily sediment as a gel-like pellet when centrifuged. Depending on the speed used to pellet the filaments and the presence of molecules able to bind the filaments the features of the pellet change. When actin filaments are sedimented alone, a minimum speed of 18000rpm is required to sediment the filaments resulting in a clear sticky gel-like pellet still rich in buffer. After increasing the centrifugation speed to 50000rpm less buffer remains trapped in the pellet resulting in a harder and less sticky pellet. Lower speed, e.g 30000rpm, can be used but at this speed some of the filaments can remain in the supernatant.

Investigating the best conditions to prepare the actin filaments, several drugs known in the literature to stabilize the filaments (e.g. phalloidin, cucurbitacin etc.) were used. The main effect of this drug was to decrease the dissociation of monomer and to help the filaments thermal stability [33, 89]. It was also demonstrated that their presence can help to sediment the filaments at lower speed (30000rpm) even if they failed to show improvement in the resolution of ssNMR spectra acquired as illustrated later in this chapter.

The sedimentation of actin filaments complexed with actin binding domains (ABDs) showed a peculiar behavior. When the filaments were saturated by the ABD, the complexes sedimented at very low speed (15000rpm) resulting in a white gel-like pellet. To determine in which concentration ABDs start to affect the process, a 20µM solution of filaments was divided into four aliquots and mixed with increasing amount of VHD. The concentration of VHD for each point of the titration is reported in Table 6.1.

	Actin filaments [µM]	VHD [µM]	Final Volume [ml]
A	20	0	16.5
B	20	20	16.5
C	20	60	16.5
D	20	120	16.5

Table 6.1 Summary of the set up for the titration

Even at low concentration of VHD the pellet already presented changes in its solidity. Increasing the concentration of VHD also the solidity of the pellet increased till, when saturated, the filaments sedimented looked like a white hard gel-like pellet (Figure 6.3).

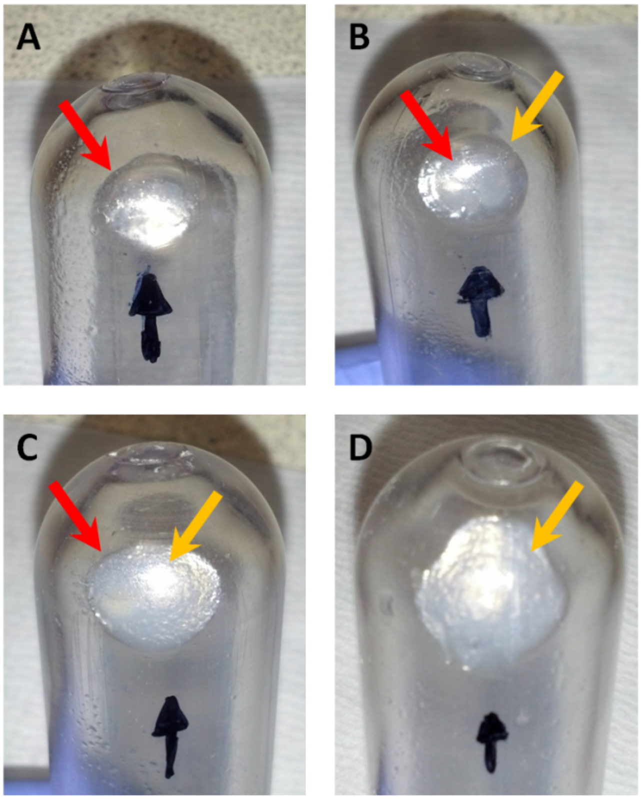

Figure 6.3 Pellet, highlighted with the black arrow, from VHD titration on filaments. Panel A shows a clear pellet, indicated by the red arrow, resulting from filaments before the addition of VHD, while panel B, C and D showed pellets of actin filaments sedimented with, respectively, VHD at 20µM, 60µM and 120µM final concentration. Increasing the amount of VHD the clear pellet, indicated by the red arrows, decrease while the white pellet, indicated by the orange arrows, increase till the filaments are saturated.

In the filament precipitation several parameters like the incubation time for the complex before the precipitation, the temperature or the centrifugation speed were taken into consideration in order to find the best and least invasive conditions. While it was observed that the incubation time before the centrifugation did not affect the process, keeping the temperature near 4°C was crucial to produce a sample in which the VHD was still folded while bound to the filaments. The other crucial parameter in this process is the centrifugation speed. Co-sedimentation assays were performed in order to investigate the best speed to sediment the complex.

5ml of a 30µM solution of filaments were added to 4ml of a 70µM solution of VHD in the same buffer. The mix was divided into aliquots of 1.5ml and each of them was centrifuged at a different speed from 10000rpm up to 30000rpm (every 2000rpm). The supernatants were separated, the pellets resuspended with an equal amount of buffer and an aliquot for each of them was collected. The aliquots from the different runs were loaded with samples of VHD at known concentration (to build a calibration curve) in an SDS-PAGE. The bands equivalent to VHD and actin were identified and their volume quantified. The calibration curve was built and the concentration of protein for each band was extrapolated. The amount of VHD bound to the actin filaments from the different runs was graphed against the speed used to centrifuge that aliquot. The resulting plot (Figure 6.4) showed that the highest amount of VHD in the pellet was achieved centrifuging at the maximum speed of 30000rpm.

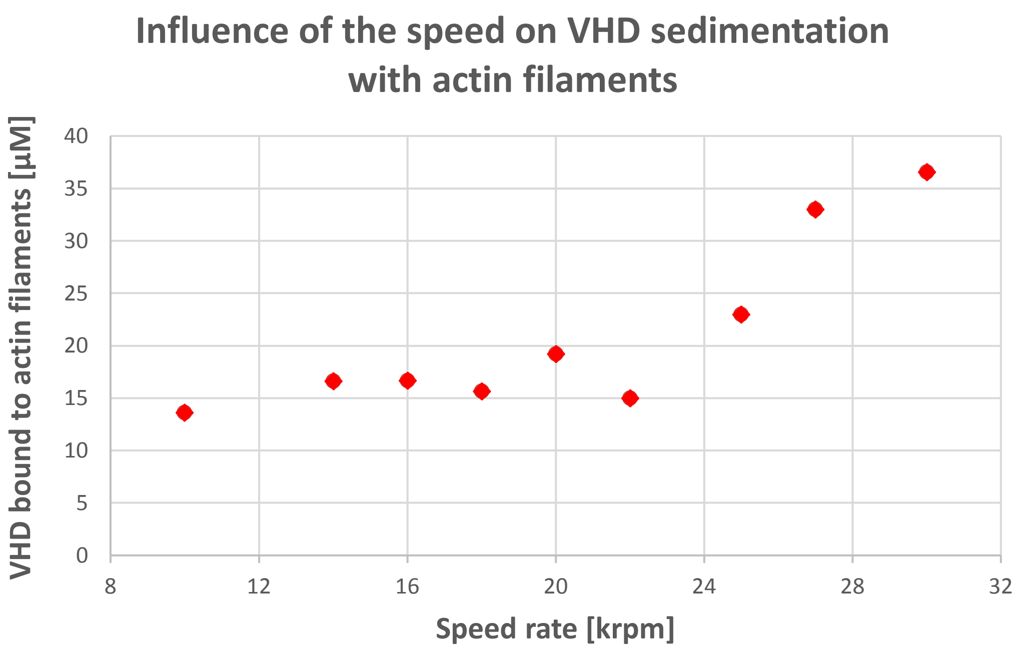

Figure 6.4 Plot showing the speed rate influence during the cosedimentation of VHD and actin filaments. The maximum coincides with the highest speed tested in the assay of 30000rpm. The pellet sedimented at speed lower than 18000rpm showed to be soft and sticky due to the presence of a high amount of buffer. For them it was difficult to efficiently collect the pellet and part of the supernatant remained in these tubes affecting their measurement.

Uniformly labelled ^{13}C-^{15}N VHD was bound to filaments and sediment at 30000rpm. ^{13}C CP MAS and ^{13}C-^{13}C correlation experiments were acquired and analysed checking the state of the VHD. Unfortunately, when compared to the chemical shift of apo VHD in solution, a general shift to higher field in the ^{13}C CP MAS spectrum (Figure 6.5, panel B) and the collapsing of cross-peak signals in the ^{13}C-^{13}C correlation spectrum (Figure 6.6) were noticed suggesting that at this speed the VHD sedimented unfolded. A lower speed of 25000rpm was then used to pellet the complex and a new set of ^{13}C experiments was acquired. Despite the amount of VHD in the complex results to be lower when compared to the filaments sedimented at 30000rpm, the ^{13}C CP MAS spectrum (Figure 6.5, panel

A) showed a dispersion of the signals in the carbonyl and α carbon regions suggesting the presence of folded VHD in the rotor.

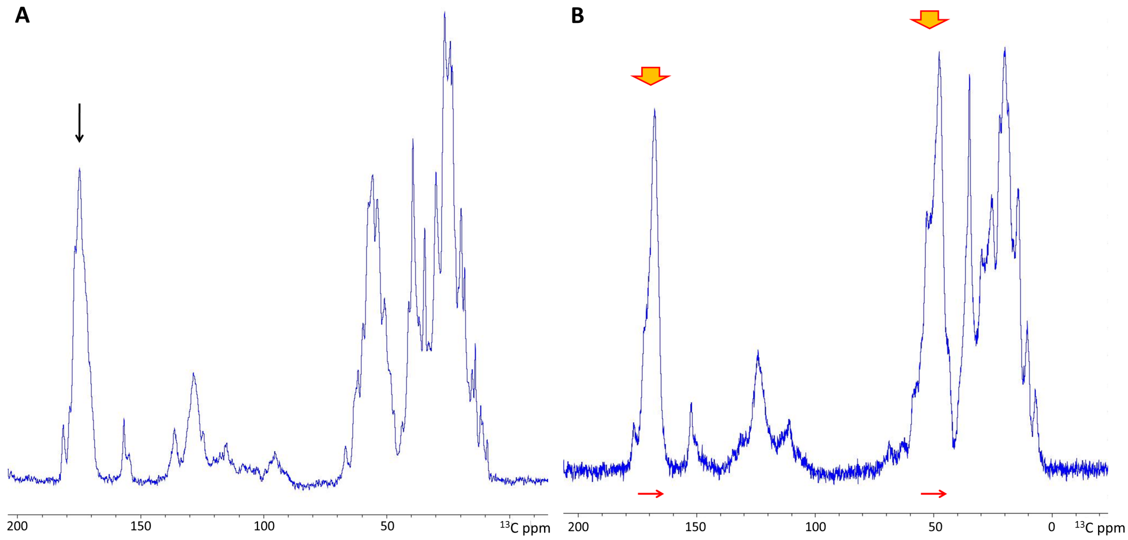

Figure 6.5 ^{13}C CP MAS spectra of ^{13}C-^{15}N VHD bound to actin filaments sedimented at different speed rate. Panel A shows the spectrum of a folded VHD bound to filaments sedimented at 25000rpm (256 scans). When the centrifuge spinning rate is higher than 30000rpm (panel B, 256 scans), an unfolded version of VHD is cosedimented with the actin filaments and it is possible to detect a general shift for the carbonyl and carbon α regions to higher field as highlighted by the red arrows. The spectra were recorded at 10kHz spinning rate, 278K in a 4mm Bruker efree probe at 11.75T (500MHz).

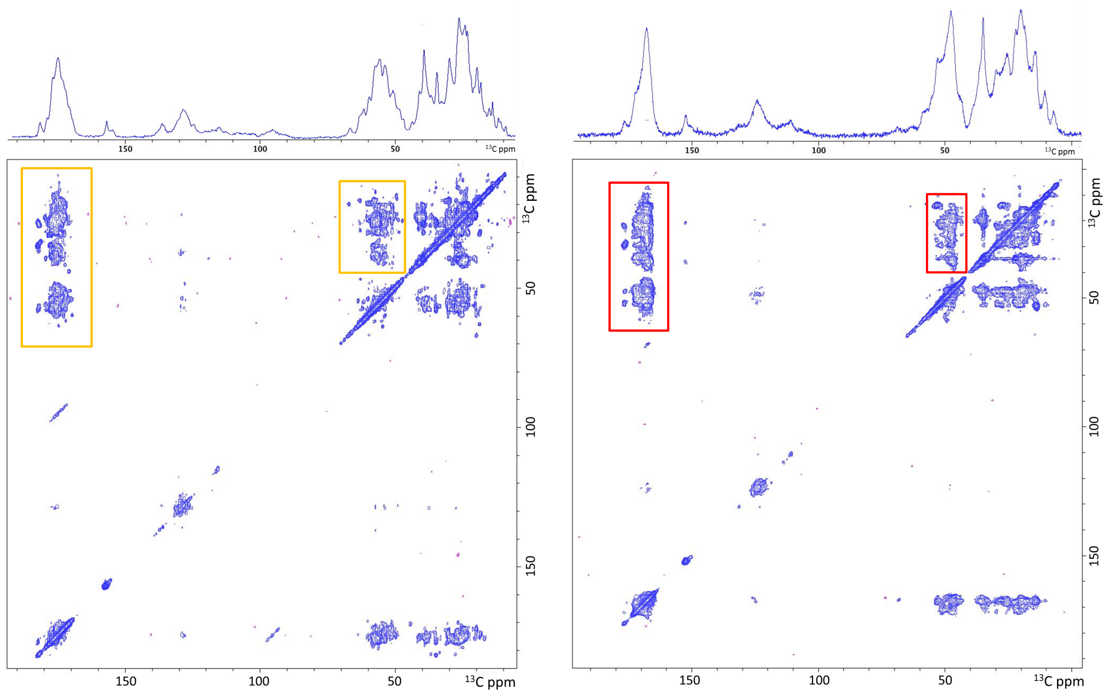

Figure 6.6 ^{13}C-^{13}C DARR spectrum of ^{13}C-^{15}N VHD cosedimented with actin filaments at 25000 rpm (left panel) and 30000rpm (right panel). When sedimented at low speed the resonances are better spread while the cross peaks correlating the carbonyl and α carbon collapsed when the complex is centrifuged at high speed resulting in an unfolded VHD. The spectra were recorded at 12.5kHz MAS rate, 278 in a 4mm Bruker efree probe at 11.75T (500MHz).

The speed used to sediment the complex is a critical aspect in the preparation of the sample. The assay performed showed that the optimal speed rate is a compromise between the speed to reach the maximum amount of VHD recovered in the complex and the speed that minimize any damage to the proper folding of the VHD.

6.4 Filling a ssNMR rotor

Several devices to fill a ssNMR rotor with powder or crystallites are commercially available. Nevertheless, the classic funnel type devices had shown to be not suitable for a sticky gel-like sample. Instead, every rotor was filled using micro-spatulas and the pellet gently sedimented to its bottom centrifuging the rotor in a refrigerated bench top centrifuge at low speed (2800rpm) at 4°C for 30 seconds. This approach allowed to fill a 4mm rotor with up to 90mg of wet sample and up to 2.5mg in a 1.3mm rotor.

Once the 4mm rotor was filled, it was loaded in the magnet and spun at 10000Hz for 5 to 10 minutes at 278K. During the spinning, the sample was squeezed to the walls of the rotor leaving part of the solution in middle space that was created by the sedimentation. The rotor was taken from the magnet again, opened and gently centrifuged upside down to centrifuge away the solution allowing to add more sample in the space left. The loss in water was estimated to be about the 60% the weight of the pellet in the rotor. Apparently, due to the gradual nature of the sedimentation process, and the fact that the sedimented matter was “wet”, the solvent was never totally removed [90]. On the other hand, a residual amount of water is necessary in the rotor to maintain the integrity of the sample and help to set up ssNMR experiments. To have a rough evaluation of the amount of protein loaded in the rotor, co-sedimentation assays were performed checking sampling from the solution before precipitation and the supernatant after centrifuge. It was evaluated that when 12-15mg of VHD were added to 35mg of filaments near 25-30mg of filaments were cosedimented with 5-6mg of VHD.

Unfortunately, differently from the 4mm rotor, once the 1.3mm rotor was filled it was not possible to re-open it and fill it again. Before loading in a probe, the cap and the bottom of this small rotor have to be sealed with glue to avoid water evaporation during the spinning at high rate. Thus, the continuously opening and sealing of the rotor leads to damages to the structure of the rotor itself. As mentioned above, if only filled once and sealed the amount of pellet in these rotors was never higher that 2.5mg, but more important the high amount of water still present created problems in the set up of heteronuclear ssNMR sequences with direct acquisition (Figure 6.7).

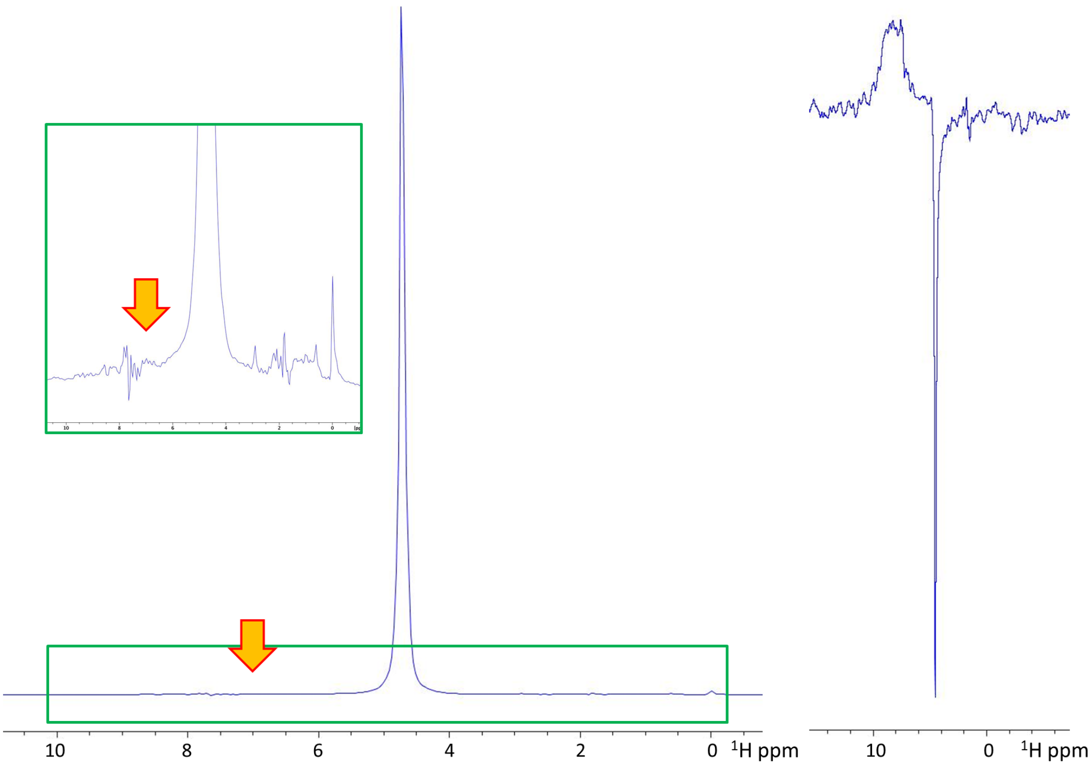

Figure 6.7 ^{1}H spectra of back-protonated ^{2}H-^{13}C-^{15}N VHD bound to actin filaments. The left panel shows the spectrum of a direct acquisition on protons. The main peak at 4.5ppm represents the signal from water and the green box shows the area magnified around this peak. The orange arrows indicate the signal from the protein. The right panel shows the first increment of a ^{1}H-^{15}N HSQC acquired using a water suppression pulse. It is evident that the suppression of water did not work properly. Both the experiments were recorded at 60kHz spinning rate, 298K in an 850MHz Bruker magnet.

Better results were obtained when the sample was initially loaded in a 4mm rotor, spun in the magnet and then used to fill a 1.3mm rotor. In this way the pellet was drier and more protein was packed in the rotor. Unfortunately, even if the set up of the heteronuclear ssNMR sequences with direct acquisition was easier than with the classic preparation, it was observed that part of VHD was unfolded. A ^{13}C CP MAS spectrum acquired on the carbonyl region clearly evidenced the shift in the resonances to higher field found to be originating from unfolded VHD (Figure 6.8). A more efficient method to fill the 1.3mm rotor is still under optimization.

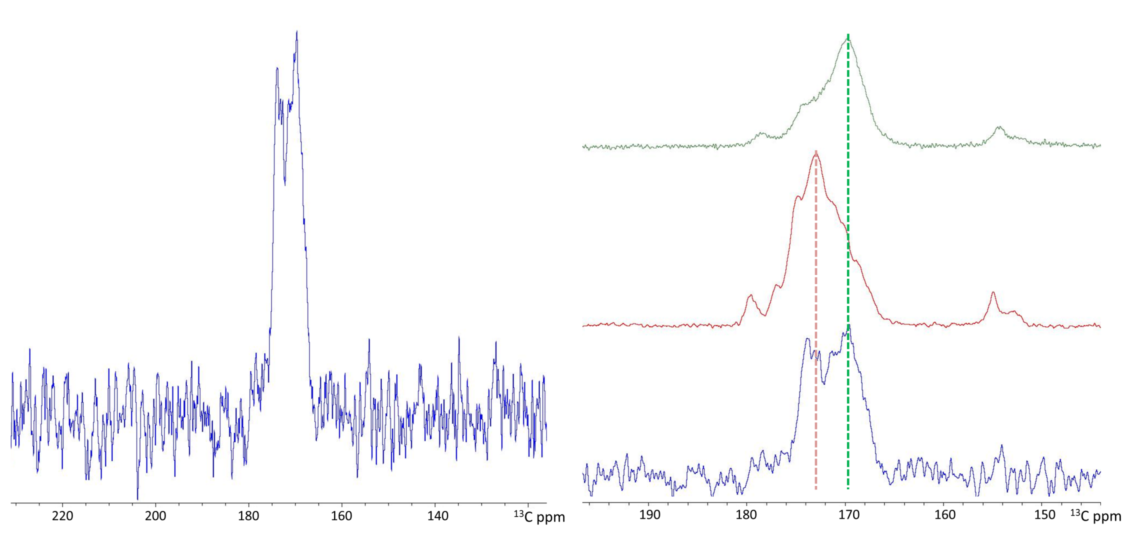

Figure 6.8 ^{13}C CP MAS spectra of carbonyl region of back-protonated ^{2}H-^{13}C-^{15}N VHD bound to actin filaments. Left panel (blue spectrum) shows the presence of two peaks centred at 172ppm and 167ppm that can be perfectly overlapped to, respectively, the carbonyl region from a folded VHD bound to actin (red spectrum in right panel) and the same region from an unfolded VHD bound to filaments (green spectrum in right panel). The blue spectrum (4096 scans) was recorded at 60kHz spinning rate, 298K in an 850MHz Bruker magnet while red (256 scans) and green spectrum (256 scans) at 10kHz spinning rate, 278K in a 400MHz Bruker magnet.

6.5 Wet and highly salty samples in ssNMR

The high power used for the proton decoupling applied to wet and highly salty biological samples can lead to a generation of heat that could affect the sample leading ultimately to its unfolding. Salty buffers are electrically conductive and they can absorb energy during the high power RF pulse and transfer it to the sample as heat. Furthermore, a decrease in the accuracy of matching and tuning of the probe was observed at higher field. The traditional buffer in which the actin filaments were stored contains 50mM KCl and 3.5mM $MgCl_2$, a salt concentration high enough to promote this heat generation. Figure 6.9 reports the proton wobble window for VHD-actin filament complex packed in a 4mm rotor and acquired at 850MHz. The poor quality of the matching and tuning for this sample are clearly visible.

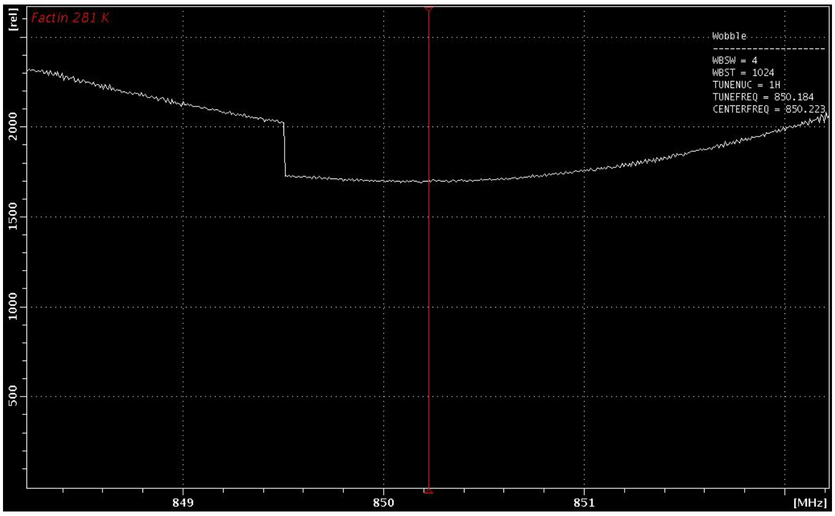

Figure 6.9 Proton wobble window at 278K for a ^{13}C-^{15}N VHD-filaments sample sedimented in presence of a high salt concentration buffer at 850MHz equipped with a 4mm three channel probe not efree. No minimum is recognizable indicating a very poor matching and tuning.

Several buffers with lower salt concentrations or with no salt were tested. Only the buffer containing 50mM glutamic acid, 50mM arginine, 10mM HEPES pH 7.3 and 2mM DTT showed a decrease in the power used for proton decoupling and an increase of the signal to noise ratio in respect the classic buffer. Unfortunately, the absence of salt promoted the unfolding of VHD in the rotor as shown in Figure 6.10. The reasons for this behavior are still under investigation.

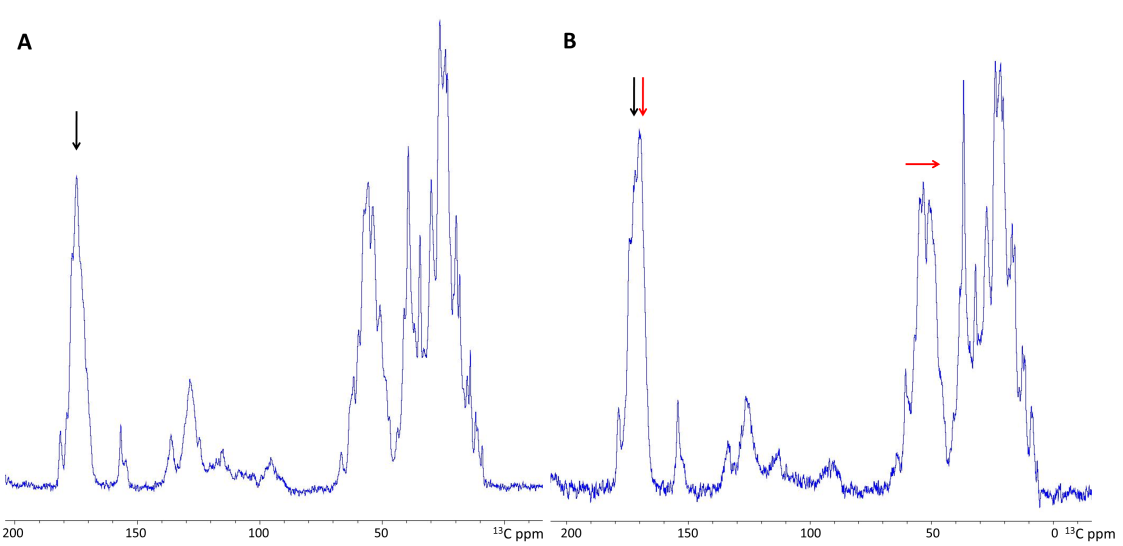

Figure 6.10 ^{13}C CP MAS spectra of ^{13}C-^{15}N VHD bound to actin filaments. Panel A shows the spectrum of a folded VHD bound to filaments when the proteins were cosedimented in high salt concentration buffer. The black arrow indicates where the carbonyl region is centred. When the proteins were transferred to a low salt concentration buffer and cosedimented, after days from the packing of the rotor part of the signals for the VHD showed a shift to higher field (Panel B) indicating the presence of a mixture of folded and unfolded protein. Spectra recorded one week later showed only unfolded VHD in the rotor. The red arrows highlighted the shift due to the presence of the unfolded VHD. The spectra (256 scans both) were recorded at 10kHz spinning rate, 278K in a 4mm Bruker efree probe at 11.75T (500MHz).

The application of a triple channel efree probe (Bruker) that combines a low inductance proton coil with a high efficiency solenoid for observing frequencies, drastically reduced the heat generation and improved the accuracy of matching and tuning. One- and two-dimensional spectra at high resolution were acquired using this set up that proved useful for the assignment of VHD. The fact that only the version for a 500MHz magnet was available limited the possibility to increase the magnetic field strength and to achieve an even better spectrum resolution.

6.6 Doped sample for ultrafast MAS ssNMR experiments

When it is possible to achieve spinning rate higher than 40kHz, the spinning speed is sufficiently fast to average the ^{1}H-^{1}H dipolar coupling to zero, making possible to record experiments acquired in the proton dimension. Nevertheless, to achieve high proton resolution it is necessary to apply this technique on a proton spin-diluted sample. For this reason, ^{2}H-^{13}C-^{15}N proteins are expressed and back-protonated changing the deuterated buffer with a 100% H_2O buffer, allowing the back exchange of protons especially in the backbone. On the other hand, the detection on ^{1}H means that the delay at the end of the acquisition in a pulse sequence is subject to the slow T_1 of ^{1}H [73]. Considering that the recycling delay is usually calculated as 3 times the length of T_1, the slow T_1 in the order of 0.5-1s forces to set a very long delay at the end of the pulse sequence in the order of 2-3s. Nevertheless, if a doped sample is prepared with the addition of a paramagnetic relaxation agent it is possible to decrease the rate of T_1 in the order of millisecond and, as result, to decrease the length of the recycling delay as well [73].

Uniformly ^{2}H-^{13}C-^{15}N protein was expressed and back-protonated as explained in 4.1.4. Prior to cosediment the protein in presence of actin filaments, Cu(II)Na_2EDTA to 10mM final concentration and TMS to 5mM final concentration were added. While Cu(II)Na_2EDTA acts as a paramagnetic relaxation reagent, DSS was added to reference the proton signal to zero. To assure that the paramagnetic reagent did not have any effect on the filaments stability, filaments added with Cu(II)Na_2EDTA were studied by fluorescence assay. A 30mM solution of pyrene modified actin filaments was divided into two equal aliquots, one of which was added with Cu(II)Na_2EDTA. The excitation spectrum was acquired for both the aliquots and compared (Figure 6.11). The two characteristic peaks at 343nm and 365nm typical of actin in the filamentous state were observable in both the samples. Considering the similar trend in the two excitation spectra, it was assumed that the small differences in shape did not depend on modification in the filaments assembling.

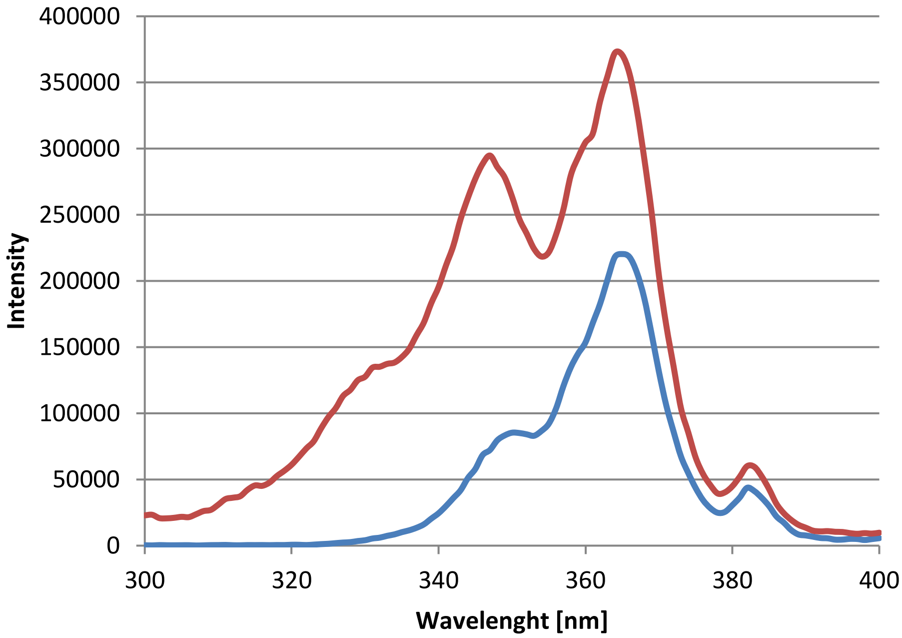

Figure 6.11 Excitation spectra for pyrene-actin filaments (red) and pyrene-actin filaments doped with the addition of 10mM final concentration of Cu(II)Na_2EDTA. The characteristic peaks at 365nm and 343nm are present in both the sample meaning that the actin was still in filamentous state after the doping.

Confirming that the paramagnetic reagent did not affect the integrity of the filament, the samples were tested over the time looking for any tendency to depolymerization that Cu(II)Na_2EDTA could eventually promote. Emission spectra for both the sample were acquired every 30s, the intensity at 385nm normalized to 1 and plot in a graph in function of the time. The similar linear decay that characterized both the preparation confirmed that the presence of paramagnetic reagent did not affect in any aspect the filaments (Figure 6.12).

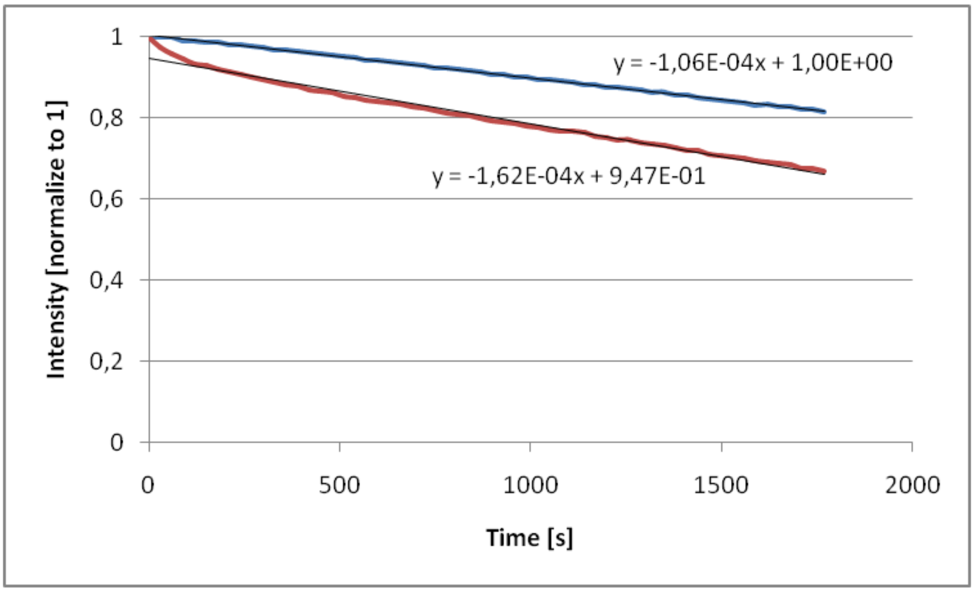

Figure 6.12 Stability over the time of a 20mM pyrene-actin filaments solution containing 10mM final concentration of Cu(II)Na_2EDTA (red) compared to the reference 20mM pyrene-actin filaments solution (blue). The fitting showed a similar linear decay only due to the exciting light that destroys part of the fluorophore every time the sample is excited confirming that the addition of Cu(II)Na_2EDTA induce no effect on the filaments.

6.7 An investigation of the optimization of filament precipitation

The sedimentation of the filaments due to ultracentrifugation is a disordered process that cannot be completely controlled. It was possible to set speed, time and temperature but it was impossible to modify the process. On the other hand, it was possible to change the conditions in which the filaments were sedimented. Actin filaments with the presence of different compounds, known in the literature to stabilize the filaments and to delay their depolymerization, were sedimented by centrifugation and checked by ssNMR in order to understand if it was possible to promote a more ordered and homogeneous process. A possible improvement was meant as an amelioration in the resolution of signals when compared to the spectrum obtained from filaments polymerized in the absence of any other compound (Figure 6.1). A series of ^{13}C CP MAS spectra were acquired for the reference and the different filament preparations and carefully scrutinized for improvement in the linewidth of well resolved signals. As illustrated in Figure 6.13, a ^{13}C CP MAS spectrum of unlabelled actin filaments, as well as of any other protein, can be roughly divided into 5 different regions which identified 5 specific carbon species of the amino acids. The region between 170-180ppm contains the carbonyl carbons of the backbone and the side chains of glutamate, aspartate, glutamine and asparagine. Between 150-156ppm are contained the C_ζ in the guanidine group of the side chains of arginine and the C_ζ of tyrosine residues. The signals from aromatic carbons are contained between 110-145ppm, between 50-70ppm the aliphatic C_α of practically all residues and between 10-50ppm the aliphatic carbons of all amino acid side chains.

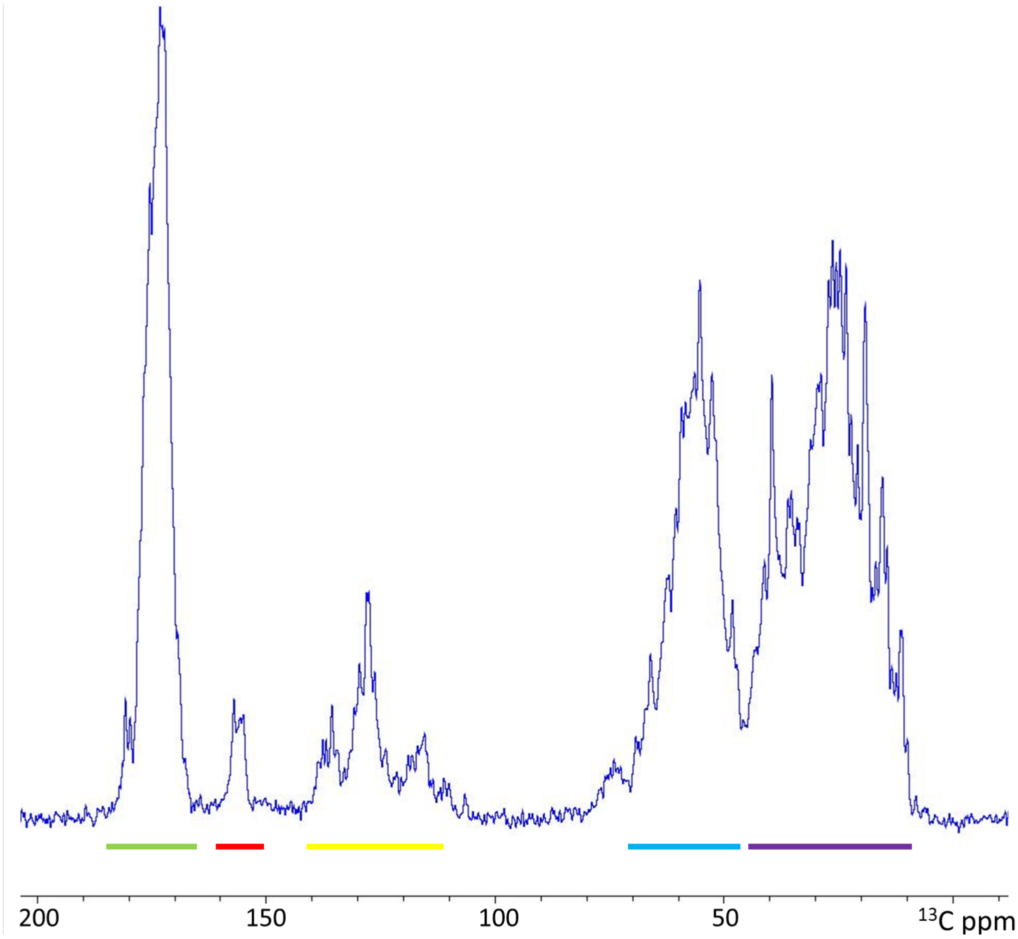

Figure 6.13 ^{13}C CP MAS spectrum of unlabelled actin filaments recorded with 32k scans at 10kHz spinning rate, 278K in a 400MHz Bruker magnet. Between 170-180ppm (underlined by green line) there is the carbonyl regions, between 150-156ppm (red line) the carbon in the guanidine group of the side chains of arginine (and also the C_ζ of tyrosine residues), between 110-145ppm (yellow line) the aromatic regions, between 50-70ppm (blue line) the aliphatic C_α of most residues and between 10-50ppm (purple line) the aliphatic carbon from amino acids side chains.

Furthermore, in order to investigate possible rearrangements in the assembly of the filaments due to the presence of these molecules, EM pictures were acquired for each preparation. Similarly to the ssNMR approach every EM picture acquired at different magnifications was compared to the reference pictures acquired on filament polymerized in the absence of any compound (Figure 6.14). The images showed the polymerization as an event that generates polymers with different length and that the filaments have a tendency to create randomly orientated bundles.

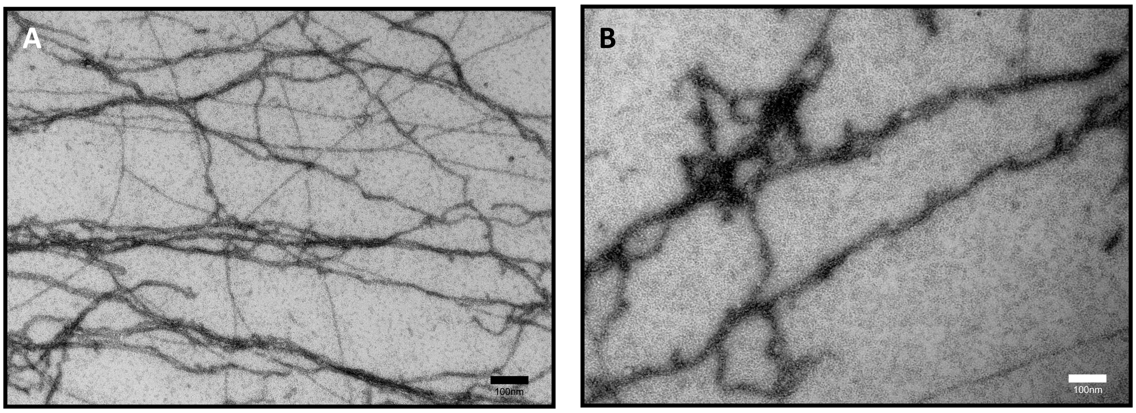

Figure 6.14 EM pictures of negatively stained actin filaments. In panel A has been used a magnification of 10500x while in panel B of 30000x. Both the images were acquired using a FEI Tecnai T20 and the bars indicate 100nm. Filaments with random length showed a tendency to create bundles.

Among all the molecules reported in the literature that can affect the rate of depolymerization of actin filaments, cucurbitacin E, phalloidin and two different analogous of the nucleotide ATP were tested.

Filaments polymerized in presence of cucurbitacin E (Figure 6.15, panel A) appeared similar to the reference filaments being characterized by a random length and the same tendency of creating bundles with no degree of order. The same result was obtained when the filaments were polymerized in presence of phalloidin (Figure 6.15, panel B). In literature is reported that cucurbitacin E covalently binds the filaments through cysteine 257 while phalloidin binds at the interface of two subunits. On the other hand, no evidently changes in the geometry of the filaments due to their presence were listed. The magnification at 18000x and 30000x (Figure 6.16, respectively panel A and B) acquired on filaments containing phalloidin showed no evidence of observable rearrangements in agreement with the literature.

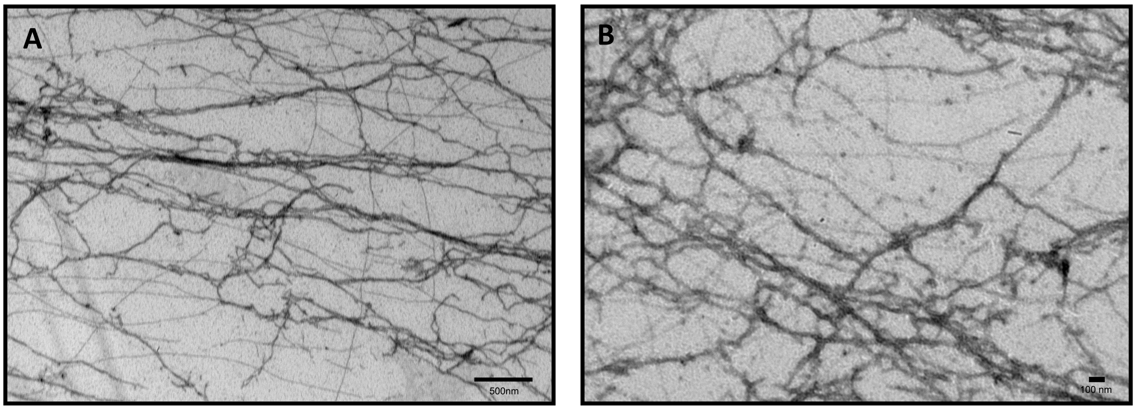

Figure 6.15 EM pictures of negatively stained actin filaments. Actin filaments polymerized in presence of cucurbitacin (panel A acquired at 9300x) and of phalloidin (panel B acquired at 13000x) showed aggregates of filaments with random orientations and length. The images were acquired using a FEI Tecnai T20 and the bar in panel A indicates 500nm while the bar in panel B 100nm.

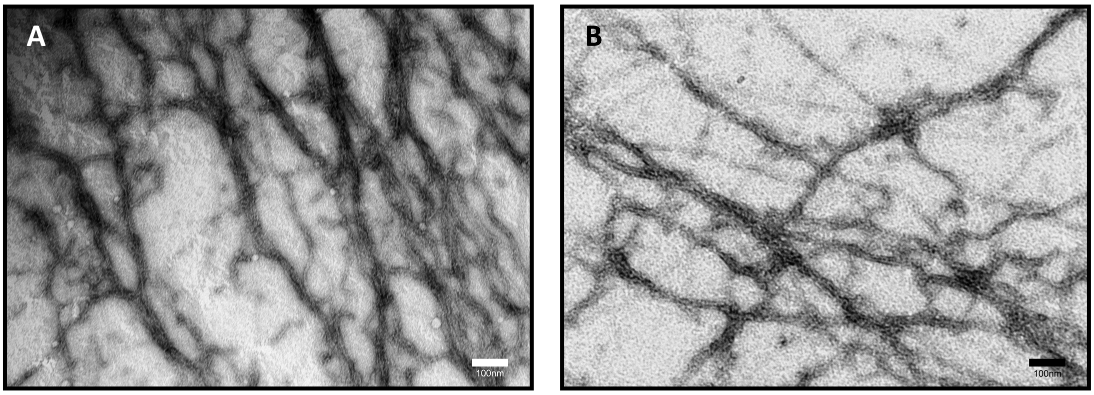

Figure 6.16 EM pictures of negatively stained actin filaments polymerized in presence of phalloidin. Panel A and panel B were acquired respectively at 18000x and 30000x and showed no evidence of rearrangements in the geometry of the filaments. The images were acquired using a FEI Tecnai T20 and the bar in panel A indicates 500nm while the bar in panel B 100nm.

Nevertheless, NMR is more sensitive to small, local changes and it could show variations in the environment of a single atom if its signal has a good resolution. Starting from this concept, the investigation was based on the hypothesis that the presence of small compounds known in the literature to bind and to stabilize the filaments could help the filaments to stay in a particular less flexible conformation helping to sediment a more homogeneous pellet. Unfortunately, none of this assumptions were effectively demonstrated to be and, as illustrated in Figure 6.17 and Figure 6.18, the ^{13}C CP MAS spectra for the filaments polymerized in presence of phalloidin and cucurbitacin E could be perfectly overlapped to the reference spectrum. The little changes in respect the reference were probably due to the noise rather than changes in homogeneity of the packaging of filaments considering that every spectrum acquired was characterized by a signal to noise ratio of near 30.

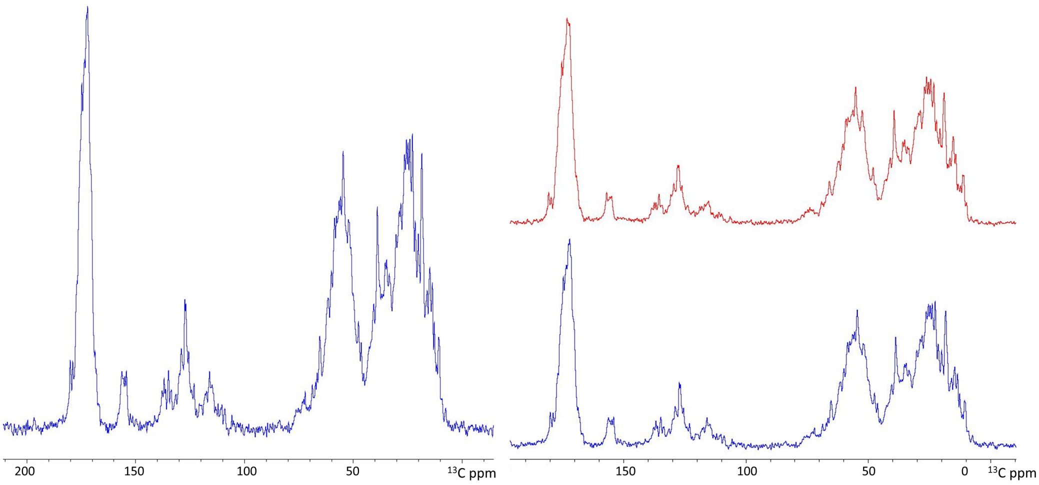

Figure 6.17 ^{13}C CP MAS spectrum of filaments polymerized in presence of phalloidin (blue spectrum in left panel). The spectrum is similar to the reference spectrum (red spectrum) as shown by their superimposition (right panel) and the small changes can be attributed to the poor signal to noise ratio that characterizes this spectra acquired on carbon at natural abundance. The experiment was recorded with 32k scans at 10kHz spinning rate, 278K in a 400MHz Bruker magnet.

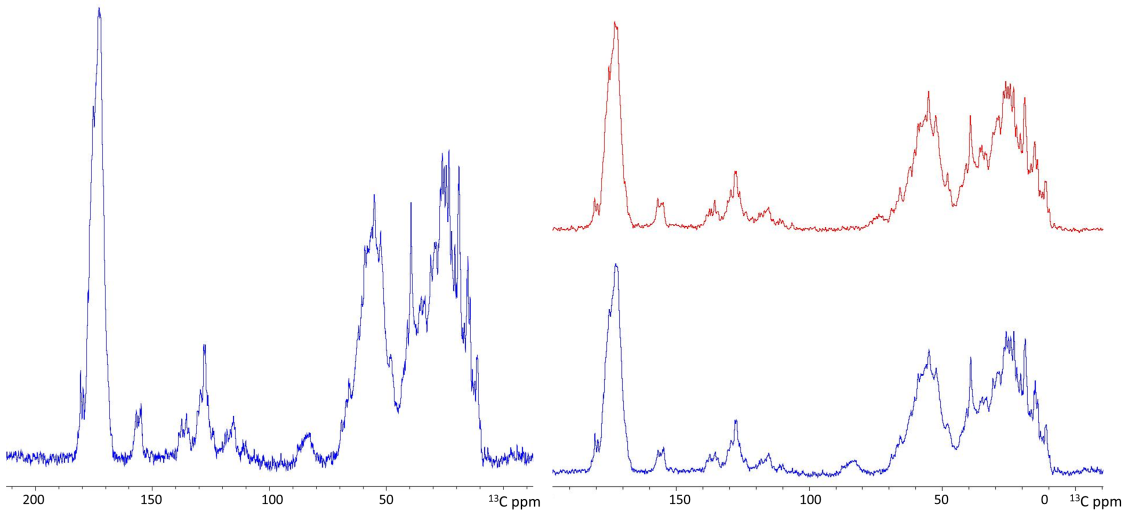

Figure 6.18 ^{13}C CP MAS spectrum of filaments polymerized in presence of cucurbitacin E (blue spectrum in left panel). The superimposition to the reference spectrum (red spectrum) is almost perfect and the small changes can be attributed to the poor signal to noise ratio (right panel). The experiment was recorded with 32k scans at 10kHz spinning rate, 278K in a 400MHz Bruker magnet.

A drastic decrease in ^{13}C CP MAS spectra resolution was obtained when filaments were polymerized in presence of ADP.BeF$_x$ and ADP.AlF$_4$, two analogous of ATP (Figure 6.19). For both the preparation the carbonyl region of ^{13}C spectra showed no evident sign of a loss in resolution, on the other hand, the aliphatic region showed major changes due to the presence of the two analogues. It was suggested that the presence of the quadrupolar nuclei beryllium or aluminum which both possess nuclear spin higher that $^1/_2$, and the fluorides associated to them could affect the broadening of the signals of residues close to the cleft contributing with their dipolar coupling.

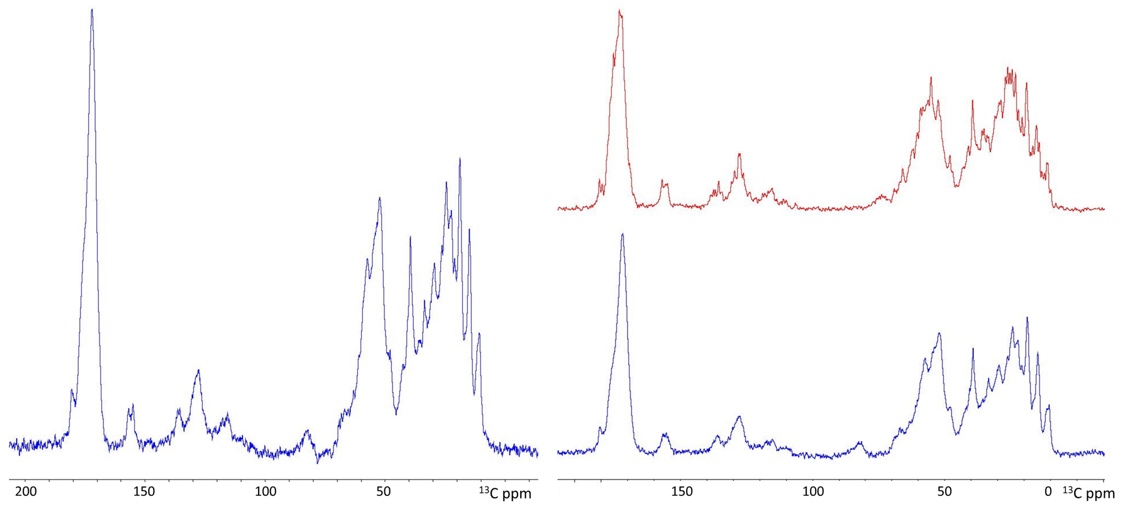

Figure 6.19 ^{13}C CP MAS spectrum of actin filaments containing the ADP.BeF$_x$, an analogous of ATP (blue spectrum in left panel). A general loss in the resolution is recognizable in the superimposition to the reference spectrum (red spectrum in right panel). This effect could not be attributed to the processing of the experiments as the same process parameters were applied to every ^{13}C CP spectrum acquired. The experiment was recorded with 32k scans at 10kHz spinning rate, 278K in a 400MHz Bruker magnet.

The EM picture acquired (Figure 6.20) confirmed no evident changes in the assembly of the filaments partially confirming the suggestion made for the loss in resolution in ssNMR spectra for these preparations.

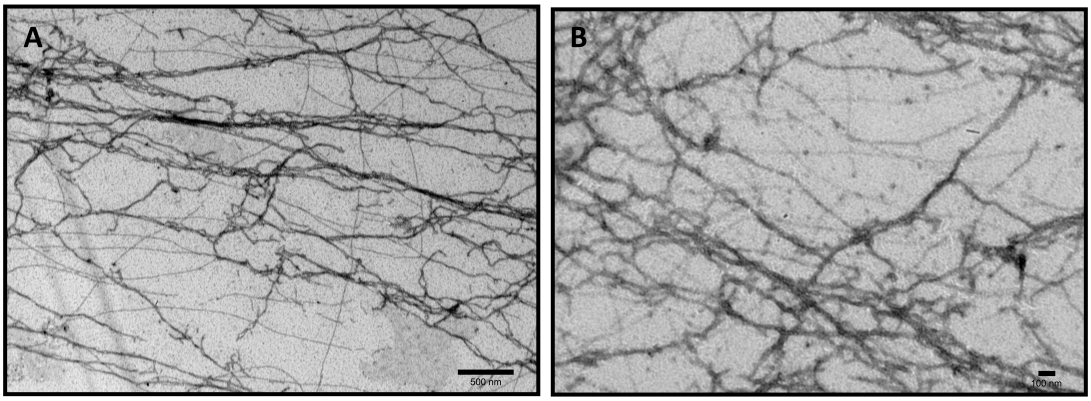

Figure 6.20 EM pictures of negatively stained actin filaments. Polymers containing ADP.BeFx (panel A acquired at 9300x) and ADP.AlF4 (panel B acquired at 13000x) showed features similar to the filaments in the reference. Random orientations and random length of the filaments in the bundles are comparable to the reference. The images were acquired using a FEI Tecnai T20 and the bar in panel A indicate 500nm while the bar in panel B 100nm.

The absence of clear changes in the filament geometry did not mean that the different preparations did not effectively change the arrangement of the filaments but only that the changes were not visible by simply acquiring a one-dimensional carbon spectrum on the unlabelled filaments or by EM. Multi-dimensional spectra which could allow a structural determination of the filaments cannot be run for ^{13}C and ^{15}N at natural abundance in protein and labelled filaments at the moment cannot be expressed. On the other hand, a straightforward approach to efficiently look at improvements in the homogeneity of the filaments packed derived from changes in their preparation was necessary for this study.

6.7.1 Double Quantum (DQ) ssNMR spectroscopy

Thinking that changes in the homogeneity of the filaments have to affect also a protein bound to them, it was proposed the possibility to investigate eventual changes that affect the filaments looking at the signals from a labelled version of VHD bound to them. Considering the difficulty to access magnet at high magnetic field equipped for solid state and that sequences such as ^{13}C-^{13}C DARR require very long acquisition time (several days), a different and faster approach was investigated. It was suggested that to find the easiest protocol it was necessary to solve two different problems, how to drastically decrease the number of resonances in the spectra and where to find a sequence able to filter the background signal originated from filaments and enhances the signals from the bound protein. While to address the first problem it was proposed a single specific amino acid labeling with ^{13}C-^{15}N alanine and protocols were already available in the literature [87, 88], it was more difficult to find a solution for the second issue. One of the most efficient ways to filter the NMR signal is to use a sequence that can select a particular coherence. It was suggested that sequences that can generate DQ coherence information should have answered all the needs we had. These sequences can efficiently reintroduce the dipolar coupling and select the signal from only ^{13}C-^{13}C J-coupled spin filtering in this way the background signals from spin not coupled.

The problem was addressed in different steps. Firstly two SBR sequences, post-C7 and spc5, that can efficiently select DQ coherence were tested on a reference sample containing ^{13}C-alanine. When the best sequence was found, a VHD-filaments complex containing uniformly ^{13}C-^{15}N VHD was used as a second test prior to move to the complex containing the [^{13}C-^{15}N Ala] VHD.

6.7.1.1 Pulse sequence selection

Post-C7 and spc5 based sequences were both tested on a ^{13}C-^{15}N alanine powder sample recorded in a 400MHz instrument at room temperature. For both the sequences the best excitation time was carefully calculated. It was estimated the same excitation time of 400µs for both the post-C7 and spc5 symmetry elements. In both cases it was rescued 30-32% of the signal if compared to the spectrum of a direct ^{13}C CP MAS experiment acquired using the same receiver gain and number of scans (Figure 6.21 and Figure 6.22).

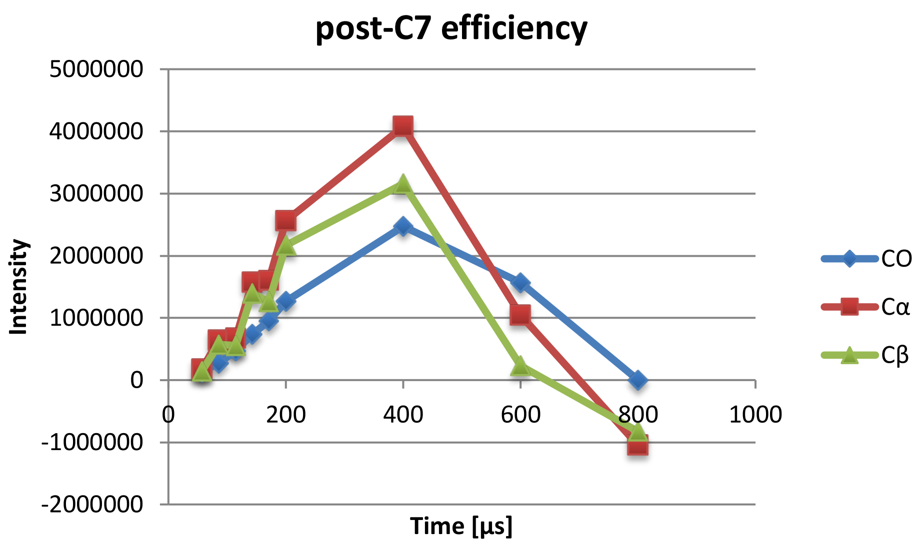

Figure 6.21 Magnetization transfer efficiency calculated for ^{13}C-^{15}N alanine powder using a post-C7 based sequence. The best efficiency was achieved 400µs. The different points were connected by straight lines to give a better indication of the shape of each curve. The spectra were recorded at room temperature in a 400MHz Bruker magnet.

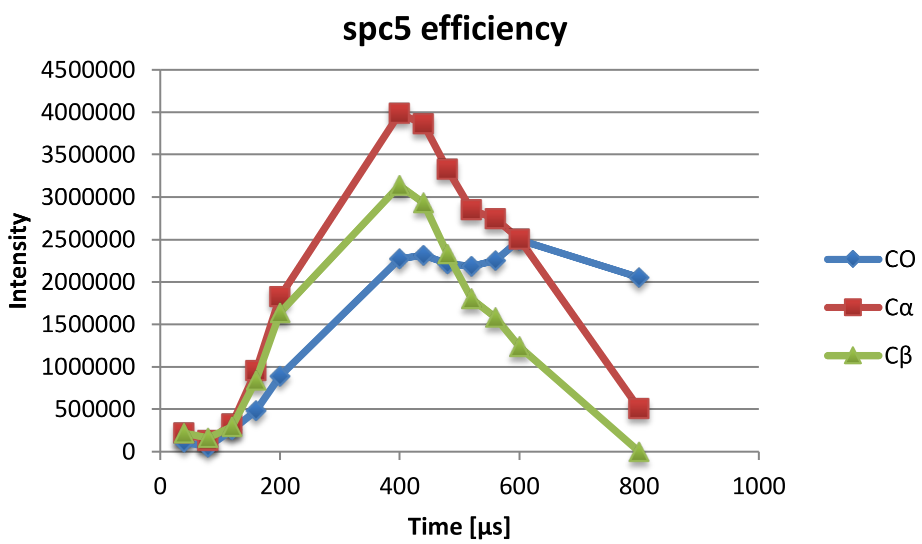

Figure 6.22 Magnetization transfer efficiency calculated for ^{13}C-^{15}N alanine powder using a spc5 based sequence. The maximum efficiency was achieved at 400µs. The different points were connected by straight lines to give a better indication of the shape of each curve. The spectra were recorded at room temperature in a 400MHz Bruker magnet.

Nevertheless, when the spc5 sequence was acquired as a 2D spectrum the resonances obtained were not at the expected positions (Figure 6.23). It seemed that this excitation basic element was not able to select only DQ coherence and the resonances revealed were generated from different MQ coherences. The reason for this behavior is still under investigation.

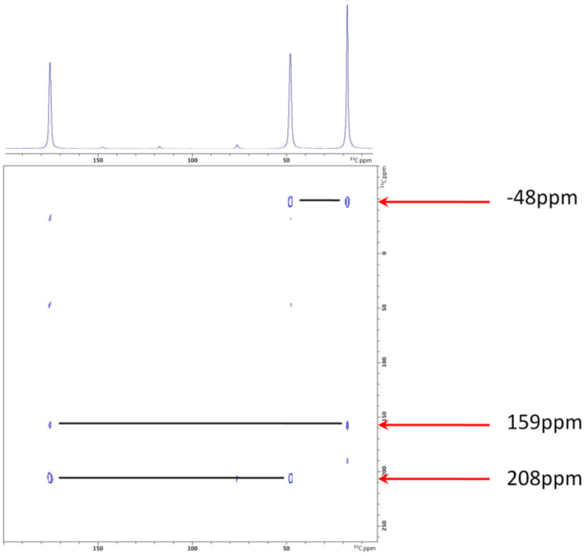

Figure 6.23 ¹³C-¹⁵N alanine DQ-SQ ¹³C-¹³C correlation spectrum using spc5 basic element. The 2D spectrum shows in the DQ dimension frequencies that are not the one expected for alanine if DQ coherence is properly selected. The spectrum was acquired at room temperature, 10kHz spinning rate using a cwlg sequence (125kHz) to decouple proton during the creation of DQ coherence in a 400MHz Bruker magnet equipped with a double resonances CP probe.

On the other hand, the post-C7 based sequence resulted in working perfectly (Figure 6.24), showing signals at the sum of the frequencies of the correlated atoms ($\omega_{CO} + \omega_{C\alpha} = 228{,}8ppm, \omega_{CO} + \omega_{C\beta} = 198{,}3ppm\ and\ \omega_{C\alpha} + \omega_{C\beta} = 70{,}5ppm$). As a result, post-C7 based sequence was selected as sequence to implement in the study of VHD-actin filament complex.

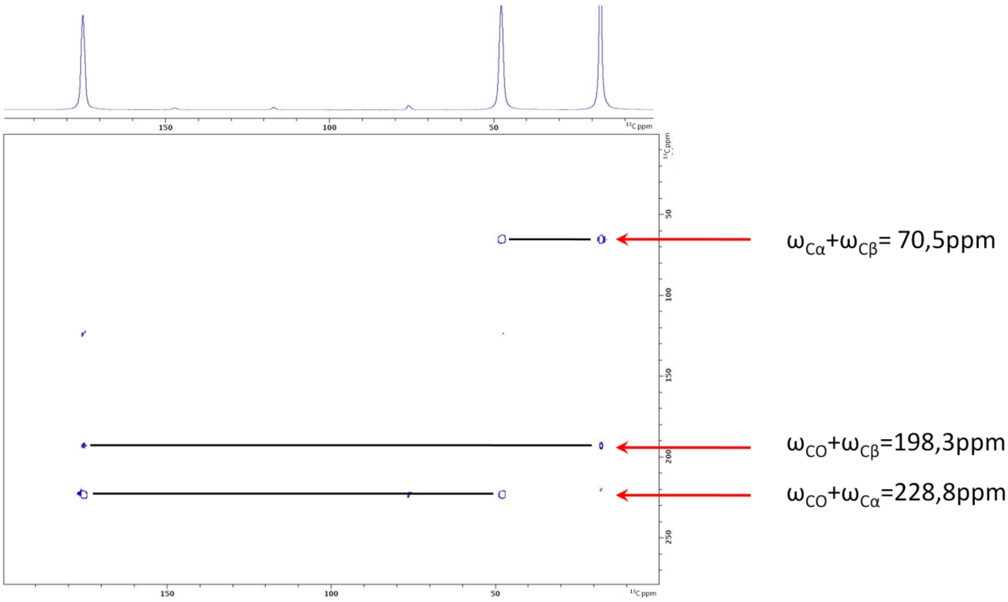

Figure 6.24 ¹³C-¹⁵N alanine DQ-SQ ¹³C-¹³C correlation spectrum using post-C7 basic element. The frequencies on DQ dimension resulted in being equal to the sum of the frequencies of the two spin coupled. In alanine powder the chemical shift for CO, Cα and Cβ are respectively 177,8ppm, 51,0ppm and 20,5ppm producing coupled signal in the DQ dimension at 228,8ppm ($\omega_{CO} + \omega_{C\alpha}$), 198,3ppm ($\omega_{CO} + \omega_{C\beta}$) and 70,5ppm ($\omega_{C\alpha} + \omega_{C\beta}$). The spectrum was acquired at room temperature, 10kHz spinning rate using a cwlg sequence (115kHz) to decouple proton during the creation of DQ coherence in a 400MHz Bruker magnet equipped with a double resonances CP probe.

6.7.1.2 Post-C7 tests on a uniformly ^{13}C-^{15}N VHD-filaments complex

After selection of a suitable DQ pulse sequence, a uniformly ^{13}C-^{15}N VHD-filaments complex was prepared and tested. It was decided to put the offset at 40ppm and acquire only the aliphatic region of VHD. The comparison of the spectrum obtained with the ^{13}C CP MAS spectrum acquired on the same sample with same receiver gain and number of scans showed that only 5% of the signal was efficiently recovered after the DQ excitation and reconversion (Figure 6.25).

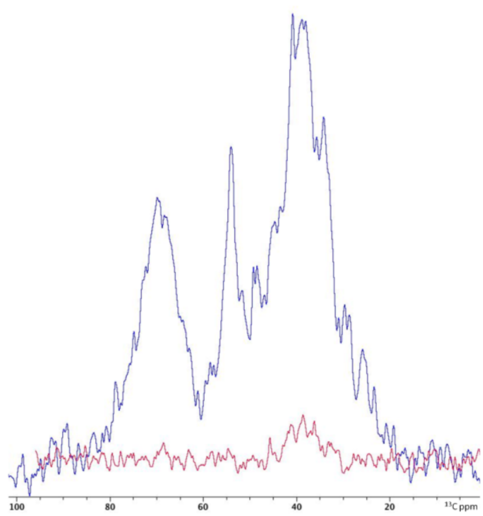

Figure 6.25 Comparison of 1D DQ-SQ ^{13}C-^{13}C correlation spectrum using post-C7 basic element spectrum (red spectrum) and ^{13}C CP MAS spectrum acquired both in the aliphatic region of ^{13}C-^{15}N VHD bound to actin filaments. Less than 5% of the total signal was recovered in the DQ experiment. Both the spectra were recorded at 278K, 10kHz spinning rate, 128 scans and same receiver gain in a 400MHz Bruker magnet equipped with a double resonances CP probe. During the excitation and reconversion of DQ coherence a cwlg sequence (120kHz) was applied on the proton channel.

Thus, to achieve a signal to noise ratio of about 30, it was necessary to acquire at least 16k scans. The low efficiency shown combined to the poor signal to noise ratio made impossible any attempt to acquire any 2D experiment using this sequence. On the other hand, the suitability of the post-C7 based sequence when only 1D experiments were acquired to reveal DQ coherence was confirmed (Figure 6.26).

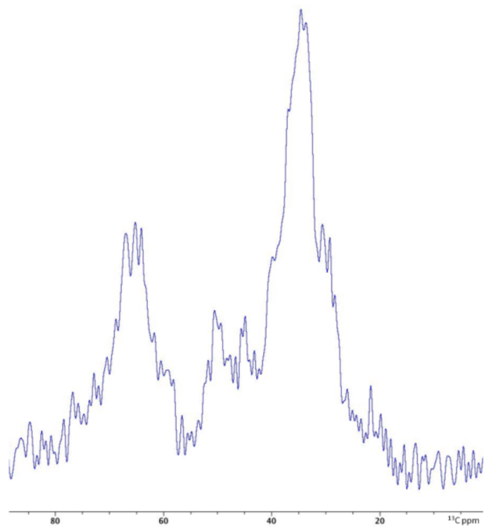

Figure 6.26 1D DQ-SQ ^{13}C-^{13}C correlation spectrum using post-C7 basic element spectrum on aliphatic c region of ^{13}C-^{15}N VHD bound to actin filaments. 16k scans were acquired to achieve a signal to noise ratio of about 30. The spectrum was acquired at 278K, 10kHz spinning rate using a cwlg sequence (120kHz) on proton channel after the CP transfer in a 400MHz Bruker magnet equipped with a double resonance CP probe.

6.7.1.3 Some consideration on the DQ analysis on [^{13}C-^{15}N Ala] VHD-filament complex

Unfortunately, any useful DQ-SQ spectrum on the [^{13}C-^{15}N Ala] VHD-filament complex has to be still recorded. The poor signal to noise that characterizes this type of experiments did not help in the acquisition of a sample in which only 2 amino acids out of 67 were labelled. Thus, it has to be considered that the specific ^{13}C-^{15}N alanine labeling was not complete and only part of the VHD expressed was efficiently enriched with the isotopic version of this amino acid, meaning that a very small percentage of the sample loaded in the rotor (in the order of μg) could effectively generate DQ coherence. This was confirmed by the fact that the ^{13}C CP MAS spectrum acquired on this complex showed a spectrum similar to the same experiment acquired on a sample containing only actin filaments rather than one containing uniformly ^{13}C-^{15}N VHD bound to filaments (Figure 6.27).

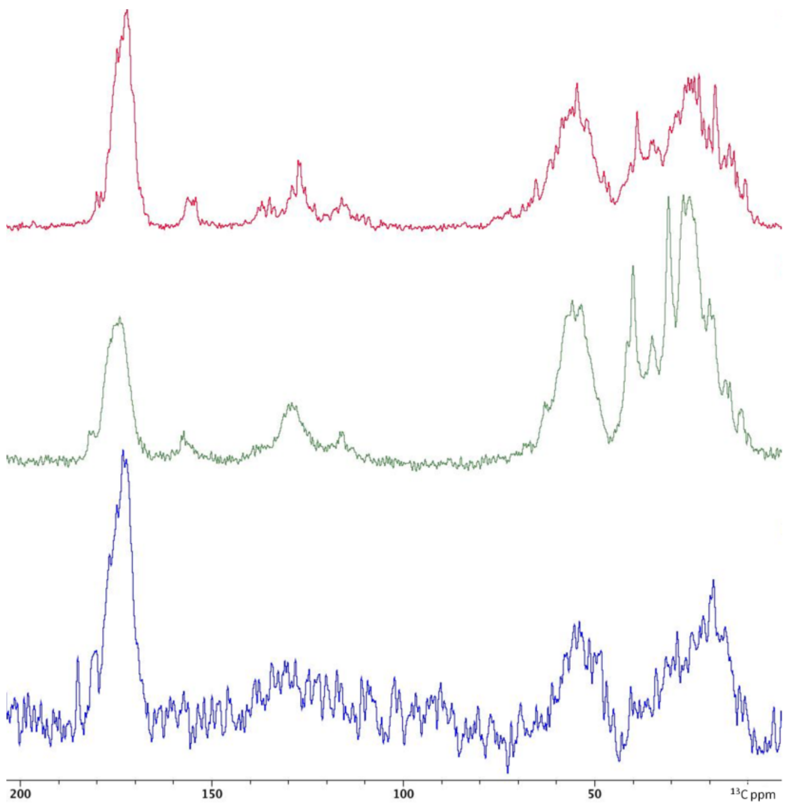

Figure 6.27 Comparison of ^{13}C CP MAS spectrum acquired on [^{13}C-^{15}N Ala] VHD bound to actin filaments (blue spectrum, 2048 scans) with uniformly ^{13}C-^{15}N VHD complexed to actin filaments (green spectrum, 128 scans) and actin filaments (red spectrum, 8192 scans). It was possible to notice that the pattern of signals arising from the complex containing the [^{13}C-^{15}N Ala] VHD had more similarity with the spectrum acquired on the filaments, meaning that the amount of enriched alanine in the VHD was not enough to be revealed against the background signals generated from no labelled species. The spectra were recorded at 278K, 10kHz spinning rate in a 400MHz Bruker magnet equipped with a double resonances CP probe.

6.8 Long term effect of packaging in a ssNMR rotor on actin filaments

During the precipitation and after the packaging of the rotor most of the water was excluded from the sample and only the water molecules intimately interacting with the filaments remained. The absence of water could severely damage the integrity of the filaments and so affect their stability during time. Verified that the preparation leads to a folded sample, it was important to establish how the time affects the filaments when packed into a ssNMR rotor. For this purpose, ^{13}C CP MAS experiments were acquired at time zero, stored at 4°C and regularly analysed at different times. At the same time, samples of pellet were collected each time, gently resuspended and analysed by EM. The same approach was used to study both filaments polymerized without any other compound and filaments polymerized in presence of phalloidin or VHD as examples of a stabilizer drugs and of an actin binding domain, respectively, that could have helped to conserve the filaments preventing an early depolymerization.

Surprisingly, the actin filaments polymerized alone were stable for a long time as shown by the almost perfect superimposition of the spectra acquired after 15 days, 30 days, 60 days and the reference acquired at time zero (Figure 6.28). The small changes were simply due to a poor signal to noise ratio for the experiments acquired.

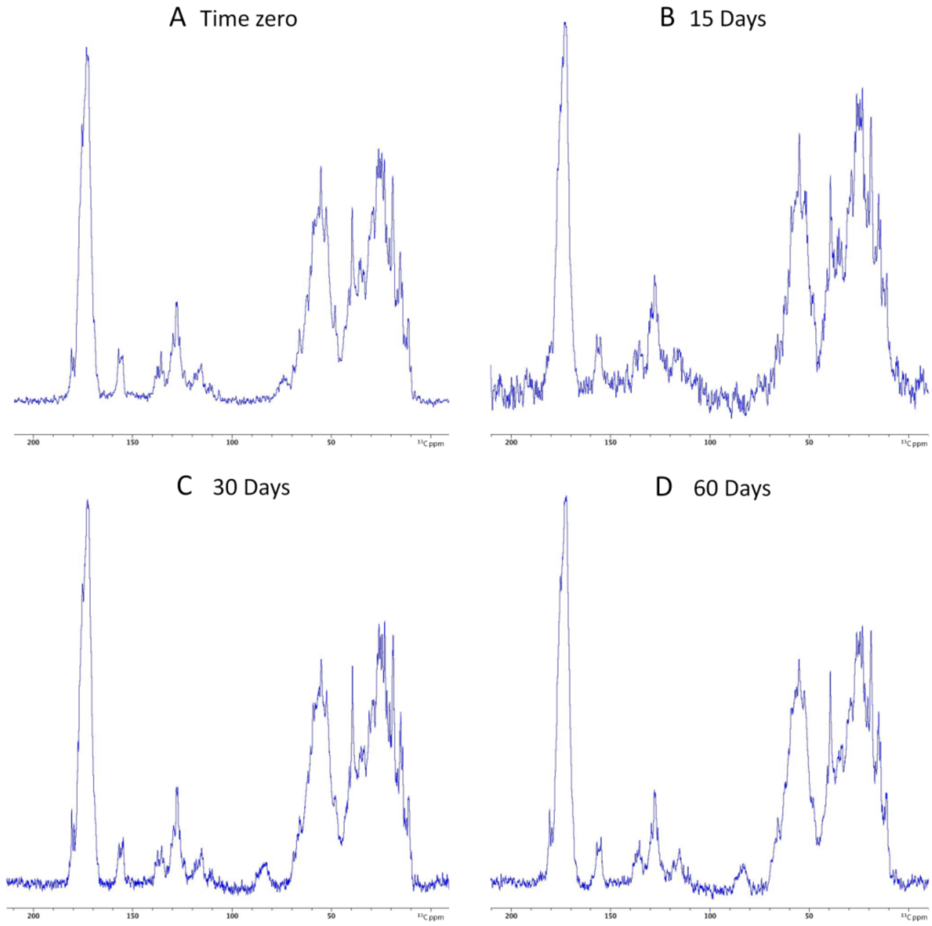

Figure 6.28 Stability over time of actin filaments in a 4mm rotor checked by ^{13}C CP MAS experiments acquired at time zero and after 15, 30 and 60 days. After 60 days from the packaging the spectrum shows no changes compared to time zero indicating a stability for the filaments over this time period. The spectra (32k scans each) were acquired at 10kHz spinning rate, 278K in a 400MHz Bruker magnet.

Furthermore, the samples collected from the rotor after 30 days, resuspended and analysed by EM showed no suggestion of depolymerization or damage of the filaments (Figure 6.29).

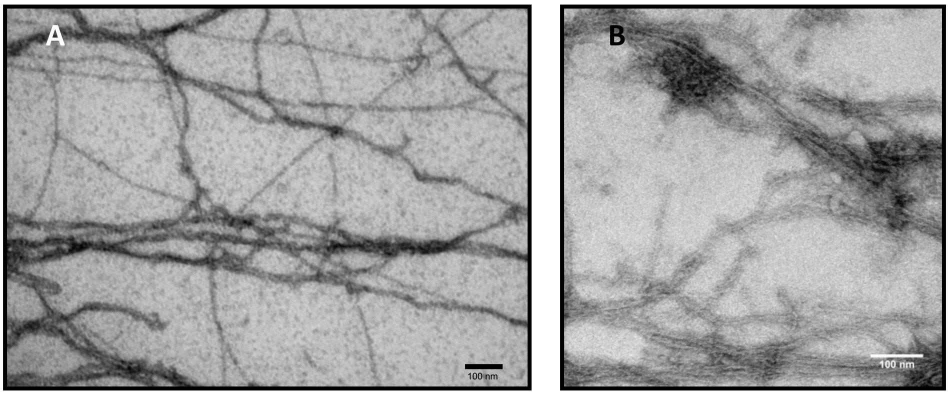

Figure 6.29 EM pictures of negatively stained actin filaments after 30 days in a 4mm rotor for ssNMR. No evidence of depolymerization and damages were recognizable in the images. The images were acquired using a FEI Tecnai T12 with a magnification of 18500x (panel A) and of 30000x (panel B). The bars indicate 100nm.

In the same way, the two other preparations showed the same stability for over 60 days. Filaments containing phalloidin showed hints of depolymerization after 90 days. A severe decrease in resolution and intensity were appreciable in its ^{13}C CP spectrum when compared to time zero (Figure 6.30) suggested that damages to the filaments were occurring.

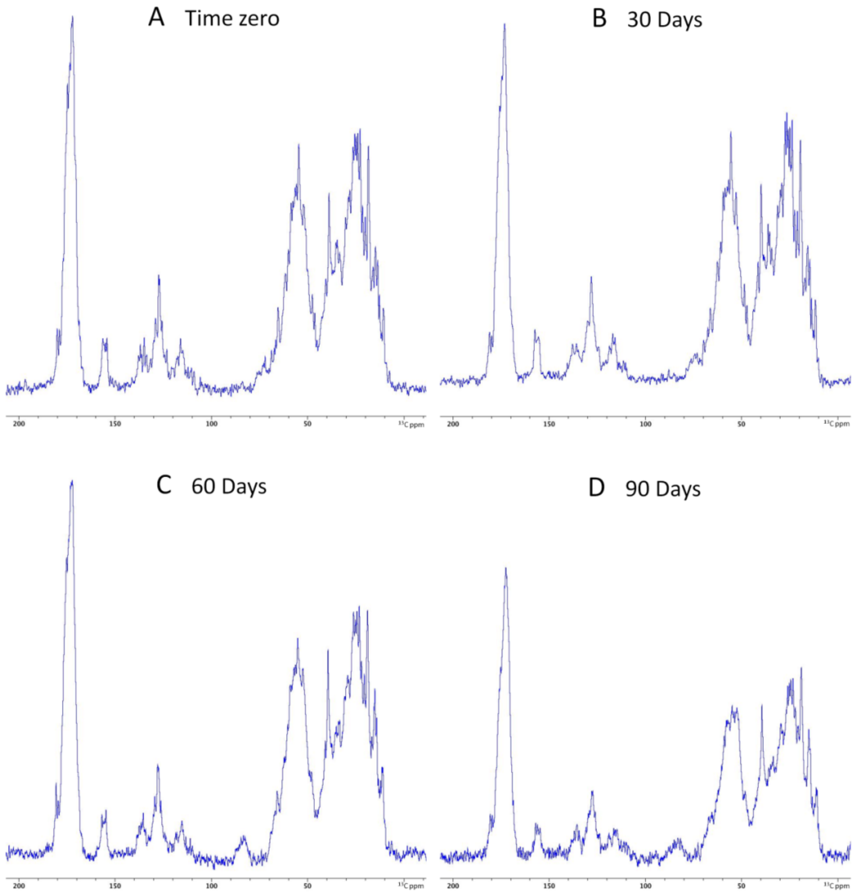

Figure 6.30 Stability over time of actin filaments polymerized in presence of phalloidin in a 4mm rotor checked by ^{13}C CP MAS experiments acquired at time zero and after 30, 60 and 90 days. After 60 days from the packaging the spectrum shows no changes compared to time zero but after 90 days a decrease in the intensity and resolution were appreciable suggesting damages in the filaments. The spectra were acquired at 10kHz spinning rate, 278K in a 400MHz Bruker magnet.

The damages were confirmed by the pictures of the samples analysed by EM that showed short and damage filaments proving that they were undergoing a process of depolymerization (Figure 6.31).

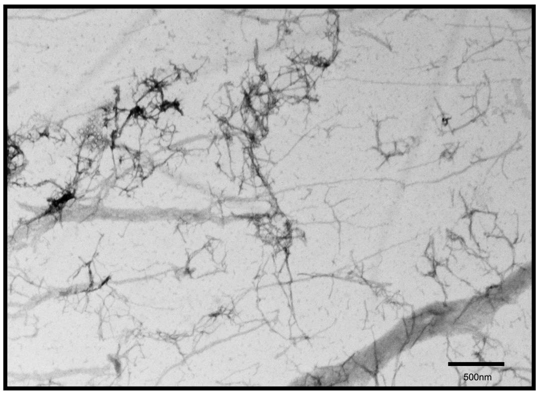

Figure 6.31 EM picture of negatively stained actin filaments containing phalloidin after two months from the filling in a 4mm rotor for ssNMR. Damages and shorter filaments were recognizable in the image. The image was acquired using a FEI Tecnai T12 with a magnification of 9300x and the bar indicates 500nm.

On the other hand, filaments complexed with VHD showed an even longer stability. ^{13}C CP MAS and ^{13}C-^{13}C correlation experiments run 90 days after their preparation showed that, when the rotor was properly stored, the spectra could have been perfectly superimposed confirming that the VHD still was in the same state of time zero (Panel A, B and C in Figure 6.33). EM pictures acquired on a fresh VHD-filaments sample before packaging (Figure 6.32) and a sample of the pellet after 90 days (Figure 6.34) still showed filaments with no evident damage. A shift in the signal of ^{13}C CP spectra to higher field started to be appreciable after 4 months from the packaging of the rotor (Panel D in Figure 6.33). Unfortunately, no EM pictures acquired on the pellet after 120 days from the precipitation could be shown due to problems during their acquisition.

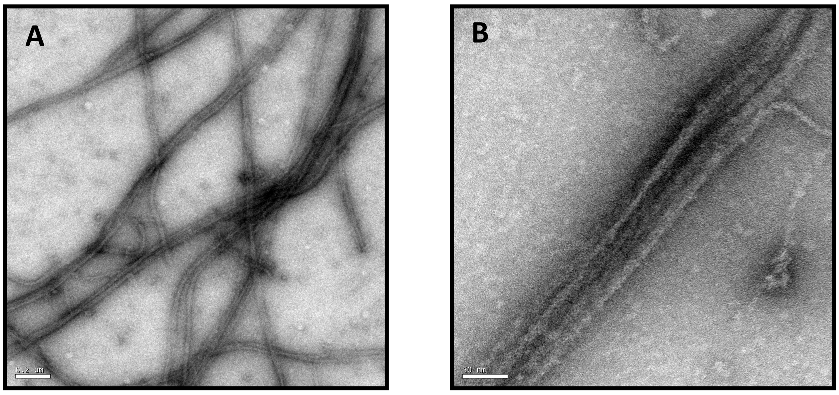

Figure 6.32 EM picture of negatively stained VHD-actin filaments before to be sedimented. The presence of VHD did not induce any evident changes in the assembly of the filaments. The images were acquired using a FEI Tecnai T12 with a magnification of 7800x (panel A) and of 50000x (panel B). The bars indicate 0.2µm for panel A and 50nm for panel B.

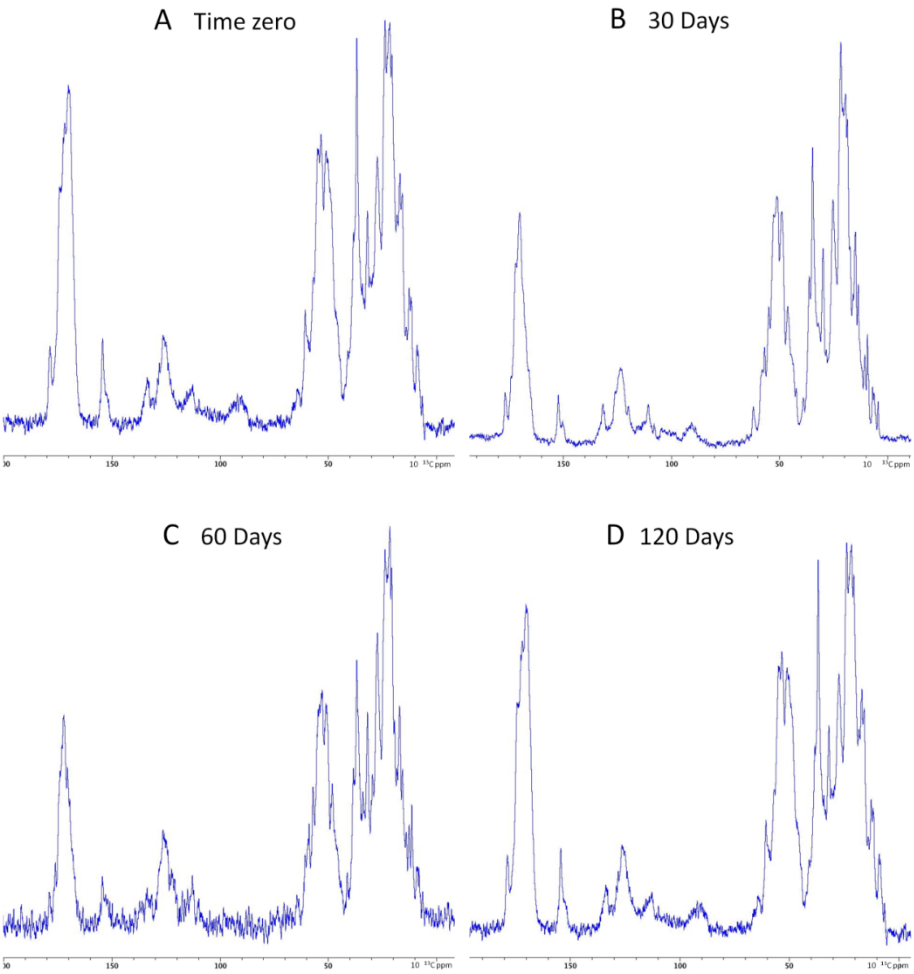

Figure 6.33 Stability over time of ^{13}C-^{15}N VHD-actin filaments in a 4mm rotor checked by ^{13}C CP MAS experiments on ^{13}C-^{15}N VHD. The spectra were acquired at time zero and after 30, 60 and 120 days. After 60 days from the packaging the spectrum shows no changes compared to time zero but after 120 days the shift to higher field in carbonyl and carbon α regions suggested the presence of a mix of folded and unfolded VHD. The spectra were acquired at 10kHz spinning rate, 278K in a 400MHz Bruker magnet.

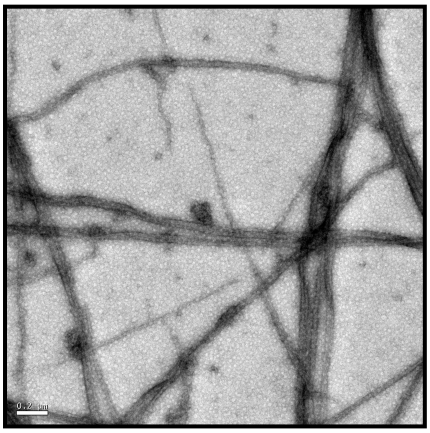

Figure 6.34 EM picture of negatively stained VHD-actin filaments 60 days after the loading in a 4mm rotor. The filaments do not show changes compared to time zero as it was expected. The images were acquired using a FEI Tecnai T20 with a magnification of 7800x. The bars indicate 0.2µm.

7 ^{31}P ssNMR spectroscopy

7.1 A brief introduction

Only one isotope of phosphorous (^{31}P) is present in nature. It has spin $^1/_2$ and a relatively high gyromagnetic ratio which has made ^{31}P an attractive nucleus for NMR studies. The idea to use ^{31}P NMR spectroscopy in this project, derived from its encouraging application in the investigation of structure and dynamics of lipid bilayers [91, 92]. The difficulty in gathering information from ^{13}C CP MAS spectra acquired on actin filaments at natural abundance created the necessity to find a suitable alternative method able to simplify the complexity that these ^{13}C CP MAS spectra of actin filaments showed. Therefore the attention focused on the investigation of alternative diluted nuclei contained in the filaments. In addition to carbon, nitrogen and protons, proteins can contain sulfur, oxygen and selenium or coordinated ions such as calcium, iron, sodium, magnesium, etc. On the other hand, some crucial biological molecules involved in fundamental physiological processes contain phosphorous atoms. It is the case of the nucleotides, organic molecules that act as subunit of nucleic acids or as carrier for energy in the form of nucleoside triphosphates. As extensively explained in 1.1.2, ATP is essential for the dynamics of actin filaments, in fact its hydrolysis into ADP is one of the principal factors that drive the polymerization event. The presence of ADP as coordinated molecule inside every actin monomer suggested to focus the investigation into it and more in particular in its two atoms of phosphorous.

Prior to study the nucleotides caged inside the actin filaments, an exhaustive characterization of ADP and ATP powder was performed in order to optimize the platform of experiments to apply in this investigation. To study the nucleotide inside filaments, a simple approach in which ^{31}P CP MAS experiments were acquired for different preparations of actin and compared to the spectrum of the reference was proposed. Filaments polymerized in absence of any compound were used as reference. Every ^{31}P CP MAS acquired was run in a 400MHz Bruker magnet equipped with a CP probe and spun at 10000Hz at 278K. A minimal number of 4096 scans were acquired for each experiment and for some of the preparations the fids of several experiments were added to reach a signal to noise ratio of at least 18-20.

7.2 ^{31}P spectrum of ATP and ADP powder

The ^{31}P CP MAS spectrum of ATP is characteristic for each of the three different hydrate complexes (mono-, di- and trihydrate) that ATP can create with water (Figure 7.1). The chemical shift in ppm reported in literature for the phosphate signals of ATP in water are reported in Table 7.1. It is interesting to notice that the chemical shift of ATP phosphates from solution have a correspondent peak also into the ssNMR spectra. For simplicity these peaks were labelled α, β and γ. This is another example that describes how peak lists assigned from experiments acquired in solution can be moved to experiments acquired by ssNMR and still be consistent.

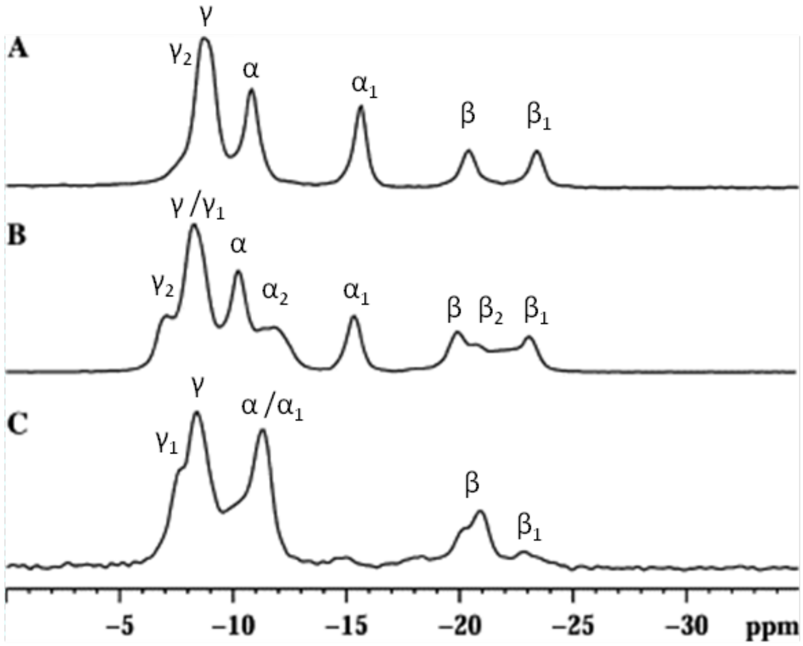

Figure 7.1 ^{31}P CP MAS spectra of ATP hydrates measured at 278K with spinning speed 8 kHz (A) trihydrate, (B) dihydrate, and (C) monohydrate [93]. For each complex the spin system was characterized and reported in the spectra.

^{31}P atom	Chemical shift (ppm)
α	-10.87
β	-20.5
γ	-6.19

Table 7.1 ^{31}P chemical shifts in ppm for the α, β and γ phosphates of ATP molecule in water.

The ATP used to prepare the solution to extract and purify the actin from muscle acetone powder was supplied by Melford and sold as ATP-disodium salt trihydrate but it is quite simple to notice that actually it is a dihydrate complex of ATP (Figure 7.2).

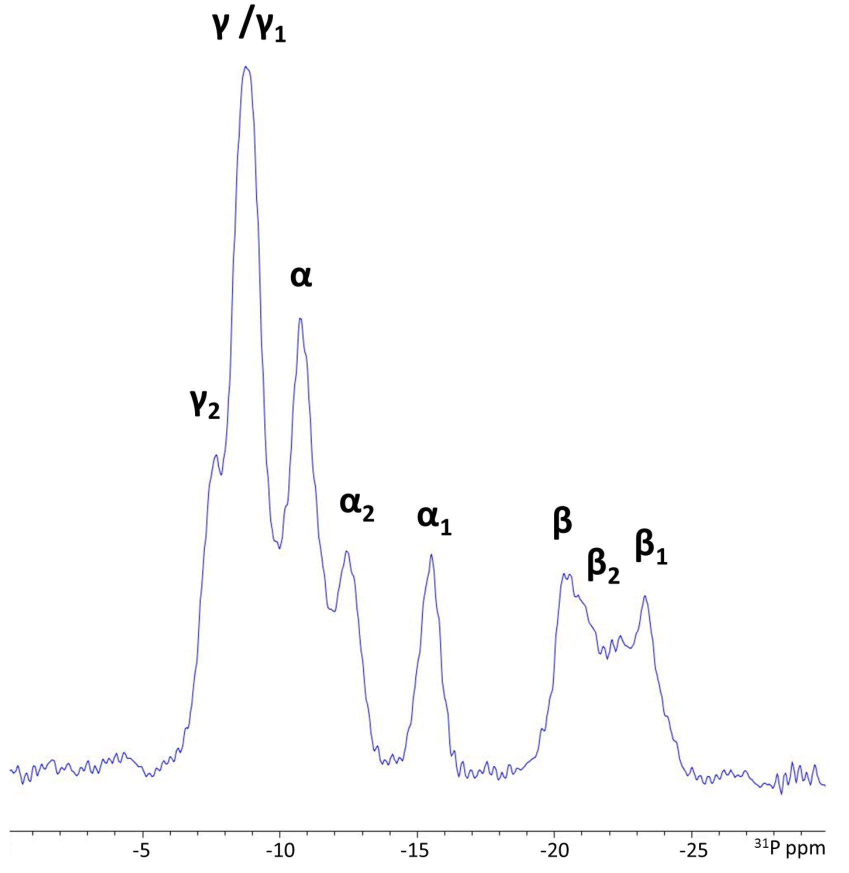

Figure 7.2 ^{31}P CP MAS spectra of ATP supplied by Melford Lab. The pattern of signal is comparable to the one originating from ATP-disodium dihydrate. The spectrum (4 scans) was recorded at 10kHz spinning rate, room temperature in a 400MHz Bruker magnet using a double CP MAS probe.

To confirm the correct hydrate complex of ATP, ^{31}P-^{31}P correlation spectra and ^{31}P-^{31}P DQ experiments using post-C7 were acquired and compared to the same experiments reported in the literature [93]. Both the ^{31}P-^{31}P correlation spectrum and the ^{31}P-^{31}P DQ-SQ spectrum were in agreement with the spectra acquired for the disodium ATP dihydrate complex (Figure 7.3 and Figure 7.4).

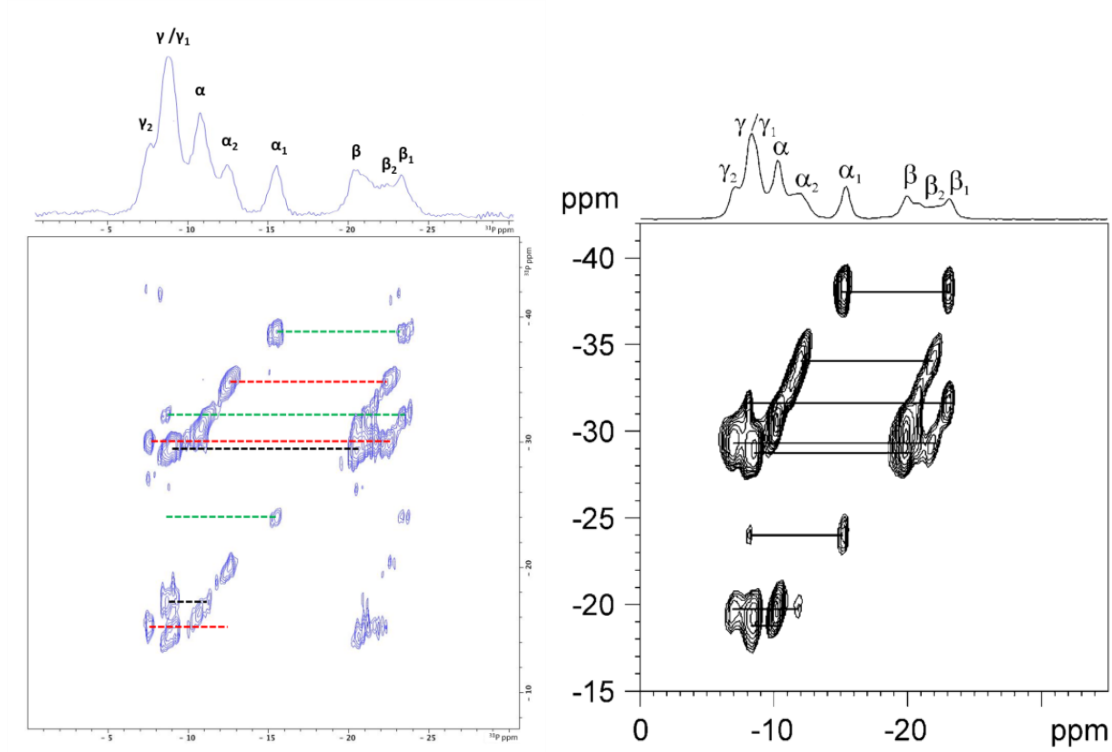

Figure 7.3 ^{31}P-^{31}P post-C7 spectrum of ATP-disodium salt trihydrate supplied by Melford Lab. (left panel) acquired at spinning rate 10kHz, room temperature in a 400MHz Bruker magnet compared to a ^{31}P-^{31}P post-C7 spectrum of a purified and crystallized ATP dihydrate complex recorded at 287 K, spinning rate 10 kHz in a 300MHz Bruker magnet (right panel)[93]. The signal pattern is comparable between the two spectra confirming that the ATP salt supplied by Melfrod Lab. is a dihydrate complex instead of a trihydrate as reported by the company.

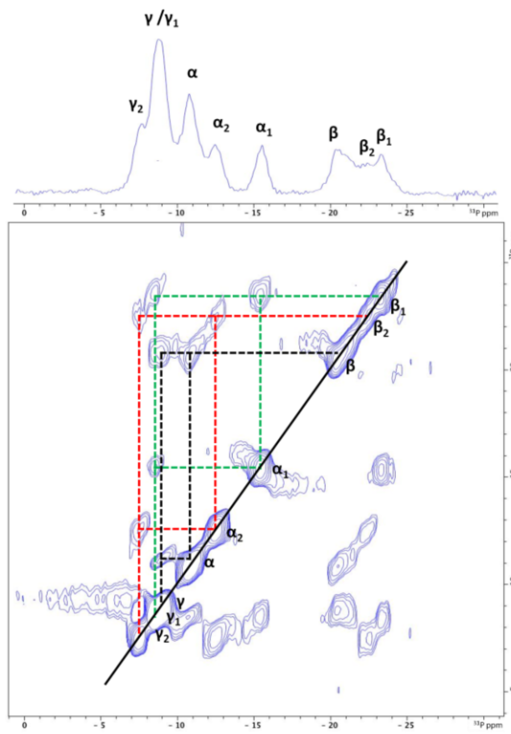

Figure 7.4 ^{31}P-^{31}P DARR spectrum of ATP-disodium salt trihydrate from Melford Lab. Three spin systems were easily recognized and were labelled as $\alpha\beta\gamma$, $\alpha_1\beta_1\gamma_1$ and $\alpha_2\beta_2\gamma_2$ as previously suggested. The spectrum was recorded at 10kHz spinning rate, room temperature in a 400MHz Bruker magnet.

When the γ-phosphate is hydrolyzed, the ATP changes into ADP. Differently from ATP, there is currently no ssNMR characterization of its hydrate complex available in the literature. ^{31}P CP MAS spectra of disodium ADP powder (Sigma) were acquired to tentatively characterize it (Figure 7.5). Two regions centred at -0.4ppm and -9.4ppm were detectable in the spectrum and they could be identified as two different species as suggested by ^{31}P-^{31}P correlation spectra acquired on this sample (Figure 7.6). Considering the assignment reported in literature for the disodium ADP phosphates in water (Table 7.2), it was suggested that both the signal from ADP collapsed into the peak centred at -9.4ppm. Even if no data are yet available to explain the poor resolution of the region centred at -0.4ppm, its presence could suggest the existence of more than one form of disodium ADP in the powder.

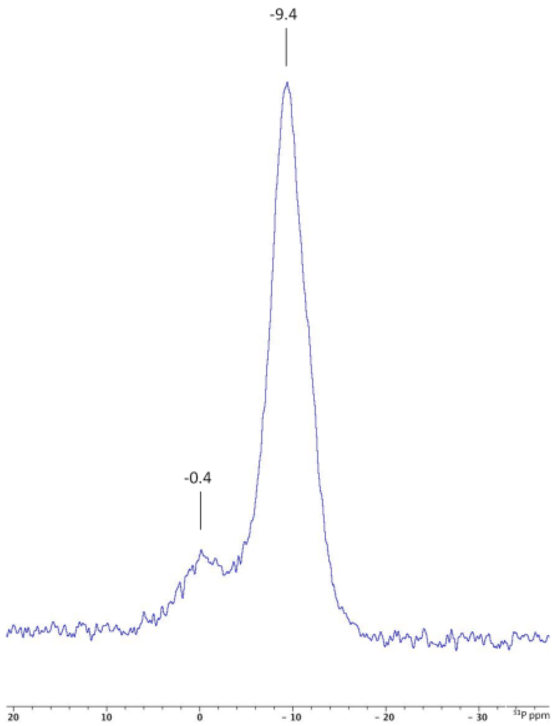

Figure 7.5 ^{31}P CP MAS spectrum of disodium ADP powder supplied by Sigma. Two different regions are recognizable centred at -0.4ppm and -9.4ppm. The spectrum (8 scans) was recorded at 10kHz spinning rate, room temperature in a 400MHz Bruker magnet using a double CP MAS probe.

^{31}P atom	Chemical shift (ppm)
A	-10.61
B	-6.33

Table 7.2 ^{31}P chemical shifts in ppm for the α and β phosphates of ADP molecule in water.

Despite a poor signal to noise ratio of the peak at -0.4ppm and a linewidth of near 770Hz for the peaks centred at -9.4ppm, ^{31}P-^{31}P correlation spectra were acquired in order to better characterize the nature of the ADP complexes (Figure 7.6). The peak centred at -9.4ppm revealed to contain two distinct peaks centred at -9.4ppm and -11.7ppm. In accordance to the chemical shift of ADP phosphates in solution, it was suggested that they were respectively the β- and α-phosphate from ADP. Nevertheless, it was not possible to confirm their assignment because the cross peak that should have been generated by their eventual correlation would be hidden by the high intensity of the two close signals making its recognition impossible.

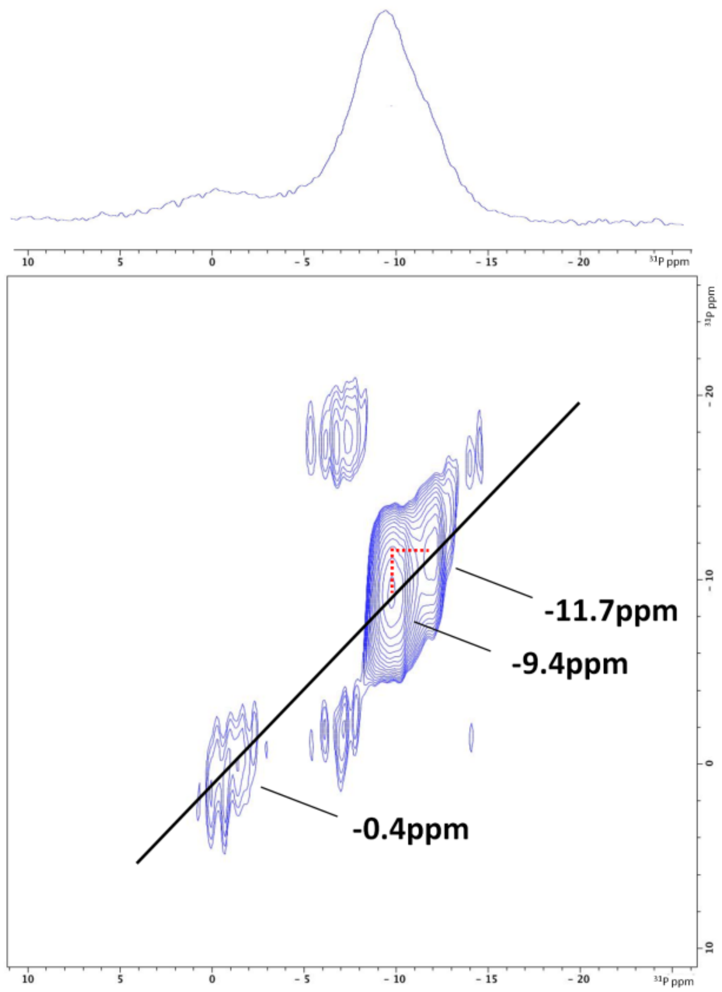

Figure 7.6 ^{31}P-^{31}P correlation spectrum of ADP supplied by Sigma. No correlations were recognized among the signals suggesting the presence of more than a hydrate ADP complex. The signal outside the diagonal (-7.1ppm and -17.7ppm) is noise from the background. The spectrum was recorded at 10kHz spinning rate, room temperature in a 400MHz Bruker magnet.

7.3 ^{31}P NMR spectroscopy of actin filaments (reference sample)

After the extensive characterization of ATP and ADP, ^{31}P CP MAS experiments were acquired for a preparation of actin filaments polymerized in the absence of any compound and it was intended as the sample to reference all the different preparations of actin filaments. Surprisingly, as shown in Figure 7.7, a single strong peak near -9.55ppm was observable in the spectrum. Its value is close to the chemical shift of the main peak for the disodium ADP powder and suggests that both α and β phosphate were included in this peak. Interestingly, its linewidth measured near 320Hz, half the linewidth of free disodium ADP powder. The narrowing of the signal from the α phosphate would suggest that its position in the filaments has less heterogeneity compared to the free ADP powder.

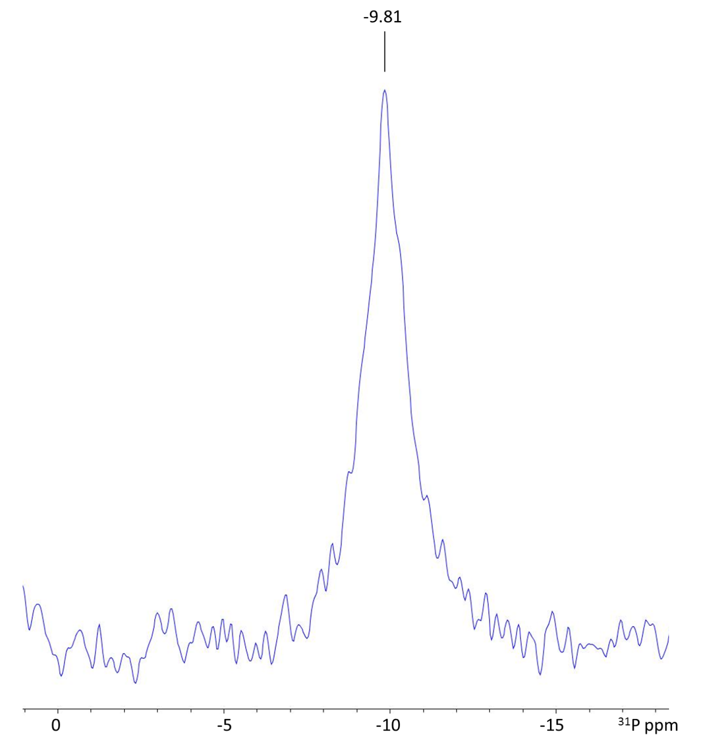

Figure 7.7 ^{31}P CP MAS spectrum of ADP contained in actin filaments. A single peak was recognizable in the spectrum at -9.55ppm characterized by a linewidth of near 324Hz suggesting that both α and β phosphate of the ADP were contained under it. The spectrum (4096 scans) was recorded at 10kHz spinning rate, 278K in a 400MHz Bruker magnet.

To investigate this hypothesis, an analogue of the ADP.Pi, the ADP.AlF_4, was synthesized modifying the ADP during the polymerization process as explained in 4.4.6. It was hypothesized that, in this blocked form, the β phosphate in the ADP would have not been able to move and its signal should have been distinguishable in the spectrum resolving the peaks. As expected, in the ^{31}P CP MAS spectrum acquired on filaments complexed with $ADP.AlF_4$ (Figure 7.8), two signals at -9.83ppm and -11.91ppm were easily spotted. Their value of chemical shift was comparable, respectively, to the chemical shift of α phosphate and β phosphate of ADP in powder, suggesting their assignment. Nevertheless, a third broad signal with maximum at -11.12ppm arose in the spectrum.

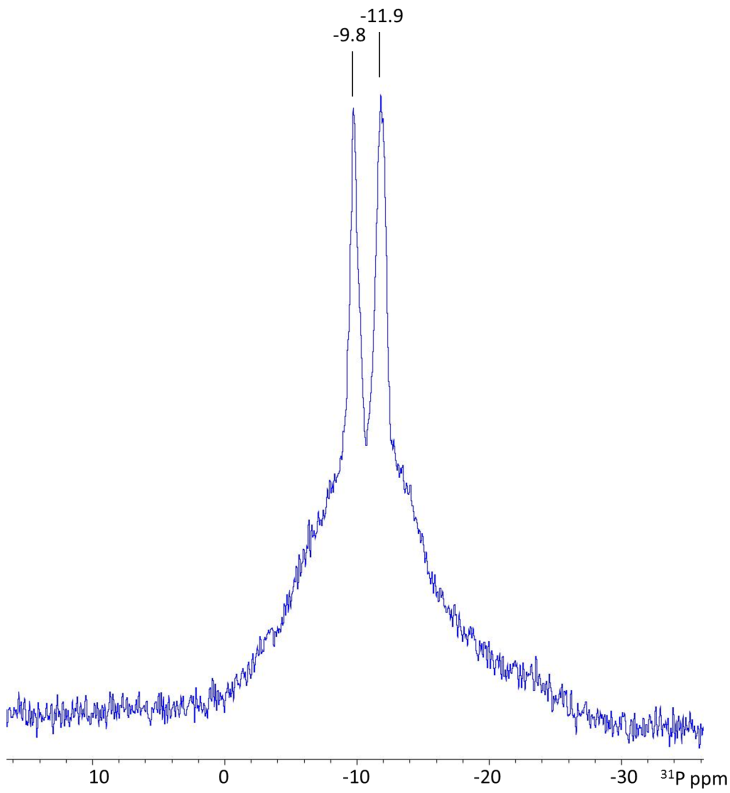

Figure 7.8 ^{31}P CP MAS spectrum of ADP and $ADP.AlF_4$ species contained in actin filaments. Using the assignment reported in literature for free ADP in water, it was suggested that the peaks at -11.91ppm and -9.83ppm were respectively the α- and β-phosphate from ADP. A third broad peak centred at near -11.12ppm was observed and it was suggested originate from the $ADP.AlF_4$ species. The spectrum (10240 scans) was recorded at 10kHz spinning rate, 278K in a 400MHz Bruker magnet.

The values of linewidths for the three signals was calculated using the line fitting macros contained in MestReNova software [78] (Figure 7.9). The signals suggested to be α- and β-phosphate (-9.83ppm and -11.93ppm) were characterized by a linewidth respectively of 115Hz and 143Hz. The linewidth for the broad signal was calculated to be almost 1887Hz. After the fitting, the possible presence of extra peaks was considered but it was difficult to demonstrate due to the complexity of the statistic calculation that should have been performed to confirm their eventual fitting.

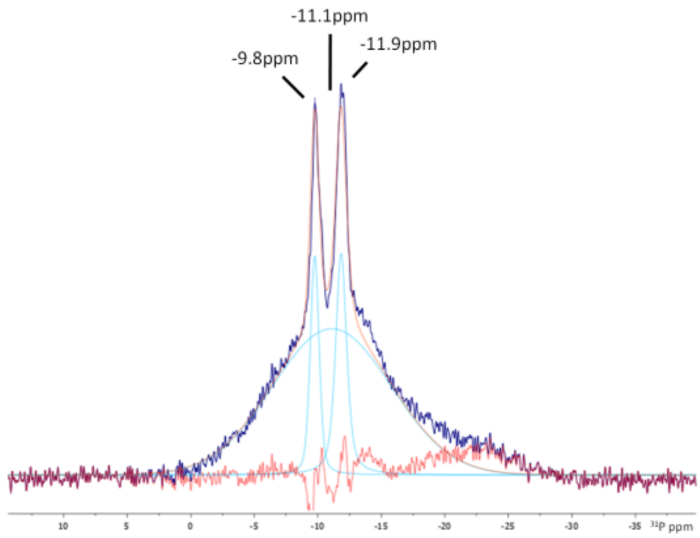

Figure 7.9 Line fitting calculation performed on the ^{31}P CP MAS spectrum of actin filaments complexed with ADP.AlF$_4$ using MestRenova software. The blue line represents the original spectrum, the cyan line the calculated peaks and the orange line the spectrum obtained from the sum of the calculated peaks. It was possible to recognize the presence of possible extra peaks but the complexity of the statistic calculation to confirm their eventual fitting resulted to be too complicated.

A contribution from the J-coupling with the quadrupolar aluminium or the fluorides was excluded due to the fact that the AlF$_4$ was not covalently bound to the ADP but it derived from an ionic interaction. On the other hand, their contribution through dipolar coupling was the main suggestion for this result. Still, it was not clear from what the third signal derived. Even if it is reported in the literature [35] that the reaction to form ADP.AlF$_4$ goes to completion, the only explanation of a third signal could derive from a defective rate of this reaction. In this case two forms of ADP, ADP and ADP.AlF$_4$, would have been contained in the sample. The presence of the analogue of ADP.Pi is known to decrease the dynamics [35] of the filaments and it could have helped in the stabilization of the pocket were the ADP is contained. In this scenario it could be possible that the two sharp signals were derived from the ADP while the broad signal could contain both the signals from the ADP.AlF$_4$ widened by the contribution of the dipolar coupling with the AlF$_4$ coordinated. Another aspect that can corroborate this hypothesis derives from the analysis of the signal integrals. The broad signal assumed to be generated by the ADP.AlF$_4$ counts for ~82% of the entire area while the two sharp signals for the remaining ~18%. The majority of the actin filaments seem to contain ADP coordinated with the AlF$_4$ with only a small part of ADP in agreement with the assumption that the reaction did not reach completion. The intensity of the signals in Figure 7.8 does not reflect the weight that the single peaks have on the total giving no information about the ratio between the two families of ADP. The high intensity of the two sharp peaks are due to their small linewidth and to the fact that those peaks are the sum of the signal from an ADP phosphate and signal from the phosphate from ADP.AlF_4.

The possibility that the broad signal is generated from free molecules of ADP.AlF_4 still present in the small part of solution that remains after the squeezing of the filaments on the wall of the rotor was excluded considering that it would not be possible to see molecule free to move when CP is used to move the magnetization to the phosphates. Thus, prior the preparation of the complex the actin filaments were sedimented and resuspended in actin binding buffer in order to wash them from residues of unwanted minor products of the reaction to produce ADP.AlF_4 (Figure 7.9).

To confirm that actin binding molecules can affect the plasticity of the filaments increasing their rigidity (and at the same time increasing the homogeneity of the filaments in the rotor), ^{31}P CP MAS spectra of actin filaments polymerized in presence of phalloidin were acquired. Phalloidin is known from literature to stabilize lateral interactions between two filament strands [33] and to inhibit the release of the ADP after its hydrolysis from ATP resulting in a decreasing in the dynamic process of polymerization of the filaments (Figure 7.10).

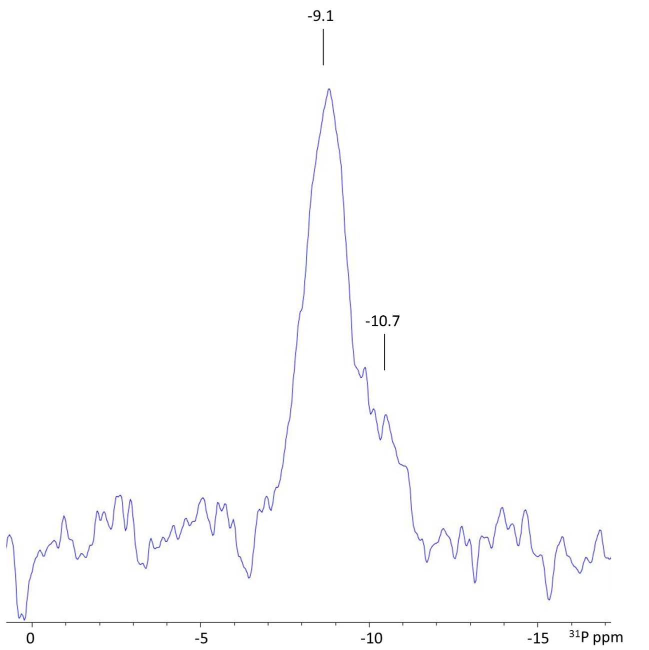

Figure 7.10 ^{31}P CP MAS spectrum of ADP in actin filaments complexed with phalloidin. The pattern of signals is consistent with the signal from the reference sample. The main peak is centred at -9.08ppm and it is characterized by a linewidth of near 265Hz suggesting that both the signal from α and β phosphate can be under this peak. Another peak could be recognized at -10.7ppm and it could refer to a different environment for the ADP but the poor resolution makes it impossible to determine. The spectrum (8192 scans) was recorded at 10kHz spinning rate, 278K in a 400MHz Bruker magnet.

In the spectrum two peaks were recognizable. The main peak was centred at -9.08ppm with a linewidth of almost 265Hz while the second peak appear to be a shoulder of the main peak centred at -10.74ppm. Despite the presence of phalloidin, the pattern was comparable to the one from the reference so it was not sufficient to confirm an unambiguous assignment of the signals. On the other hand, the behaviour could be explained by the different mechanism of action of phalloidin with respect to ADP.AlF_4. The analogues of ATP act inside the cleft and directly on the ADP molecule blocking its release from the filaments while phalloidin interacts with the filaments at the interface of two filaments strand less affecting the cleft in which the ADP is contained.

Actin filaments polymerized in presence of cucurbitacin E were then prepared and analysed. Cucurbitacin E is known to interfere with the depolymerization specifically binding to filamentous actin (F-actin) and forming a covalent bond at residue Cys257 only when in filamentous state [36]. Its mechanism of action has more analogies to phalloidin than ADP.AlF_4, suggesting a similar behaviour in the rearrangement of ADP phosphate resonances in ^{31}P CP MAS experiments. As expected, the same pattern of signal arose from this complex and two peaks centred at -9.84ppm and -10.83ppm were recognizable in the ^{31}P CP MAS acquired. Similarly to the actin polymerized in the presence of ADP.AlF_4 the spectrum was not sufficient to assign the signal for the phosphate from the nucleotide caged in the cleft.

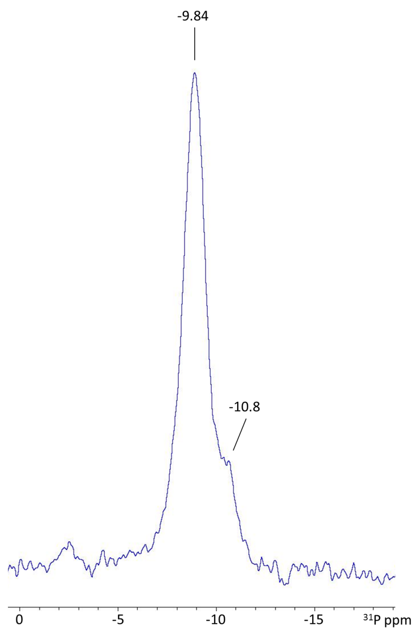

Figure 7.11 ^{31}P CP MAS spectrum of ADP in actin filaments complexed with cucurbitacin E. Two peaks are recognizable in the spectrum, a main peak centred at -9.08ppm characterized by a linewidth of near 250Hz and another peak at -10.8pp. The spectrum (4096 scans) was recorded at 10kHz spinning rate, 278K in a 400MHz Bruker magnet.

7.4 ^{31}P NMR spectroscopy of actin binding protein-filaments complexes

To benefit from the sensitivity of ^{31}P NMR spectroscopy to show changes in the nature of the ADP molecule in the cleft that reflect a probable modification in its environment, I decided to apply this technique to the investigation of possible rearrangements in the filaments when an actin binding protein is bound to them. Several ABD-filament complexes were taken into consideration and for each preparation ^{31}P CP MAS experiments were acquired. After the acquisition of the ssNMR spectra, from every rotor part of the pellet was sampled and analysed by SDS-PAGE to confirm the presence of the complexes in it.

VHD-actin filaments was the first complex analysed. In the first approach, ^{13}C-^{15}N VHD were used and, due to its cost, a ratio 1:5 of VHD to filaments was prepared meaning that in this sample the filaments were not saturated. The use of a double labelled protein was suggested by the possibility to run successive ^{13}C experiments on this complex to confirm the presence of the VHD as a folded protein. Data acquired about the affinity of the VHD-actin filaments interaction (chapter 6.2) revealed a k_D of near 2.5µM meaning a modestly tight binding of VHD to the filaments. The ^{31}P CP MAS spectrum acquired (Figure 7.12) exhibited three peaks at near -4.84ppm, -11.84 and -13.00ppm characterized, respectively, by a linewidth of near 146Hz, 234Hz and 121Hz. The linewidth values for the peak at -11.8ppm and -13.00ppm were calculated by fitting the two peaks using the proper "peak fitting" suite developed by ACD/Lab or MestReNova (validation of the method reported in Appendix B).

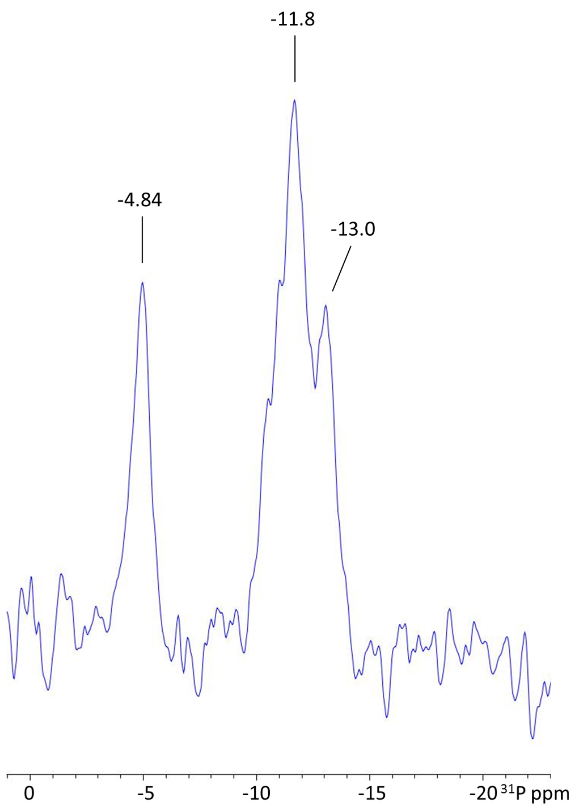

Figure 7.12 ^{31}P CP MAS spectrum of ADP contained in actin filaments not fully saturated by VHD. Three peaks centred at -4.8ppm, -11.8ppm and -13ppm were observed in the spectrum. The new pattern suggested the presence of rearrangements that affected actin residues able to affect the structure of the cleft containing the nucleotide. The spectrum (4096 scans) was recorded at 10kHz spinning rate, 278K in a 400MHz Bruker magnet.

Despite the small change in chemical shift, it was easy to connect the peaks at –13.00ppm and –11.84ppm to the α and β phosphate signals from ADP contained in filaments in apo form as later confirmed by two-dimensional ^{31}P-^{31}P correlation spectrum. On the other hand, the peak at –4.84ppm suggested the presence of a different environment for some of the ADP in the cleft maybe generated by a possible rearrangement of the filaments due to the binding of the VHD. The position on the surface of the filaments where the VHD interacts with them is still unknown. This means that it was impossible to define the stoichiometry of the interaction as this ABD could bind both actin at the interface of more monomers or bound 1:1 to them. A stoichiometry different from 1:1 could explain the presence of more than one environment for the ADP molecules. Part of the contents of the rotor was analysed by SDS-PAGE and the presence of both proteins was confirmed.

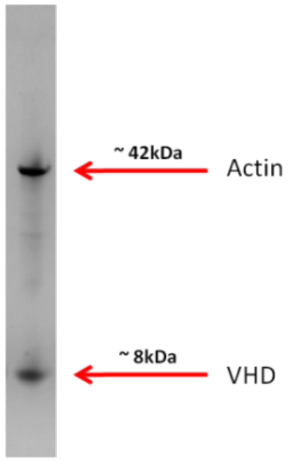

Figure 7.13 SDS gel from aliquot collect from the rotor containing actin filaments complexed with VHD. A band at 42kDa characteristic of actin and another at 8kDa typical of VHD were observable.

A new preparation of filaments saturated by unlabelled VHD was prepared. The same series of experiments were acquired but, differently from before, in the ^{31}P CP MAS spectrum acquired the two peaks at -13.00ppm and -11.84pm exhibited a surprisingly improvement in their resolution showing a linewidth, respectively, of 102Hz and 67Hz (Figure 7.14). It was suggested that the narrowing in the linewidths could be due to a more homogeneous sample implicating that the presence of VHD bound to actin filaments helps in a more ordered precipitations during the sedimentation of the complex.

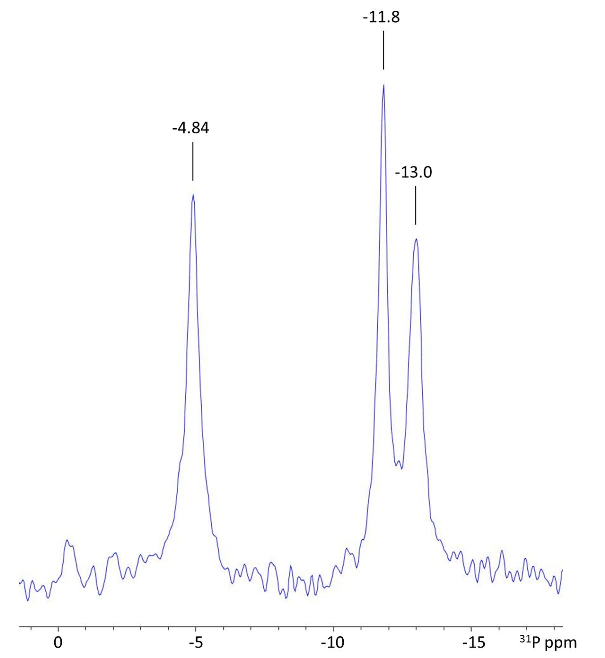

Figure 7.14 ^{31}P CP MAS spectrum of ADP from saturated VHD-actin filaments sample. The three peaks centred at -4.8ppm, -11.8ppm and -13ppm shown an improvement in their linewidth suggesting that the bound of VHD to the filaments helps to obtain a more homogeneous sample. The spectrum (4096 scans) was recorded at 10kHz spinning rate, 278K in a 400MHz Bruker magnet.

A ^{31}P-^{31}P DARR experiment was acquired in order to analyse the relationship among the signals. Due to the low resolution of the spectrum, it was not possible to observe a clear cross peak between the two signals at -13.00ppm and -11.84ppm, it is most likely, however, that they are correlated and that the cross peak is hidden by their high intensity. As no cross peak was detectable among the signal at -4.84ppm and the other resonances, it can be confirmed that no spatial correlations exist among them.

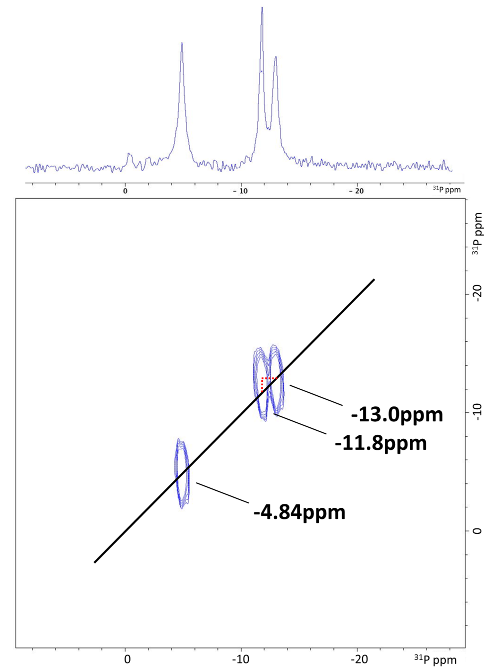

Figure 7.15 ^{31}P-^{31}P DARR spectrum of VHD-actin filaments complex showing the probable presence of two species of ADP. As expected, the two signals at lower field are correlated to each other while no correlation arose with the signal at higher field. The spectrum was recorded at 10kHz spinning rate, 278K in a 400MHz Bruker magnet.

To exclude residual phosphate ions from the solution in which the VHD was stored as possible source of this new signal, filaments resuspended in the same phosphate buffer were precipitated and analysed. As shown in Figure 7.16, a main peak centred at -9.55ppm and a small peak at -3.81ppm were observed. The main peak corresponded to the peak for α and β ADP phosphate in filaments precipitated alone while the origin of the small peak at -3.81ppm is still under investigation. Nevertheless, it was possible to exclude that the peak at -4.84ppm in the spectrum of the VHD-filaments complex originated from phosphate species from the buffer.

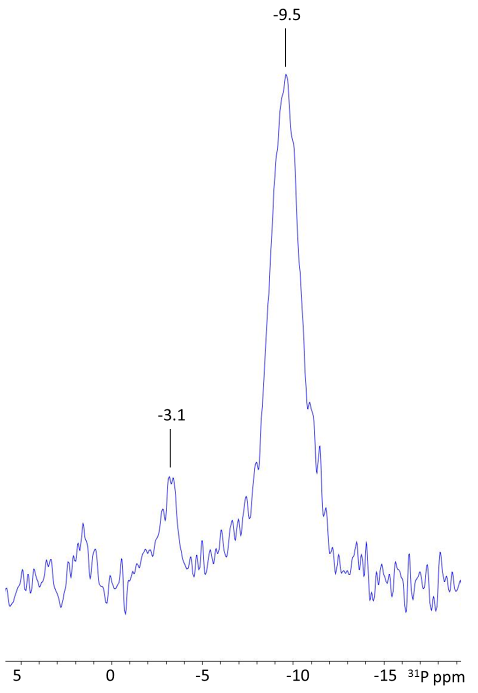

Figure 7.16 ^{31}P CP spectrum of ADP in actin filaments resuspended in phosphate buffer and then precipitate. The main peak centred at -9.5 ppm contains the signal from the α and β ADP phosphate while the peak at -3.1ppm is still under investigation. The spectrum (8192 scans) was recorded at 10kHz spinning rate, 278K in a 400MHz Bruker magnet.

To investigate how VHD affects the filaments, different ratios of VHD bound to actin were prepared. A 20µM solution of filaments was split in 5 equal aliquots each of them was added with an increasing amount of VHD till their saturation. Table 7.3 shows the concentration used for each preparation. For each condition the same amount of near 36-40mg of wet pellet was loaded in a 4mm rotor for ssNMR.

Actin [µM]	VHD [µM]	Final Volume [ml]
20	0	16
20	40	16
20	120	16
20	250	16

Table 7.3 Conditions for the samples in the titration

For each point of the titration, a ^{31}P CP MAS experiment was acquired and the value of linewidth calculated using ACD/Lab "line fitting" tool. The resulted spectra (Figure 7.17) and the values of linewidth calculated (Table 7.4) are reported below. The fitting of the curves originating from the calculated values of linewidth plotted against the concentration of VHD cosedimented with the filaments (Chart 7.1) showed a similar exponential decay trend for each signals, suggesting that the increase of the VHD bound to the filaments helps to improve the resolution of the ADP phosphate signals. It was hypothesized that a reduction in the heterogeneity of filaments can be the response to the increasing binding of VHD.

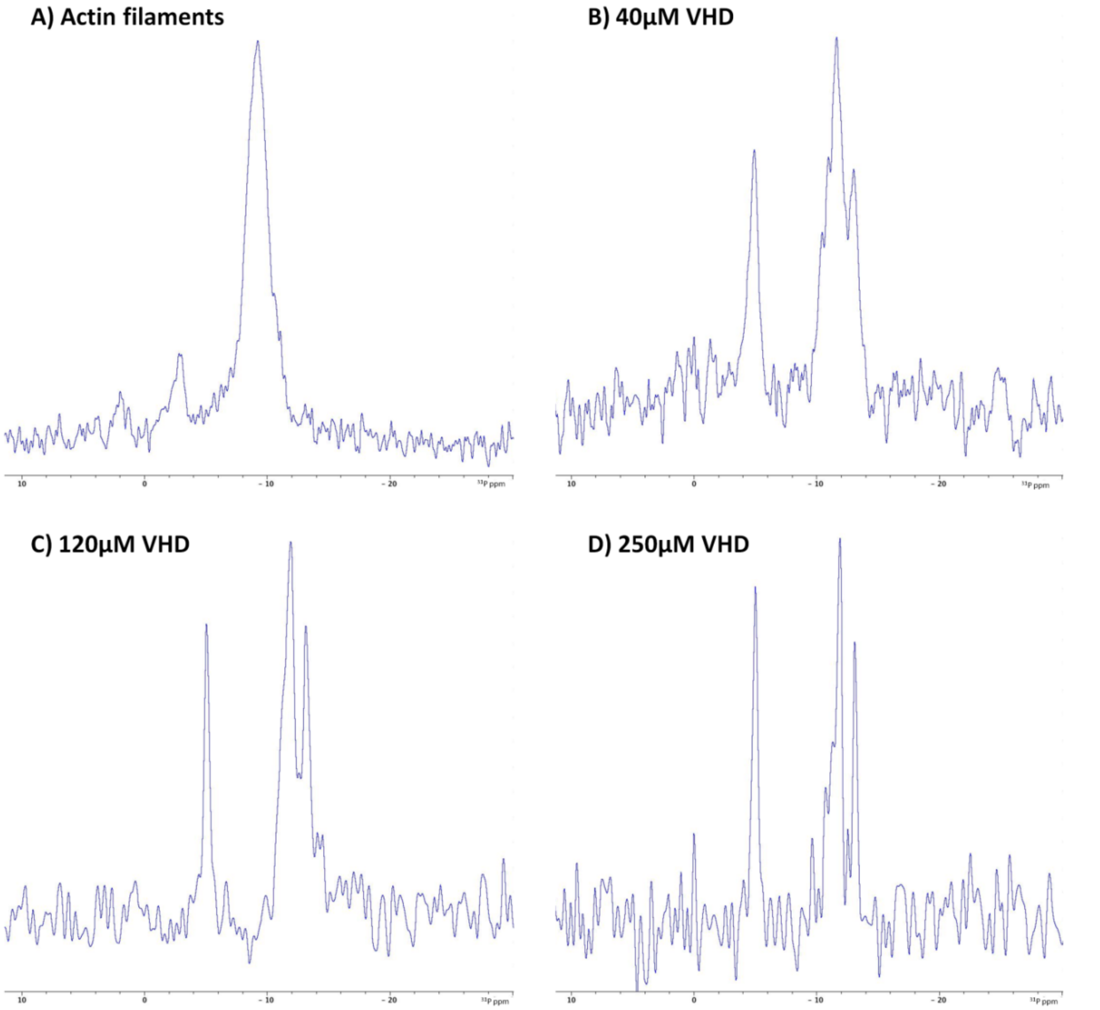

Figure 7.17 ^{31}P CP MAS spectra of ADP arising in each point of the VHD to actin filaments titration. In panel A is reported the spectrum of actin filaments sedimented alone. From panel B to D an increasing amount of VHD was progressively added. It was clear how the increasing amount of VHD helps to narrow the linewidth of the signals. Each spectrum (8192 scans) was recorded at 10kHz spinning rate, 278K in a 400MHz Bruker magnet.

	Linewidth in Hz			
	Actin alone	**40 µM VHD**	**120 µM VHD**	**250 µM VHD**
-4.83ppm	n.a	142.95	128.21	83.31
-9.98ppm	324.02	n.a	n.a	n.a
-11.8ppm	n.a	278.33	197.09	138.19
-13.0ppm	n.a	165.10	119.19	84.67

Table 7.4 Linewidth calculated using ACD/Lab dedicated suite for the VHD-actin filaments complex in the titration. Increasing the amount of VHD the linewidth of every signal decrease till the filaments are saturated by VHD.

The graph of the linewidth values plotted against the concentration of VHD cosedimented with the filaments showed a similar exponential decay trend for each signals (Chart 7.1). The increasing saturation of filaments by VHD corresponded with a resolving of the signal.

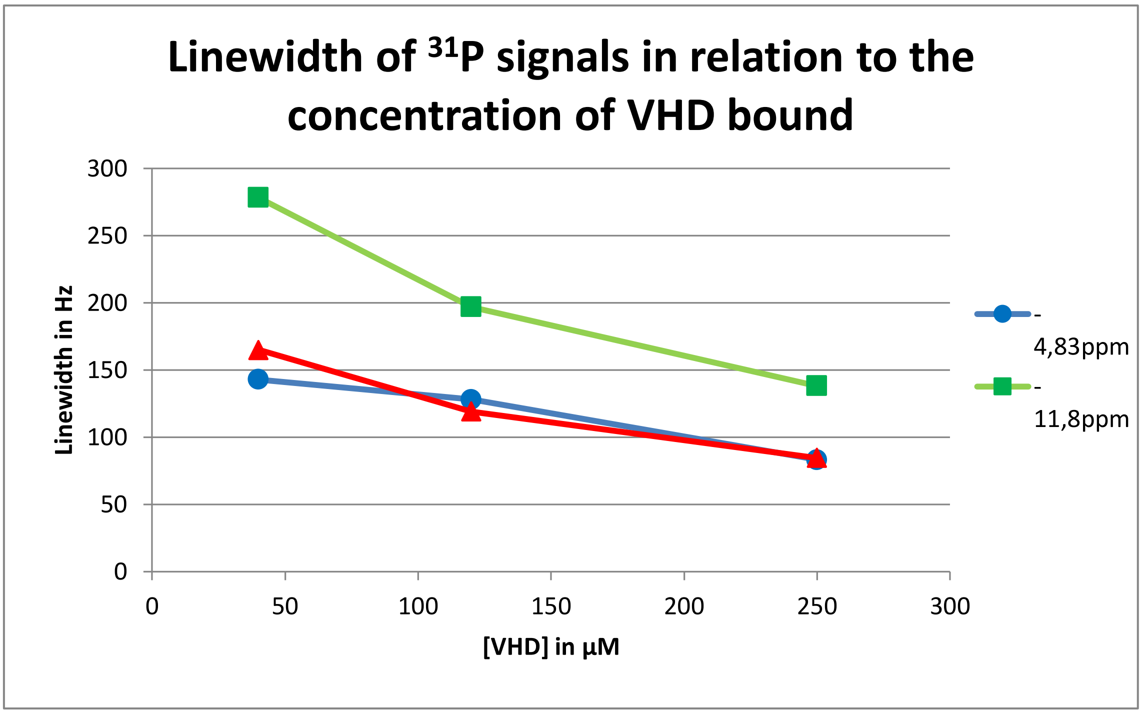

Chart 7.1 Plot of the value of linewidth calculated using ACD/Lab "line fitting" tool against the concentration of VHD in each complex. Green squares indicate the peak at -11.8ppm, blue dots the peak at -4.83ppm and red triangles the peak the peak at -13ppm

To confirm that the peak at -4.84ppm derived from a rearrangement near the cleft where the nucleotide is caged due to the binding of VHD to the filaments, a different actin binding domain called ABD1 was tested. ABD1 is a 8kDa domain of MS1 [46] a protein expressed mostly in cardiac and skeletal muscle that contributes the development of hypertrophy. Interestingly, ABD1 is not structured when in apo form but after the binding to actin filaments the protein presumably folds into a 3D structure [46]. Unfortunately, the structure have not been resolved yet. The complex was prepared using the same protocol described for the VHD-filaments complex using an excess of protein in ratio of 4:1 ABD1 to filaments. Similarly to the previous complex, the ^{31}P CP MAS spectrum of ABD1 bound to actin filaments (Figure 7.18) exhibited the extra peak at -4.96ppm and two peaks centred at -11.8ppm and -13ppm. They were characterized, respectively, by a linewidth of near 180Hz, 230Hz and 250Hz (peak fitting calculated using ACD/Lab software). Even if the alignment of the amino acids sequence between VHD and ABD1 shown poor homology (Figure 7.19) the same pattern of signal in the ^{31}P spectrum was observed suggesting that the two proteins could share the same binding region on the filaments.

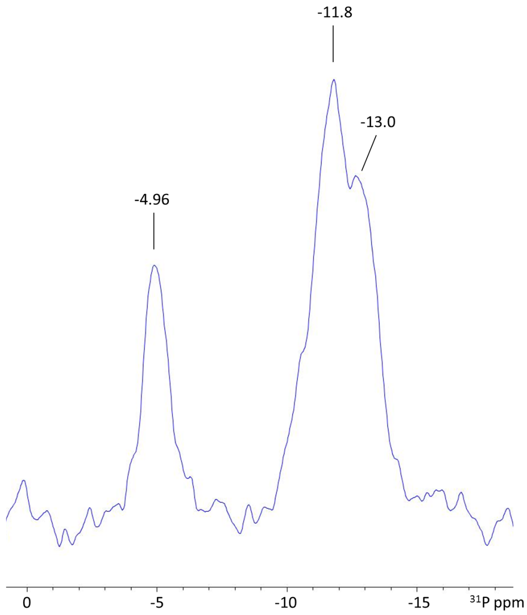

Figure 7.18 ^{31}P CP MAS spectrum of ADP contained in actin filaments complexed to ABD1. Three peaks centred at -4.9ppm, -11.8ppm and -13ppm were observed in the spectrum similarly to the ^{31}P CP from VHD-filament complexes. The spectrum (4096 scans) was recorded at 10kHz spinning rate, 278K in a 400MHz Bruker magnet.

```
VHD     -QY-KI--YPYDSLI-VTNRIR-V-KLPKD--VDRT--RL-ERHLS-PEEFQEVF--G-- 43
ABD1    GAMARAEEHIYREIMELCFVIRTMARHRRDGKIQVTFGELFDRYVRISDKVVGILMRARK 60
            :   : * .:: :    ** : :  :*   :: *   .* :*::   .::.  ::  .

VHD     MSIEEFD-RLALWKRNDLKKKAL-LF- 67
ABD1    HGLVHFEGEM-LWQGKD-DHVVITLLE 85
         .: .*: .: **: :* .: .: *:
```

Figure 7.19 VHD and ABD1 amino acid sequence alignment made using Clustal W [94]. In green are highlighted the residues on VHD that are known to be crucial for the binding to actin filaments while in yellow their corresponding residues in the sequence of ABD1.

Nevertheless, this identical result in the ^{31}P spectra despite the distance in their sequences aroused several doubts in the truthfulness of this approach. Interested in solving this ambiguity, different ABDs with threedimensional models of interaction with actin filaments already reported in the literature were tested. The results were interpreted looking for a correlation between the pattern of signals originating from their interaction with the filaments and their model of interaction reported.

The fragment 1-228 of calponin, a protein assumed to have a central role in the modulation of actin function [21], was complexed with actin filaments and ^{31}P CP MAS spectra were acquired. This fragment contains the CH domain of calponin, the structural module acknowledged to bind the actin filament in calponin. Only one peak centred at -12.30ppm characterized by a linewidth of near 294Hz (calculates using MestReNova) arose in the spectrum (Figure 7.19). The pattern was similar to the spectrum acquired for the filament alone (Figure 7.7) and only a shift of 3ppm was recognizable. The SDS-gel confirmed the presence of both calponin and actin in the rotor (Figure 7.21).

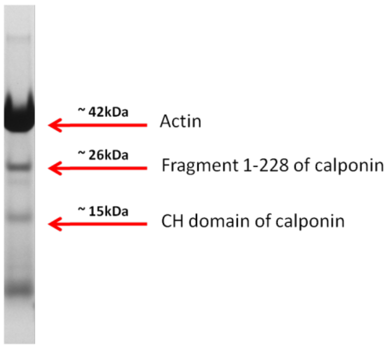

Figure 7.20 SDS gel from aliquot collect from the rotor containing actin filaments complexed with the fragment 1-228 of calponin. A band at 42kDa characteristic of actin and another at 26kDa typical of this fragment calponin were observable. It was suggested that the band at 15kDa indicates the fragment 1-130 of calponin containing the CH domain while the band a low molecular weight represent products of degradation.

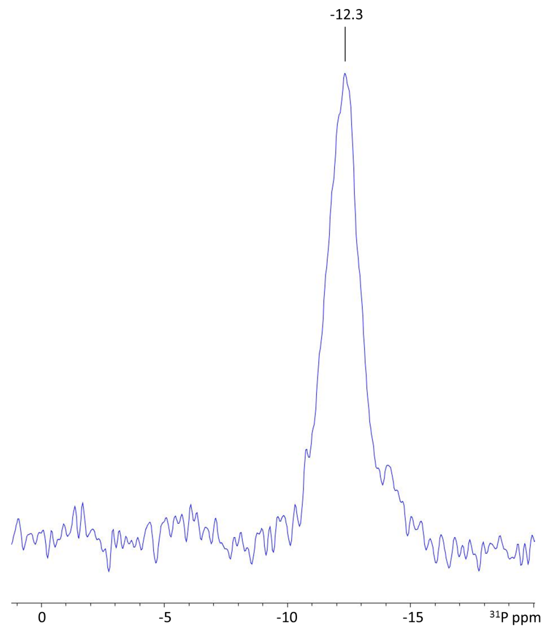

Figure 7.21 ^{31}P CP MAS spectrum of ADP from actin filaments bound to the CH domain of calponin. A single peak centred at -12.3ppm was observed. Only a shift of near 3ppm was observed when compared to the reference. The spectrum (sum of four FIDs of 4096 scans each) was recorded at 10kHz spinning rate, 278K in a 400MHz Bruker magnet.

On the other hand, a different pattern of signals similar to the one originating from the VHD-filaments complex was observed when the recombinant calponin fragment 131-228aa, known from the literature to contain actin and calmodulin recognition regions [21], was tested. Three peaks centred at -5.01ppm, -11.35ppm and -12.98ppm were recognizable in the spectrum (Figure 7.22). It is interesting to observe that the intensity for the two peaks at -5.01ppm and -12.98ppm is 10 times lower than the main peak centred at -11.35oom. An excess of fragment was added to the filaments in order to achieve saturation. The SDS-gel run on an aliquot from the rotor showed the presence of both the proteins (Figure 7.23).

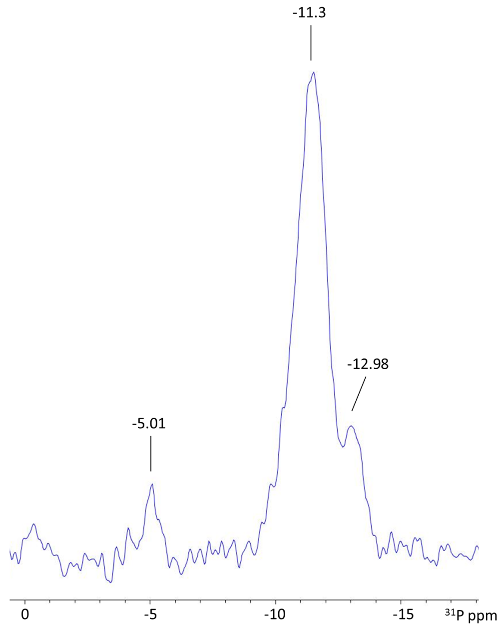

Figure 7.22 ^{31}P CP MAS spectrum of ADP in actin filaments complexed with the calponin fragment 131-228. Three peaks centred at -5ppm, -11.3ppm and -12.9ppm were observed differently from the spectrum originating from Calponin-filament complexes. The spectrum (sum of four FIDs of 4096 scans each) was recorded at 10kHz spinning rate, 278K in a 400MHz Bruker magnet.

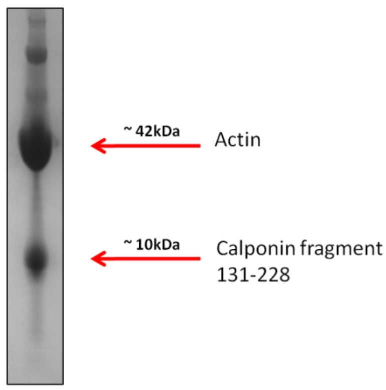

Figure 7.23 SDS gel from aliquot collect from the rotor containing actin filaments complexed with calponin fragment 131-228. A band at 42kDa characteristic of actin and another at 10kDa typical of calponin fragment were observable.

The same pattern arose from the ^{31}P CP MAS experiments run on filaments complexed with the linker between domains C1 and C2 of human cardiac myosyn binding protein C, shortened hcLNK1 (Figure 7.24) and complexed with the actin binding domain of α-actinin, structurally defined as a tandem calponin homology domain (Figure 7.25). The

SDS-PAGE run on the contents of both the rotors confirmed the presence of the proper complex in both the preparation (Figure 7.26 and Figure 7.27).

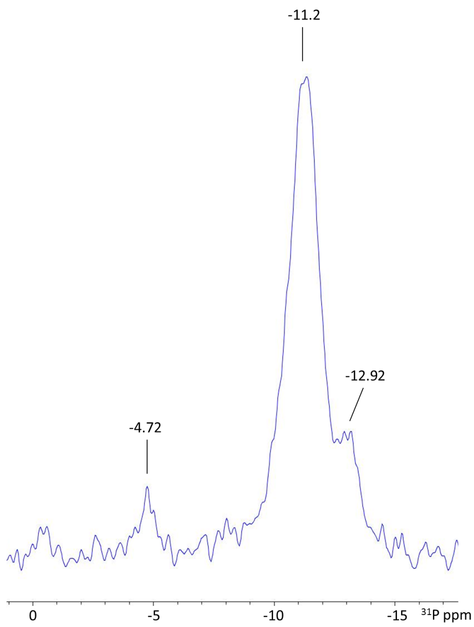

Figure 7.24 ^{31}P CP MAS spectrum of ADP actin filaments bound to the linker between domains C1 and C2 of human cardiac myosin binding protein C. Three peaks centred at -4.72ppm, -11.2ppm and -12.9ppm were observed. The spectrum (11k scans) was recorded at 10kHz spinning rate, 278K in a 400MHz Bruker magnet.

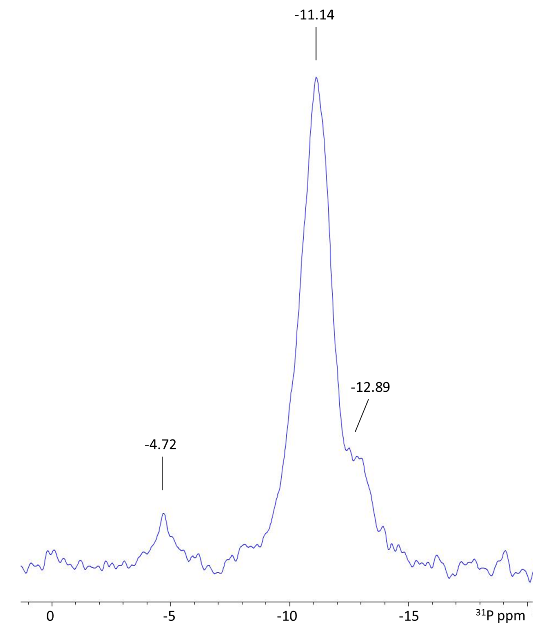

Figure 7.25 ^{31}P CP MAS spectrum of ADP contained in actin filaments complexed with the CH domain of α-actinin. The same three peaks of originating from actin bound by calponin fragment and the human cardiac linker, centred at -4.72ppm, -11.3ppm and -12.9ppm, were observed. The spectrum (sum of three FIDs of 10k scans each) was recorded at 10kHz spinning rate, 278K in a 400MHz Bruker magnet.

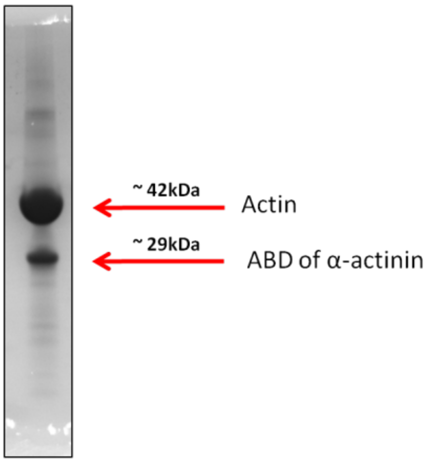

Figure 7.26 SDS gel from aliquot collect from the rotor containing actin filaments complexed with the actin binding domain of α-actinin. A band at 42kDa characteristic of actin and another at 29kDa identifying the ABD from α-actinin were observable.

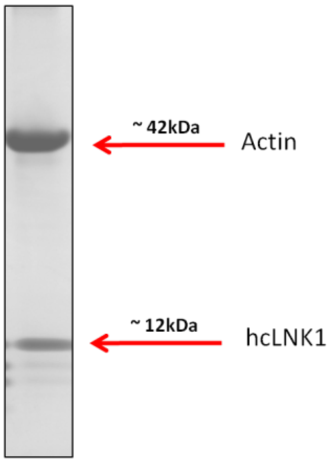

Figure 7.27 SDS gel from aliquot collect from the rotor containing actin filaments complexed with hcLNK1. A band at 42kDa characteristic of actin and another at 12kDa identifying the hcLNK1 were observable.

The actin binding domain of myosin, commonly known as S1 domain, was next complexed with actin filaments and analysed. The ^{31}P CP MAS spectra acquired exhibited the same pattern of signals of VHD and ABD1 complexed with filaments (Figure 7.28). The three peaks centred at -4,94ppm, -11.91ppm and -13.15ppm were characterized by a linewidth respectively of 148Hz, 141Hz and 154Hz. The SDS-PAGE run on this sample confirmed the presence of S1 domain and actin in the rotor (Figure 7.29).

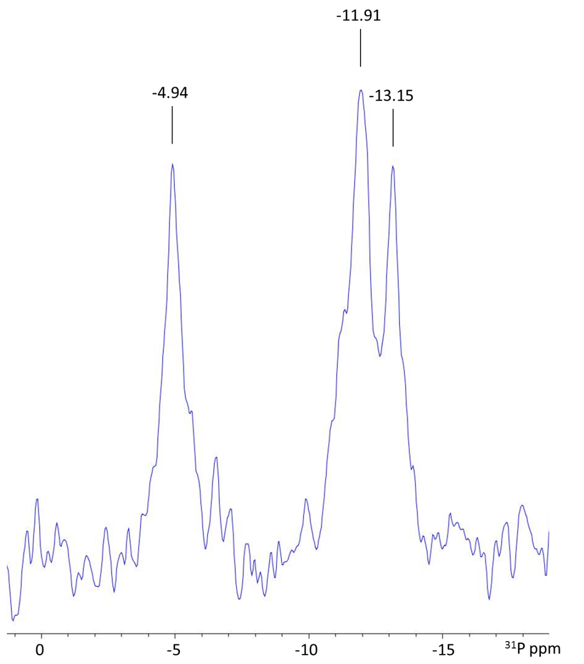

Figure 7.28 ^{31}P CP MAS spectrum of ADP from the S1-actin filament complex. The same three peaks pattern originating from actin bound by VHD and ABD1, centred at -4.94ppm, -11.91ppm and -13.335ppm, were observed. The spectrum (sum of ten FIDs of 8192 scans each) was recorded at 10kHz spinning rate, 278K in a 400MHz Bruker magnet.

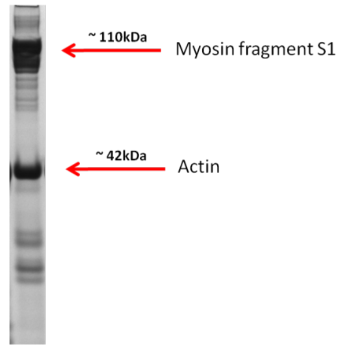

Figure 7.29 SDS gel from aliquot collect from the rotor containing actin filaments complexed with myosin. A band at 42kDa characteristic of actin and another at 110kDa typical of myosin were observable. The bands at low molecular weight represent degraded proteins probably due to a too hard sampling.

A different result was obtained when tropomyosin was bound to actin filaments. As shown in Figure 7.30, it was possible to identify 4 peaks at -13.29ppm, -11.6ppm, -4.86ppm and at -0.5ppm that respectively shown a linewidth of approximately 148Hz, 272Hz, 172Hz and 157Hz (peak fitting calculated using ACD/Lab software). Unfortunately, a very poor signal to noise was observed in the spectra for this complex, requiring the acquisition of twelve experiments and the sum of their FIDs to reach a signal to noise ratio of near 18 as shown in Figure 7.31. This prevented the acquisition of any multidimensional experiments that could have helped in the unravelling the mystery about the origin of the fourth peak. The SDS-PAGE run on this sample confirmed the presence of tropomyosin and actin in the rotor (Figure 7.31).

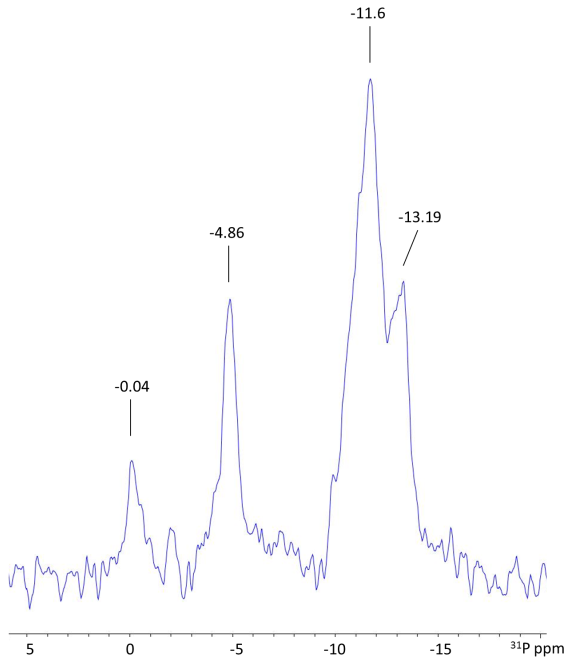

Figure 7.30 ^{31}P CP MAS spectrum of ADP in actin filament complexed to tropomyosin. The spectrum show the same three peaks centred at -4.8ppm, -11.6ppm and -13.3ppm similarly to actin complexed with myosin and VHD. Surprisingly another peak centred at -0.5ppm arose in the spectrum. The reason of its originating is still under investigation but the poor signal to noise ratio make difficult its study. The spectrum (sum of twelve FIDs of 10240 scans each) was recorded at 10kHz spinning rate, 278K in a 400MHz Bruker magnet.

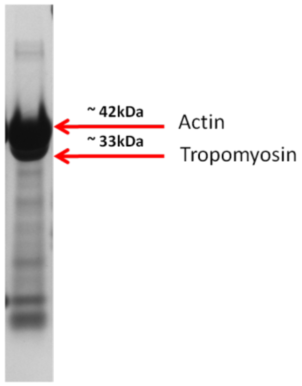

Figure 7.31 SDS gel from aliquot collect from the rotor containing actin filaments complexed with tropomyosin. A band at 42kDa characteristic of actin and another at 33kDa typical of tropomyosin were observable. The bands at low molecular weight represent degraded proteins probably due to a too hard sampling.

^{31}P NMR spectroscopy revealed itself as an elegant and powerful tool for the study of actin filament complexes and the data produced were useful in the tentatively determination of the surface of VHD that should interact with the filaments.

8 Partial assignment of VHD bound to actin filaments

8.1 Structure determination by NMR

In 1990 NMR in solution was considered the second technique, in addition to protein crystallography, for protein determination at atomic resolution [95]. A classic protocol for a structure determination by NMR could be identified in four principal steps (Figure 8.1)[95]. Initially there is the sample preparation that includes the expression of the protein of interest (labelled, non labelled or partially labelled), its purification, etc. The second step consists in the acquisition of NMR experiments and in their optimization. In the third step, the so called "protein assignment", every NMR signal is linked to the respective nucleus in the protein. Its dependence of the quality of the spectra acquired in terms of signal resolution, lead to the identification of the assignment as the bottle neck in this protocol. Depending of the complexity of the spectra analysis, a complete assignment could take several months or even years to be properly done. Once the assignment is performed, in the last step, the structure of the protein is calculated. In this last step the constrains to build the structure, such as dihedral angles or atoms distances, are collected and used to calculated structure that satisfy those constrains. A family of structures is calculated instead of a single structure and each of them is evaluated and validated. The Smaller the deviation in the family the better the quality of the structures calculated.

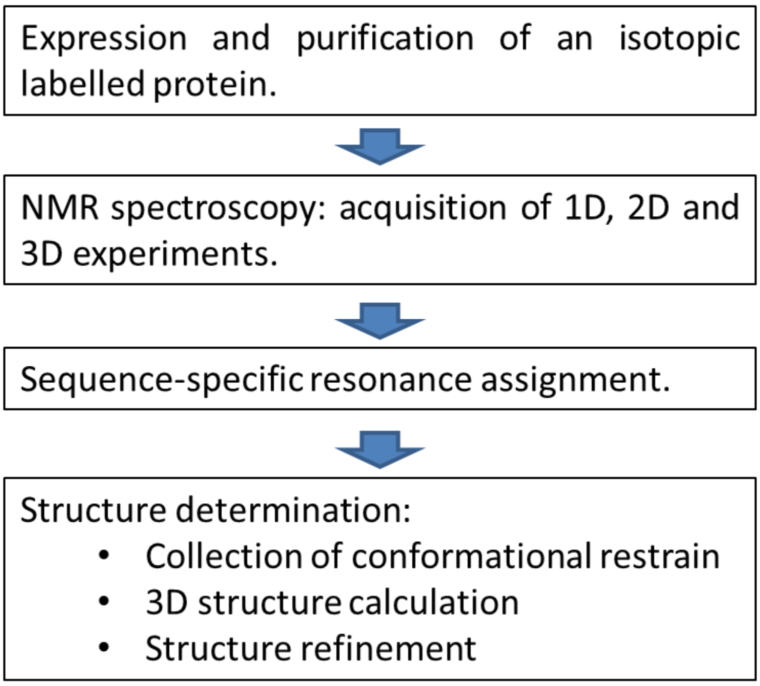

Figure 8.1 Diagrams representing the four principal steps in the protocol for the structure determination by NMR (Adaptation from diagrams from [95]).

More or less the same protocol is used when protein structures are solved using ssNMR. Nevertheless, in the ssNMR approach, the assignment is not considered the only bottle neck anymore because even the sample preparation and the spectra acquisition still require a lot of optimization due to the lack in standard procedures already available for this almost new technique (that is still in continuous development). Thus, until few years ago, strong proton coupling has made impossible the acquisition of indirect experiments relegating the assignment only to nitrogen and carbon atoms. The introduction of ultrafast spinning probes was a big step in the simplification of protein assignments by ssNMR allowing the acquisition of all those experiments that are acquired in proton dimension.

However, the acquisition of ^{13}C-^{13}C and ^{13}C-^{15}N experiments is still the routine approach. In ssNMR, two-dimensional DARR, PDSD, CHHC, NHHC or C_XN and three-dimensional NC_O-C_X, NC_α-C_X or NC_α-C_β experiments are the common spectra acquired to assign the resonances of a protein. The expression of proteins presenting different carbon labelling schemes is usually taken into consideration to facilitate the assignment of these spectra. Unfortunately, in ssNMR, the collection of the constraints indispensable for the calculation of the structure is not as straightforward as in solution NMR. The issues arising from the problematic acquisition of experiments on proton dimension that make still difficult the collection of ^1H-^1H NOE signals. In ssNMR, atom distances can be collected from PDSD experiments in the same way ^1H-^1H are collected in solution NMR that relate a cross peak intensity to the distance between the atoms that have generated the cross peak. The analysis of resonance intensities such as conformation-independent distances between sequential Cα, methyl groups within leucine and valine, and Cα and Cγ within one amino acid and between Cβ and Cγ of the leucines can be used as reference to build up the intensity-distance curve that is used as reference [84]. Other distance related information can be gathered by the addition of a paramagnetic center to the protein of interest. A brief discussion into paramagnetic ssNMR is presented in the next chapter. The calculation of the structure follows the same protocol both for ssNMR and solution NMR.

The atom distances and the torsion angles collected will be added to empirical data reported in literature that include the length of all covalent bonds and the relative angles. All these information are loaded in specific softwares (ROSETTA, ARIA, CYANA, Xplor-NIH, etc.) that will generate the structure. Firstly, the program will generate random structures based only on the empirical data and, in a second time, it will use the constrains uploaded to calculate structures until they satisfy the inter-atomic distances collected. The software assigns to each structure calculated an energy value and, at the end of the calculation, it returns as output a family of structures that contains the structures that minimize this energy value.

8.2 Assignment of ^{13}C-^{15}N VHD bound to actin filaments

8.2.1 Complete assignment of the uniformly labelled ^{13}C-^{15}N VHD by solution NMR

As previously described, the assignment of uniformly ^{13}C-^{15}N VHD in free state was already available in literature (BMRB entry 17206) and it was used as reference to both help the assignment of frequencies in ssNMR spectra and to identify the binding site by calculating the chemical shift perturbation of residues involved in binding to the filaments. The gaps in the assignment for arginine and lysine side chains were filled using specific C_xN pulse sequences optimized to resolve those regions at physiological pH (as explained in chapter 8). For the complete assignment performed in solution refer to APPENDIX E.

8.2.2 Experiments performed using a 4mm rotor: assignment of carbon and nitrogen frequencies

160scans for each of the 512 increments were recorded in every ^{13}C-^{13}C DARR spectrum acquired. Considering as reference set up an experiment with mixing time of 20ms the average acquisition time for a ^{13}C-^{13}C DARR spectrum was in the order of 2 days 18 hours. Increasing the length of mixing time, the acquisition time increases as consequence. E.g. if the mixing time is increased to 100ms the acquisition increases by almost 2 hours while if set to 250ms, 5 hours have to be added to the average time.

^{13}C-^{13}C DARR with 20ms mixing time was the first dataset acquired (Figure 8.2). A similar experiment for solution NMR, called ^{1}H-^{13}C-^{13}C-^{1}H TOCSY, was acquired on the aliphatic carbon region of a uniformly labelled ^{13}C-^{15}N VHD in free state (Figure 8.4). The ^{13}C-^{13}C projection was extrapolated (using CCPNMR software) and compared to the ssNMR ^{13}C-^{13}C DARR spectrum. To mimic the characteristic linewidth of ssNMR experiments, the TOCSY spectrum was processed exaggerating the broadening (EM for both F1 and F2 of 60Hz) (Figure 8.5).

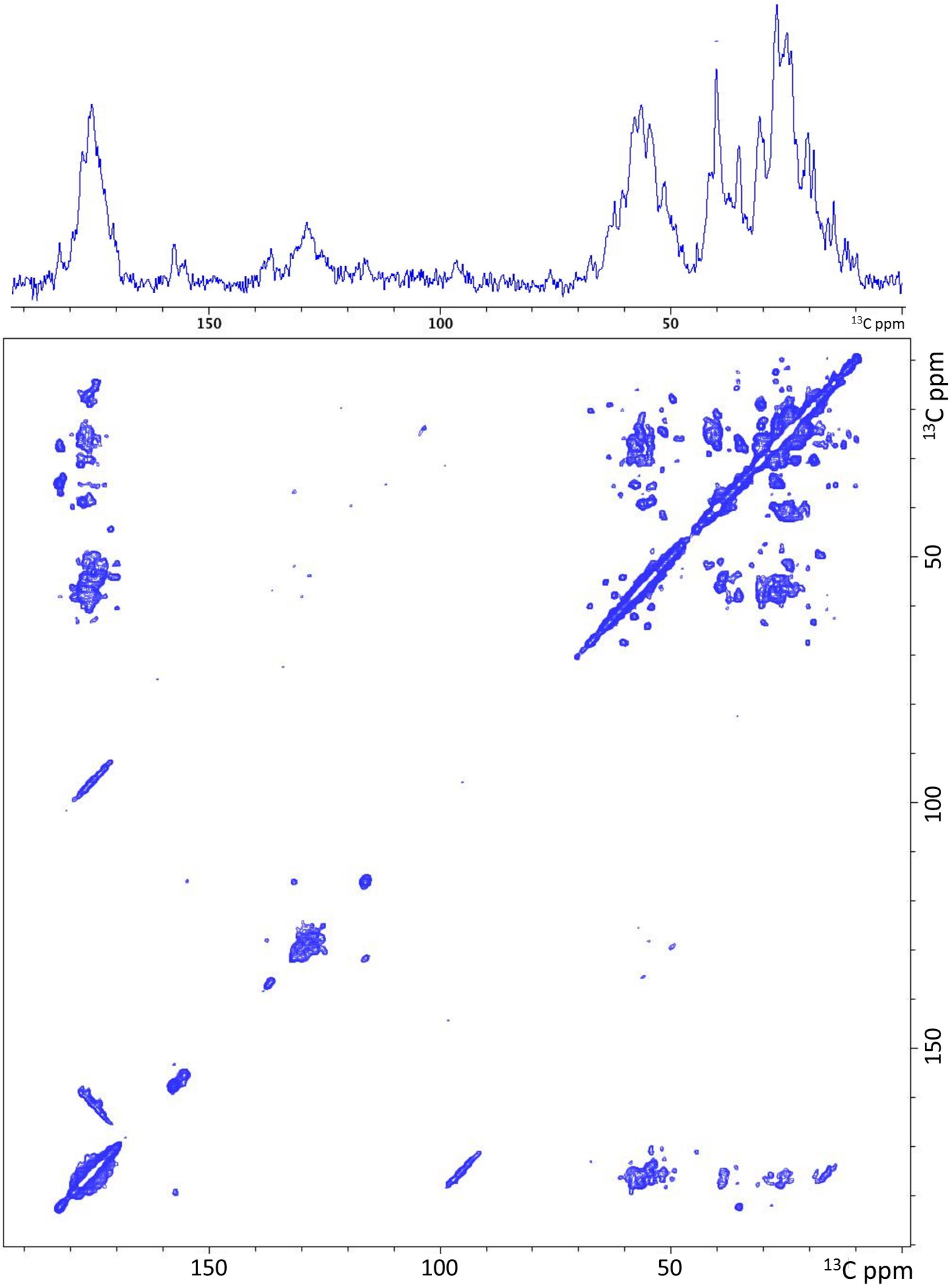

Figure 8.2 ^{13}C-^{13}C DARR spectrum using a 20ms mixing time during the ^{13}C-^{13}C recoupling for a uniformly labelled ^{13}C-^{15}N VHD bound to actin filaments. It was possible to recognize several well resolved resonances but for the majority of atoms the correlation signals were overlapped. The spectrum was acquired at 278K, 10kHz spinning rate using a 500MHz Bruker magnets equipped with triple resonance 4mm e-free probe.

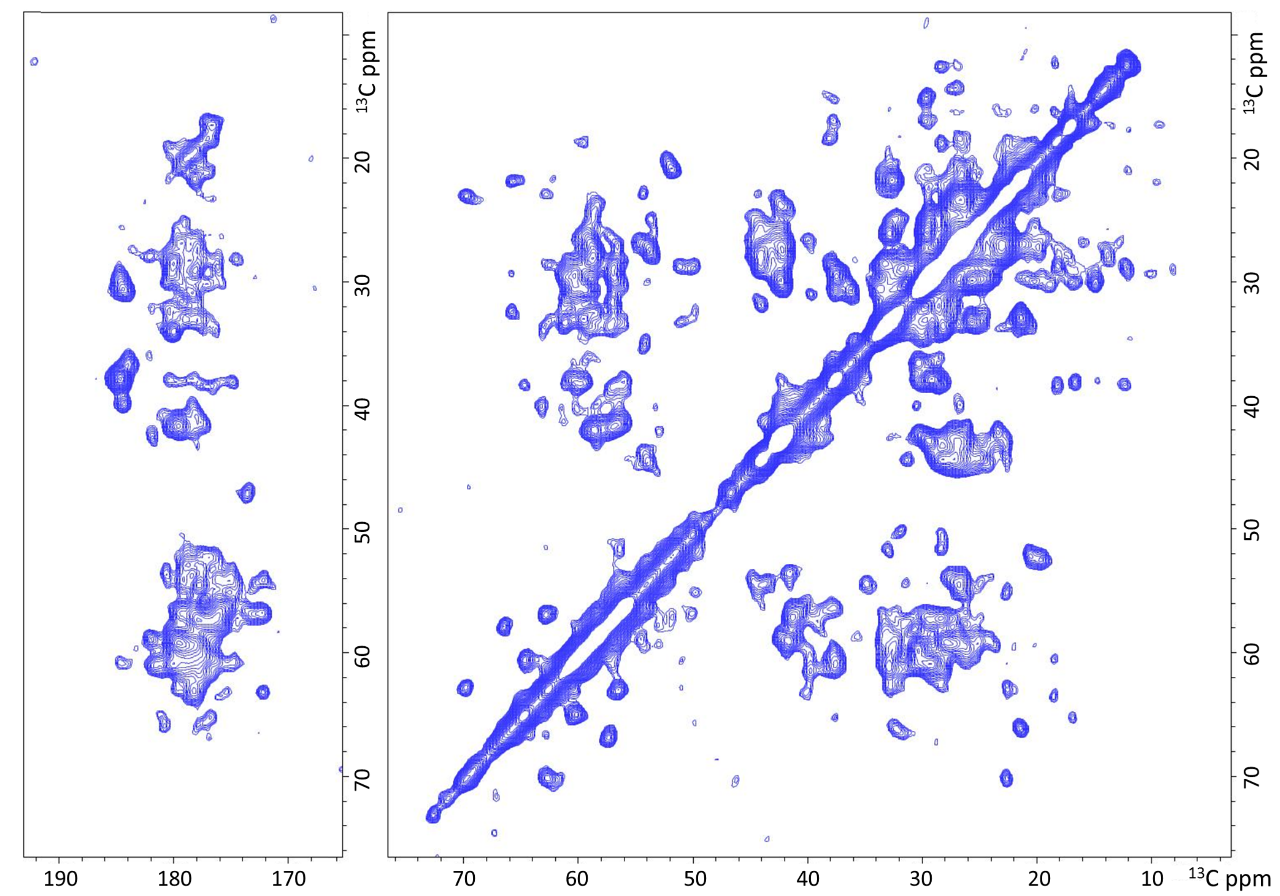

Figure 8.3 Magnification of carbonyl and aromatic cross peak region to aliphatic carbons (left panel) and aliphatic region (right panel) of a ^{13}C-^{13}C DARR spectrum acquired on a uniformly ^{13}C-^{15}N VHD bound to actin filaments using 20ms mixing time. No aromatic-aliphatic carbon correlations were observable in the spectrum using this short mixing time. The spectrum was recorded at 278K, 10kHz spinning rate in a 500MHz Bruker magnets equipped with a triple resonances e-free prob

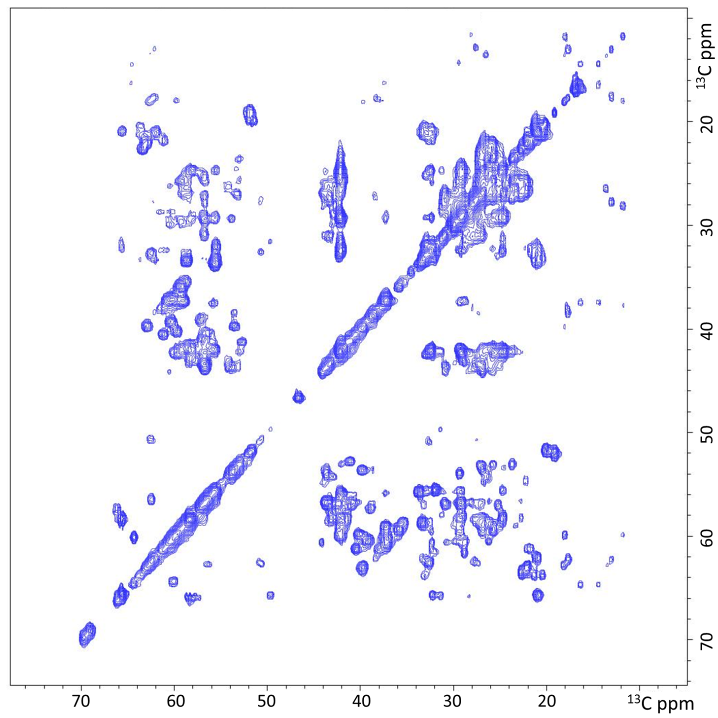

Figure 8.4 ^{13}C-^{13}C projection calculated from a HCCH TOCSY experiment for a uniformly labelled apo ^{13}C-^{15}N VHD in solution. The spectrum was processed using a EM window function with 60Hz of line broadening to mimic the linewidth that characterize the signals in ^{13}C-^{13}C DARR ssNMR spectra. The spectrum was recorded at room temperature using a 500MHz Bruker magnet equipped with a triple resonances cryoprobe.

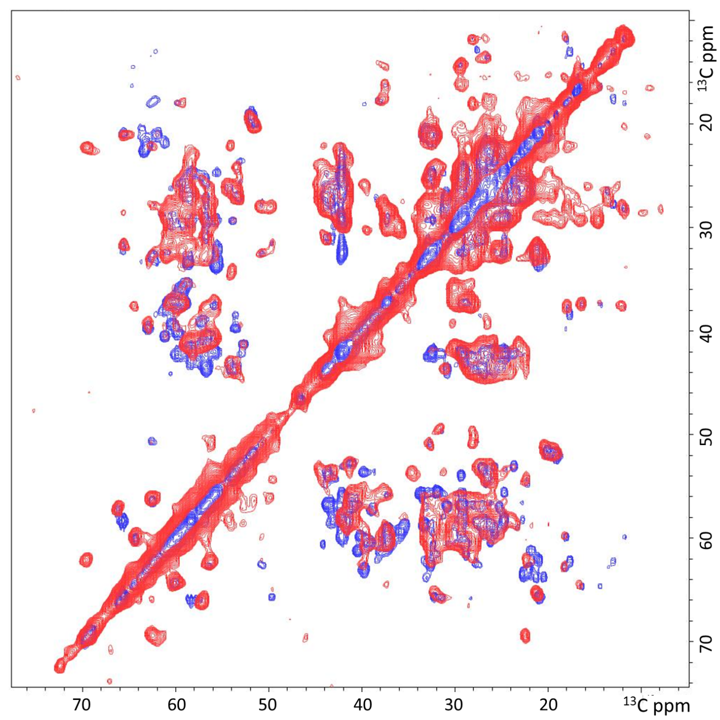

Figure 8.5 Superimposition of ^{13}C-^{13}C DARR spectrum using 20ms mixing time (red spectrum) and the ^{13}C-^{13}C projection from a HCCH TOCSY experiment (blue spectrum). The several resonances that maintain the same chemical shift before and after the event of binding were used to help the assignment of signals in the ssNMR spectrum. Several regions in which resonances are missing are clearly visible.

Numerous resonances were not affected by the binding of VHD to the filaments, maintaining the same chemical shift. On the other hand it is clearly visible that a few regions between the overlapped spectra show cross peaks that do not correspond (Figure 8.6, Figure 8.7, Figure 8.8 and Figure 8.9).

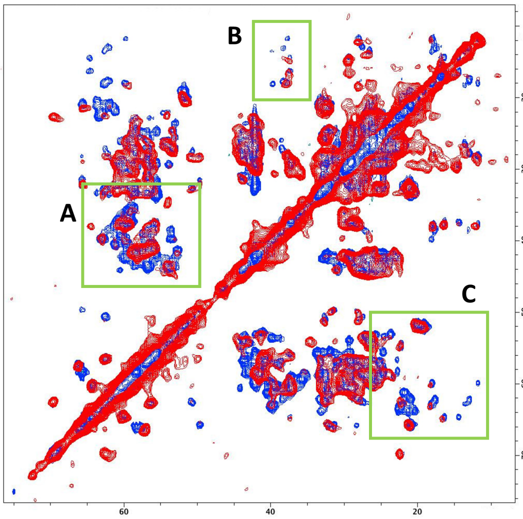

Figure 8.6 Superimposition of ^{13}C-^{13}C DARR spectrum using 20ms mixing time (red spectrum) and the ^{13}C-^{13}C projection from a HCCH TOCSY experiment (blue spectrum). To better characterise the residues that show differences when the protein is in apo and holo state, three regions (encircled by green squares) showing appreciable differences were magnified and analysed.

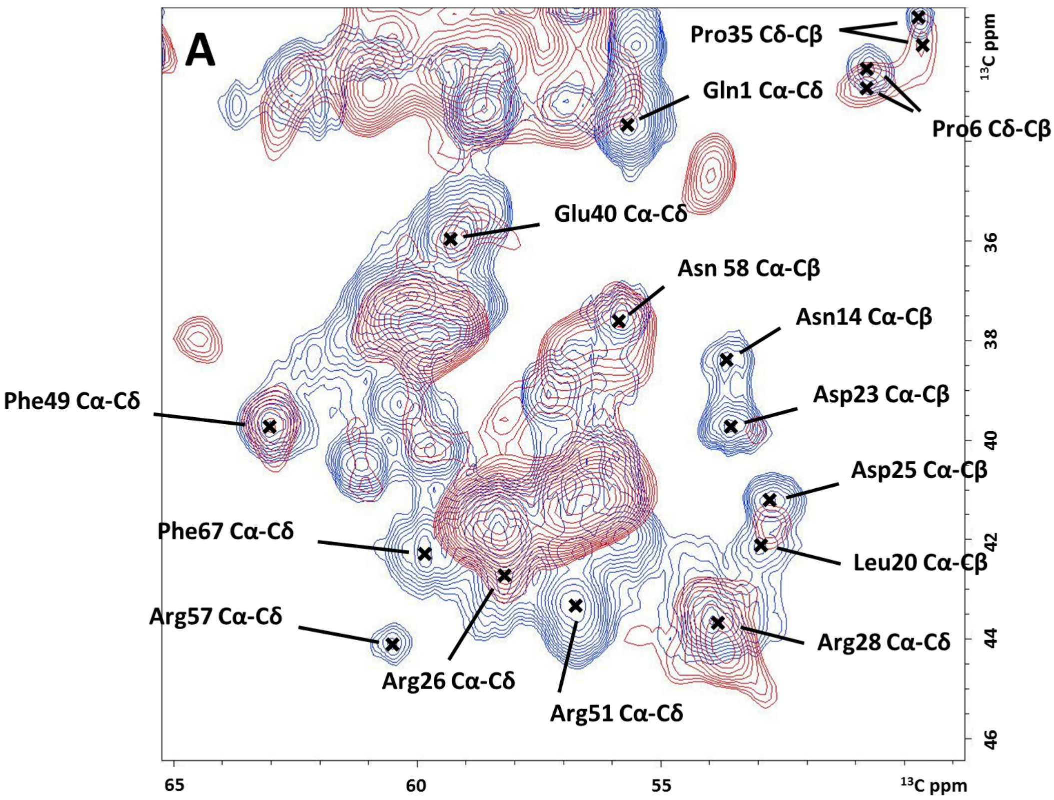

Figure 8.7 Magnification of region A in the superimposition of ^{13}C-^{13}C DARR spectrum using 20ms mixing time (red spectrum) and the ^{13}C-^{13}C projection from a HCCH TOCSY experiment (blue spectrum). It is easy to recognize how many resonances in the DARR spectrum are missing.

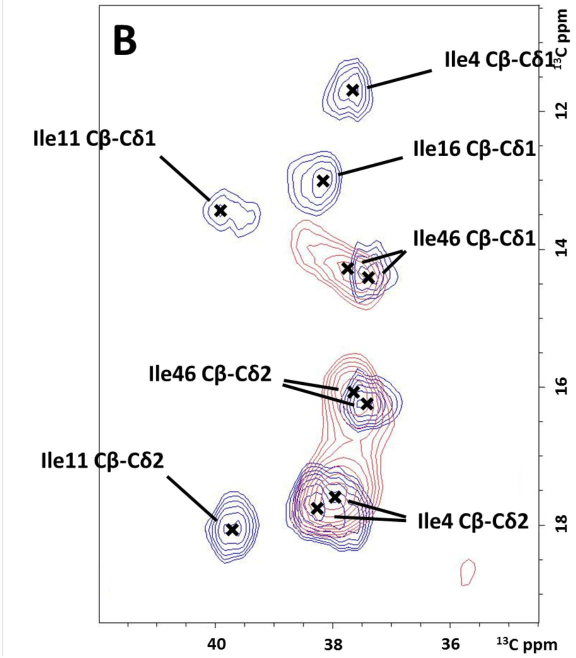

Figure 8.8 Magnification of region B in the superimposition of ^{13}C-^{13}C DARR spectrum using 20ms mixing time (red spectrum) and the ^{13}C-^{13}C projection from a HCCH TOCSY experiment (blue spectrum). This region includes the cross peaks for the sidechains of Isoleucine. It is easy to recognize how many resonances in the DARR spectrum are missing.

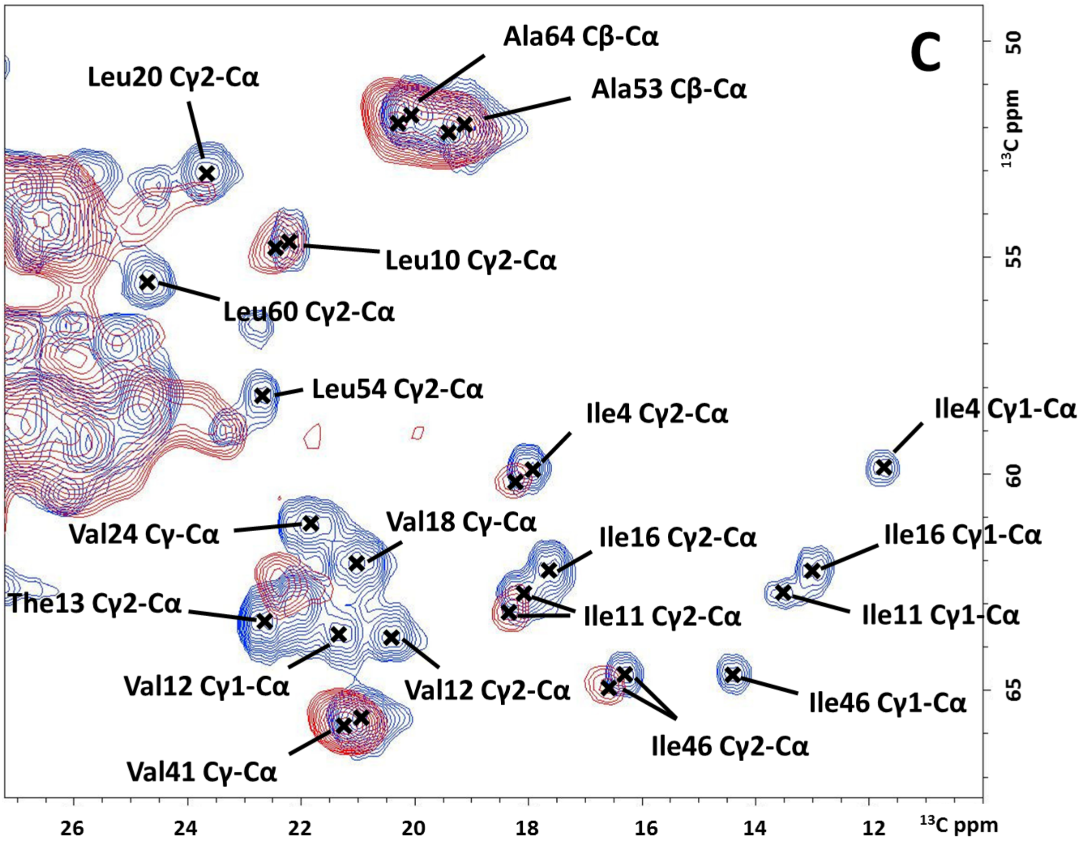

Figure 8.9 Magnification of region C in the superimposition of ^{13}C-^{13}C DARR spectrum using 20ms mixing time (red spectrum) and the ^{13}C-^{13}C projection from a HCCH TOCSY experiment (blue spectrum). This region includes the cross peaks for the sidechains of different aliphatic residues. It is easy to recognize how many resonances in the DARR spectrum are missing.

There could be two reasons for these differences. It could be possible that the dissimilarities are due to changes in the conformation between the apo and the holo protein. In this case there will be changes in the environment of those nuclei that are affected by the structural modification affecting their chemical shift. Otherwise, it can be possible that the different resonances belong to nuclei in a portion of the VHD that is flexible. It is important at this stage to remember that nuclei in flexible regions show a different contact time value for the optimal magnetization transfer in respect of the nuclei in the rigid part of the protein. In all the experiments that were acquired, the contact time was chosen as the time that reflected the value in which the highest total signal intensity was achievable. This means that it could be possible that the different resonances derive from nuclei that have the same chemical shift between the holo and apo VHD but the intensity of those signals is low enough that they cannot be distinguished from the background noise. This could be the case for the region containing the Cα and Cγ cross peak of valine side chains (Figure 8.10).

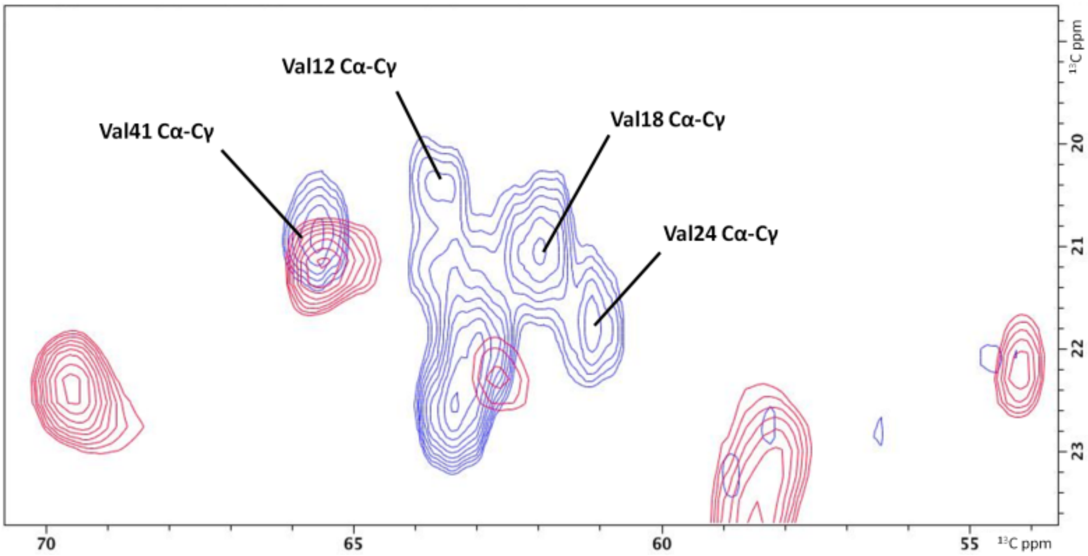

Figure 8.10 Magnification of the region containing the valine CαCγ correlation peaks. The cross peak related to Valine 41 was the only one that was possible to recognise in the overlapping between the ^{13}C-^{13}C DARR spectrum (red spectrum) and ^{13}C-^{13}C projection from a HCCH TOCSY (blue spectrum).

In this region the cross peak related to valine 41 is easily recognizable while the cross peaks for valine 12, 18 and 24 are missing. It can be easily suggested that the differences in this region are related to a possible change in the structure of the VHD after its binding to the filaments. To confirm this suggestion, valine 12, 18 and 24 are located in the same portion of the VHD surface while valine 41 is contained in another portion of the protein (Figure 8.11). Interestingly, the region containing valine 12, 18 and 24 is the same region that contain the residue reported in literature to be crucial for the binding of VHD to actin filaments.

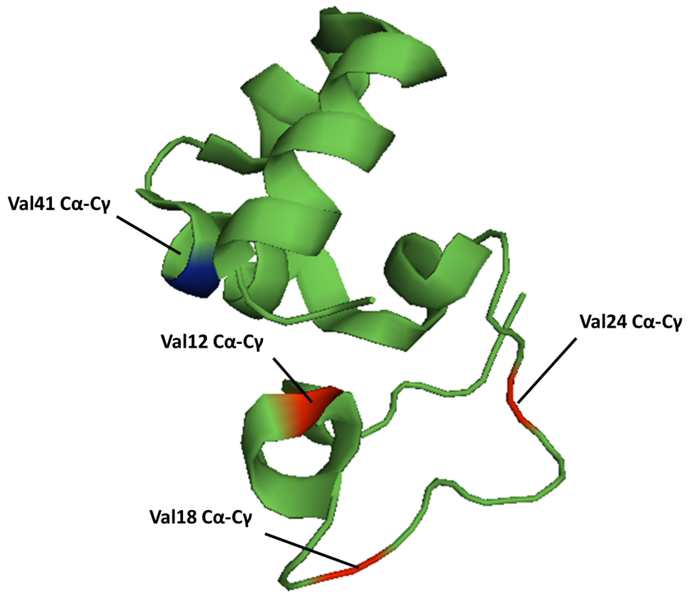

Figure 8.11 Highlighting of the valines position on the VHD ribbon scheme. Valine 12, 18 and 24 (red) share the same region on the surface of VHD while valine 41 (blue) is located in another portion of the protein. The model was generated in PyMol software using VHD structure deposited as on PDB (2L3X).

On the other hand, even more interestingly, valine 12, 18 and 24 are situated in a region of the protein that is more flexible if compared to the region in which is contained valine 41. This it confirmed by the calculation of T1 and T2 for the VHD where it is possible to recognize that the region at the N-terminal is more flexible than the C-terminal region (Figure 8.12). This can suggest that these signals are missing not due to a shift in their resonances due to change in the VHD structure but more likely because the magnetization transfer was not optimized for these nuclei in flexible region. As a consequence the intensity of these resonances can be too low to be recognizable from the background noise.

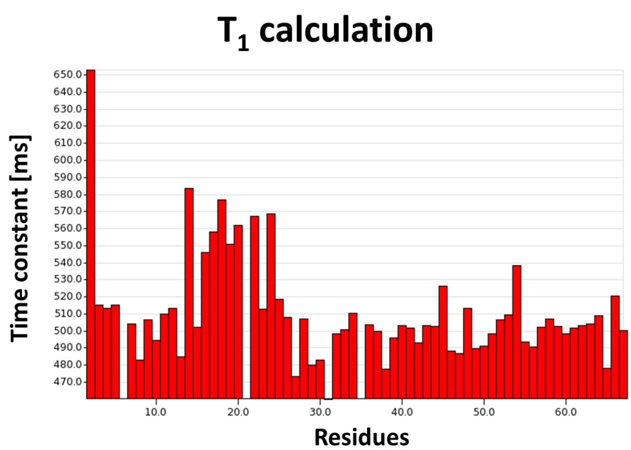

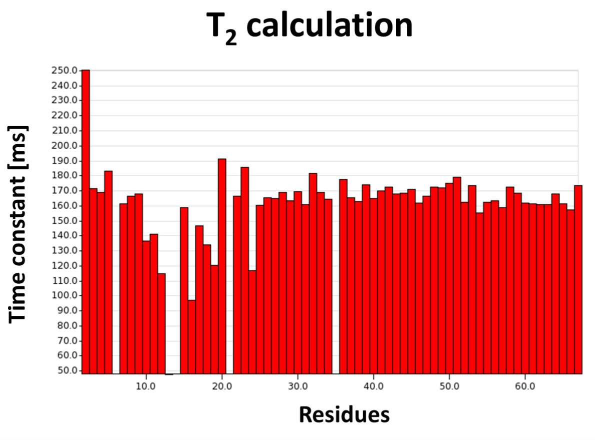

Figure 8.12 T_1 and T_2 calculation for the VHD in solution. It is possible to appreciate how the portion between the residues from 13 to 23 are more flexible in respect the rest of the protein.

To unravel this mystery it would require to acquire a new ^{13}C-^{13}C DARR in which the CP is optimized on these flexible regions but, unfortunately, due to difficulties to obtain time with instruments at high magnetic field it has not been acquired yet.

The spin systems that preserve the same position in both the spectra from the apo and the holo VHD were easily assigned moving the available assignment for the apo VHD to the protein bound to the filaments. Nevertheless, it is important to consider that, in many cases the chemical shift of many atoms in solution is similar and their difference is less than 1ppm. Remembering that the average linewidth of ssNMR signals is often a few ppm, it was often impossible to distinguish the signals of several atoms when they were too close in chemical shift. For example, take into consideration threonine 13 and 27. The chemical shift differences for their C_α, C_β, C_γ and C_O frequencies acquired in solution are all less than 0.8ppm (Table 8.1).

	C	Cα	Cβ	Cγ
Thr13	174,61	63,31	68,92	22,55
Thr27	175,35	62,85	69,44	22,02

Table 8.1 Chemical shift (in ppm) for residues threonine 13 and threonine 27 for a uniformly labelled apo ^{13}C-^{15}N VHD in solution.

When the ssNMR spectrum was analysed, it was possible to recognize only one spin system in which both the residues were likely included considering the cross peak linewidth of near 2ppm (Figure 8.13) twice the difference seen in solution.

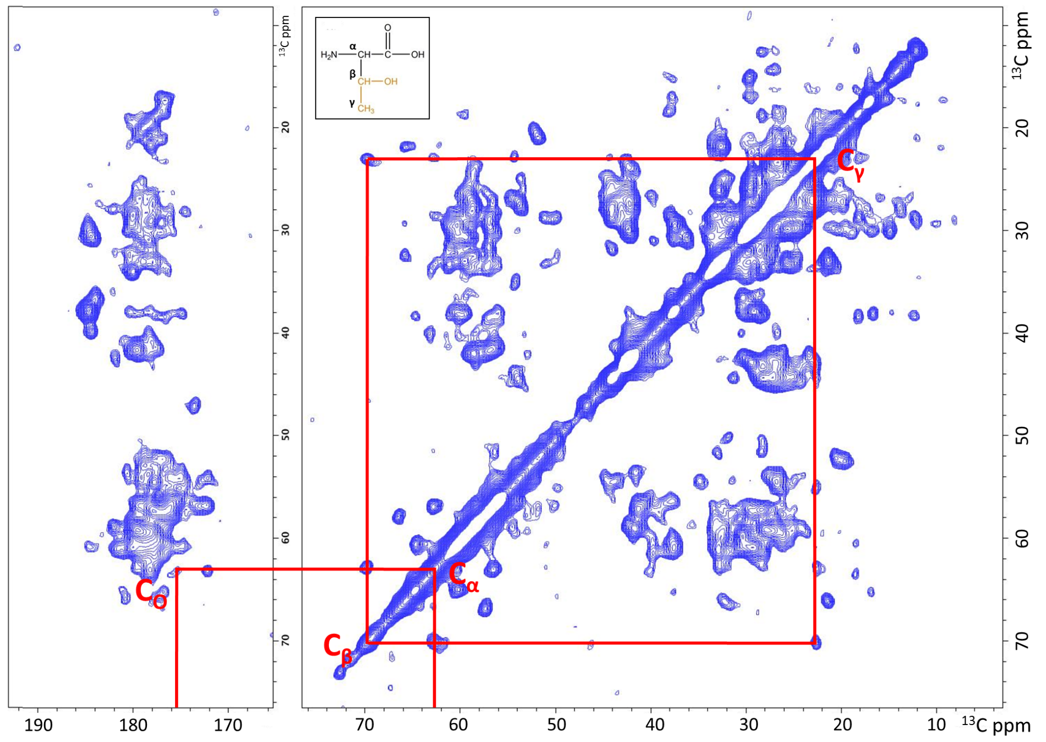

Figure 8.13 Assignment of spin system for threonine 13 and 27 in ^{13}C-^{13}C DARR (20 ms mixing time). The signals from the two residues were overlapped and an assignment as separate spin system was not achievable. The spectrum was acquired at 278K, 10kHz spinning rate using a 500MHz Bruker magnet equipped with triple resonance 4mm e-free probe.

	C	Cα	Cβ	Cγ
Thr13, Thr27	175.66	62.5	69.11	21.92

Table 8.2 Chemical shift (in ppm) for residues threonine 13 and threonine 27 for a uniformly labelled ^{13}C-^{15}N VHD bound to actin filaments.

On the other hand, the ssNMR experiment helped to achieve information that would have required specific optimized experiments to be collected in solution NMR [96]. For example, consider the eight glutamate residues, Glu30, Glu36, Glu37, Glu40, Glu47 and Glu48 contained in VHD sequence. They were completely characterized in solution with the only exception of the carbonyl C_δ (Table 8.3).

	C	Cα	Cβ	Cγ	Cδ
Glu30	177,12	58,47	27,38	33,12	-
Glu36	179,68	60,63	28,66	37,14	-
Glu37	177,93	60,23	29,87	39,16	-
Glu40	178,03	59,23	29,73	35,75	-
Glu47	179,53	59,93	28,65	36,94	-
Glu48	179,04	58,83	29,85	37,1	-

Table 8.3 Chemical shift (in ppm) of glutamate residues as performed on apo ^{13}C-^{15}N VHD in solution.

Similarly for the assignment of threonine most of the resonances were overlapped and it was not possible to define the single glutamate spin systems. Nevertheless, using the assignment performed in solution, it was possible to define the $C_\beta C_\gamma$ systems for most of them (Figure 8.14) and, using the C_γ shift calculated it was also possible to move further the assignment and identify the $C_\gamma C_\delta$ correlation for most of them (Figure 8.15 and Table 8.4).

	Cβ	Cγ	Cδ
Glu30	-	32.88	183.4
Glu36	28.35629	36.6	184.25
Glu37	29.963	38.94	184.05
Glu40	29.65744	35.66	183.36
Glu47	28.35629	36.6	184.25
Glu48	-	36.6	184.25

Table 8.4 Chemical shift (in ppm) assigned for glutamate residue performed on VHD complex to filaments.

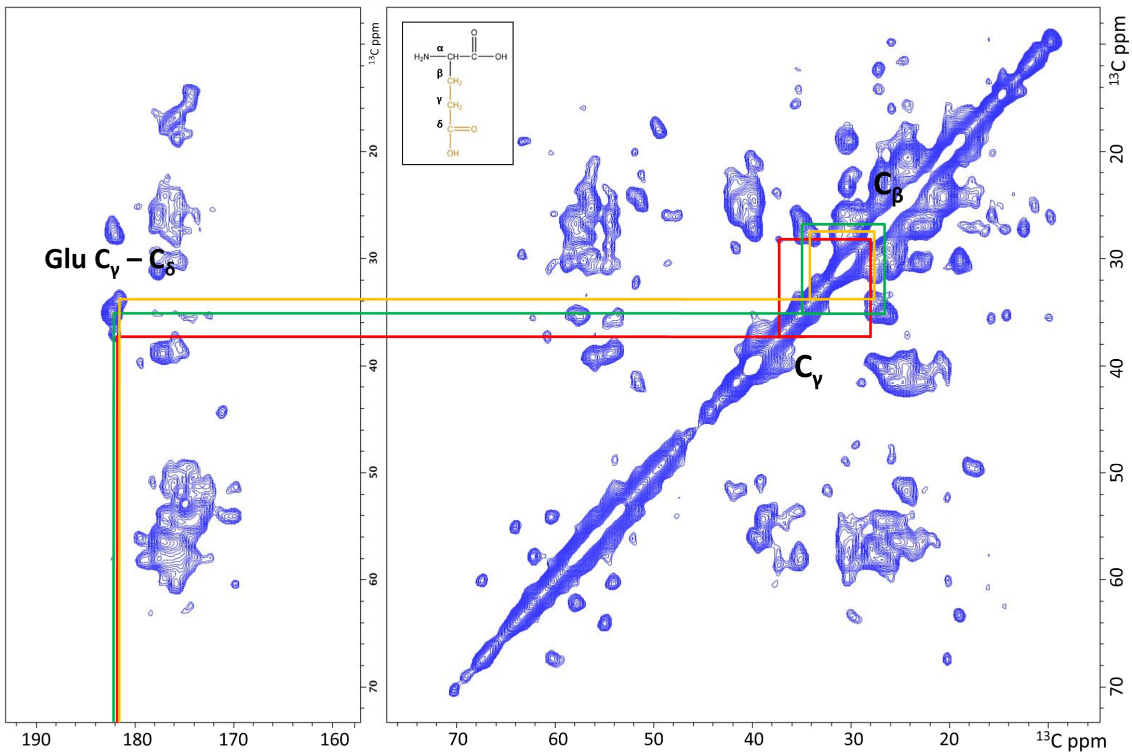

Figure 8.14 Partial assignment of $C_\beta C_\gamma$ and $C_\gamma C_\delta$ correlations for glutamate residues performed on a ^{13}C-^{15}N VHD bound to filaments (the green lines represent the spin system of Glu36, 47 and 48, yellow lines the spin system of Glu40 and red lines the spin system of Glu37). The spectrum was acquired at 278K, 10kHz spinning rate using a 500MHz Bruker magnets equipped with triple resonances 4mm e-free probe.

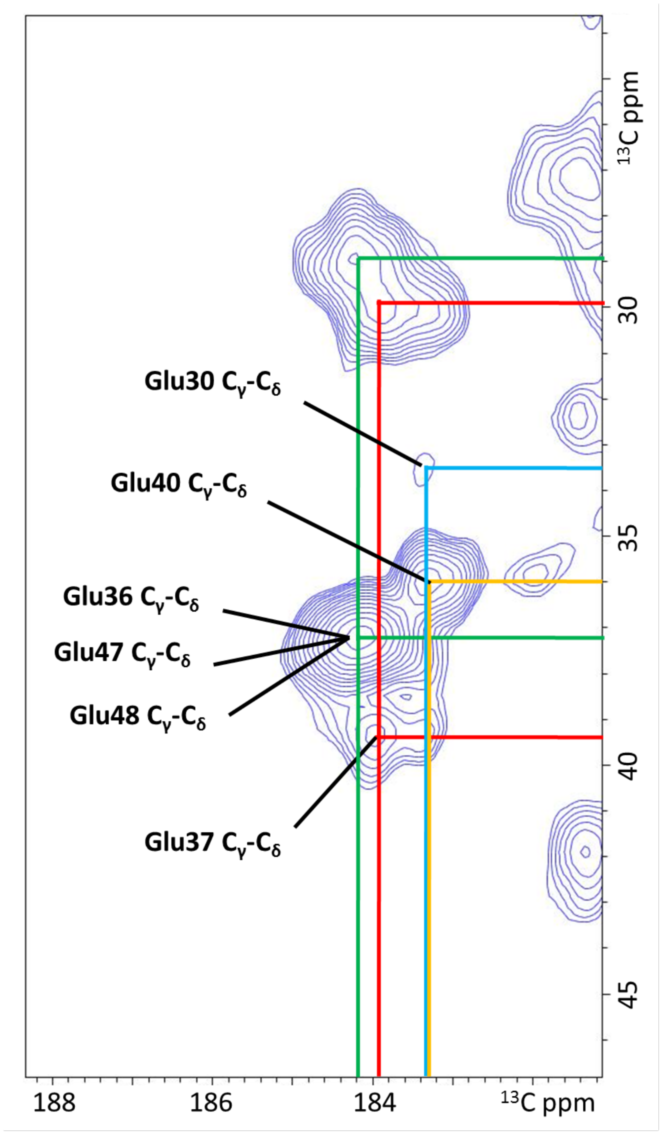

Figure 8.15 Magnification of CγCδ correlation region for glutamate residues. The assignment of the resonance for all the carbonyl Cδ of glutamate was easily performed using this experiment.

Unfortunately, most of the signals were overlapped and it was impossible to define their assignment. ^{13}C-^{13}C DARR with increased mixing time of 100ms and 250ms were acquired (Figure 8.17 and Figure 8.19) and new resonances were identified using the long distance correlations arising. Similarly to the spreading of magnetization in NOESY experiments, the mixing time applied during the ^{13}C-^{13}C recoupling can reveal different correlations depending in its length [62]. While using very short mixing time (20ms to 40ms) reveals atoms very close in space (preferentially the neighbor atoms), when a longer mixing time is applied (100ms to 300ms) it is possible to reveal longer correlation through the space but, in some cases, losing the shorter correlation. Consider the cross peak region for the aromatic-aliphatic carbon correlations in VHD ^{13}C-^{13}C spectra to better understand how the magnetization is spread increasing the mixing time. When

20ms were used to recouple the ^{13}C-^{13}C dipolar coupling only noise was revealed, but increasing the mixing time different ^{13}C-^{13}C correlations were preferentially observed (Figure 8.16).

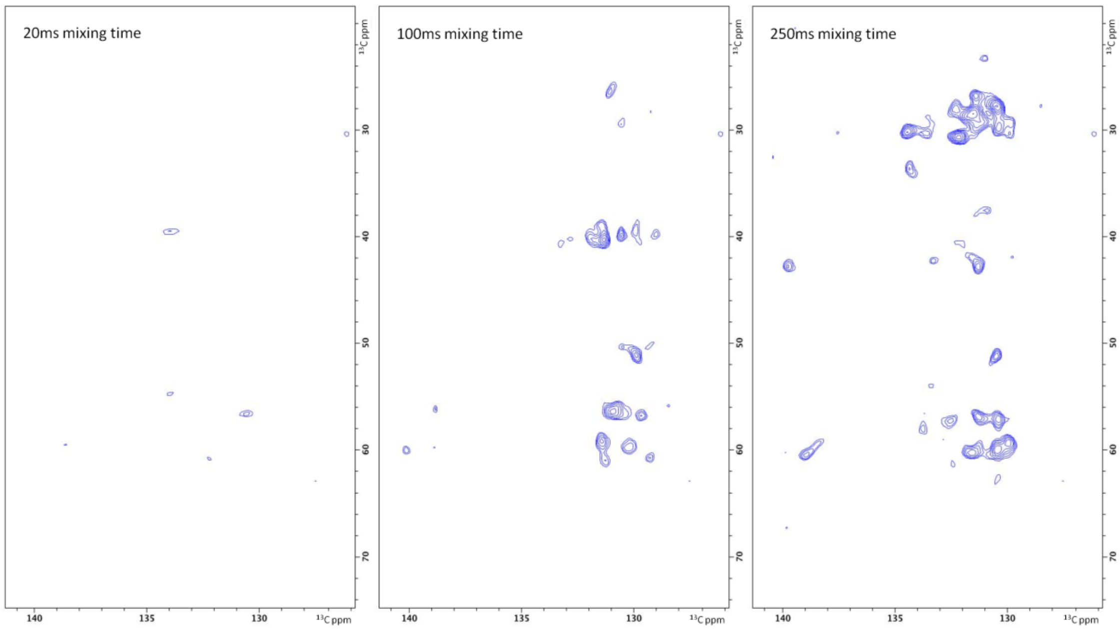

Figure 8.16 Effect of different mixing time on the cross peak region for the aromatic-aliphatic carbon correlations. Increasing the length for the recoupling event more correlations can be observed. All the spectra were recorded at 278K, 10kHz spinning rate using a 500MHz Bruker magnets equipped with triple resonances 4mm e-free probe.

Unfortunately, most of the signals were overlapped also in these spectra and a proper assignment of these frequencies was not possible. Nevertheless, these experiments acquired with long mixing time will be very useful once the assignment is done because they can be analysed again to collect distance restrains for structural calculation. The magnetization transfer in DARR experiments is through space (similarly to the NOESY experiments) instead of through chemical bound (similarly to COSY or TOCSY experiments) and both the identification of inter-residue cross peaks and the analysis of their intensity can lead to distance information.

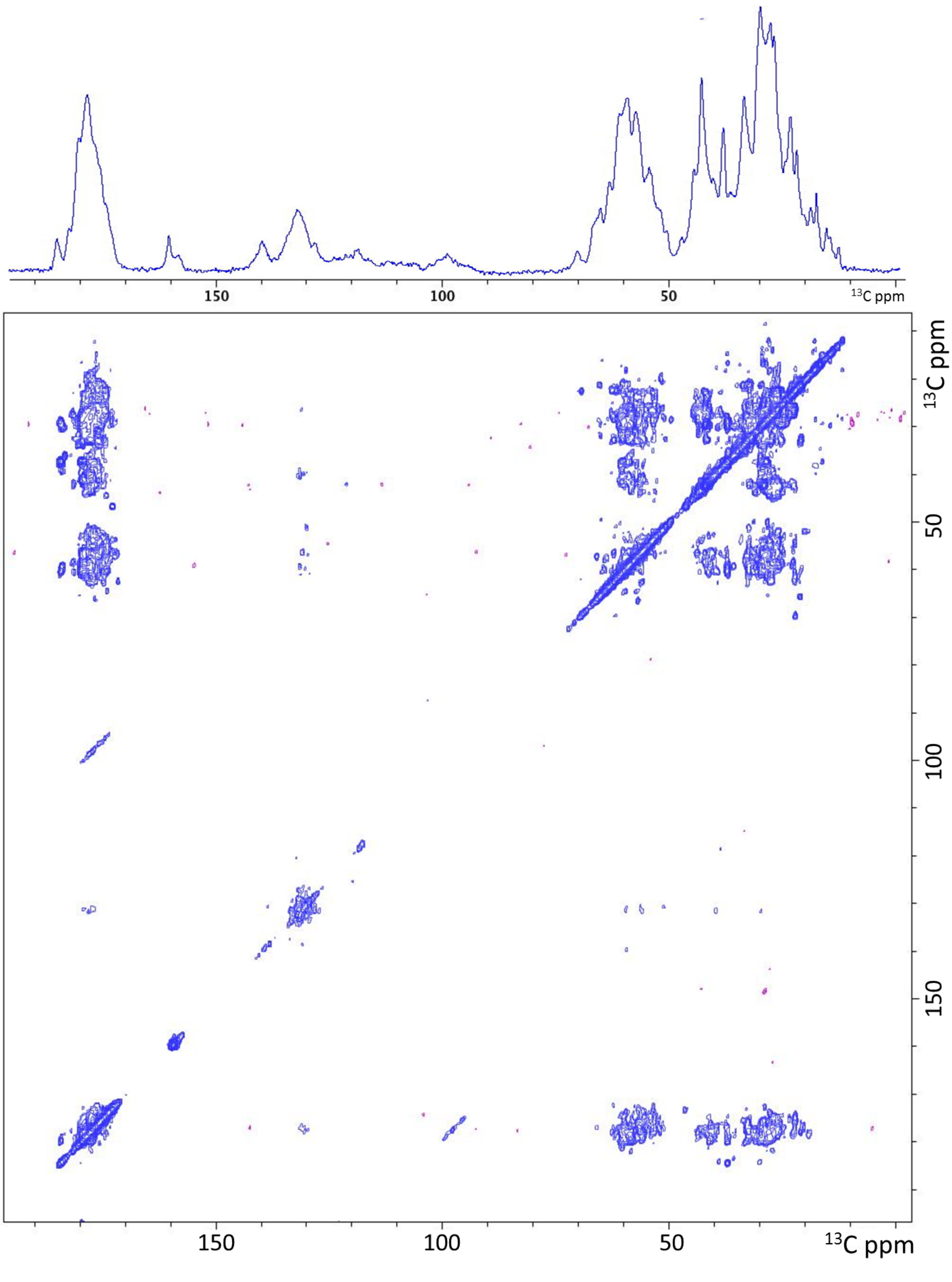

Figure 8.17 ^{13}C-^{13}C DARR spectrum for a uniformly labelled ^{13}C-^{15}N VHD bound to actin filaments acquired setting 100ms mixing time during the ^{13}C-^{13}C recoupling. New spare resonances were identified and it was possible to recognize long range correlations among the same spin systems while the overlapped regions became more crowded. In the region for the aromatic side chains it was possible to identify some resonances. The spectrum was acquired at 278K, 10kHz spinning rate using a 500MHz Bruker magnet equipped with triple resonance 4mm e-free probe.

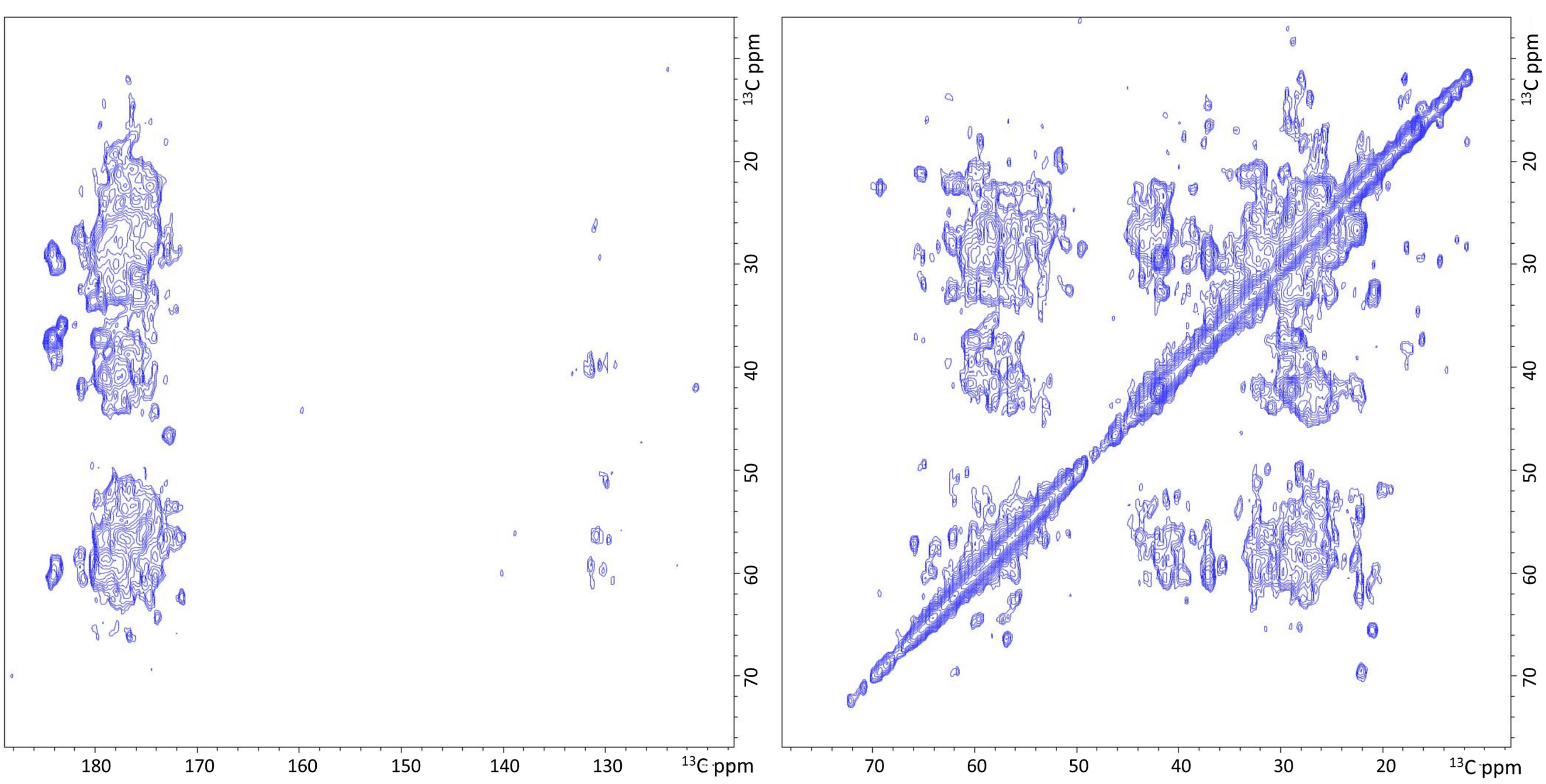

Figure 8.18 Magnification of carbonyl and aromatic cross peak region to aliphatic carbons (left panel) and aliphatic region (right panel) of a ^{13}C-^{13}C DARR spectrum acquired on a uniformly ^{13}C-^{15}N VHD bound to actin filaments using 100ms mixing time. The spectrum was recorded at 278K, 10kHz spinning rate in a 500MHz Bruker magnet equipped with a triple resonance e-free probe.

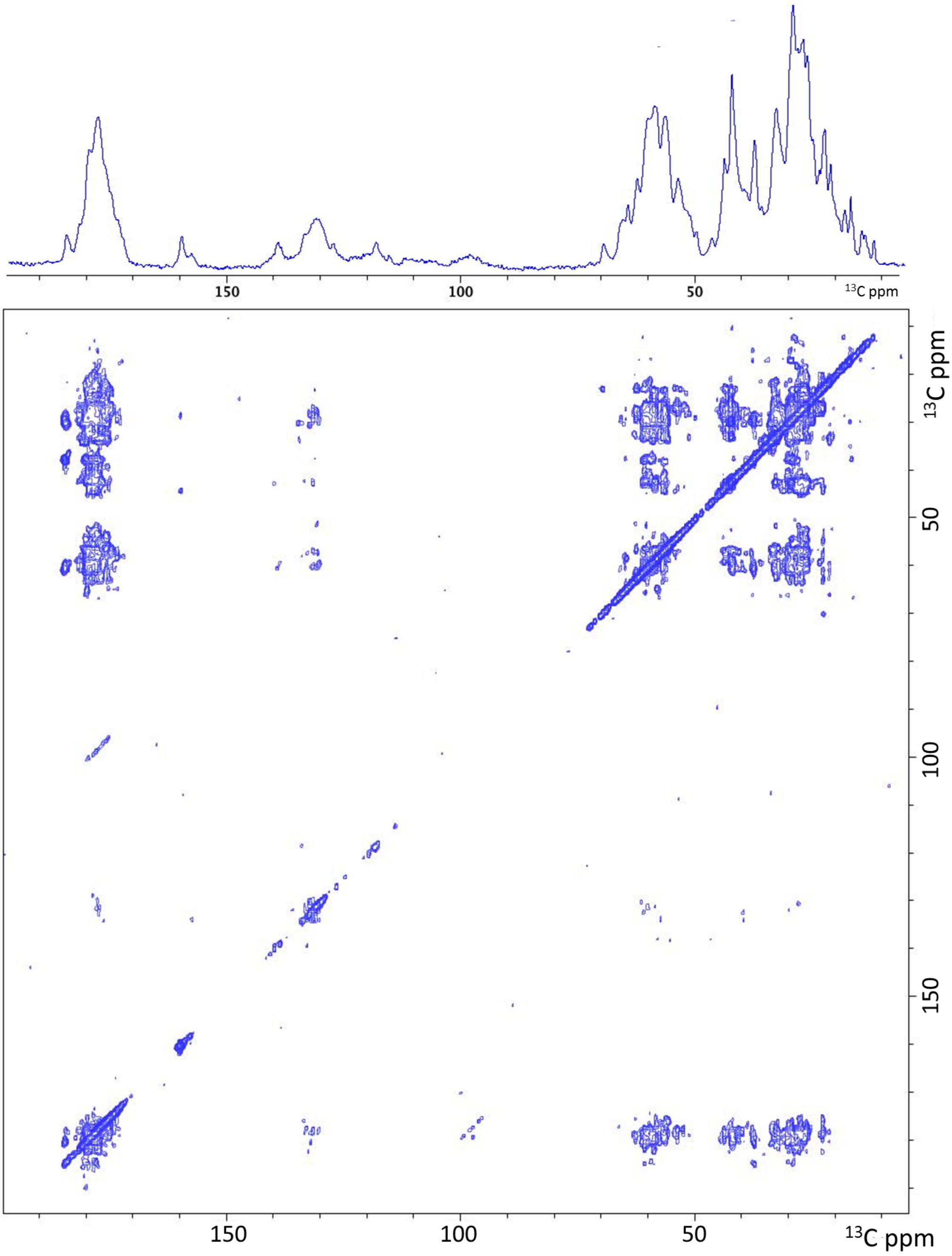

Figure 8.19 ^{13}C-^{13}C DARR spectrum for a uniformly labelled ^{13}C-^{15}N VHD bound to actin filaments acquired setting 250ms mixing time during the ^{13}C-^{13}C recoupling. The long mixing time did not help for the assignment due to fact that the signals become overlapped in almost all the regions of the spectrum. On the other hand, it was possible to start the analysis of the resonances in the region of aromatic residues side chains. The spectrum was acquired at 278K, 10kHz spinning rate using a 500MHz Bruker magnet equipped with triple resonance 4mm e-free probe.

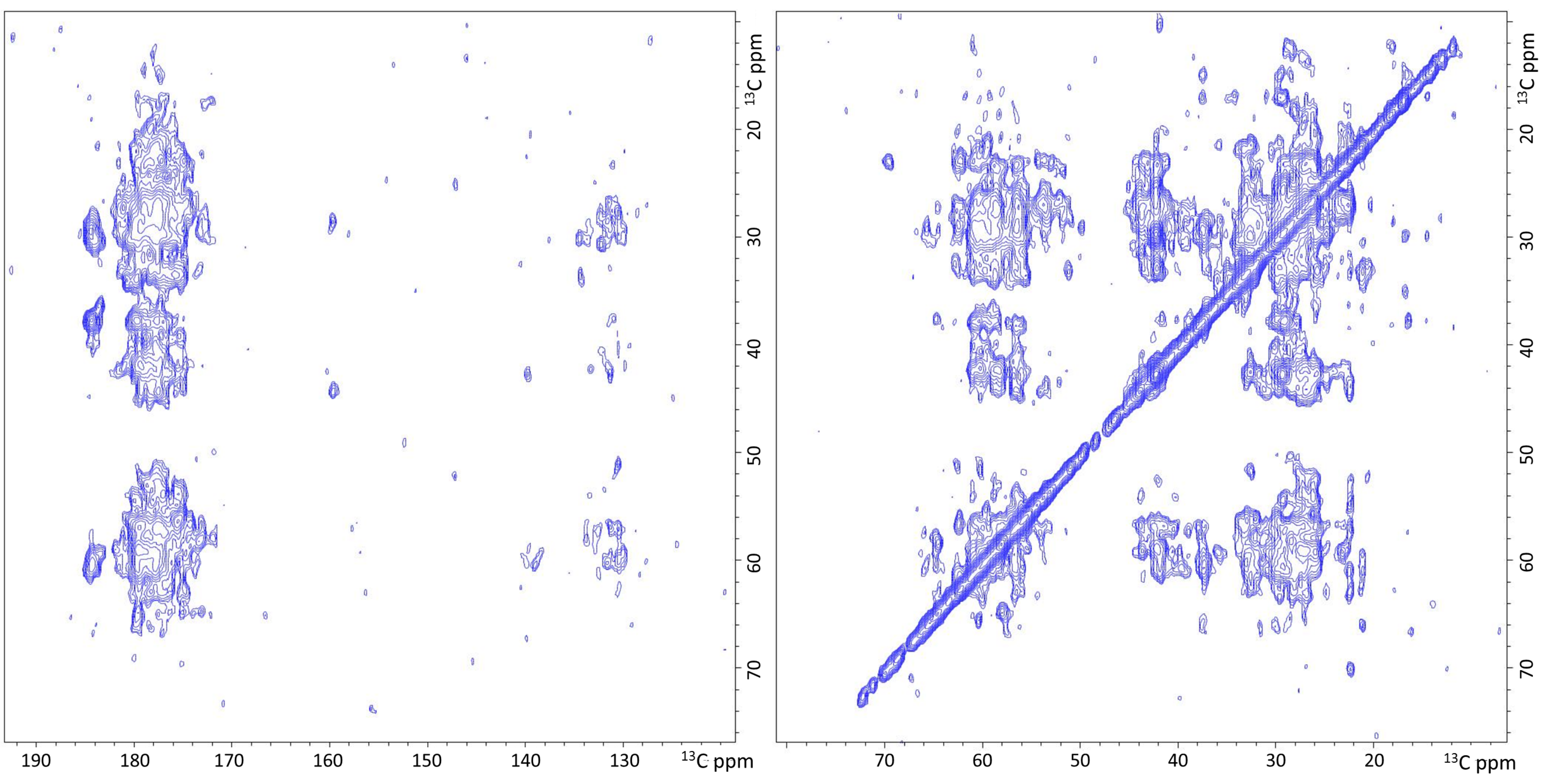

Figure 8.20 Magnification of carbonyl and aromatic cross peak region to aliphatic carbons (left panel) and aliphatic region (right panel) of a ^{13}C-^{13}C DARR spectrum acquired on a uniformly ^{13}C-^{15}N VHD bound to actin filaments using 250ms mixing time. It is interesting to notice the presence of cross peak generating from the Cζ of arginine residues (near 158ppm) that correlates to Cδ and Cγ in the aliphatic region. The spectrum was recorded at 278K, 10kHz spinning rate in a 500MHz Bruker magnets equipped with a triple resonances e-free probe.

To resolve the overlapped regions it was necessary to decrease the number of resonances, rather than increase the length of mixing time looking for new long-range correlations, two uniformly ^{15}N but selectively ^{13}C labelled VHD (originating from the addition of one of the two different isotopes of glycerol, 4.1.5 were expressed and cosedimented with actin filaments. The labeling patterns arising from the expression in presence of 1,3 ^{13}C glycerol ([1,3-^{13}C]-^{15}N VHD) and 2 ^{13}C glycerol ([2-^{13}C]-^{15}N VHD) were extensively discussed in 5.2.2 (Figure 8.21).

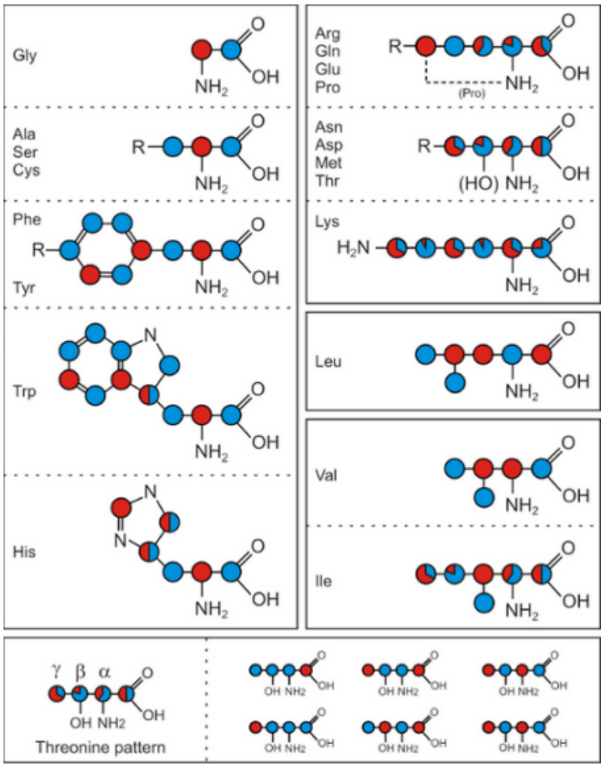

Figure 8.21 Schematic representation of the effective ^{13}C labeling obtained by protein expression in *E. coli* BL21 (DE3). The blue color corresponds to the ^{13}C labeling pattern obtained adding [1,3-^{13}C]glycerol to the minimal medium while in red is reported the one arising adding [2-^{13}C]glycerol [84].

Analyzing the pattern arising from the different addition of the glycerol isotopes it was possible to predict the eventual number of resonances in the spectrum and to know the best mixing time to setup. The limited access to instruments at high magnetic field (500MHz or 850MHz) made it crucial to make this a priori estimation. While it seemed appropriate to acquire long mixing time for both the preparations it was assumed that only cross peaks from the C_α-C_β of valine and C_β-C_γ of leucine residues were to be identified using short mixing time for the [2-^{13}C]-^{15}N VHD in the complex. Two dataset using 20ms and 100ms were recorded on [1,3-^{13}C]-^{15}N VHD-F.actin complex (Figure 8.22 and Figure 8.24) while only one dataset at 100ms were acquired for the opposite labeling ([2-^{13}C]-^{15}N VHD) (Figure 8.26). A shorter dataset of 13h (160scan for 80 increments and 20ms mixing time) was acquired to confirm the prediction made (Figure

8.28). It is important to keep in mind that these selective labeling schemes lead to spectra in which most of the correlation peaks are lost. Consider for example the amino acid glycine and its labeling using this protocol. Depending on the labeling only one carbon atom is enriched each time and, as result, it easy to anticipate that the intra-residue C_OC_α cross peak cannot be ever identified for this amino acid. For this reason, a continuous referring to the spectra recorded on the uniformly ^{13}C-^{15}N VHD bound to filaments and a comparison between the spectra from these labeling schemes is crucial to properly interpret and assign the resonances in them.

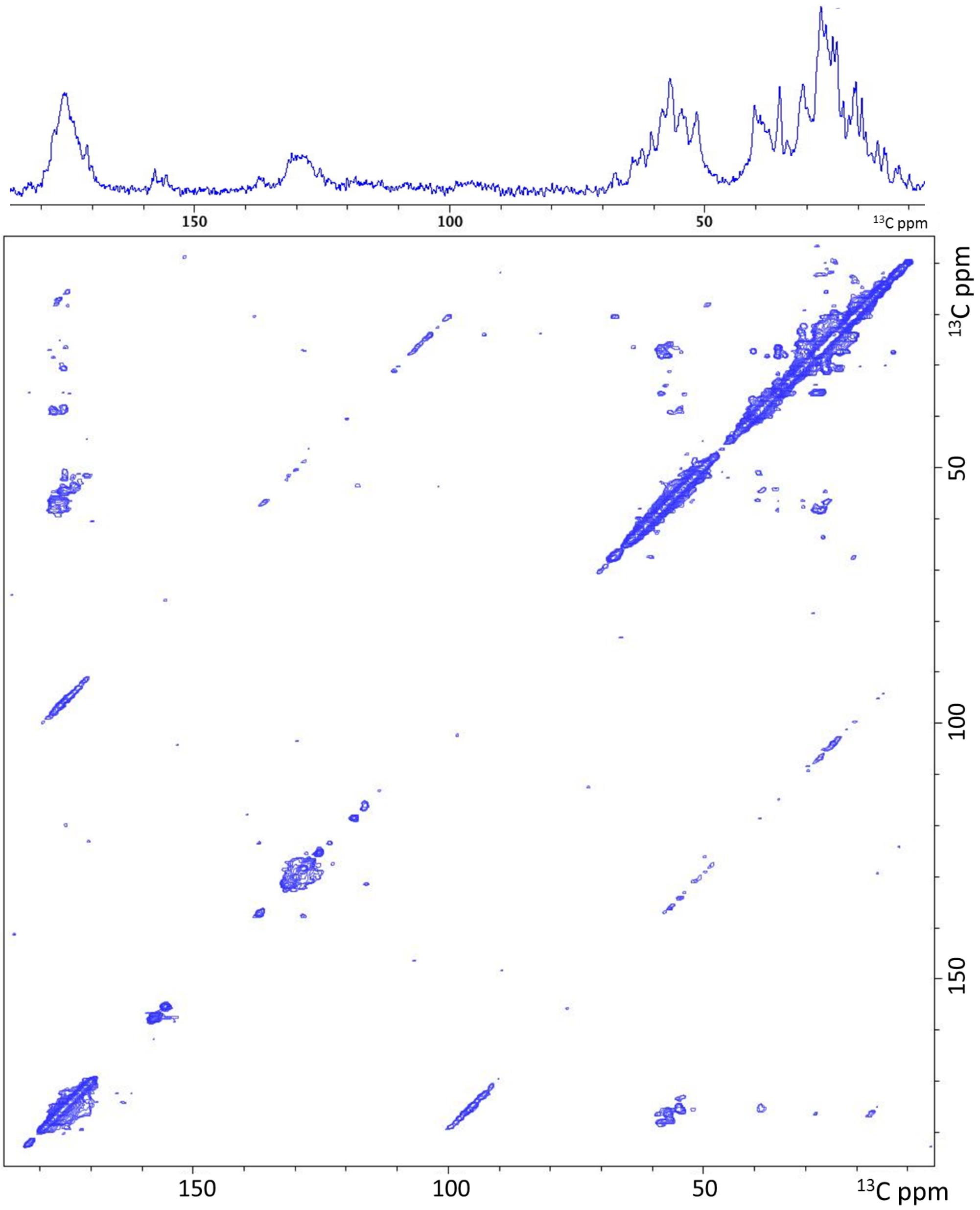

Figure 8.22 ^{13}C-^{13}C DARR spectrum for [1,3-^{13}C]-^{15}N VHD bound to actin filaments acquired with 20ms mixing time. The lower number of resonances in the spectrum allowed the assignment of several resonances. It is important to remember that this labeling cannot reveal an entire amino acid spin system and for a proper assignment it has to be analysed coupled with the spectrum acquired for the other carbon labeling (uniformly and selective). The spectrum was acquired at 278K, 10kHz spinning rate using a 500MHz Bruker magnet equipped with triple resonance 4mm e-free probe.

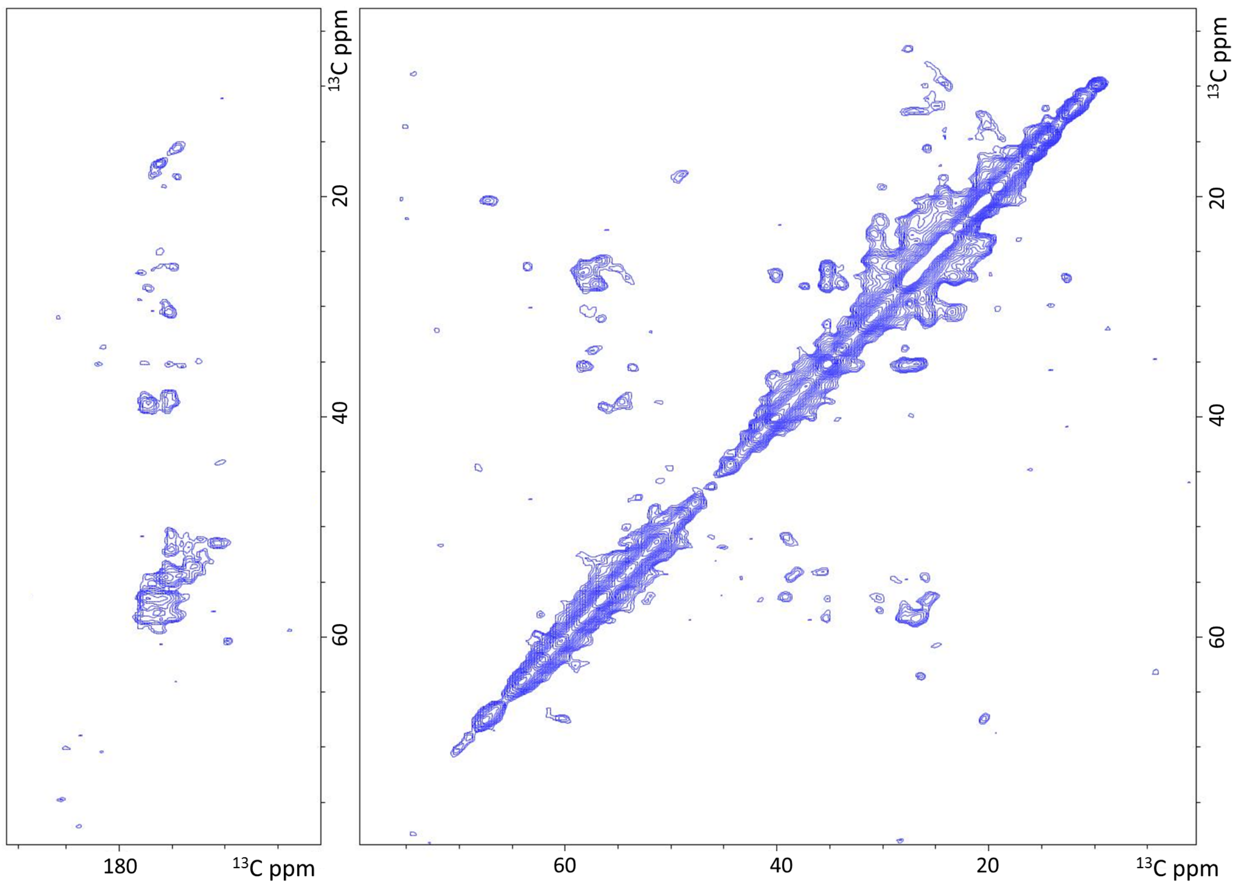

Figure 8.23 Magnification of carbonyl and aromatic cross peak region to aliphatic carbons (left panel) and aliphatic region (right panel) of a ^{13}C-^{13}C DARR spectrum acquired on a uniformly [1,3-^{13}C]-^{15}N VHD bound to actin filaments using 20ms mixing time. Few correlations were observable in the spectrum as expected using this selective labeling. The spectrum was recorded at 278K, 10kHz spinning rate in a 500MHz Bruker magnet equipped with a triple resonance e-free probe.

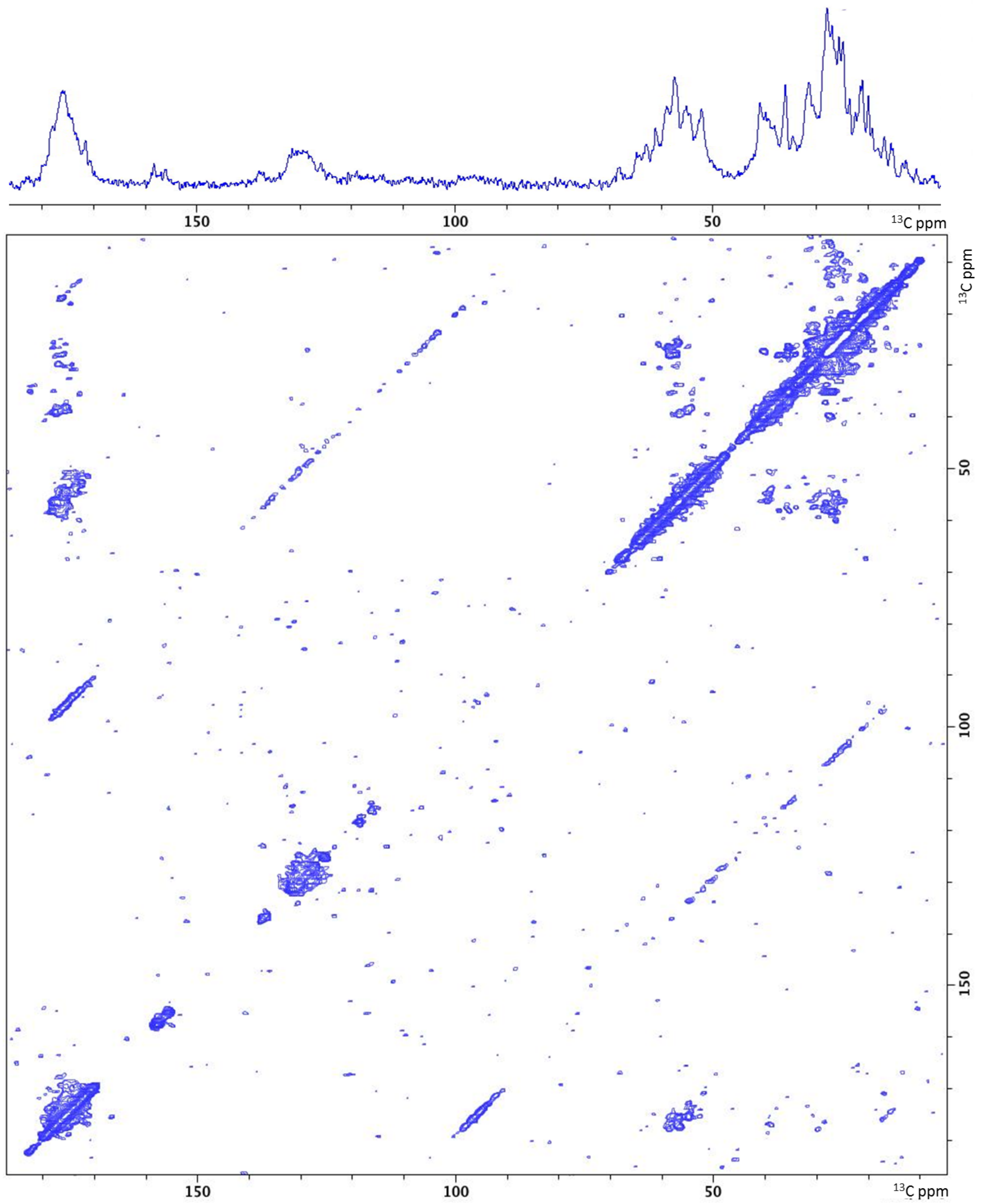

Figure 8.24 ^{13}C-^{13}C DARR spectrum for [1,3-^{13}C]-^{15}N VHD bound to actin filaments acquired with 100ms mixing time. Several spare resonances were observable in this spectrum and some were suggested to arise from inter-residue correlations. Nevertheless, the complexity of the overlapped regions made impossible to assign most of the signals. The spectrum was acquired at 278K, 10kHz spinning rate using a 500MHz Bruker magnet equipped with triple resonance 4mm e-free probe.

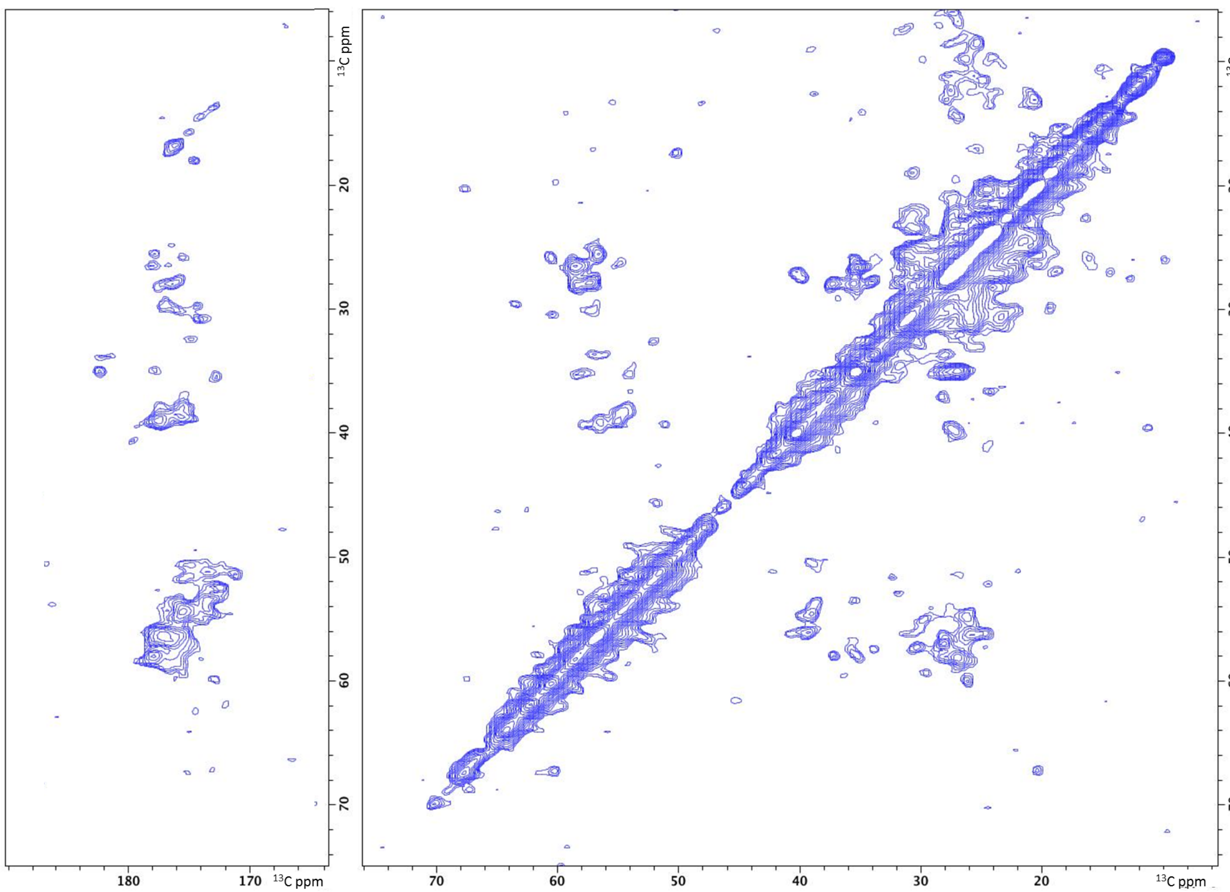

Figure 8.25 Magnification of carbonyl and aromatic cross peak region to aliphatic carbons (left panel) and aliphatic region (right panel) of a ^{13}C-^{13}C DARR spectrum acquired on a uniformly [1,3-^{13}C]-^{15}N VHD bound to actin filaments using 100ms mixing time. More correlations (likely inter-residues) were observable in the spectrum increasing the mixing time. The spectrum was recorded at 278K, 10kHz spinning rate in a 500MHz Bruker magnet equipped with a triple resonance e-free probe.

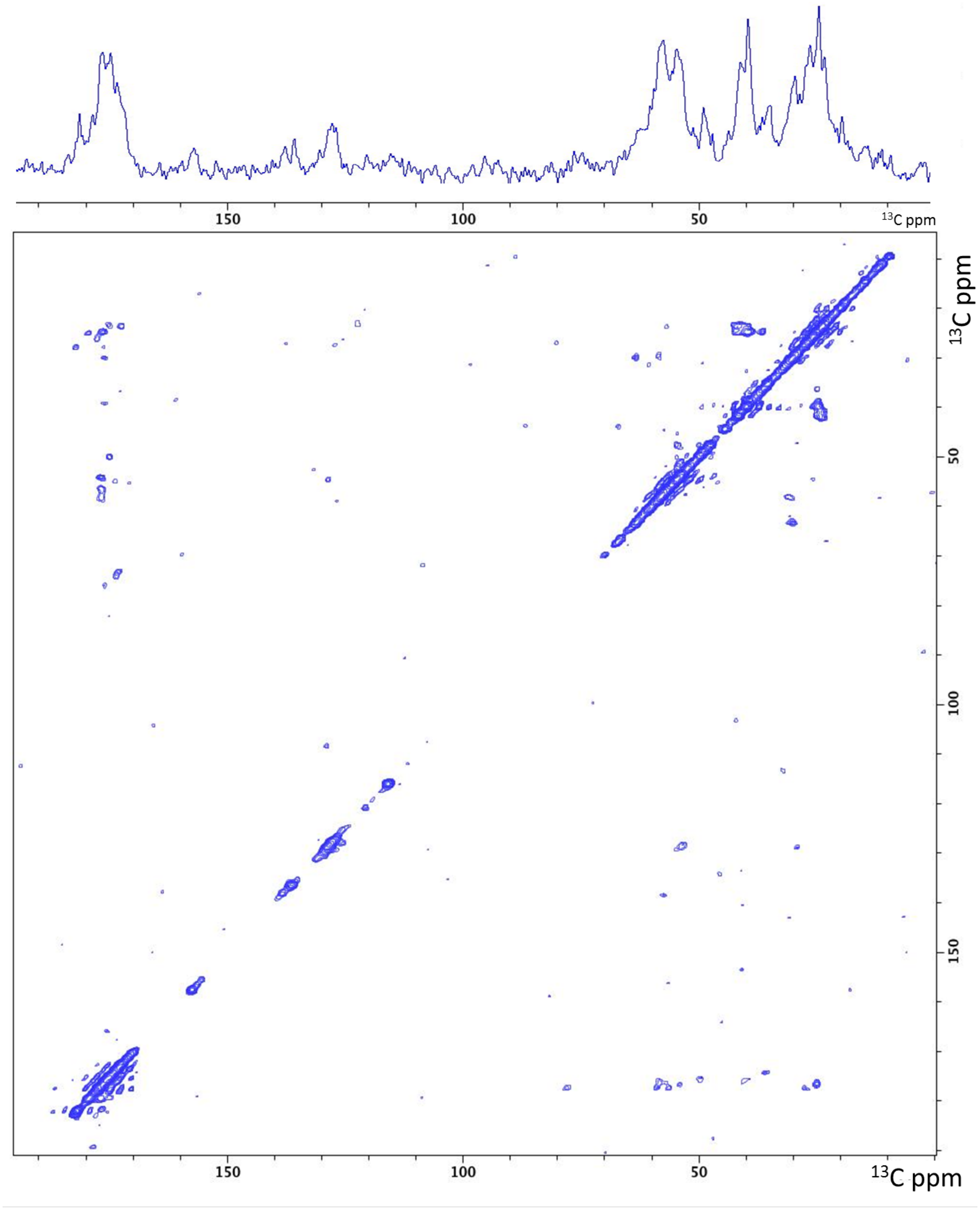

Figure 8.26 ^{13}C-^{13}C DARR spectrum for [2-^{13}C]-^{15}N VHD bound to actin filaments acquired with 100ms mixing time. Their analysis of this spectrum in correlation to the spectra in Figure 8.2 allowed the assignment of the majority of the resonances contained especially for the region correspondent to the cross peaks among carbonyl and aliphatic carbons. The spectrum was acquired at 278K, 10kHz spinning rate using a 500MHz Bruker magnet equipped with triple resonance 4mm e-free probe.

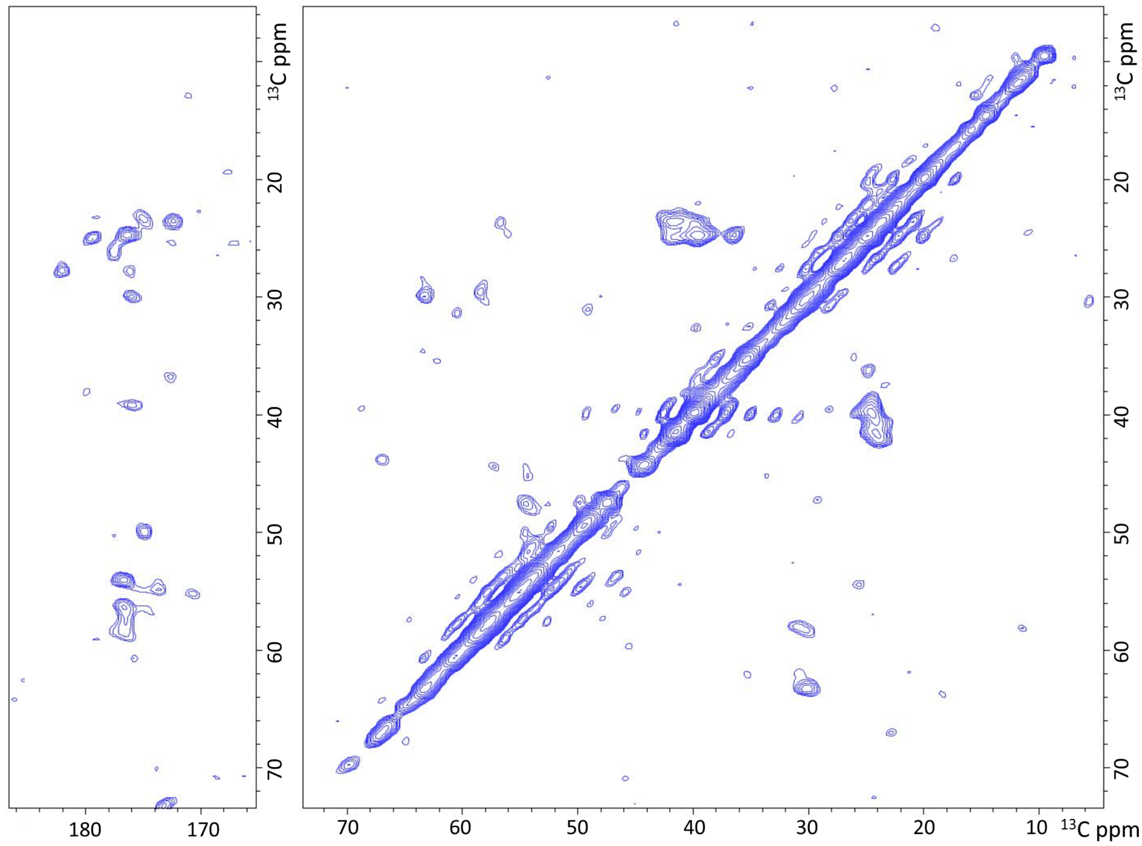

Figure 8.27 Magnification of carbonyl and aromatic cross peak region to aliphatic carbons (left panel) and aliphatic region (right panel) of a ^{13}C-^{13}C DARR spectrum acquired on a uniformly [2-^{13}C]-^{15}N VHD bound to actin filaments using 100ms mixing time. As expected few correlations were observable but still, their assignment was not possible. The spectrum was recorded at 278K, 10kHz spinning rate in a 500MHz Bruker magnet equipped with a triple resonance e-free probe.

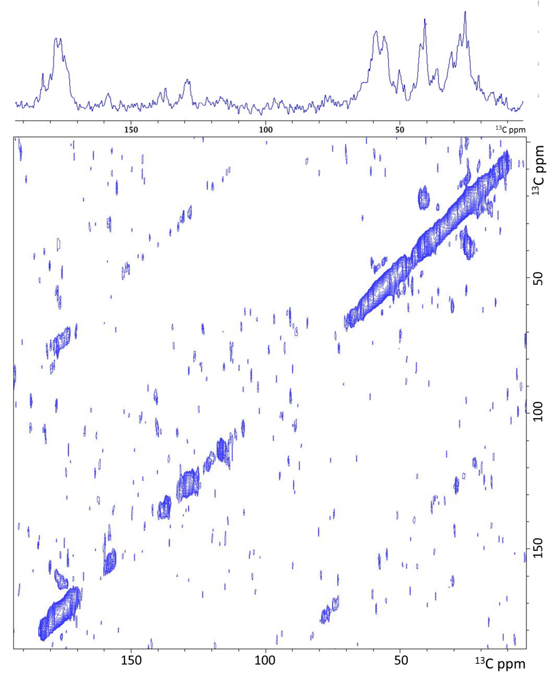

Figure 8.28 ^{13}C-^{13}C DARR spectrum for [2-^{13}C]-^{15}N VHD bound to actin filaments acquired with 20ms mixing time. As expecting looking at the pattern of labeling originating using 2-^{13}C glycerol as carbon source, only the cross peaks originating from $C_{\beta}C_{\gamma}$ of leucine and isoleucine are recognizable. Strangely, it was not possible to recognize the cross peaks for $C_{\alpha}C_{\beta}$ of valine. The spectrum was acquired at 278K, 10kHz spinning rate using a 500MHz Bruker magnet equipped with triple resonance 4mm e-free probe.

The reduced number of resonances helped to assign other few frequencies but, still, it was not possible to link most of them to a unique atom. To complete the assignment it became crucial to find a protocol to resolve the overlapped regions and it was proposed to spread the carbon signals through the nitrogen dimension. A different approach based on the acquisition of C_xN correlation spectra on a uniformly labelled ^{13}C-^{15}N VHD bound to filaments was then attempted. For the assignment of the backbone, it is possible to acquire two versions of C-N correlation spectra, C_ON and $C_\alpha N$ experiments. In a C_ON spectrum, the C_O from residue *n* and the N from residue *n-1* were correlated while in $C_\alpha N$ spectra the C_α and N from the same residue *n* were linked. Prior their acquisition, $(^{15}NH_4)_2SO_4$ powder was acquired in order to use this spectrum as ^{15}N reference. The two ammonium groups in this sulphate salt generates a sharp doublet centred at 24.1ppm at room temperature [97]. The magnetization in a C_xN experiment CP based is generated exciting protons and then it is moved to the nitrogen dimension using a CP block of pulses. A second CP moves the magnetization to carbon dimension where it is recorded. The optimization of two CP blocks of pulses proved to be essential for these sequences. A simple ^{15}N CP MAS experiments was used to optimize the first transfer of magnetization from ^1H to ^{15}N (Figure 8.29). It was also useful to reference the ^{15}N dimension for the C_xN spectra to zero and to have preliminary rough data on the range of chemical shifts that characterize guanidine and amine group from the side chain of, respectively, arginine and lysine residues when VHD is bound to actin filaments. Nevertheless, it also showed a poor signal to noise ratio when these charged groups were taken into consideration.

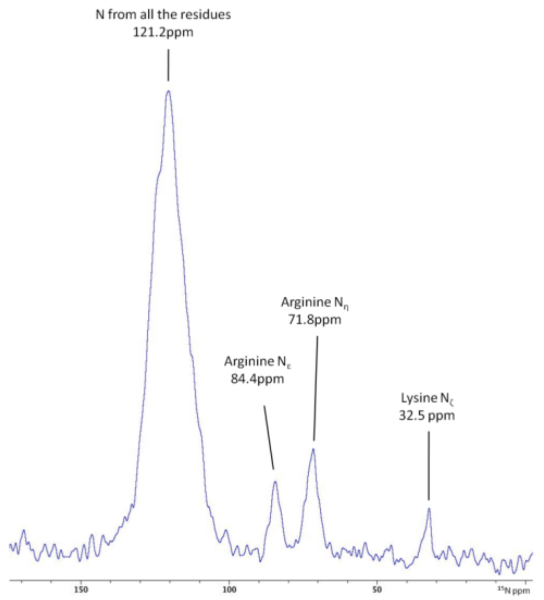

Figure 8.29 ^{15}N CP MAS spectrum of uniformly 13C-15N VHD bound to actin filaments. The different signals originating from the N atoms in the backbone, guanidine Nε and Nη from arginine and amine Nζ from lysine were identified centred at, respectively, 121ppm, 84ppm, 72ppm and 33ppm. The spectrum was recorded at 278K, 12.5kHz spinning rate using a 500MHz Bruker magnetsequipped with triple resonance 4mm e-free probe.

Two C_ON experiments (18 hours each) were acquired and their resulting FIDs were summed together and processed. The resulting spectrum was then compared to the C_ON projection calculated from an HNCO experiment acquired on a uniformly labelled ^{13}C-^{15}N VHD in free state (Figure 8.32). Several resonances were assigned but many of were overlapped and impossible to distinguish from each other (Figure 8.30).

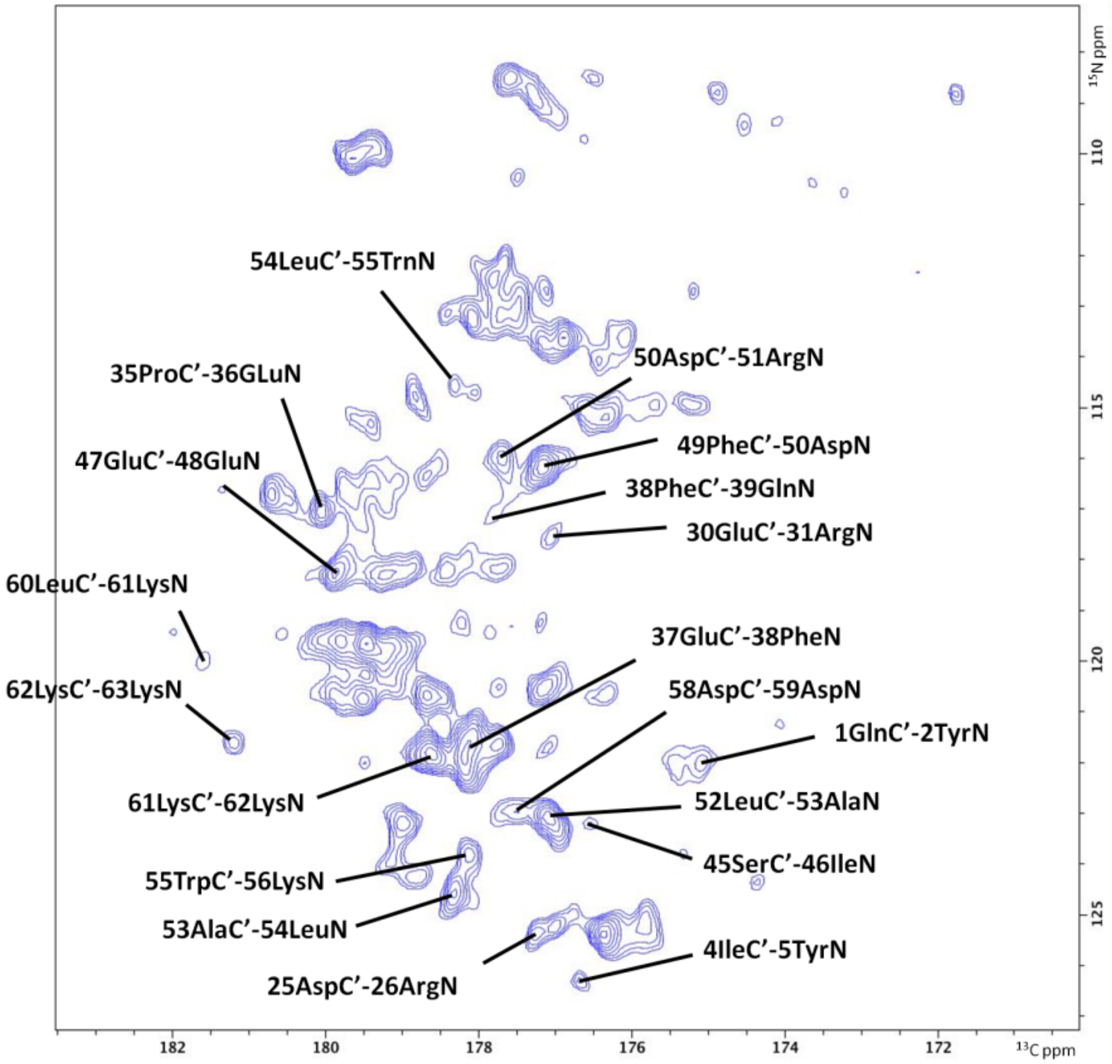

Figure 8.30 C_ON spectrum of uniformly ^{13}C-^{15}N VHD bound to filaments. Some of the assigned resonances are reported. The spectrum was recorded at 278K, 12.5kHz spinning rate using a 500MHz Bruker magnets equipped with triple resonances 4mm e-free probe.

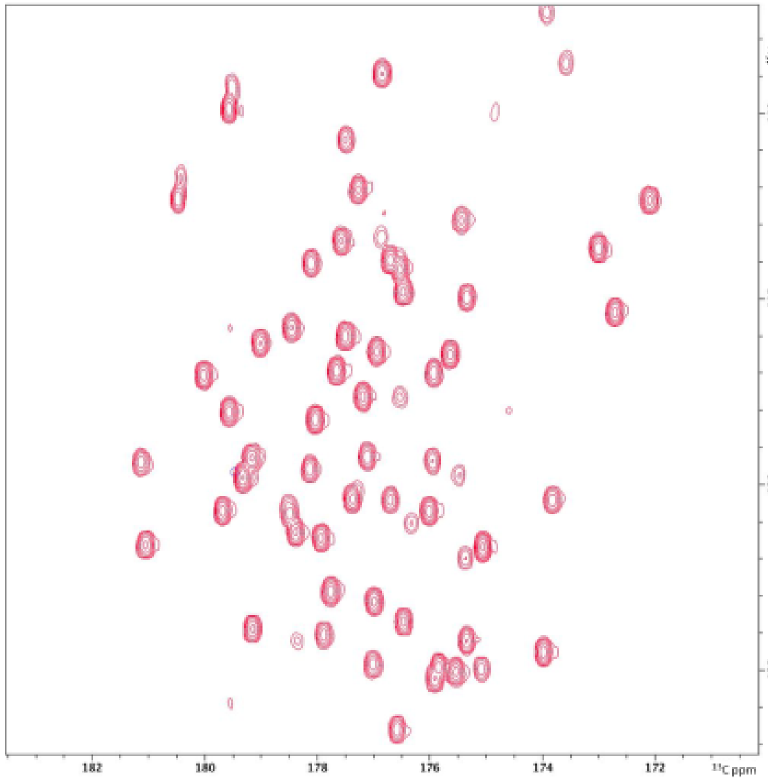

Figure 8.31 C_ON projection calculated from HNCO experiment acquired on a uniformly apo ^{13}C-^{15}N VHD in solution. The spectrum was recorded at room temperature using a 500MHz Bruker magnet equipped with a triple resonance cryoprobe.

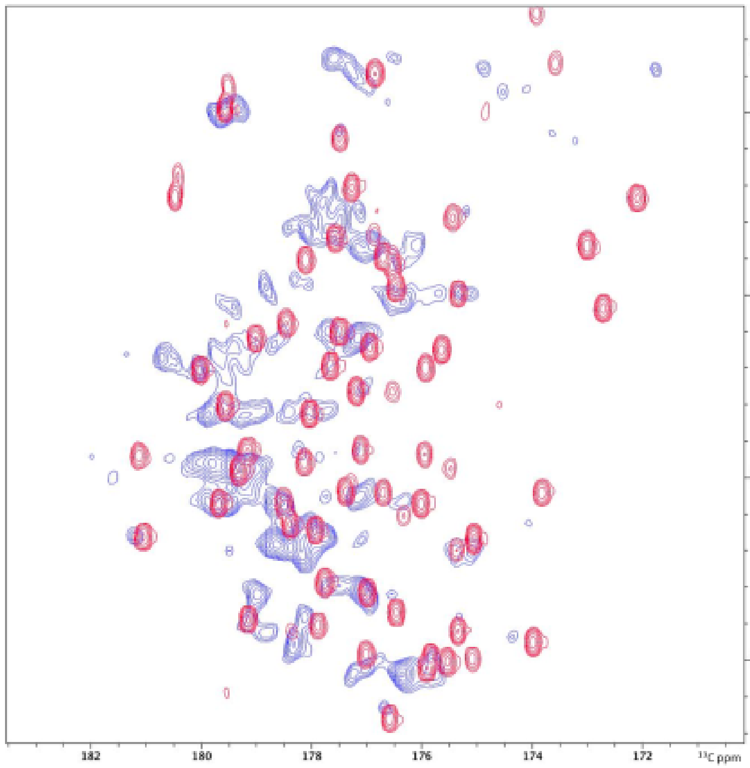

Figure 8.32 Superimposition of C_ON projection on uniformly apo ^{13}C-^{15}N VHD in solution (red spectrum) and C_ON spectrum of uniformly ^{13}C-^{15}N VHD bound to filaments. Several resonances were not affected by the binding event and their assignment was performed.

To simplify the number of resonances, the same C_ON experiments were recorded on two sample containing [1,3-^{13}C]-^{15}N VHD or [2-^{13}C]-^{15}N VHD bound to filaments. The spectra from [2-^{13}C]-^{15}N VHD complexed with actin did not show any peaks probably due to the low ^{13}C enrichment that this labelling provides on C_O positions. On the other hand, the other ^{13}C selective labelled VHD produced a C_ON spectrum with a reduced number of resonances. Knowing the pattern of ^{13}C enrichment originating from the labelling using [1,3-^{13}C] glycerol it was possible to recognize most of those resonances and link them to the respective atoms on the VHD sequence (Figure 8.33).

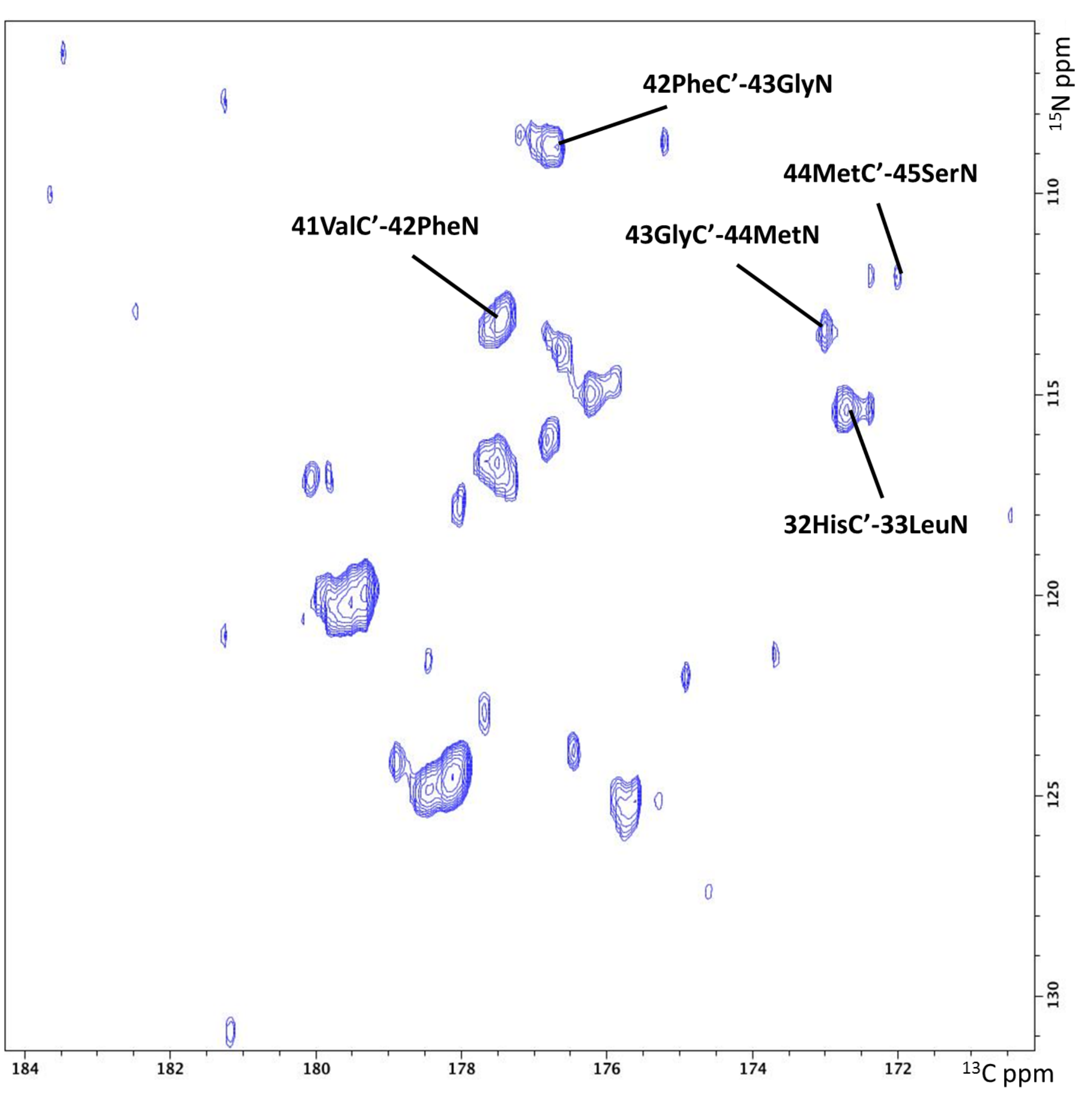

Figure 8.33 C_ON spectrum of [1,3-^{13}C]-^{15}N VHD bound to filaments. Most of the resonances were identified and assigned. Only the few new resonances that were assigned using this experiment are reported. The spectrum was recorded at 278K, 12.5kHz spinning rate using a 500MHz Bruker magnet equipped with triple resonance 4mm e-free probe.

Similarly for the C_ON spectra, the $C_\alpha N$ spectrum for the uniformly ^{13}C-^{15}N VHD bound to filaments was obtained from the processing of the FID resulting from the sum of two

$C_\alpha N$ experiments (21 hours each). Unfortunately, the signal to noise ratio for this spectrum was poor and only few resolved resonances were easily assigned. While in the $C_O N$ experiments the strong J_{CoN} characterizes an efficiency of the magnetization transfer near 28% if compared to direct ^1H-^{13}C CP, in the $C_\alpha N$ experiments the efficiency dropped to near 18% due to a weaker $J_{C\alpha N}$. The poor efficiency in $C_\alpha N$ experiments resulted in spectra with a poor signal to noise ratio, meaning that many resonances are hidden in the noise (Figure 8.34). As a consequence, the assignment for most of the signals in this spectrum was not possible.

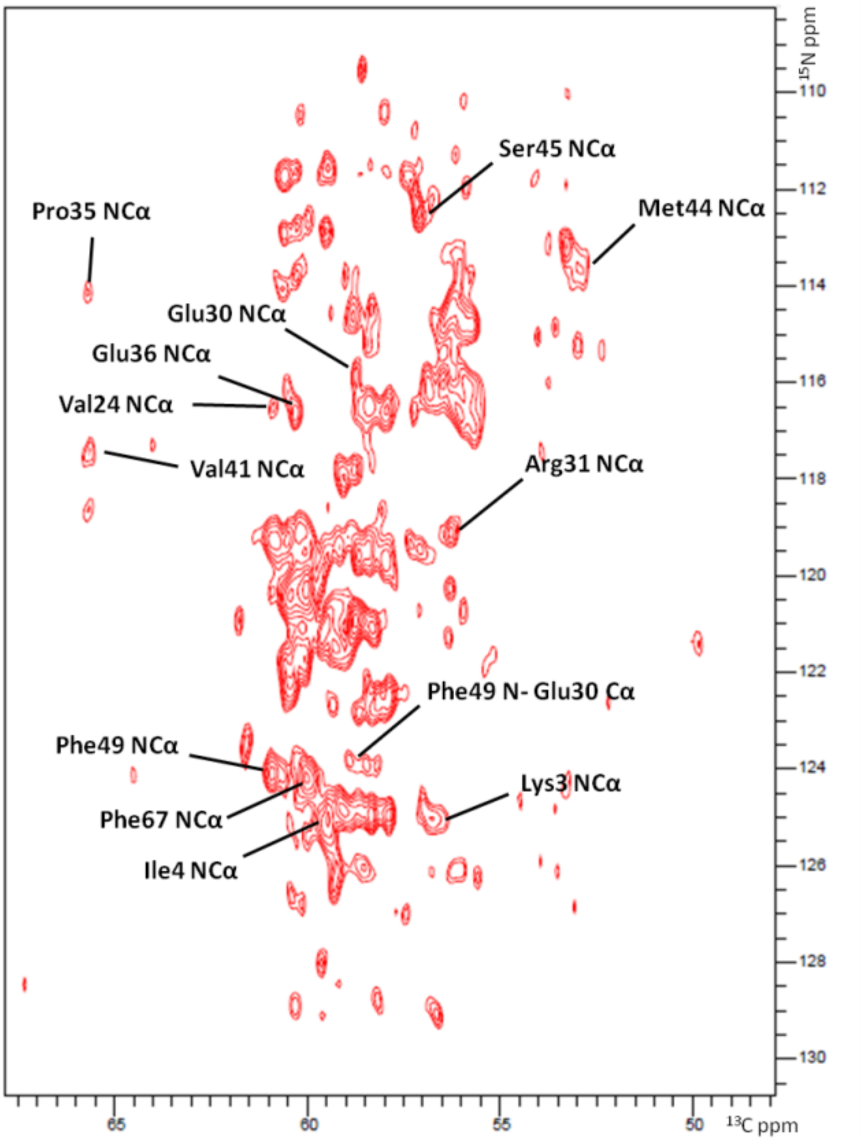

Figure 8.34 CαN spectrum of uniformly ^{13}C-^{15}N VHD bound to filaments. Some of the resonances that were assigned are reported. The spectrum was recorded at 278K, 12.5kHz spinning rate using a 500MHz Bruker magnets equipped with triple resonances 4mm e-free probe.

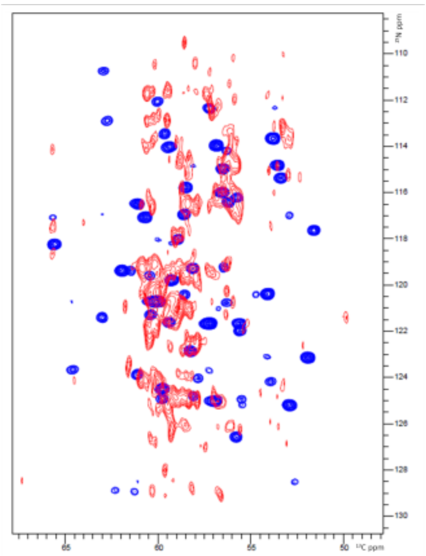

Figure 8.35 Superimposition of CαN spectrum of uniformly ^{13}C-^{15}N VHD bound to filaments (red spectrum) and CαN projection calculated from HNCα experiment acquired on uniformly apo ^{13}C-^{15}N VHD in solution (blue spectrum).

The partial assignment by ssNMR of VHD bound to F-actin performed so far is reported in Table 8.5. As explained, the chemical shifts of several atoms are still missing because their resonances were overlapped and impossible to be identified. On the other hand, the binding to filaments might induce structural changes in VHD that could affect the resonances of several residues shifting their frequencies. As a result, it was not possible anymore to identify these atoms by simply comparing the spectra acquired on apo and holo VHD.

	N	C	Cα	Cβ	Cγ	Cδ	Cε
Gln1	-	174,97	-	-	-	-	
Tyr2	121,97	-	56,54	38,68	-	-	-
Lys3	125,05	-	56,86	32,52	-	-	-
Ile4	125,07	176,52	59,43	37,23	27,62 - 17,31	11,17	
Tyr5	126,33	-	56,31	-	-	133,58	-
Pro6	-	177,84	61,99	32,49	27,67	50,42	
Tyr7	128,87	-	61,07	-	-	-	-
Asp8	-	-	-	-	-		
Ser9	-	-	59,49	63,9			
Leu10	-	-	54,03	-	-	22,26	
Ile11	-	178	62,2	39,8	26,7	13,25	
Val12	-	-	-	-	-		
Thr13	-	-	-	68,83	-		
Asn14	-	175,48	-	-	-		
Arg15	120,01	-	-	-	-	-	

Ile16	-	-	-	37,8	27,52 - 18,01	12,79	
Arg17	-	-	-	-	-	-	
Val18	-	175	62,1	-	-		
Lys19	-	-	-	-	-	-	-
Leu20	-	-	52,77	41,82	26,31	23,62	
Pro21	-	-	-	-	-	-	
Lys22	-	-	-	-	-	-	-
Asp23	-	175,68	52,95	-	-		
Val24	116,79	175,82	60,93	-	-		
Asp25	126,41	177,1	52,16	40,89	-		
Arg26	125,38	-	-	-	-	-	
Thr27	-	175,66	62,51	69,11	21,93		
Arg28	-	-	53,58	30,62	-	-	
Leu29	-	178,49	-	-	-	-	
Glu30	116,25	177,06	58,51	-	32,72	-	
Arg31	119,35	-	56,34	-	-	-	
His32	-	172,15	56,22	-	-	-	-
Leu33	115,39	178,7	52,96	-	-	48.26,3	
Ser34	121,92	-	55,84	61,97			
Pro35	117,4	179,93	64,87	31,31	27,75	49,09	
Glu36	117,08	-	60,16	-	-	-	
Glu37	-	178,03	-	29,96	38,94	-	
Phe38	121,89	177,6	62,77	39,15	-	-	-
Gln39	117,18	-	-	-	33,14	179,49	
Glu40	-	-	-	29,66	35,46	-	
Val41	118,6	177,48	64,84	31,81	20,7		
Phe42	113,50	176,85	-	-	-	-	-
Gly43	108,54	172,75	46,04				
Met44	113,54	171,79	53,07	33,98	28,62		16,59
Ser45	112,38	176,43	56,75	65,78			
Ile46	123,3	176,42	64,14	36,97	29,01 - 15,8	13,98	
Glu47	-	179,63	59,77	28,36	36,78	-	
Glu48	118,23	-	59,06	-	-	-	
Phe49	124,11	176,97	60,09	-	-	-	-
Asp50	116,35	177,54	56,39	40,49	-		
Arg51	116,07	-	56,83	-	27,41	43,68	
Leu52	-	176,93	53,44	-	25,81	21,75	
Ala53	123,17	178,18	51,37	18,93			
Leu54	124,59	178,18	59,11	-	-	-	
Trp55	114,61	178	59,52	-	-	-	-

Lys56	123,82	-	-	-	-	-	-
Arg57	-	-	60,43	-	28,31	-	
Asn58	-	177,52	-	-	-		
Asp59	123,12	179,23	58,01	-	-		
Leu60	-	181,44	57,78	-	-	-	
Lys61	120,01	178,49	60,26	-	-	-	-
Lys62	121,84	180,91	59,88	32,19	-	-	-
Lys63	121,63	-	59,14	31,87	24,95	-	-
Ala64	117,92	176,67	51,7	19,72			
Leu65	-	-	-	-	-	-	
Leu66	-	174,2	-	-	-	-	
Phe67	124,45	-	60,01	-	-	-	-

Table 8.5 ^{13}C and ^{15}N frequencies table in ppm of ^{13}C-^{15}N enriched VHD bound to actin filaments so far obtained.

8.2.3 Ultrafast spinning ssNMR: early attempts on ^{1}H acquisition

To fill the gaps in the assignment, an ultrafast spinning MAS approach was attempted with the collaboration of Dr. Lewandowski. The experiments were recorded at the Physics department in Warwick University using a 850MHz Bruker magnet equipped with a triple resonance 1.3mm rotor probe. 2D ^{1}H-^{15}N correlation experiments were acquired on two different batches that differ on the protocol used to fill the rotor, both containing ^{2}H-^{13}C-^{15}N VHD back-protonated with 100% H_20 bound to filaments. The evaluation of the temperature during the acquisition was performed as described in 0.

The 2D ^{1}H-^{15}N correlation experiments recorded on the first sample using CP as magnetization transfer (^{1}H-^{15}N INVCP from INVerted CP) showed spectra affected both by the presence of a strong water signal and by a low amount of labelled sample in the rotor. It was estimated that in the almost 2,5mg of sample in the rotor less than 0,2mg were labelled VHD. Thus, the amount of water in the rotor generated a signal that the water suppression pulse scheme was not able to minimize interfering with the optimization of the sequence. As a result, the signals were hidden in the noise and it was not possible to link any of the signals to the VHD atoms (Figure 8.36).

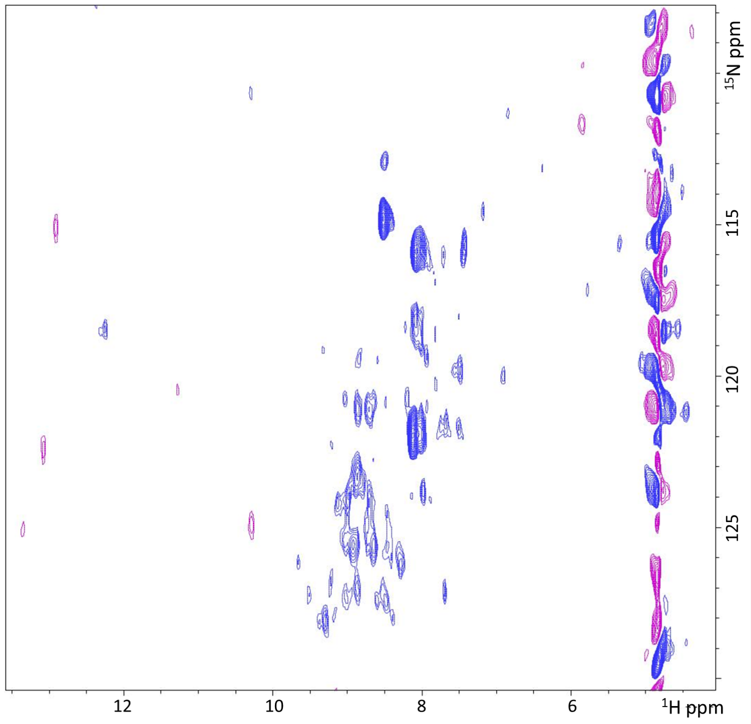

Figure 8.36 Spectrum of 2D ^{1}H-^{15}N correlation experiment implementing CP as magnetization transfer on first preparation of uniformly ^{2}H-^{13}C-^{15}N VHD back-protonated with 100% $H_2$0 bound to filaments. The FID obtained by the sum of 10 experiments was processed and analysed. Each experiment was recorded at near 301K, 60kHz spinning rate using a 850MHz Bruker magnet equipped with triple resonance 1.3mm probe.

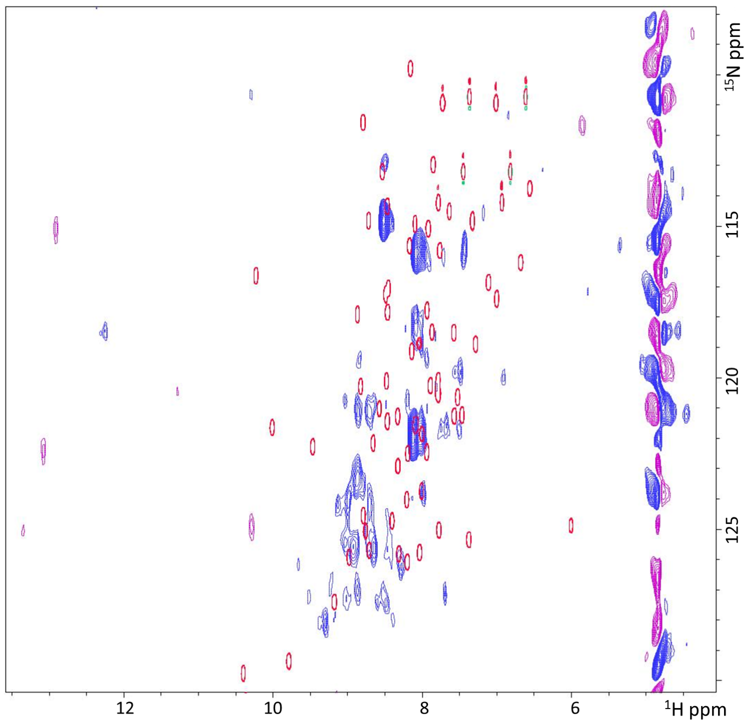

Figure 8.37 Superimposition of spectrum from ^{1}H-^{15}N INVCP experiment on first preparation of uniformly ^{2}H-^{13}C-^{15}N VHD back-protonated with 100% $H_2$0 bound to filaments (blue spectrum) and the ^{1}H-^{15}N HSQC spectrum from apo ^{13}C-^{15}N VHD in solution.

Changing the protocol to pack the rotor, the rotor was filled with almost 4mg of sample and it was estimated that nearly 1mg of it was labelled VHD. The amount of water was drastically decreased and it helped in the set up of the sequences used. Even if the amount of signal acquired was ten times higher compared to the previous preparation, the ^{1}H-^{15}N INVCP spectrum showed a strong unique signal (Figure 8.38). This kind of spectra could be generated either by the presence of unfolded protein or by too short value for T_1 and T_2 relaxation parameters for proton or nitrogen bulk magnetization.

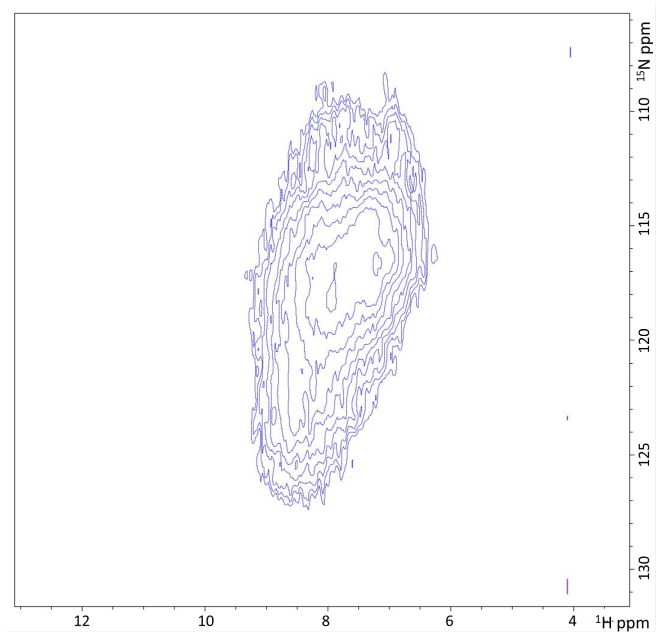

Figure 8.38 Spectrum of ^{1}H-^{15}N INVCP on second preparation of uniformly ^{2}H-^{13}C-^{15}N VHD back-protonated with 100% H_20 bound to filaments. A unique signal in which all the resonances were collapsed was observable. The FID obtained by the sum of 10 experiments was processed and analysed. Each experiment was recorded at near 301K, 60kHz spinning rate using a 850MHz Bruker magnet equipped with triple resonance 1.3mm probe.

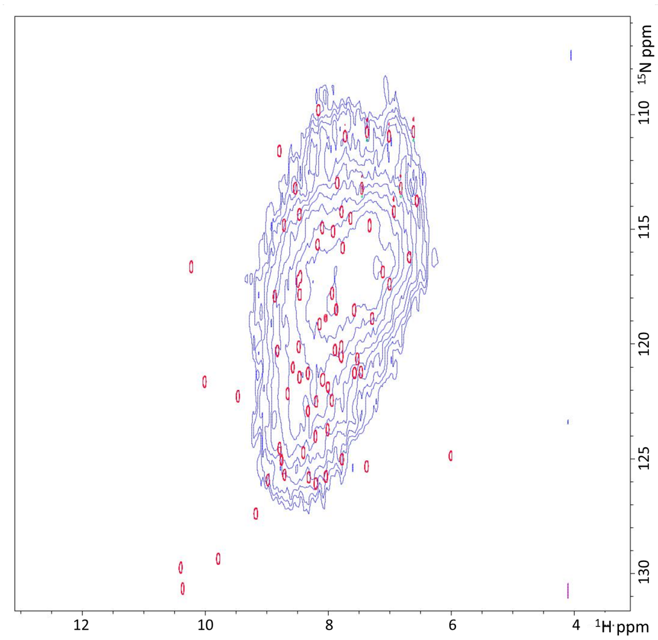

Figure 8.39 Superimposition of ^{1}H-^{15}N INVCP on second preparation of uniformly ^{2}H-^{13}C-^{15}N VHD back-protonated with 100% H_20 bound to filaments (blue spectrum) and the ^{1}H-^{15}N HSQC spectrum from apo ^{13}C-^{15}N VHD in solution.

Prior to realizing that this protocol to fill the rotor was too hard on the VHD, promoting its unfolding, (chapter 6.4), the T_1 and T_2 relaxation parameters both for proton and nitrogen bulk magnetization were roughly measured. Four different modified 1D ^{1}H-^{15}N INVCP pulse sequences, optimized in Warwick University for either nitrogen or proton T_1 or T_2 evaluation, were implemented in this calculation. While for the estimation of T_2 a classic spin echo pulse was added in the sequence (for ^{15}N after the first CP event and for ^{1}H after the first 90° pulse) and the delay before it was progressively increased, to calculate T_1 an extra pulse long τ was included in the sequence (after the first CP event for ^{15}N estimation and after the second CP for ^{1}H) and progressively increases in length.

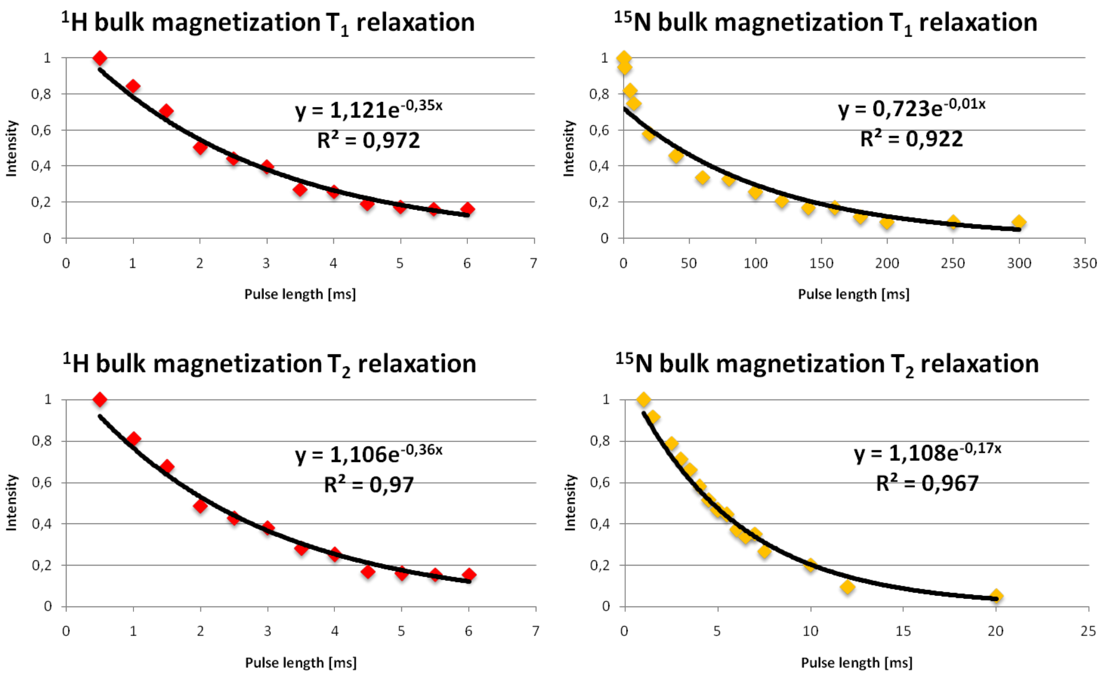

Figure 8.40 Fitting for the evaluation of T_1 and T_1 relaxation parameters for proton (red fitting) and nitrogen (yellow fitting) bulk magnetization.

The relaxation parameters were roughly estimated as the value of time in millisecond in which the signal intensity reaches 20% of the total intensity. It was calculated that, for the ^{1}H bulk magnetization, the relaxation parameters T_1 and T_2 were, respectively, 3.5ms and 3.3ms while for ^{15}N bulk magnetization were 110ms and 9ms (Figure 8.40).

Differently from solution NMR, in ssNMR the tumbling of the molecules is avoided. This results in a number of important consequences when carrying dynamic studies. It is important to remember that in ssNMR the anisotropic interactions (most notably the dipolar coupling in this case) are not average out by the molecular tumbling. Moreover, the dipolar coupling largely dominate the behaviour of the transverse relaxation (T_2). In this scenario, transverse relaxation parameters in solid are very difficult to access and their interpretation are still ambiguous. On the other hand, T_1 calculation is particularly useful. More precisely, it allows the measurement of local structural fluctuations and can provide information on both geometry and motions, especially when it is calculated for each residues in a protein [98]. Despite its importance in dynamic studies, T_1 and T_2 for bulk magnetization can also explain about the average resolution quality you can obtain from a sample. Precisely, very short T_1 and T_2 would be reflected in very broad signal. However, considering those values in the order of millisecond (value in order of micro- or nanoseconds would be considered short values) the lack in resolution in the spectra was not ascribed to problem in the relaxation mechanisms.

After the acquisition of a ^{1}H-^{13}C CP MAS experiment (centred in the carbonyl region), it became clear that the collapse of signals resulted from the presence of unfolded back-protonated ^{2}H-^{13}C-^{15}N VHD in the rotor (Figure 8.41).

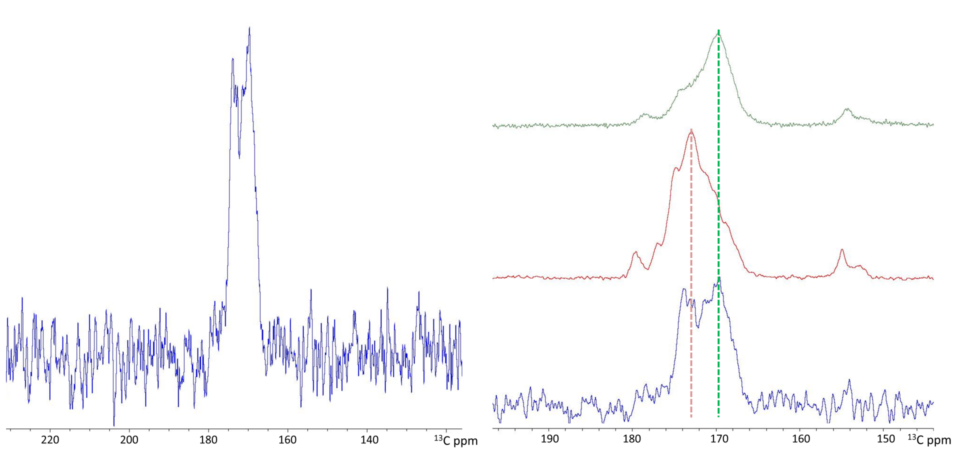

Figure 8.41 ^{13}C CP MAS spectra of carbonyl region of back-protonated ^{2}H-^{13}C-^{15}N VHD bound to actin filaments. Left panel (blue spectrum) shows the presence of two peaks centred at 172ppm and 167ppm that can be perfectly overlapped to, respectively, on the carbonyl region from a folded VHD bound to actin (red spectrum in right panel) and the same region from an unfolded VHD bound to filaments (green spectrum in right panel). Blue spectrum was recorded at 60kHz spinning rate, 301K in a 850MHz Bruker magnet while red and green spectrum at 10kHz spinning rate, 278K in a 400MHz Bruker magnet.

Assuming that the unfolded part was not free to move (the CP transfer works efficiently on atoms that are not free to move suggesting that unique signal was likely arising from the collapsed signal from the unfolded VHD), 2D ^{1}H-^{15}N correlation experiments using INEPT transfer were recorded in order to reveal any NH on the folded part of VHD still bound to the filaments that maintained a degree of movement. The FIDs from 10 experiments (almost 1h each) were summed together, the result processed and the proton and nitrogen dimension properly referenced. Even if the spectrum showed a poor signal to noise ratio, several spare frequencies were observable (Figure 8.42). When overlapped to the ^{1}H-^{15}N HSQC acquired on VHD in free state some resonances showed to be in the same position but because of the poor quality of the spectra it was not possible to confirm that the signals were originating from the same atoms (Figure 8.43).

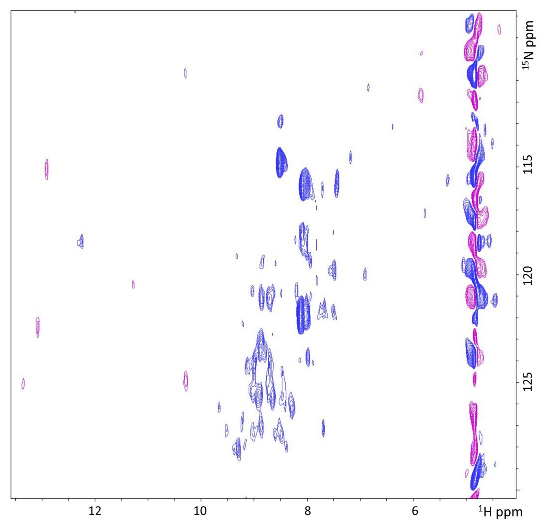

Figure 8.42 Spectrum of 2D ^{1}H-^{15}N correlation experiment implementing INEPT as magnetization transfer on second preparation of ^{2}H-^{13}C-^{15}N VHD back-protonated with 100% $H_{2}0$ bound to filaments. The FID obtained by the sum of 10 experiments was processed and analysed. Each experiment was recorded at near 301K, 60kHz spinning rate using a 850MHz Bruker magnet equipped with triple resonance 1.3mm probe.

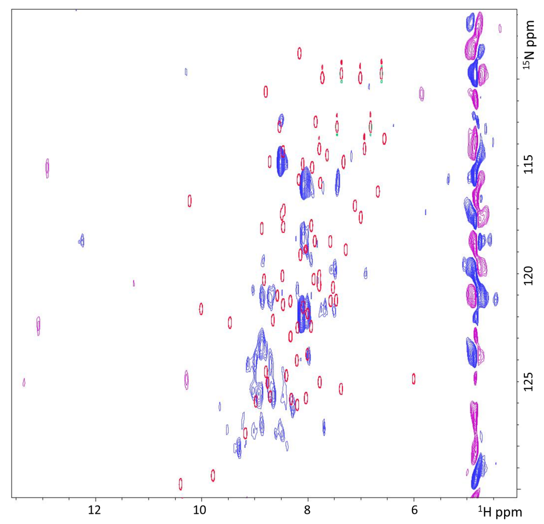

Figure 8.43 Superimposition of 2D ^{1}H-^{15}N correlation spectrum implementing INEPT as magnetization transfer acquired on second preparation of uniformly ^{2}H-^{13}C-^{15}N VHD back-protonated with 100% $H_{2}0$ bound to filaments (blue spectrum) and the ^{1}H-^{15}N HSQC spectrum from apo ^{13}C-^{15}N VHD in solution. Several overlapped resonances were reported even their assignment is still to confirm.

Even if the dataset acquired using the ultrafast MAS approach revealed several problems that has to be still addressed (especially in the sample preparation), they demonstrated that the VHD-filament complex can be studied applying this approach and dataset useful for an eventual assignment of VHD can be generated.

9 Characterization of VHD binding site to actin filaments

9.1 Side chain assignment of positively charged residues by solution NMR

As explained in 1.5, for the chicken isoform of VHD there are three important regions involved in the binding with high affinity to actin filaments. A hydrophobic “cap” formed by residues L63 and W64, an alternate charged “crown” below the cap containing E72 and K71 and a positively charged “patch” composed of the residues K65, K70, K73, K38 and R37 and the C-terminal carboxylate of F76 [43, 44, 99].
Despite the importance that charged residues have in many mechanisms of interaction (protein-protein or ligand-protein interaction), their characterization by NMR in solution proves to be challenging. The guanidine group in arginine and the amino group in lysine, the regions in their side chains that are positively charged, have characteristic chemical shift and, at physiologic pH, they can exchange protons with the water. In accordance to the rate of the exchange that can be slow, fast and medium when compared to the NMR time scale, this event can affect differently the NMR signals making the acquisition of these charged regions difficult. Decreasing the pH lower than the pKa of these charged regions, the exchange stops and these residues appear to be in a protonated state. In this state, the effects deriving from the proton exchange are nullified and these charged regions can be acquired using the same sequences used for the backbone assignment. On the other hand, these resonances reflect a state of the protein far from the physiological condition and they cannot be used for physiological consideration. Acknowledging the important role that these residues have in proteins, in the last few years new approaches were developed and optimized C_xN_x correlation pulse sequences acquired on carbon dimension were proposed as solution of the problem [100, 101]. In these experiments the magnetization is generated by direct excitation of carbon atoms (arginine C_ζ for C_ON based sequence or arginine C_δ and lysine C_ε for C_αN based sequence), moved to the close nitrogen (N_ε and N_η for arginine and N_ζ for lysine) and moved again to the bound carbon (C_δ and C_ζ for arginine and C_ε for lysine) where the acquisition is performed. During the sequence the proton dimension is continuously decoupled while nitrogen is decoupled only during the acquisition.

Seven arginine (arg15, arg17, arg26, arg28, arg31, arg51 and arg57) and seven lysine (lys3, lys19, lys22, lys56, lys61, lys62, lys63) are present in the sequence of VHD. Due to the problems in their acquisition the assignment pübliches in the literature was missing the resonances of the guanidine group of arginine and the amino group of lysine.

```
1          10          20          30           40          50         60     66
QYKIYPYDSLIVTNRIRVKLPKDVDRTRLERHLSPEEFQEVFGMSIEEFDRLALWKRNDLKKKALLF
```

Figure 9.1 Amino acid sequence of VHD. The arginine (red) and lysine (blue) are highlighted on the sequence.

To complete the assignment in solution of arginine guanidine groups, ^1H-^{15}N HSQC, $C_\zeta N_\varepsilon/N_\eta$ ($C_O N$ optimized pulse sequence) and $C_\delta N_\varepsilon$ experiments ($C_\alpha N$ optimized sequence) were acquired. The HSQC was recorded with a large spectral width on nitrogen dimension in order to properly reference the nitrogen dimension in the other spectra. On the other side, the carbon dimension was referenced using a $C_\delta N_\varepsilon$ experiment in which the chemical shift of C_δ atoms was already available from the VHD assignment deposited. Analyzing the ^1H-^{15}N HSQC spectra it was possible to identify the $H_\varepsilon N_\varepsilon$ signals from arginine residues but an assignment based only on these information was impossible (Figure 9.2). The potential exchange of H_ε with the solvent will result in the broadening of the signals that could be lost in the background noise.

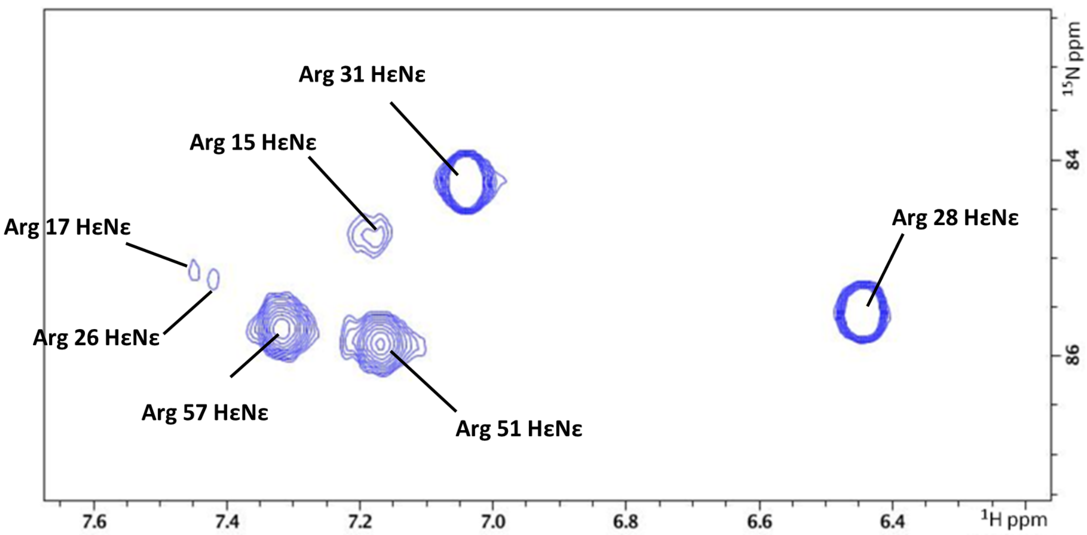

Figure 9.2 Arginine Nε region in ^1H-^{15}N HSQC spectrum acquired on an apo ^{13}C-^{15}N VHD in solution. In the spectrum only four of the seven arginine are easily identifiable. It means that the other three residues easily exchange with the solvent. The spectrum was acquired at room temperature in a 500MHz Bruker magnet equipped with a triple resonance cryoprobe.

Using the assignment reported in literature, it was possible to identify in the ^{13}C-^{13}C TOCSY spectrum the crosspeaks for the $C_\delta C_\beta$ correlations of all the arginine in the VHD. These crosspeaks were then used to identified the C_δ atoms in the $C_\delta N_\varepsilon$ spectrum linking them to the respective N_ε (Figure 9.3).

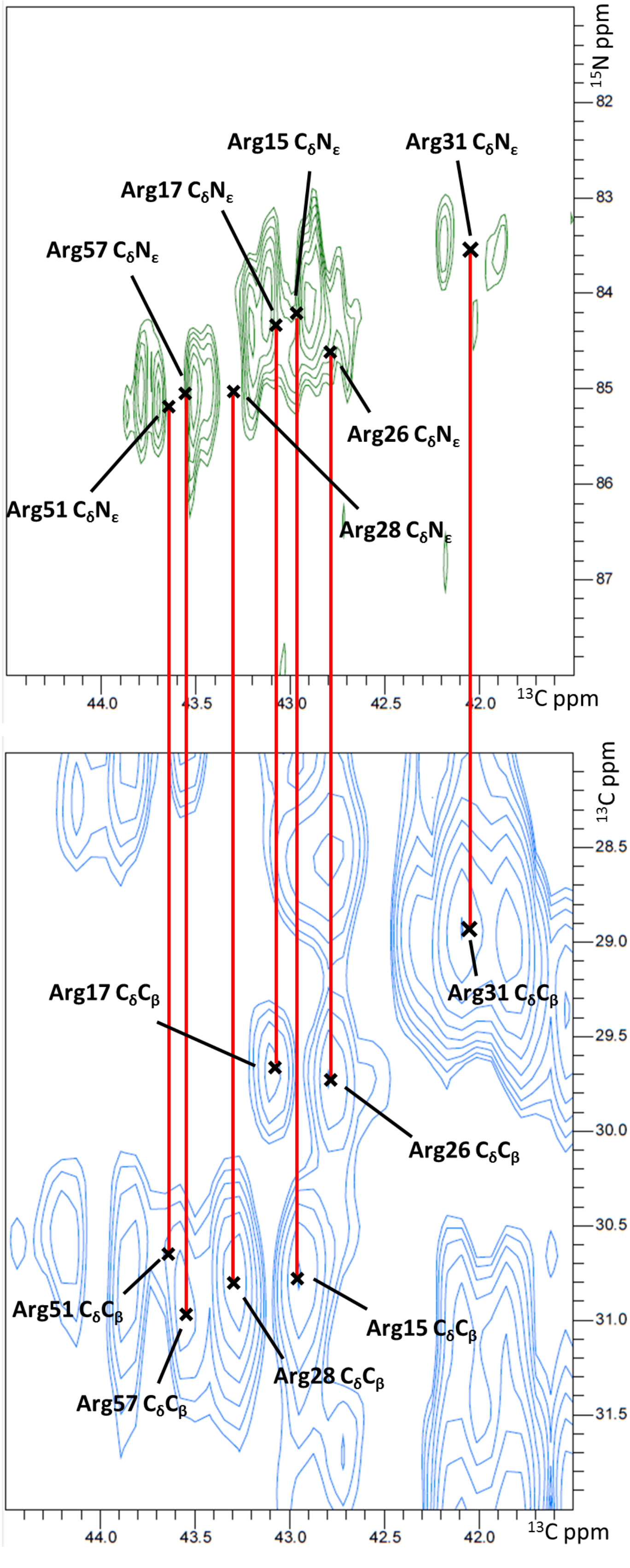

Figure 9.3 Assignment strategy implemented to assign the CδNε peaks. Starting from the resonances for the CδCβ crosspeaks contained in the 13C-13C TOCSY experiment (blue spectrum at the bottom), it was possible to move to the CδNε spectrum (green spectrumat the top) and identifies the CδNε resonances for all the arginine in the VHD. The residues and their relative assignment are reported in both the spectra.

Finally, each $C_\delta N_\varepsilon$ peak was related to the proper H_ε analysing again the HSCQ. Unfortunately, these experiments are affected by the J coupling between C_γ and C_δ that causes a split of the signals in the carbon dimension and their interpretation can present some difficulties (Figure 9.4).

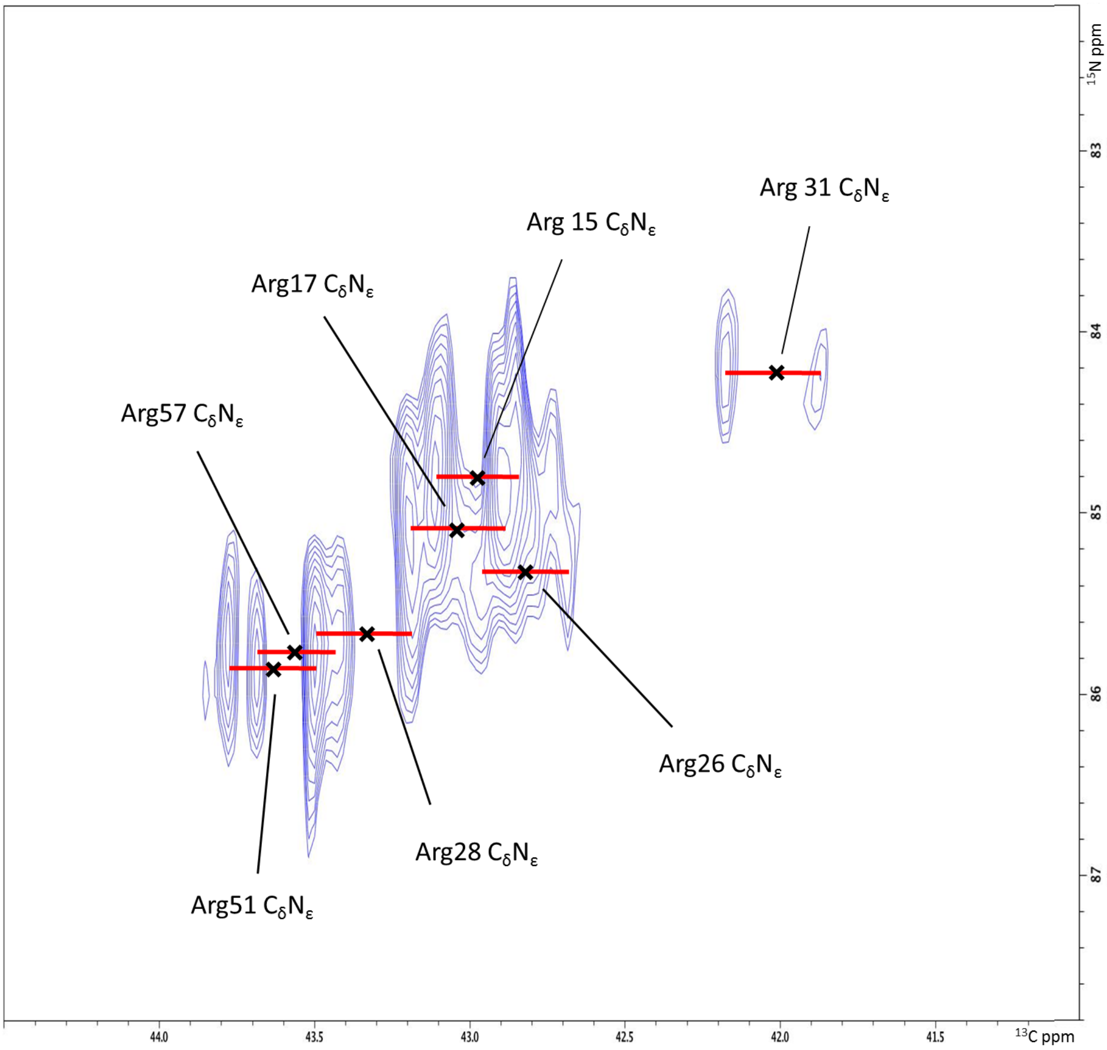

Figure 9.4 CδNε spectrum acquired on apo ^{13}C-^{15}N VHD in solution. The splitting of signals in doublet is due to remaining the J coupling between Cγ and Cδ. The assignment of the seven CδNε arginine frequencies is reported. The spectrum was acquired at room temperature in a 500MHz Bruker magnet equipped with a triple resonance cryoprobe.

To accurately identify the chemical shift of C_δ atoms in the $C_\delta N_\varepsilon$ spectrum, nitrogen projections at 84,33ppm, 84,92ppm, 85,45ppm and 85,91ppm were calculated. In each projection, the possible pair of signals generated by every C_δ was identified using the available assignment. For each pair of signals, the $^1J_{CC}$ was calculated and compared to the average $^1J_{CC}$ value reported in literature for the alkanes (35Hz) confirming that the pair of signals were real and not noise (Figure 9.5).

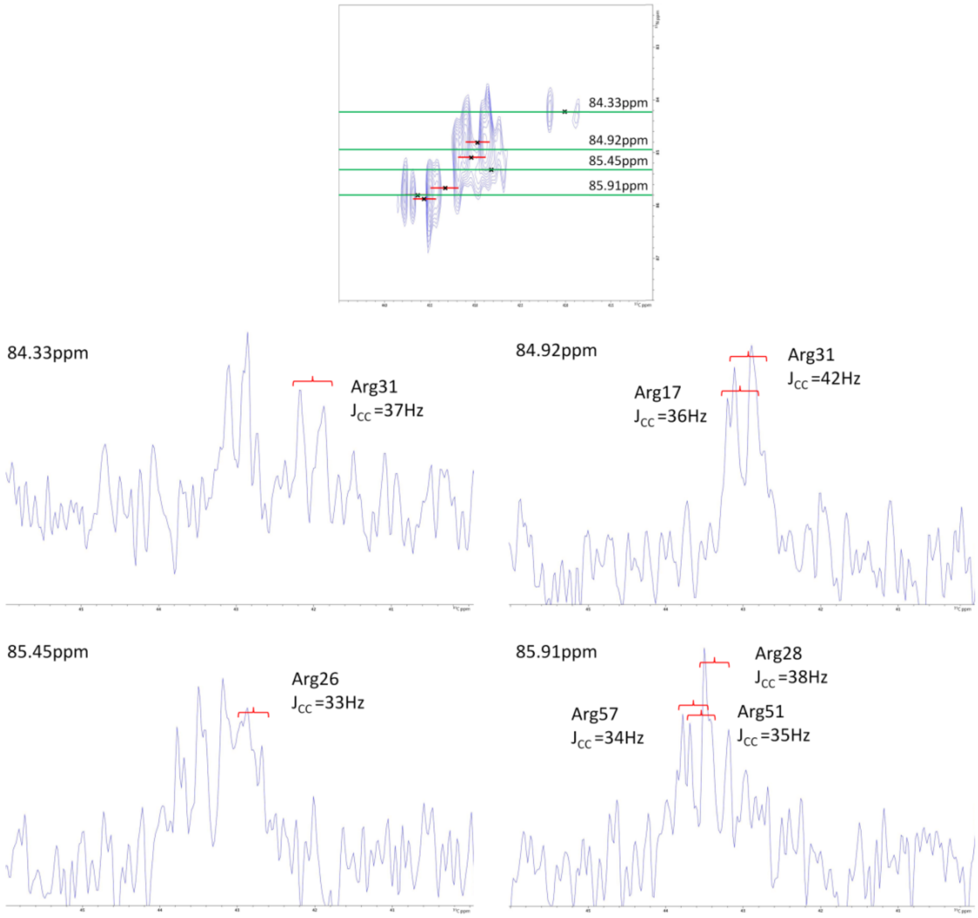

Figure 9.5 ^{15}N projections calculated at 84,33ppm, 84,92ppm, 85,45ppm and 85,91ppm from the CδNε spectrum to help the proper assignment of arginine Cδ atoms affected by the split due to the J coupling between Cγ and Cδ.

The analysis of the $C_\zeta N_\varepsilon/N_\eta$ spectrum helped to complete the assignment of the guanidine group (Figure 9.7 and Figure 9.8). The interpretation of these experiments was not an easy task due to the presence of a series of artifacts that arose during the acquisition and in many cases overlapped the real signals (Figure 9.6). The artifact identification was possible only because their chemical shift showed a dependence to the offset and the size of the spectral width. Simply acquiring the $C_\zeta N_\varepsilon/N_\eta$ spectra using a parameter set to confine these artifacts in a region of the spectrum that did not interfere with the real signals was sufficient to overcome this problem. The complete guanidine assignment is reported in Table 9.1 and the assignment strategy used is reported in Figure 9.7 and Figure 9.8.

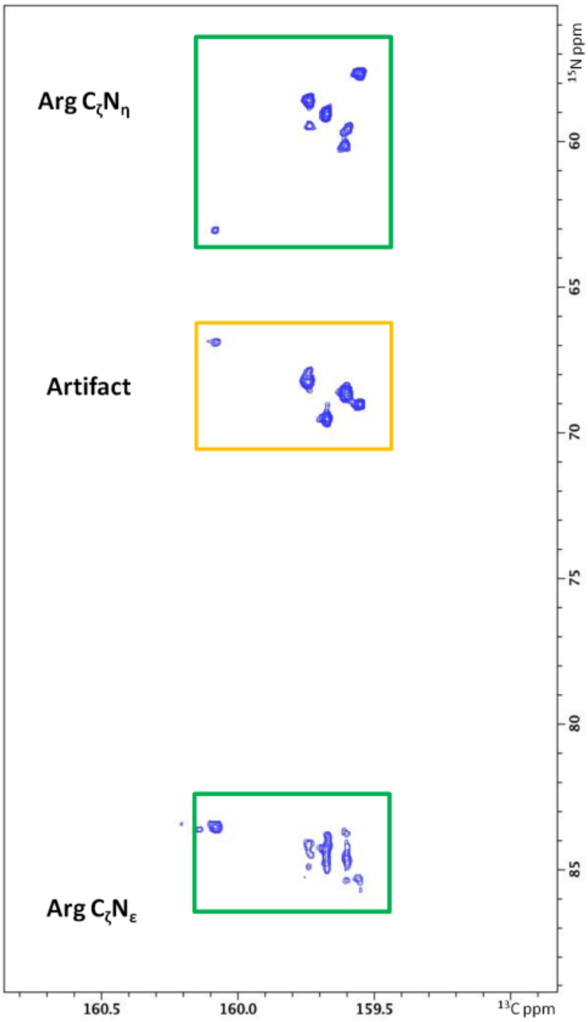

Figure 9.6 CζNε/Nη spectrum acquired on apo ^{13}C-^{15}N VHD in solution. The yellow square surrounds the artifacts that arise during the recording of the experiments. It was proved that those artifacts were depending on the spectral width and offset and using the proper setting it was possible to move the artifacts in a region of the spectrum that did not interfere with real signal from the CζNε/Nη correlation (signals contained in the green squares). The spectrum was acquired at room temperature in a 500MHz Bruker magnet equipped with a triple resonance cryoprobe.

	C_δ	N_ε	H_ε	C_ζ	N_η
arg31	42,03	84,22	7,04	160,08	63,71
arg26	42,82	85,21	7,41	159,59	60,81
arg15	43,00	84,76	7,18	159,74	60,22
arg17	43,07	85,12	7,44	159,67	59,71
arg28	43,30	85,54	6,45	159,60	60,14
arg51	43,54	85,88	7,16	159,74	58,37
arg57	43,65	85,7	7,31	159,52	59,25

Table 9.1 Chemical shift (in ppm) of arginine guanidine groups for apo ^{13}C-^{15}N VHD in solution.

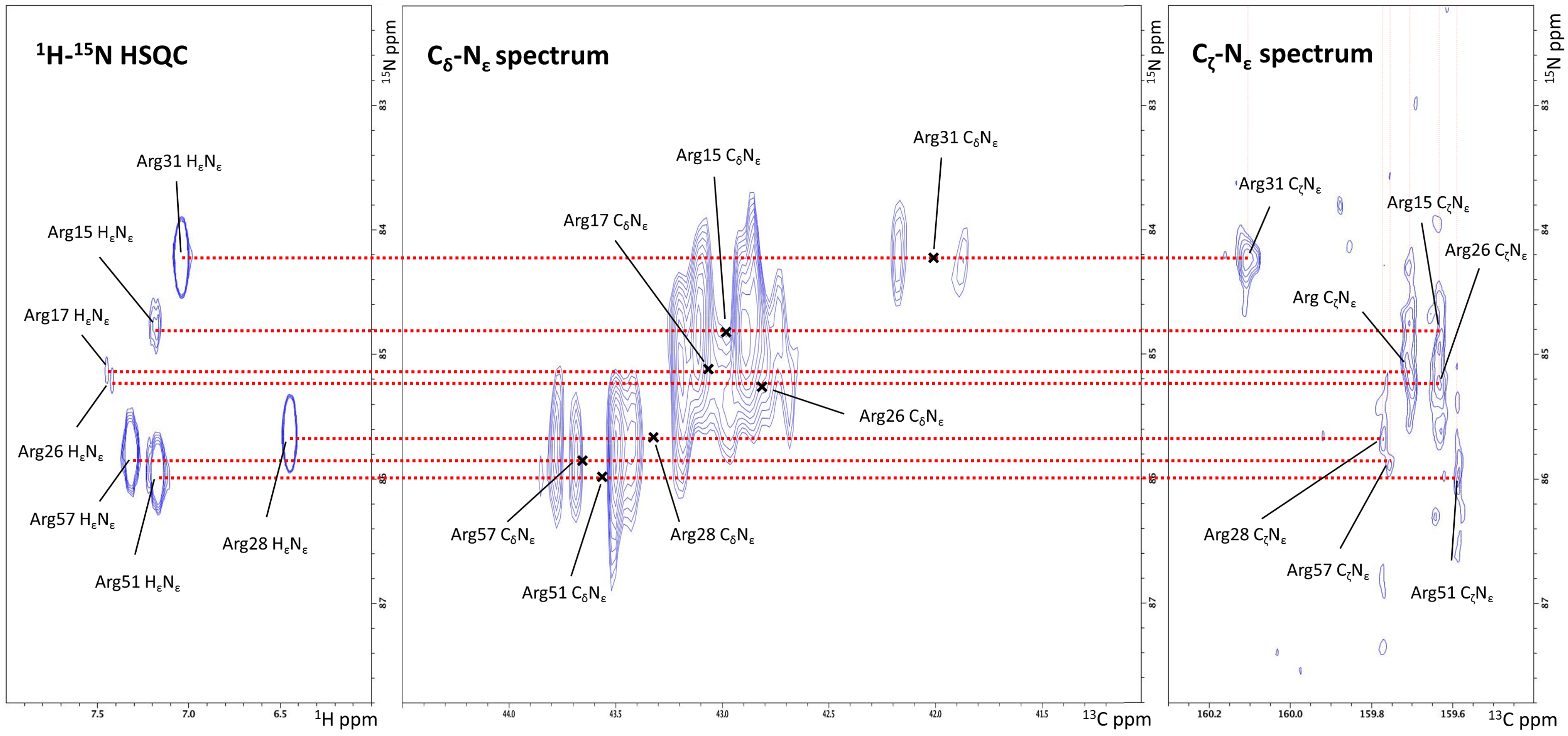

Figure 9.7 Assignment strategy implemented for the identification of guanidine group of arginine in apo ^{13}C-^{15}N VHD in solution. Starting from the Cδ assignment available in literature it was possible to assign the CδNε spectrum and from this spread the assignment to the ^{1}H-^{15}N HSQC and to the CζNε experiments. The residues and their relative assignment are reported in the spectra.

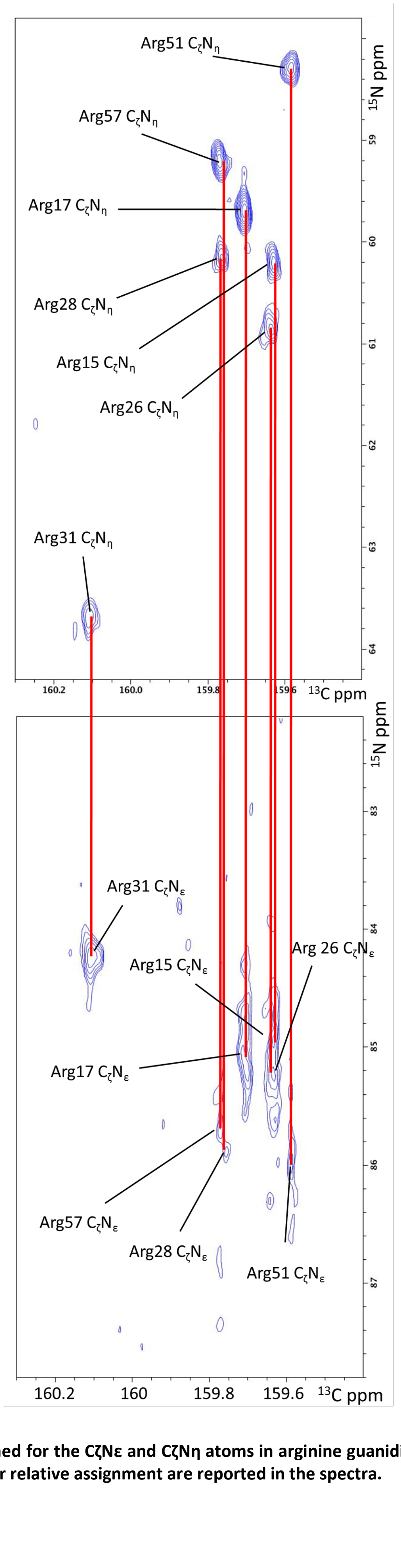

Figure 9.8 Assignment performed for the CζNε and CζNη atoms in arginine guanidine group in apo ^{13}C-^{15}N VHD in solution. The residues and their relative assignment are reported in the spectra.

Similar experiments were recorded to assign the amino group of lysines. To reference the nitrogen dimension the same ^{1}H-^{15}N HSQC with large spectral width analysed for guanidine assignment was used. Unfortunately, analyzing this spectrum it was not possible to collect the chemical shift from H_ζ atoms because the resonances for all the seven $H_\zeta N_\zeta$ were overlapped in a single signal. On the other hand, the signals in the $C_\varepsilon N_\zeta$ spectrum (based on $C_O N$ pulse sequence) acquired and processed using a virtual suppression of J-coupling macros (splitcomb macros from Bruker) were sufficiently resolved (Figure 9.9) to make possible the assignment of all seven N_ζ. The chemical shift of the amino groups assigned is reported in Table 9.2.

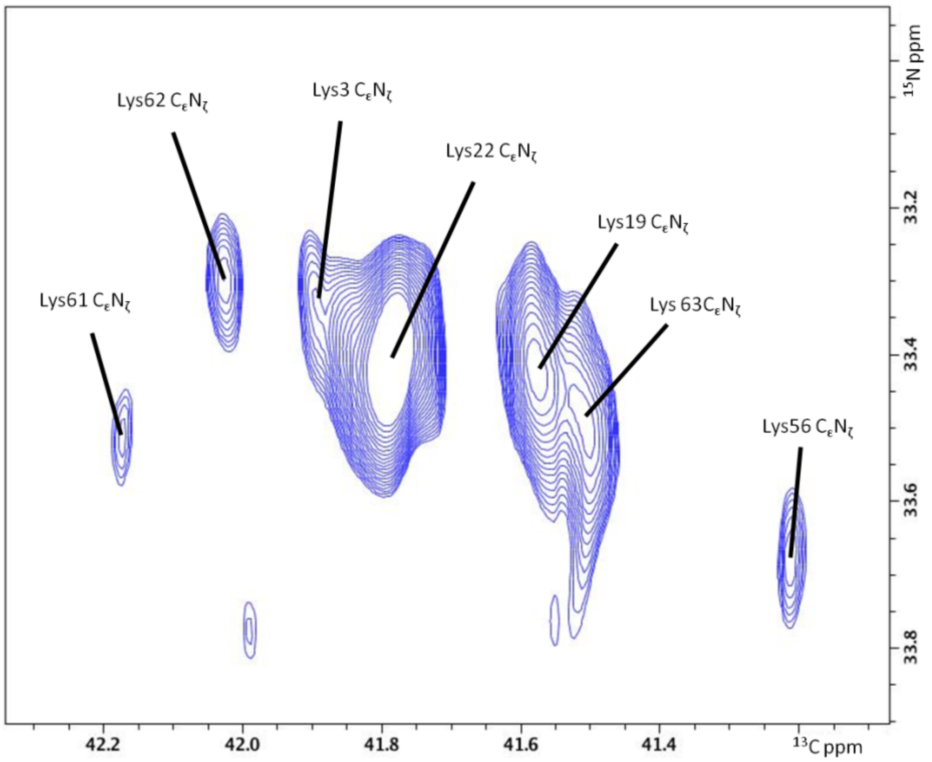

Figure 9.9 CεNζ spectrum acquired on apo ^{13}C-^{15}N VHD in solution. The assignment of the seven lysine CεNζ frequency is reported. The spectrum was acquired at room temperature in a 500MHz Bruker magnet equipped with a triple resonance cryoprobe.

	C_ε	N_ζ
Lys56	41,2	33,67
Lys63	41,5	33,49
Lys19	41,63	33,42
Lys22	41,8	33,4
Lys3	41,92	33,32
Lys62	42,03	33,29
Lys61	42,24	33,51

Table 9.2 Chemical shift (in ppm) of lysine amine groups for apo ^{13}C-^{15}N VHD in solution.

Despite the success in the assignment of guanidine and amine groups for the free state of VHD in solution, their assignment in VHD complexed with filaments is still in development. Unfortunately, the only data available were collected analyzing a ^{15}N CP MAS spectrum in which was possible to extrapolate only the range of chemical shift where the different nitrogen types are clustered. It was estimated that the resonances for N_{ε} and N_{η} for VHD arginine guanidine group in the complex were all close around, respectively, 84ppm and 72ppm, while for the lysine amine group near 33ppm. While the chemical shift for N_{ε} atoms is comparable to the one for apo VHD, the resonances for N_{η} are quite different. The average chemical shift for these atoms in apo VHD is around 60ppm, almost 10ppm different than the same atoms in the holo VHD suggesting a drastic rearrangement of guanidine groups after the binding. On the other hand, it seems that the lysine amine groups are not affected by the binding event showing comparable chemical shift before and after the binding.

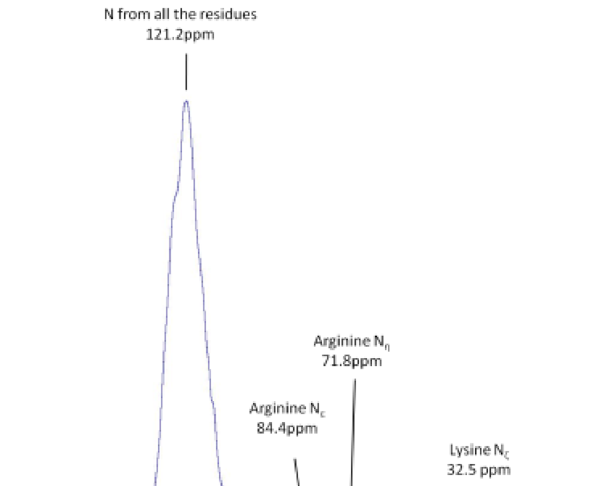

Figure 9.10 ^{15}N CP MAS spectrum of uniformly ^{13}C-^{15}N VHD bound to actin filaments. The different signals originating from the N atoms in the backbone, guanidine Nε and Nη from arginine and amine Nζ from lysine were identified centred at, respectively, 121ppm, 84ppm, 72ppm and 33ppm. The spectrum was recorded at 278K, 12.5kHz spinning rate using a 500MHz Bruker magnet equipped with triple resonance 4mm e-free probe.

Nevertheless, even if it was not possible to investigate the role that arginine and lysine have in VHD binding to actin filaments, a classic mutagenesis approach was developed in order to identify which of these positively charged residues were effectively involved in the binding and which were essential only for the correct folding of the protein.

9.2 Mutagenesis for identification of residues involved in binding to actin

As previously described, the residues in chicken VHD that play a key role in the binding to actin filaments are reported in the literature and most of them are positively charged amino acids. The alignment of the sequence of chicken VHD and the human VHD from ABLIM2 revealed that those residues are mostly conserved.

```
                10         20          30         40         50         60
Chicken         PTKLETFPLDVL--VNTAAEDLPRGVDPSRKENHLSDEDFKAVFGMTRSAFANLPLWKQQ
                  1        10          20         30         40         50
hABLIM2         --QYKIYPYDSLIVTNRIRVKLPKDVDRTRLERHLSPEEFQEVFGMSIEEFDRLALWKRN
                  : : :* * *  .*     .**: ** :* *.*** *:*: ****: . * .* ***::

                  70   75
Chicken         NLKKEKGLF
                 60    66
hABLIM2         DLKKKALLF
                :***:  **
```

Figure 9.11 Sequence alignment (performed using Clustal Omega (EBI) between chicken VHD and human VHD from ABLIM2 showing that the residue involved in the binding of VHD to actin at high affinity are conserved between these species.

It is also reported in the literature that not all the isoforms of VHD maintain their ability to bind actin filaments with high affinity and the alternately charged surface determine their affinity to actin [43, 99]. To better understand the effective importance that those positively charged residues posses in the modulation of the affinity to actin filaments for the VHD isoform from ABLIM2, different ABLIM2-VHD mutants for arginine and lysine were expressed. For each mutant, the solubility was analysed as parameter to define a mutation that affects the folding of the protein and the affinity to actin was measured by cosedimentation assay for the soluble mutants. The limitations of the mutagenesis approach to the positively charged residues had the purpose to link the results to a possible NMR characterization of these residues that, unfortunately, is still in development.

```
1        10         20         30          40         50        60    66
QYKIYPYDSLIVTNRIRVKLPKDVDRTRLERHLSPEEFQEVFGMSIEEFDRLALWKRNDLKKKALLF
```

Figure 9.12 Sequence from human VHD from ABLIM2. In red are highlighted the positions of the different positively charged residues that were mutated.

The mutants expressed and the respective primers designed for the mutagenesis are reported in Table 9.3. The sequence of each couple of primers was designed using the NEBbasechanger™ online tool provided by the New England BioLabs®, while the melting temperature (T_m) was reported by the supplier of the oligonucleotides (Sigma). The annealing temperature (T_a) applied during the PCR step was calculated as

$$T_a = T_m - 4°C$$

Each plasmid generated after the mutagenesis step was then sequenced to confirm the insertion of the mutation in the desired position using primer designed on the T7 promoter. The alignment of all the sequences containing a point mutation against the wild type are reported in APPENDIX D.

Mutants	**Primers used**	**Tm**
R15A and R17A	F- GCCGTGGTGAAACTGCCCAAAGAC R- AATGGCGTTTGTGACGATGAGGGAG	63°C
R26A and R28A	F- GGCCCTGGAGAGACACTTGTCG R- GTGGCGTCCACGTCTTTGGGCAG	65°C
R26A, R28A and R31A	F- CCACTTGTCGCCCGAGGAGTTCCAG R- GCCTCCAGGGCCGTGGCGTCCAC	68°C
R31A	F- CCACTTGTCGCCCGAGGAGTTC R- GCCTCCAGTCTCGTCCGGTCCAC	65°C
K62A and K63A	F- GCCAAAGCCCTTTTGTTCTGAATG R- GGCGTCATTCCTCTTCCAGAG	59°C
K61A	F- CCTTAAGAAGGCCGCCCTTTTGTTCTG R- TCATTCCTCTTCCAGAGG	58°C

Table 9.3 List of different mutants for VHD expressed. For each mutant it is reported also the mutagenesis primer used and the Tm temperature for each couple of primer as calculated by the oligonucleotides supplier (Sigma).

In the literature it is reported that the three lysine residues 61 to 63 are crucial for binding. While it seems that lysine 62 and 63 are involved in the modulation of the binding, lysine 61 is implicated in the formation of a salt bridge with glutamic acid 30 (E30) and it is essential for the correct folding of VHD. It was not possible to purify the mutant K61A confirming that the disruption of this salt bridge causes interferes with the proper folding of VHD and a tendency to precipitate (Figure 9.13). On the other hand, mutant K62A/K63A was expressed and purified (Figure 9.14). The affinity calculated (3.8µM) for this mutant was slightly lower than the one calculated for the wild type VHD bound to actin filaments of 2.5µM (Figure 9.15).

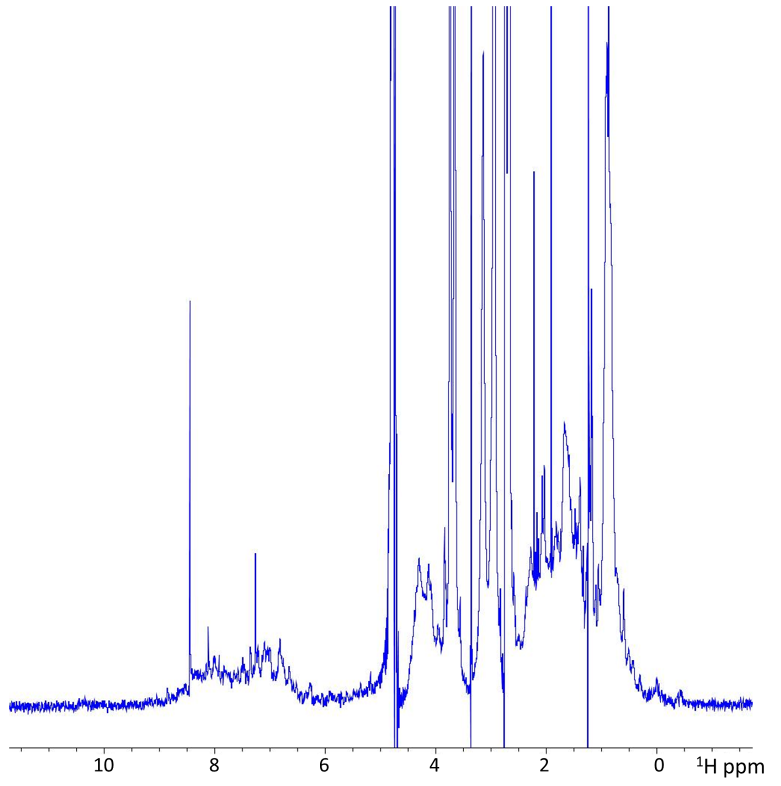

Figure 9.13 1D ^{1}H proton detection on K61A mutant of VHD. The mutation of lysine 61 in alanine drastically affected the proper folding of the protein as shown by the collapsing of the signals from proton atoms bound to the nitrogen in the backbone and the missing of the signals that characterized a folded VHD around -0.5ppm. The spectrum was acquired at room temperature in a 500MHz Bruker magnet equipped with a triple resonance cryoprobe.

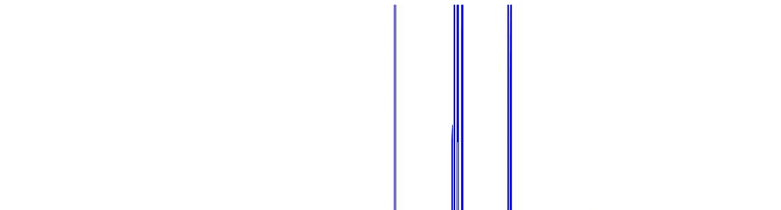

Figure 9.14 1D ^{1}H proton detection on K62A/K63A mutant of VHD. No suggestion of structural damage or problem in VHD folding was observable in the spectrum. The spectrum was acquired at room temperature in a 500MHz Bruker magnet equipped with a triple resonance cryoprobe.

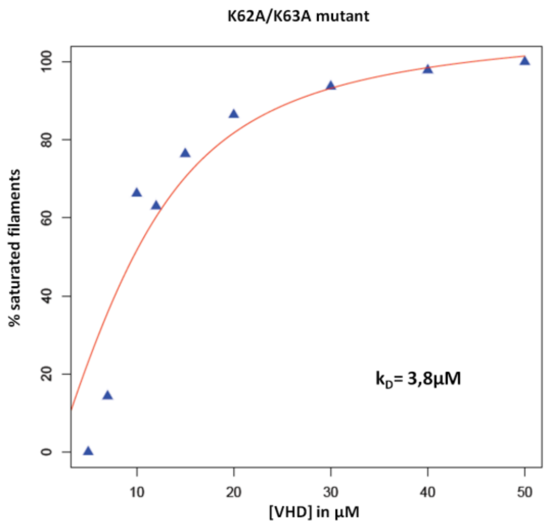

Figure 9.15 Fitting of the data from binding affinity assay for K62A/K63A mutant of VHD. The calculated k_D of approximately value of 3.8µM was slightly lower than the one calculated for the wild type VHD of 2.5µM. The fitting was performed using R software.

Similarly to the K61A mutant, the R15A/R17A had the tendency to precipitate and it was not possible to measure its affinity suggesting a structural involvement rather than a role in the binding to the filaments for these residues (Figure 9.16).

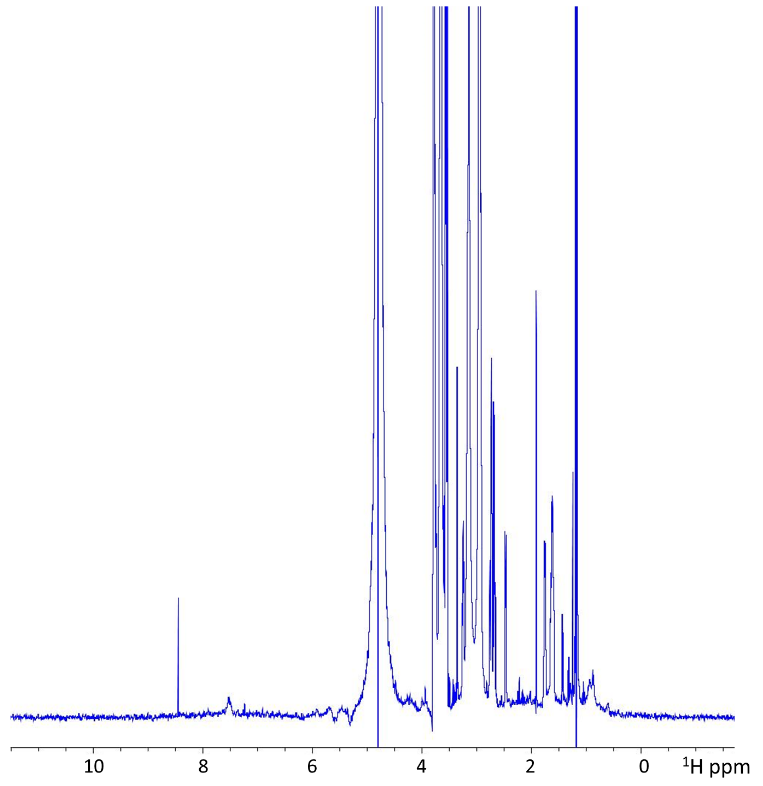

Figure 9.16 1D ^{1}H proton detection on R15A/R18A mutant of VHD. The mutation of arginine 15 and 18 in alanine produced a protein with the tendency to precipitate and unfold. The spectrum was acquired at room temperature in a 500MHz Bruker magnet equipped with a triple resonances cryoprobe.

The different mutants on the R26, R28 and R31 were all successfully purified (Figure 9.17, Figure 9.18 and Figure 9.19). The binding affinity calculated for mutant R26A/R28A showed to be slightly lower (3µM) than the wild type VHD (2µM) while mutant R31A showed the same affinity constant of wild type (2µM). Mutant R26A/R28A/R31A was the only one that showed a modest decrease in the binding affinity (9.7µM) when compared to the wild type, suggesting that all of them are equally but only moderately involved in the binding event (Figure 9.20).

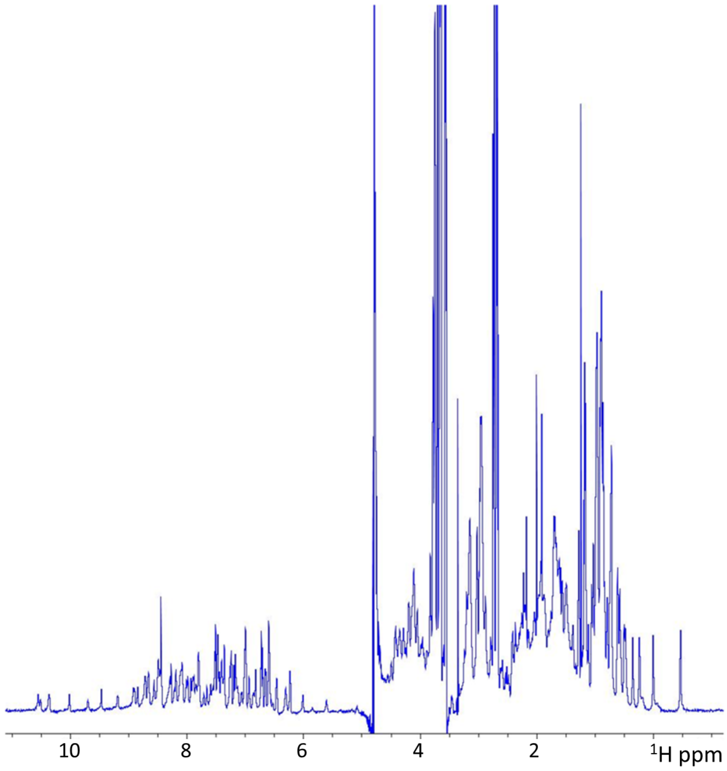

Figure 9.17 1D ^{1}H proton detection on R31A mutant of VHD. No suggestion of structural damage or problem in VHD folding was observable in the spectrum. The spectrum was acquired at room temperature in a 500MHz Bruker magnet equipped with a triple resonance cryoprobe.

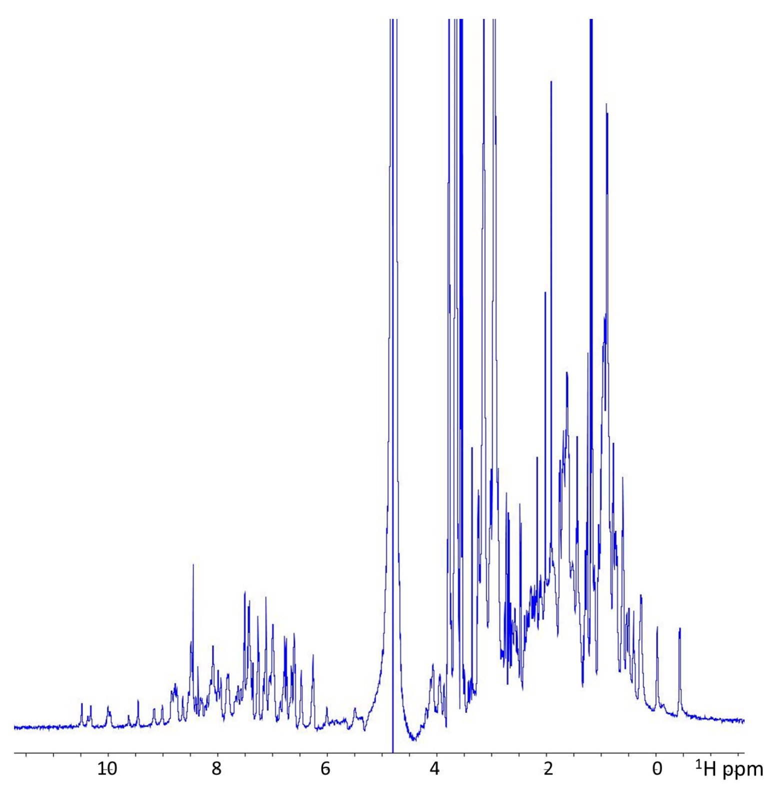

Figure 9.18 1D ^{1}H proton detection on R26A/R28A mutant of VHD. No suggestion of structural damage or problem in VHD folding was observable in the spectrum. The spectrum was acquired at room temperature in a 500MHz Bruker magnet equipped with a triple resonance cryoprobe.

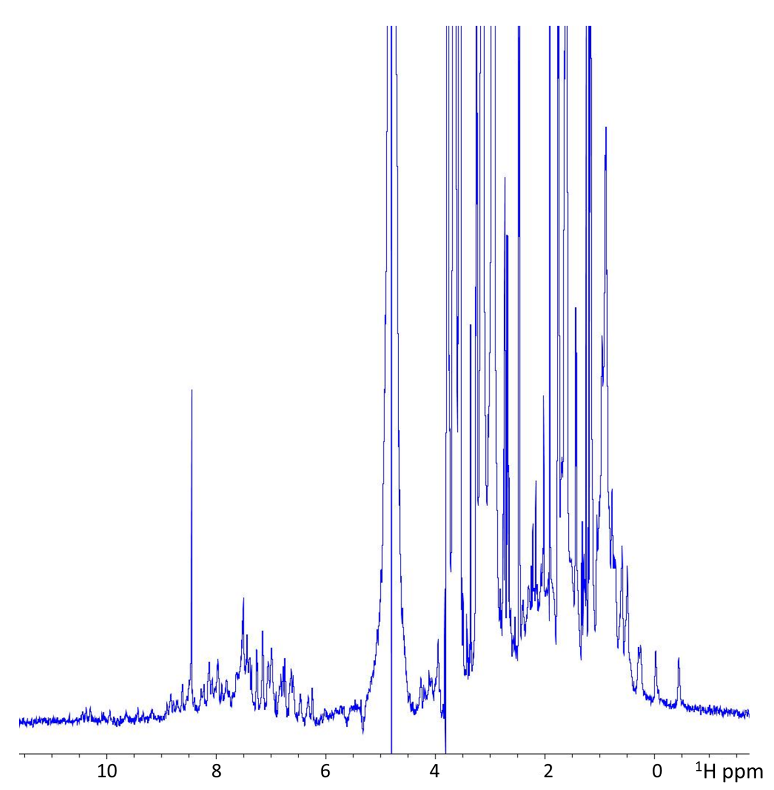

Figure 9.19 1D ^{1}H proton detection on R26A/R28A/R31A mutant of VHD. No suggestion of structural damage or problem in VHD folding was observable in the spectrum. The spectrum was acquired at room temperature in a 500MHz Bruker magnet equipped with a triple resonance cryoprobe.

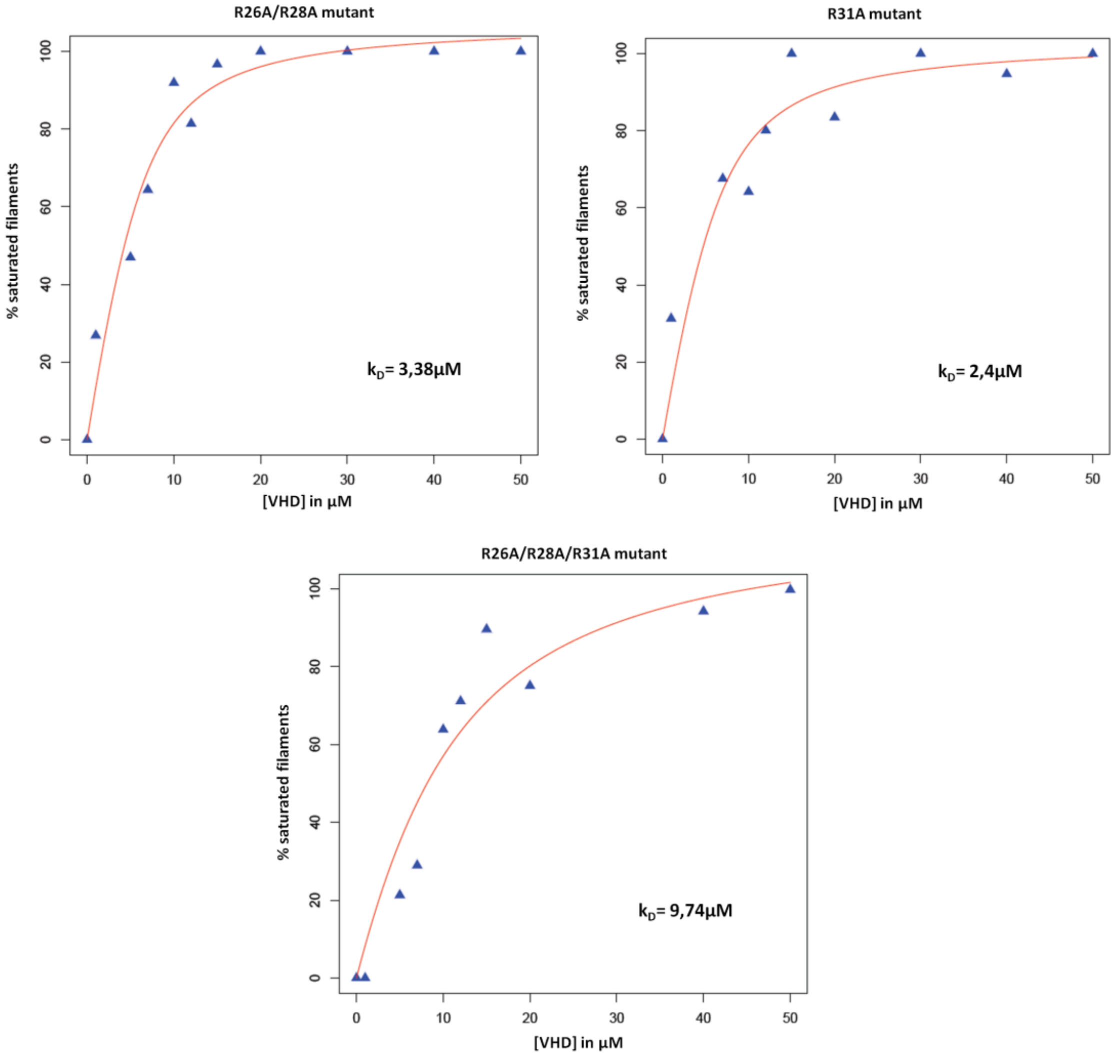

Figure 9.20 Fitting of the data from binding affinity assay for the mutants in the residues R26, R28 and R31. The R31 mutation showed a protein with the same binding affinity to actin showed by the wild type VHD. When both R26 and R28 were mutated the affinity slightly decreased to 3,4µM, while the simultaneous mutation of R26, R28 and R31 dropped the affinity to almost 10µM. The fitting was performed using the script written by Dr. Pfuhl and computed in R software.

The results obtained in the mutagenesis showed a partial involvement of positively charged residues in the binding of actin filaments but a more crucial role played in the correct folding of the protein. Remembering that it is reported that the alternate charge of the surface of VHD is essential for the binding of VHD to actin filaments, the results could simply suggest that it is not a single residue that can modulate the binding affinity but more likely a global effect from all the positively charged residues. To better understand how the binding is actually modulated, it will be necessary to express different mutants of VHD containing both mutations of the positively charged patch and the crown. The phenotype for the mutants expressed is summarized in Table 9.4.

Mutants	Effect on VHD
R15A and R17A	Crucial in VHD proper folding
R26A and R28A	Almost the same affinity of wt VHD
R26A, R28A and R31A	Lower affinity to filaments
R31A	Same affinity of wt VHD
K62A and K63A	Almost the same affinity of wt VHD
K61A	Crucial in VHD proper folding

Table 9.4 List of VHD mutants expressed and phenotypic effect produced by each mutation.

9.3 Early data in actin filaments regions involved in binding to VHD: paramagnetic ssNMR spectroscopy

Despite the less stringent limitations on the molecular size and the crystalline state that characterize ssNMR spectroscopy in respect of solution NMR and X-ray diffraction, ssNMR lacks in the methods to collect long-range data. It was possible to overcome this problem by the addition in selected sites of a macromolecule of a covalently bound paramagnetic center. In a paramagnetic center, unpaired electrons can couple with the nuclei in the surrounding and the interactions can appear in solution NMR spectra in three different ways each exhibiting long-range structural information: Paramagnetic Relaxation Enhancements (PREs), Pseudo-Contact Shifts (PCSs, i.e. contributions to the chemical shift) and Residual Dipolar Couplings (RDC) (Figure 9.21) [102]. PCSs and RDCs will not be taken into account in this dissertation that will be focused only in the effect of PREs.

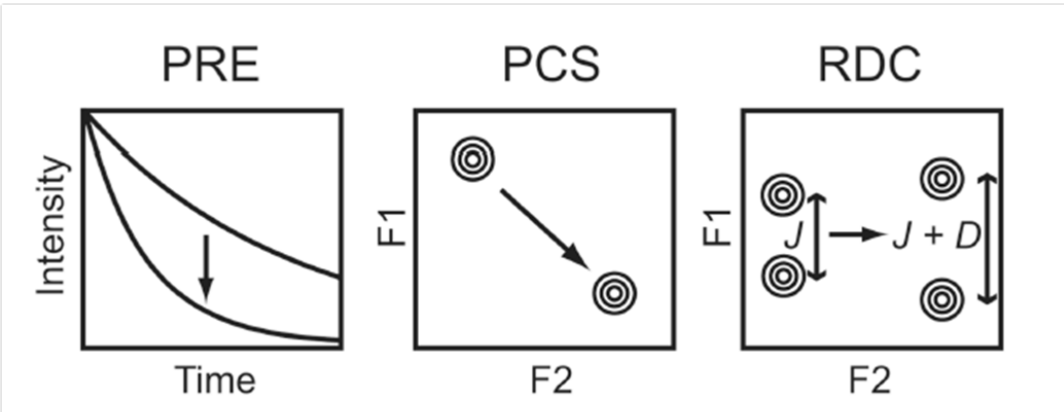

Figure 9.21 Long-range structural information achievable using paramagnetic NMR spectroscopy: Paramagnetic Relaxation Enhancements (PREs), Pseudo-Contact Shifts (PCSs, i.e. contributions to the chemical shift) and Residual Dipolar Couplings (RDC) [102].

A paramagnetic center can be introduced into a protein by either substitution of the metal ion in metalloproteins or by covalently binding of metal-binding peptides or small molecule tags coordinating a paramagnetic metal ion [103]. Every paramagnetic species, such as nitroxide spin label (i.e. MTSL), Gd, Mn, Cu, etc. exhibit PREs that leads to line-broadening in a distance dependent manner. Both longitudinal and transversal relaxation rates are affected by the presence of the spin label and the Solomon dipolar relaxation is considered as the primary mechanism responsible for causing longitudinal (Γ1) and transverse (Γ2) nuclear PREs. In ssNMR the coupling among electron nuclei is assumed to be modulated mainly by rapid electron spin relaxation and molecular dynamics (Figure 9.22), approximating the two types of relaxation as:

$$\Gamma_1 \approx 2k\frac{\gamma_I^2 S(S+1)}{r^6}\left(\frac{3\tau_e}{1+\omega_I^2\tau_e^2}+\frac{7\tau_e}{1+\omega_S^2\tau_e^2}\right)$$

$$\Gamma_2 \approx k\frac{\gamma_I^2 S(S+1)}{r^6}\left(4\tau_e+\frac{3\tau_e}{1+\omega_I^2\tau_e^2}+\frac{13\tau_e}{1+\omega_S^2\tau_e^2}\right)$$

where r is the distance between the paramagnetic center and the nucleus observed, γ_I is the gyromagnetic ratio of nucleus observed, S is the electron spin, ω_I and ω_S are respectively the nuclear and electron Larmor frequencies, τ_e is the correlation time and the constant k contains:

$$k = \frac{1}{15}\left(\frac{\mu_0}{4\pi}\right)^2 \hbar^2 g_e^2 \mu_B^2$$

where μ_0 is the free space permittivity, $\hbar$ is Plsnk's constant dividev by 2π, g_e is the free electron g-factor and μ_B is the the Bohr electron magneton [104]. It is important to consider that the PREs effect on the surrounding spins depends to the sixth power of the distance from the center, meaning that its influence is appreciable in spins closer than 25-30Å from the paramagnetic spin label [105]. The fact that the relaxation depends on the square of the gyromagnetic ratio of the affected nucleus (γ_I) means that ^{1}H is the most sensitive nucleus to the paramagnetic relaxation and that ^{13}C and ^{15}N are, respectively, 16 and 100 times less sensitive [106].

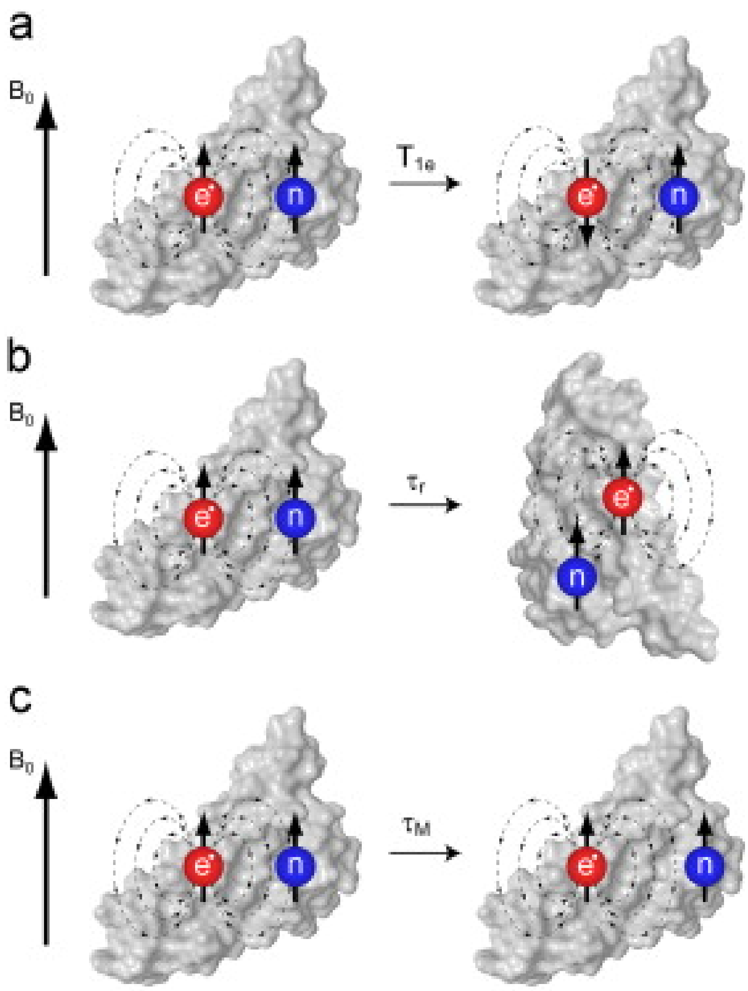

Figure 9.22 Rapresentation of the magnetic field fluctutation leading to enhanced nuclear spin relaxation: (a) electron spin relaxation, (b) molecular reorientation and (c) chemical exchange. The spin label and nucleus are labelled as e• and n, respectively, and B_0 represents the external applied magnetic field. The dipolar field generated by the spin label at the nucleus fluctuates as a function of time in (a) direction, (c) intensity, or (b) a combination of direction and intensity [107].

The basic concept behind the paramagnetic ssNMR spectroscopy is that it would be possible to determine the distance of a resonance from a paramagnetic center comparing the intensity of its signal with the intensity that has in a reference spectrum recorded without the presence of the spin label on the protein. A decrease in the amplitude between them means that the nucleus is spatially near the spin label and the quantification of the decrease could return the effective distance to use as restrain in the calculation of the structure of a protein (Figure 9.23) [108].

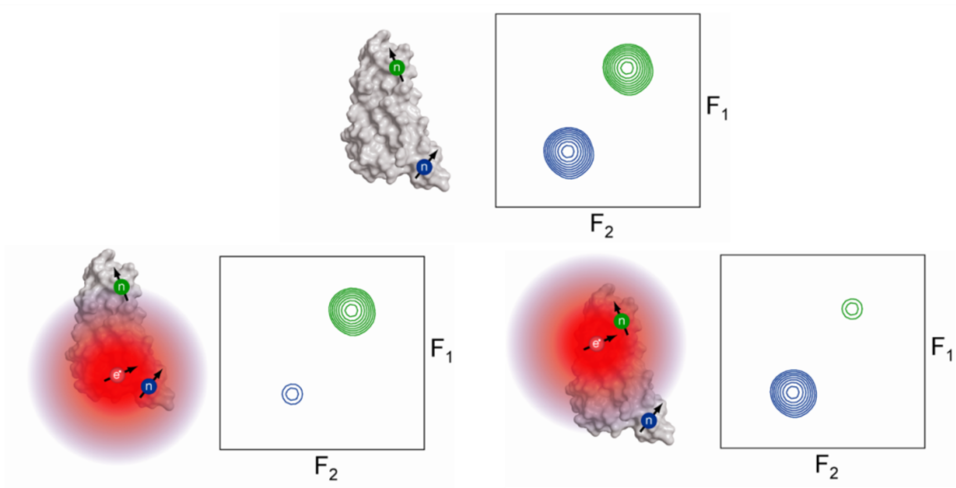

Figure 9.23 Schematic 2D NMR spectra for a diamagnetic protein (top) and two of its variants containing covalent paramagnetic tags, showing the PREs dependence on the distance observing the intensity of the nuclear spin signals (green and blue) based on their proximity to the paramagnetic center (red sphere). The effect of the PRE effect is represented by the red sphere around the spin label that fade away in respect to the distance from the spin label [108].

To better clarify the reason behind this intensity changes due to the presence of a paramagnetic center in solid state experiment is necessary to focus on the point that the presence of the spin label enhances the relaxation rate of the nuclei in its surrounding. This means that, as a consequence, the dipolar coupling associated to them will be affected as well. Remembering that the magnetization transfer mediated by cross polarization occurs among coupled spins, changes in the dipolar coupling will be reflected by changes in the conditions that allow the optimal transfer of magnetization among those nuclei. To obtain preliminary data about the filaments region that makes contact with VHD, actin subunits were modified with the covalently addition to cysteine 374 of a molecule of (1-oxy-2,2,5,5-tetramethyl-delta3-pyrroline-3-methyl) methane thiosulfonate (MTSL) that acts as a paramagnetic center. A ^{13}C-^{13}C DARR experiment (using a 20ms mixing time) on a uniformly labelled ^{13}C-^{15}N VHD bound to these modified filaments was acquired and the spectrum obtained was compared to the spectrum (acquired with the same parameters) of ^{13}C-^{15}N VHD-F.actin complex in which the filaments were not modified. The position of the paramagnetic center on the surface of actin filaments was calculated covalently by docking the MTSL to Cys374 of an actin monomer using CovDock (software contained in the Schrodinger suite BioLuminate [109]). The software creates the covalent bond and it calculated the most probable orientation of the spin label on the surface of the actin monomers (Figure 9.24). As shown in Figure 9.23, it was assumed that observing a decrease in the amplitude of signals from the ^{13}C-^{15}N VHD bound to them it would have been possible to define the region on actin that could eventually be involved in the binding. Surprisingly the comparison of the ^{13}C-^{13}C DARR spectrum acquired in presence of the paramagnetic with the reference did not show any appreciable decreasing in the amplitude of any signal, suggesting that the paramagnetic spin label on actin was spatially too far (at least 25-30Å) from the VHD to affect the relaxation of it. Despite the negative results, this simple experiment narrowed the number of positions on the filament surface where the VHD can interact generating useful early data that could be used in future in the optimization of a structural model for the interaction between VHD and actin filaments.

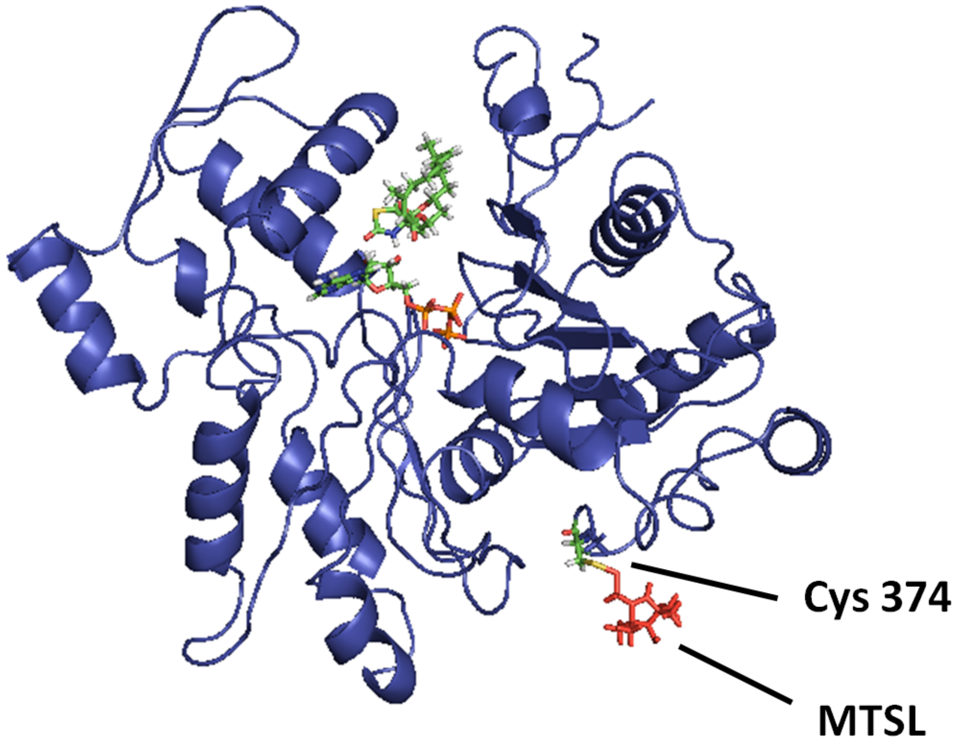

Figure 9.24 Ribbon scheme of an actin monomer modified with the covalently addition of a molecule of MTSL. The position was determinate by covalent docking simulation using the CovDock suites of Schrodinger software. The model was generated in PyMol software using a single actin subunit from the tropomyosin-myosin-F.actin model solved at 7.7Å deposited on PDB as (4A7F).

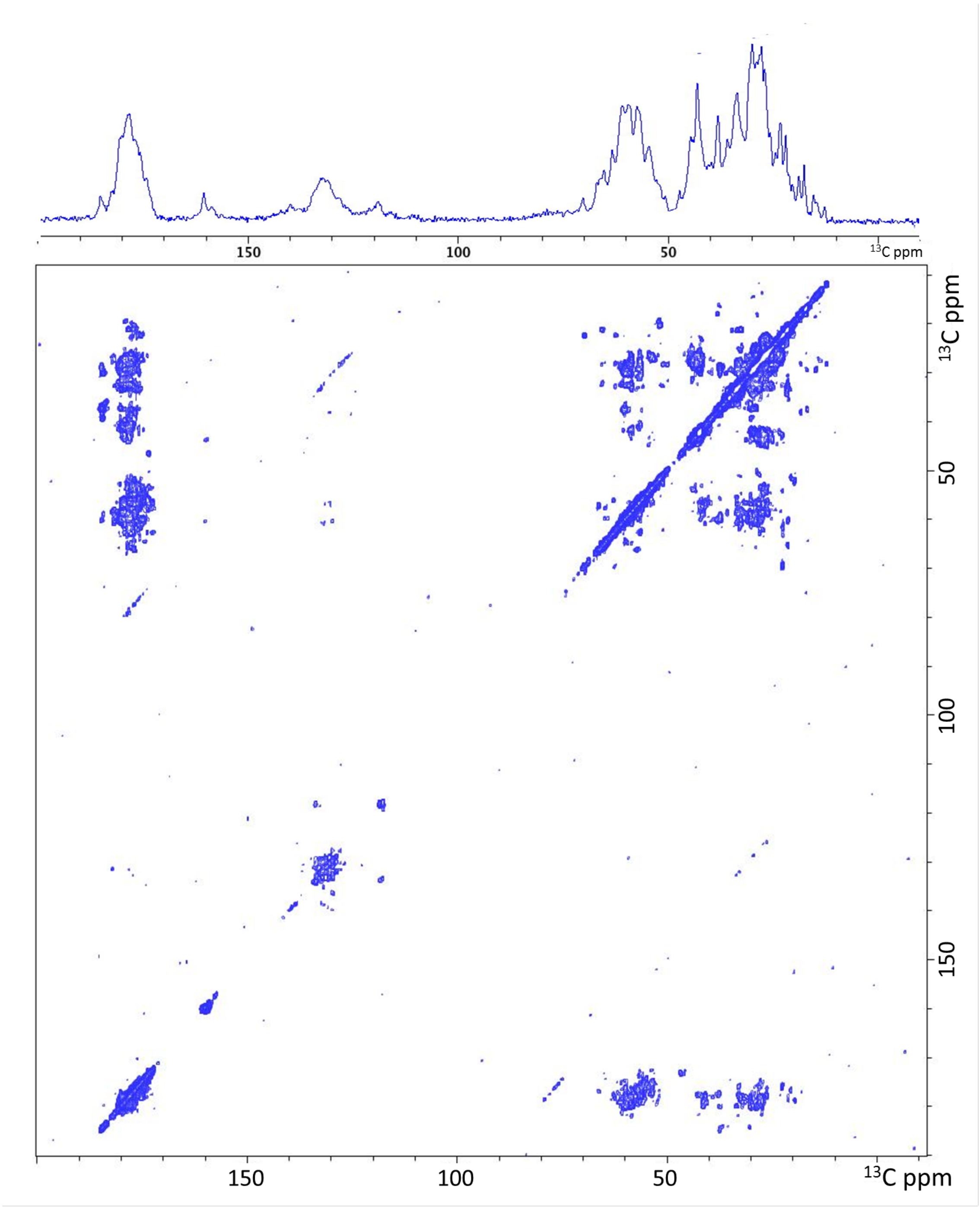

Figure 9.25 ^{13}C-^{13}C DARR spectrum (20ms mixing time) for a uniformly ^{13}C-^{15}N VHD bound to actin filaments covalently bound to MTSL. The spectrum obtained it is perfectly overlapped to the same experiment acquired on uniformly ^{13}C-^{15}N VHD bound to actin filaments without the spin label, meaning that the VHD is at least 6Å far from the spatial position of MTSL. The spectrum was acquired at 278K, 10kHz spinning rate using a 500MHz Bruker magnet equipped with triple resonance 4mm e-free probe.

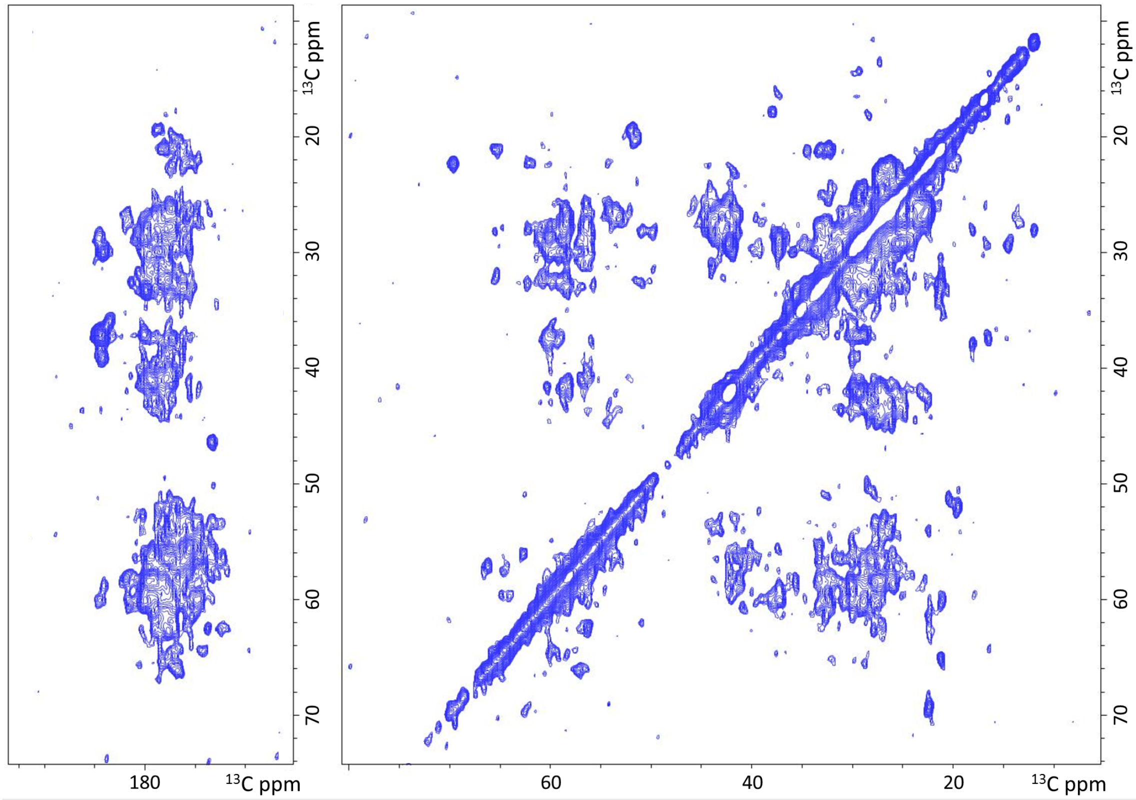

Figure 9.26 Magnification of carbonyl and aromatic cross peak region to aliphatic carbons (left panel) and aliphatic region (right panel) of a ^{13}C-^{13}C DARR spectrum acquired on a uniformly ^{13}C-^{15}N VHD bound to actin filaments modified with a covalently bound paramagnetic center. The spectrum was recorded at 278K, 10kHz spinning rate in a 500MHz Bruker magnet equipped with a triple resonance e-free probe.

10 Human skeletal Actin expression in *P. pastoris*

10.1 An insight about heterologuos protein expression in *P.pastoris*

P.pastoris is a yeast species widely used for the production of recombinant proteins. Yeast are eukaryotes and they share the same intracellular environment and many of the post-translational protein modification of higher eukaryotes, including humans. Thus, most important, they share a similar machinery for the folding of proteins that could help in the correctly expression of functional eukaryotic proteins [110].

P.pastoris is a methylotrophic yeast, capable of metabolizing methanol as its sole carbon source. Two regions in chromosome 4, *AOX1* and *AOX2*, encode for the enzyme alcohol oxidase, even if the majority of alcohol oxidase activity is due to the product of *AOX1* gene [111]. Expression of this gene is regulated at the level of transcription. In medium containing methanol as carbon source, approximately 5% of poly-A^+ RNA produced by *Pichia* is from the *AOX1* region but no expression of *AOX1* is detectable if the cells are growth in presence of glycerol only. For these reason, heterologous protein expression in *P.pastoris* is under the control of the promoter for the production of the enzyme alcohol oxidase.

Methanol enters the peroxisome and is oxidized to hydrogen peroxide and formaldehyde by AOX1, utilizing oxygen as an electron acceptor. The peroxide is oxidized to water and oxygen by peroxisomal catalase. In the methanol oxidation pathway, oxygen acts as the limiting reagent for the uptake and metabolism of methanol and becoming one of the critical parameters in the successful utilization of *P.pastoris* as host for heterologous protein production. The formaldehyde produced then enters the cytosol to some extent and it is used for the production of energy and biomass (Figure 10.1).

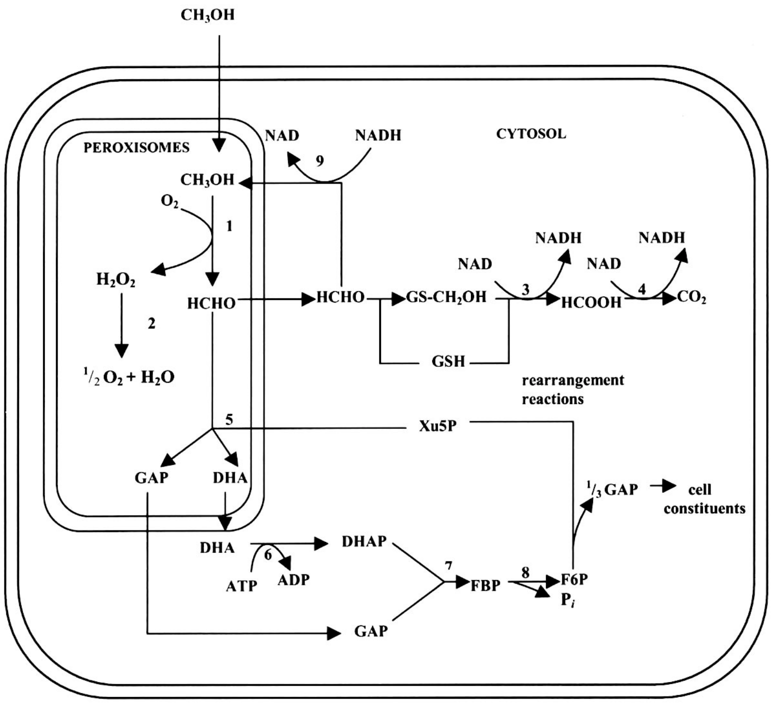

Figure 10.1 Methanol metabolism pathways and their compartimentation in methylotrophic yeasts. 1) alcohol oxidase, 2) catalase, 3) formaldehyde dehydrogenase, 4) formate dehydrogenase, 5) dihydroxyacetone synthase, 6) dihydroxyacetone kinase, 7) fructose-1,6-bisphosphate aldolase, 8) fructose-1,6-bisphosphotase, 9) formaldehyde reductas. Methanol is transformed in formaldehyde by AOX1. Formaldehyde moves to cytosol where it forms a complex with reduced glutathione and is oxidized to carbon dioxide by two subsequent dehydrogenase reactions. In the first step, formaldehyde dehydrogenase catalyzes the production of formate, subsequently, from which carbon dioxide is generated by the action of formate dehydrogenase. In the assimilatory pathway, formaldehyde that remains in the peroxisome reacts with xylulose-5-phosphate. In this reaction, catalyzed by dihydroxyacetone synthase, two C3 compounds, dihydroxyacetone and glyceraldehyde-3-phosphate, are produced [112].

The Phillips Petroleum Company was the first to develop media and protocols for growing *P.pastoris* on methanol in continuous culture at high cell density for the production of food for animal feeding in the '70 [113]. The crisis in oil in the middle of '70 increased the price of methane, the precursor for the production of methanol, and consequently the use of *P.pastoris* as host for the expression of protein for food for animal feeding was abandoned. Nevertheless, in the following decades, Phillips Petroleum started a partnership with the biotech company SIBIA (La Jolla, Ca, USA) that lead to the characterization of *P.pastoris* as a system for the heterologous protein expression [113]. From that point, *P.pastoris* has started to be widely used to produce a variety of proteins from different species and since 2002 there has been a great increase in recombinant protein production using *Pichia* [114].

The reasons for the rising of *Pichia* as a successful expression system can be summarized in the two points reported below:

- the transcription of heterologous protein is strictly regulated by a repression/derepression mechanism. The induction by methanol allows a two step protocol in which a cell grown at high density can be achieved before the activation of protein expression by the switching of media to methanol.
- the yield of protein expressed can be very high (from milligrams to grams) even if the protein is toxic for the cells [113].

10.2 Human Skeletal Actin (hACTs) expression

10.2.1 *hACTs* cloning into pPICzA vector

The six isoforms of actin in human possess very similar amino acid sequences, with no isoform sharing less than 93% identity with any other isoform (Figure 10.2). Four of them, $\alpha_{skeleta}$l-actin, $\alpha_{cardiac}$-actin, α_{smoot}h-actin, and γ_{smooth}-actin, are expressed primarily in skeletal, cardiac, and smooth muscle while the two remaining, β_{cyto}-actin and γ_{cyto}-actin are ubiquitously expressed [115].

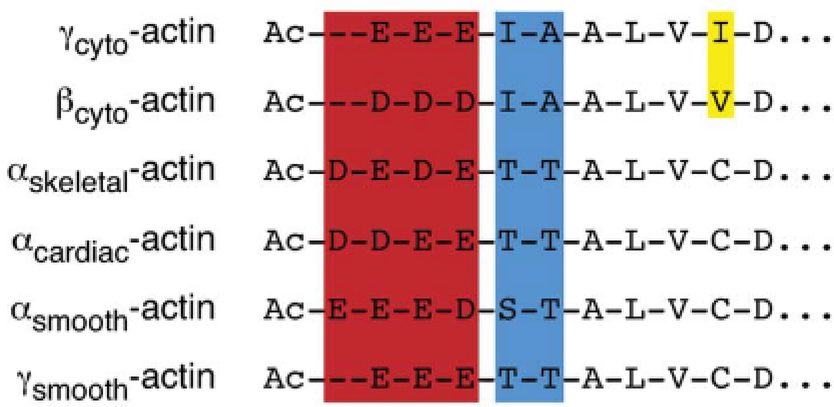

Figure 10.2 Alignment of the N-terminal ends of the six mammalian actin isoforms. The residues in red exhibit the most variability within and between muscle and cytoplasmic isoforms. Blue residues primarily vary between cytoplasmic and muscle isoforms.

Showing this high homology, to correctly select the right nucleic sequence for human skeletal actin (*hACT1s*), instead of to start from a human gene library, it was preferred to buy the clone IRAUp969C0654D containing the gene *hACT1s* from eBioscience. The complete sequence of *hACT1s* (1131bp) is reported below:

ATGTGCGACGAAGACGAGACCACCGCCCTCGTGTGCGACAATGGCTCCGGCCTGGTGAAAGC
CGGCTTCGCCGGGGATGACGCCCCTAGGGCCGTGTTCCCGTCCATCGTGGGCCGCCCCCGAC
ACCAGGGCGTCATGGTCGGTATGGGTCAGAAAGATTCCTACGTGGGCGACGAGGCTCAGAGC
AAGAGAGGTATCCTGACCCTGAAGTACCCTATCGAGCACGGCATCATCACCAACTGGGATGAC
ATGGAGAAGATCTGGCACCACACCTTCTACAACGAGCTTCGCGTGGCTCCCGAGGAGCACCCC
ACCCTGCTCACCGAGGCCCCCCTCAATCCCAAGGCCAACCGCGAGAAGATGACCCAGATCATG
TTTGAGACCTTCAACGTGCCCGCCATGTACGTGGCCATCCAGGCCGTGCTGTCCCTCTACGCCT
CCGGCAGGACCACCGGCATCGTGCTGGACTCCGGCGACGGCGTCACCCACAACGTGCCCATTT
ATGAGGGCTACGCGCTGCCGCACGCCATCATGCGCCTGGACCTGGCGGGCCGCGATCTCACC
GACTACCTGATGAAGATCCTCACTGAGCGTGGCTACTCCTTCGTGACCACAGCTGAGCGCGAG
ATCGTGCGCGACATCAAGGAGAAGCTGTGCTACGTGGCCCTGGACTTCGAGAACGAGATGGC
GACGGCCGCCTCCTCCTCCTCCCTGGAAAAGAGCTACGAGCTGCCAGACGGGCAGGTCATCAC
CATCGGCAACGAGCGCTTCCGCTGCCCGGAGACGCTCTTCCAGCCCTCCTTCATCGGTATGGA
GTCGGCGGGCATTCACGAGACCACCTACAACAGCATCATGAAGTGTGACATCGACATCAGGA
AGGACCTGTATGCCAACAACGTCATGTCGGGGGGCACCACGATGTACCCTGGGATCGCTGAC
CGCATGCAGAAAGAGATCACCGCGCTGGCACCCAGCACCATGAAGATCAAGATCATCGCCCC
GCCGGAGCGCAAATACTCGGTGTGGATCGGCGGCTCCATCCTGGCCTCGCTGTCCACCTTCCA
GCAGATGTGGATCACCAAGCAGGAGTACGACGAGGCCGGCCCTTCCATCGTCCACCGCAAAT
GCTTC.

The clone was inoculated in 5ml of LB medium without antibiotic and incubated overnight at 37°C in a shaker. The cells were then centrifuged and the plasmid containing the gene of interest purified using PureLink® HiPure Plasmid Midiprep Kit from Invitrogen.

The pPICzA vector (3329 nucleotides) was chosen as receiver vector for *P.pastoris*. pPICzA included the gene that confers the resistance to Zeocin^{TM}, an high-copy-number ColE1/pMB1/pBR322/pUC origin of replication and the inducible promoter by methanol *AOX1*.

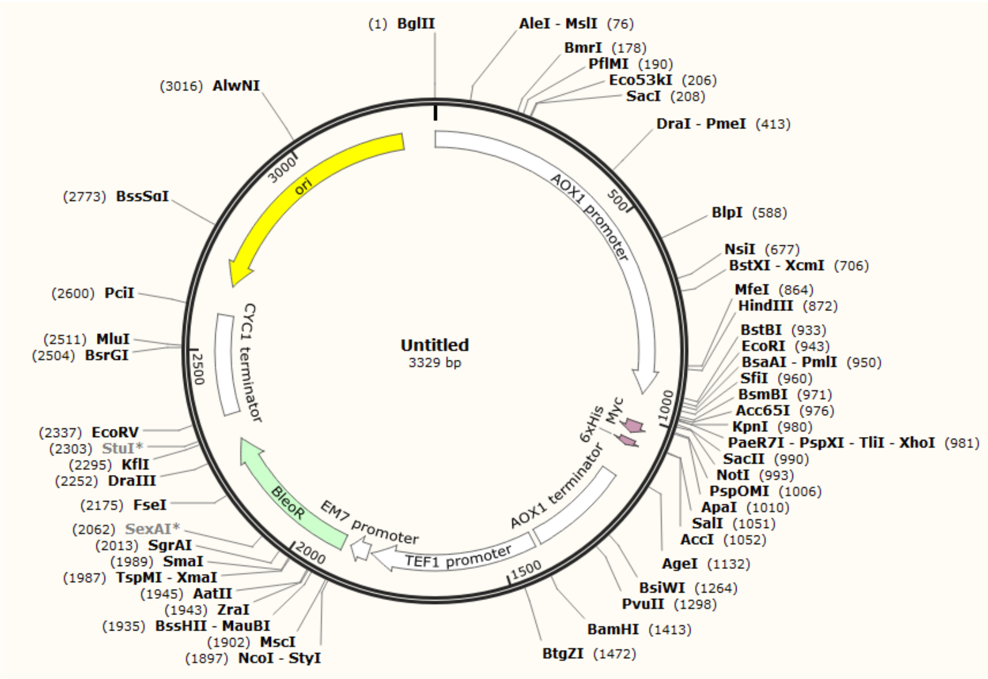

Figure 10.3 pPICzA vector map. The vector included: 5´ AOX1 promoter region: bases 1-941, 5´ end of AOX1 mRNA: base 824, 5´ AOX1 priming site: bases 855-875, Multiple cloning site: bases 932-1011, c-myc epitope tag: bases 1012-1044, Polyhistidine tag: bases 1057-1077, 3´ AOX priming site: bases 1159-1179, 3´ end of mRNA: base 1250, AOX1 transcription termination region: bases 1078-1418, Fragment containing TEF1 promoter: bases 1419-1830, EM7 promoter: bases 1831-1898, Sh ble ORF: bases 1899-2273, CYC1 transcription termination region: bases 2274-2591, pUC origin: bases 2602-3275 (complementary strand) [Invitrogen website].

Zeocin™ is a basic, water-soluble compound isolated from *Streptomyces verticillus* as a copper-chelated glycopeptide that belongs to a family of structurally related bleomycin/phleomycin-type antibiotics isolated from *Streptomyces*. Antibiotics in this family are broad spectrum antibiotics that act as strong antibacterial and anti-tumor drugs. They show strong toxicity against bacteria, fungi (including yeast), plants, and mammalian cells. The mechanism of action for Zeocin™ is still unknown but it was hypothesized that it acts as a DNA restriction enzyme causing the death of the cell.

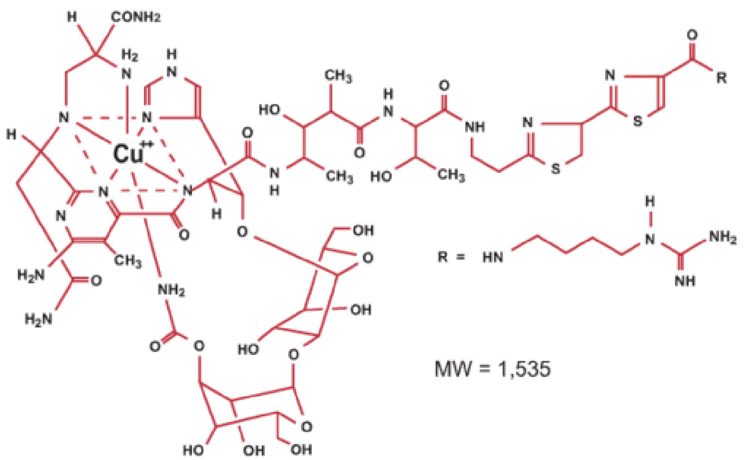

Figure 10.4 Structure of Zeocin™.

At the C-terminal of the protein a c-Myc tag epitope and a 6 histidine repeat were included in the vector, respectively, for an easy recognition and a fast purification of the protein expressed. The multiple cloning site sequence was reported in Figure 10.5. KpnI (GGTACC) and ApaI (GGGCCC) were chosen as restriction site to insert the *hACTs* gene.

```
                 5′ end of AOX1 mRNA                                   5′ AOX1 priming site
811   AACCTTTTTT TTTATCATCA TTATTAGCTT ACTTTCATAA TTGCGACTGG TTCCAATTGA

871   CAAGCTTTTG ATTTTAACGA CTTTTAACGA CAACTTGAGA AGATCAAAAA ACAACTAATT

        Sfu I         EcoR I      Pml I          Sfi I          BsmB I Asp718 I  Kpn I Xho I
931   ATTCGAAACG AGGAATTCAC GTGGCCCAGC CGGCCGTCTC GGATCGGTAC CTCGAGCCGC

     Sac II  Not I               Apa I                 myc epitope
991   GGCGGCCGCC AGCTT GGGCCC GAA CAA AAA CTC ATC TCA GAA GAG GAT CTG
                               Glu Gln Lys Leu Ile Ser Glu Glu Asp Leu

                                        Polyhistidine tag
1042  AAT AGC GCC GTC GAC CAT CAT CAT CAT CAT CAT TGA GTTTTAGCCT TAGACATGAC
      Asn Ser Ala Val Asp His His His His His His ***

1098  TGTTCCTCAG TTCAAGTTGG GCACTTACGA GAAGACCGGT CTTGCTAGAT TCTAATCAAG

              3′ AOX1 priming site
1158  AGGATGTCAG AATGCCATTT GCCTGAGAGA TGCAGGCTTC ATTTTTGATA CTTTTTTATT

                                              3′polyadenylation site
1218  TGTAACCTAT ATAGTATAGG ATTTTTTTTG TCATTTTGTT
```

Figure 10.5 Multicloning site sequence for pPICzA.

Despite the presence of two tags at the C-terminal of the protein no cleavage site was inserted in the sequence of pPICzA vector. For this reason, the primer designed for the C-terminal included two amino acids as a bridge and a cleavage site for TEV protease among the sequence for the ApaI (Figure 10.6). The best amplification was obtained using Taq polymerase over the Pfu polymerase due to the length of the reverse primer (Figure 10.7).

```
Forward primer
5′ – GCCGGCCGGTACCATGTGCGACGAAGACGAGACC – 3′
            KpnI

Reverse primer
5′ – GCCGCGCAGGGCCCGCTCTGAAAGTACAGATCCTCAGCAGCGAAGCATTTGCGGTGGACGATG – 3′
              ApaI     TEV cleavage site    Bridge
```

Figure 10.6 Sequence for forward and reverse primers used during the amplification of *hACTs*. The blue nucleotides in the forward primer identified the starting codon for the translation.

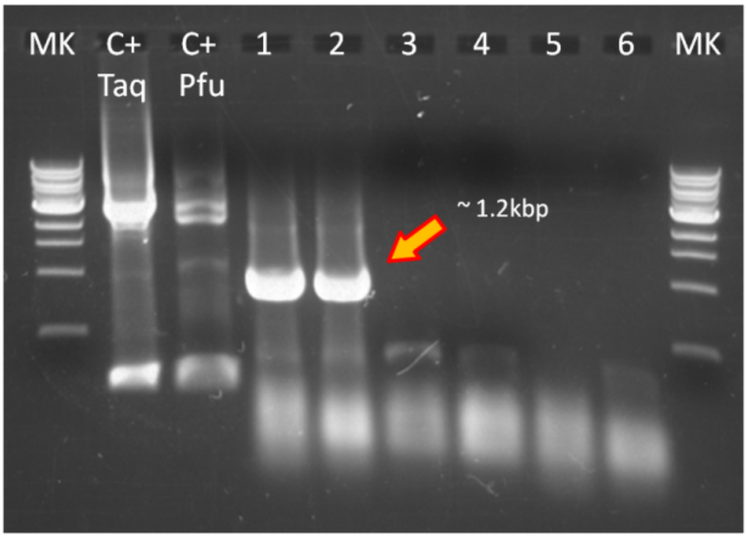

Figure 10.7 Agarose gel of the amplification of *hACTs* gene. 1kb ladder was added in the first and last line to follow the running of the sample in the gel. Positive control for Taq polymerase (C+ Taq) and Pfu polymerase (C+ Pfu) were used to validate the gel. Line 1 and 2 contains *hACTs* amplified using Taq polymerase while 3, 4, 5 and 6 using Pfu polymerase. The *hACTs* gene amplified is present only in line 1 and 2 indicating the failure by Pfu polymerase to amplify the gene.

The insert was successfully cloned inside the pPICzA plasmid and used to transform *E.coli* Top10 cells. The positive colonies grown in presence of Zeocin were then analysed by PCR to screen the false positive from the positive colonies (Figure 10.8). The ratio of positive colonies was poor but the few of them when sequenced confirmed the presence of the *hACTs* gene and they showed no error inserted by the poor fidelity Taq polymerase in the sequence.

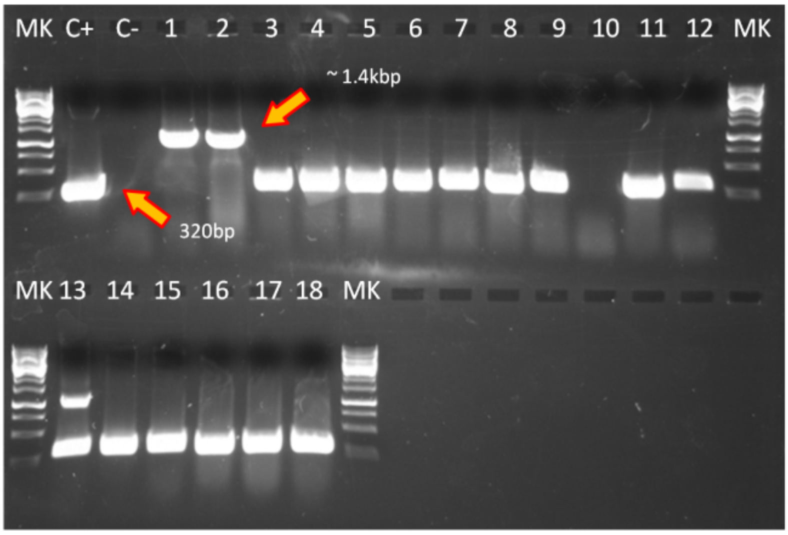

Figure 10.8 Agarose gel for colony PCR run on Top10 *E. coli* colonies transformed with pPICzA plasmid containing *hACTS* gene. Control positive (C+) in which it was amplified empty pPICzA plasmid and negative control (C-) in which no DNA was added to the master mix were added in order to validate the gel. The gel shows only two colonies transformed with the plasmid containing the gene of interest while all the other show a band similar to the C+ suggesting that the rate of incorporation of the *hACTs* gene in the plasmid was very poor.

10.2.2 Transformation of *P.pastoris*

The transformed cells were grown to produce a high amount of vector and after its purification, pPICzA containing *hACTs* gene was used to transform *P.pastoris* X33 strain. Electroporation and lithium acetate protocols were tested and it was determined that electroporation was the protocol with the highest efficiency of transformation.

The incorporation of DNA in P.pastoris occurs via homologous recombination between the transforming DNA and the regions of homology within the genome [116]. Differently from bacteria that keep the foreign plasmid carrying the gene of interest, this integration guarantees an extreme stability in the absence of selective pressure even when present as multiple copies. A single crossover event at the *AOX1* loci of both pPICzA and the genome of *P.Pastoris* resulted in the insertion of one or more copies of the vector upstream of the *AOX1* gene (Figure 10.9). The phenotype of such a transformant was Mut^{+}.

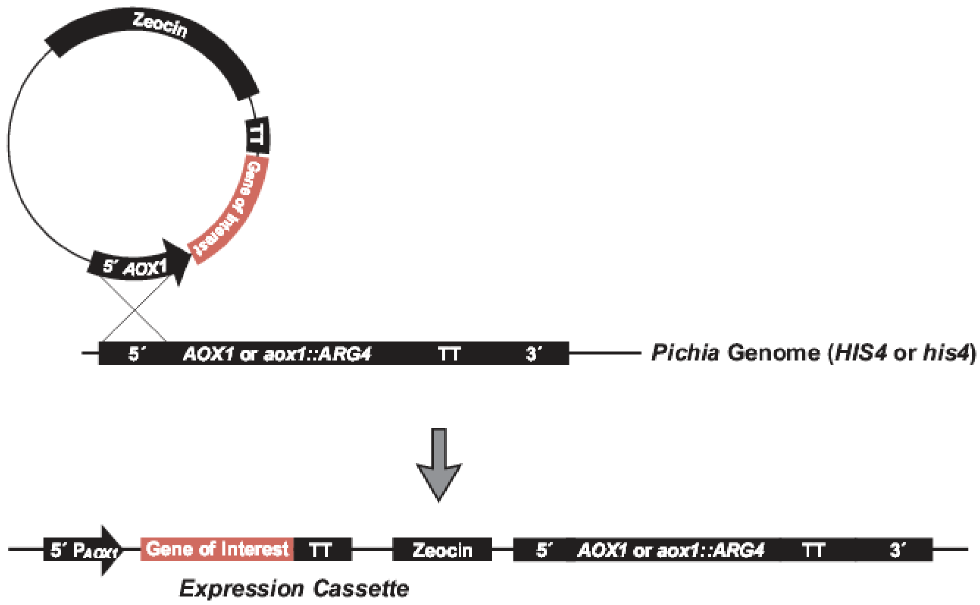

Figure 10.9 Mechanism for the insertion of pPICzA vector in the genome of *P.pastoris* by an event of recombination.

The lithium acetate protocol has not produced any transformed colony while the transformation ratio using the electroporation was poor. According to the literature it should have been in the order of thousand of transformed colonies from a single transformation event by electroporation. The few colonies obtained where tested by PCR for the incorporation of the plasmid in their genome (Figure 10.10).

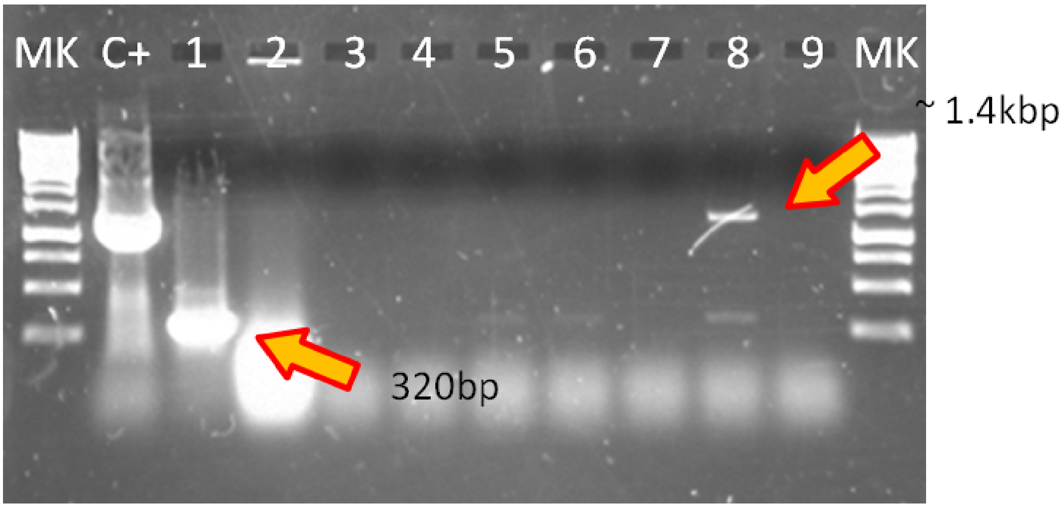

Figure 10.10 Agarose gel for colony PCR run on *P.pastoris* colonies transformed with pPICzA plasmid containing *hACTS* gene. Control positive (C+) in which it was amplified pPICzA plasmid containing *hACTs* (purified) was added in order to validate the gel. The gel shows only one colony transformed with the plasmid containing the gene of interest while most of the others show a band at 320bp (empty vector) or nothing at all.

10.2.3 Expression of hACTs in *P.pastoris*

The transformed colonies were checked for their ability to metabolize methanol. One of the colonies showing the Mut$^+$ phenotype was isolated and inoculated in 5ml of fresh YPD medium containing 15% glycerol. The culture was left to grow overnight at 30°C in a shaking incubator. The day after, the medium was centrifuges at 5000rpm for 10 minutes at room temperature. The pellet was resuspended in 2ml of fresh YPD medium containing 15% glycerol and subsequently divided in aliquot of 50µl, frozen in liquid nitrogen and stored at -80°C.

A single aliquot was left defrosting in ice and used to inoculate 5ml of fresh YPD medium and left grown overnight at 30°C in a shaking incubator. Accordingly on the protocol used the culture was centrifuge and resuspended in the appropriate minimal medium containing glycerol or glucose. When the O.D. at 600nm reached the desired value the cell were centrifuged again and resuspended in the same minimal medium previously used but containing methanol instead of glycerol or glucose to promote the expression. Initially, MM, BMM or BMMY media were tested. Unfortunately, in none of them it was possible to observe the expression of human skeletal actin. Other two different media, FM22 and FM23, were tested but no expression of heterologous actin was measured.

The list of all the media used and the recipes for their preparation is reported in Table 10.1.

Medium	Recipe	Concentration
MM	YNB Biotin Glycerol → Methanol	1.34% $4 \cdot 10^{-5}$% 1% → 0.5%
BMM	Potassium phosphate, pH 6.0 YNB Biotin Glycerol → Methanol	100 mM 1.34% $4 \cdot 10^{-5}$% 1% → 0.5%
BMMY	Yeast extract Peptone Potassium phosphate, pH 6.0 YNB Biotin Glycerol → Methanol	1% 2% 100mM 1.34% $4 \cdot 10^{-5}$% 1% → 0.5%
FM22	$CaSo_4$ K_2SO_4 $MgSO_4$ Biotin PTM1 Salt NH_4Cl Glucose → Methanol	0.1% 1.43% 1.17% $4 \cdot 10^{-5}$% $1 \cdot 10^{-4}$% 0.5% 5% → 0.5%
FM23	YNB Biotin $(NH_4)_2SO_4$ K_2HPO_4 KH_2PO_4 PTM1 Salt NH_4Cl Glucose → Methanol	0.8% 2mg/L 1.2% 0.3% 0.28% $2 \cdot 10^{-4}$% 1.2% 3% → 0.5%

Table 10.1 Minimal medium used in human skeletal actin expression trials in *P.pastoris*. The recipe for each medium is reported.

Considering the probable causes, it was assumed that it was likely improbable that the presence of the tag at the C-terminus in the cloned actin could interfere in the expression of the heterologous protein. On the other hand, the length of this tag could have a role in possible problems that could arise in the polymerization of these actin monomers. It has been published in early 2015 [117] a paper in which it is reported the first expression in *P.pastoris* of a labelled version of the heterologous actin from *Drosophila*. A collaboration started in the last few months with the author of the cited papers, Dr. Rosen (UT Southwestern in the University of Texas), revealed interesting insights in the method they used that could explain the failing in the human actin expression. They were able to express *Drosophila* actin at high levels (10mg/L of culture) when the sequence of actin was modified in order to block its ability to polymerize. This could imply that the heterologous version of actin interferes in the polymerization of endogenous actin which is toxic for the cells. Nevertheless, sampling the medium after induction no decrease in the cell mass was observed, contradicting this possible toxic action by human actin. Recently, Dr. Rosen reported (confidential data) that they were able to express at very low levels a version of wild type *Drosophila* actin. It is interesting to consider that to promote an efficient expression (even if producing small amount of actin in order of less than a milligram for liter of culture) they modified the entire nucleotide sequence of *Drosophila* actin in order to agree with the different codon usage of *P.pastoris*. The same sequence modification for the human skeletal actin is now under investigation. Despite the encouraging data reported, it is important to consider that the amount of heterologous actin that they can obtain is still not sufficient to start the development of expression protocols for the isotopic labelling of human skeletal wild type actin due to the cost that this would have. For this reason, a different expression system that could improve the expression of actin and still provide an efficient and low-cost system for an isotopic labelling protocol is also under investigation.

11 Discussion

11.1 Is ssNMR really suitable for the characterization of thin filament complexes?

ssNMR spectroscopy is considered as the last frontier in structural biology. Even if it is not a new approach, as the first NMR study on a solid was published in 1945 [118], it could be considered as an empty box in which a lot of effort (and money) to push it to its limits it has been invested. In a few years, we passed from the idea that it would have been impossible to acquire ssNMR spectra on protons at high resolution to almost routinely running ultrafast MAS experiments that can average to zero the ^{1}H-^{1}H dipolar contribution thus generating proton spectra at high resolution. The implementation of ssNMR spectroscopy to address biological problems is an even more recent field of application of this technique. As of now, there are only 81 structures of proteins solved by ssNMR deposited in the PDB database and, when compared to the number of structures solved by x-ray crystallography (101613) and solution NMR (11096), it is possible to understand how new this technique is in this field. On the other hand, looking at the types of structures deposited (amyloid fibrils, helical signal transduction filaments, proteins in membrane environment, etc.), it is easy to understand all the excitement in the structural biology community around ssNMR. Structures at atomic resolution, sample preparation that does not involve the growth of high ordered crystals and potentially no limit in the size of the biological compound analysed are some of the best features that characterize this technique.

In ssNMR spectroscopy, the resolution achievable in a spectrum is strictly dependent on the homogeneity of the sample analysed. For this reason, it is essential to determine the best conditions to prepare the most homogeneous sample possible, making this crucial step the bottle neck in ssNMR of biomolecules. This is even more important when actin filament complexes are taken into consideration due to their gel-like appearance. Firstly the suitability of using ssNMR as a powerful tool to study thin filaments was addressed and secondly the complex between actin filaments and a small protein called VHD was investigated.

Analysis of the filaments at ^{13}C natural abundance revealed that high resolution was achievable with ^{13}C CP MAS experiments if acquired for a long time (at least 30k scans for a total of 15-18h)(Figure 11.1).

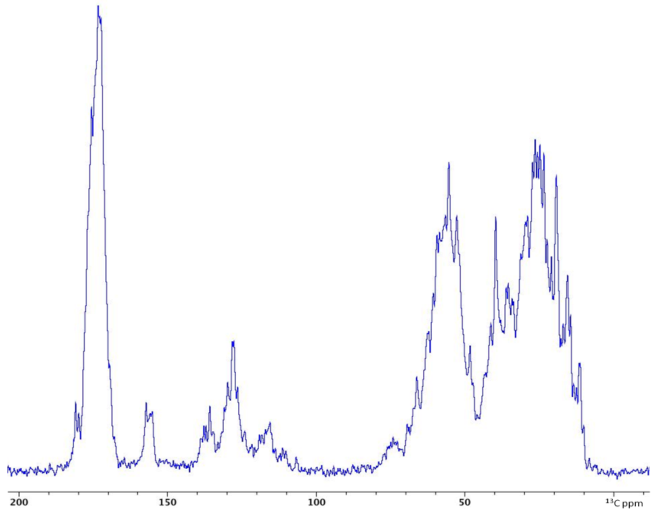

Figure 11.1 ^{13}C CP MAS spectrum (32k scans) of actin filaments recorded at 10kHz spinning rate, 278K in a 400MHz Bruker magnet.

Nevertheless, it was not possible to follow how different filament preparations could affect their arrangement by acquiring simple ^{13}C CP MAS experiments due to their poor resolution (Figure 11.2).

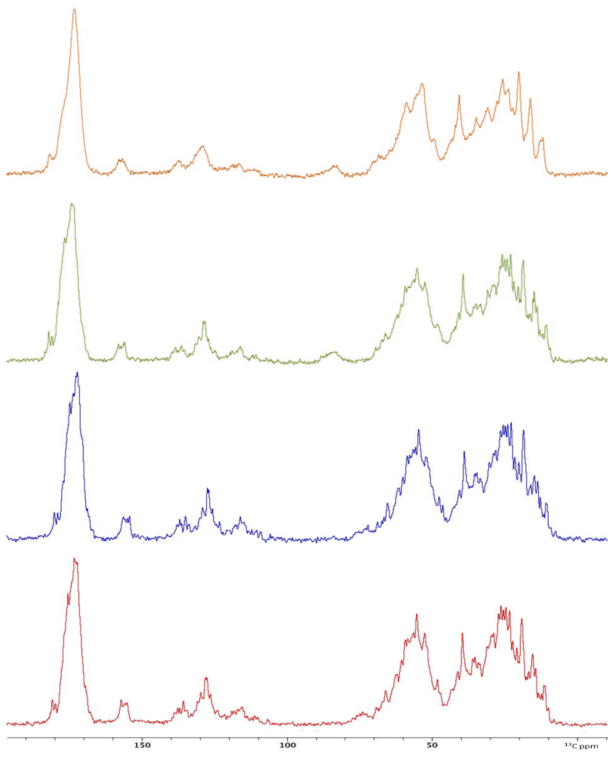

Figure 11.2 13C CP MAS spectrum of different preparations of actin filaments. Actin polymerized alone (red spectrum) and in presence of phalloidin (blue spectrum), cucurbitacin E (green spectrum) and ADP.BeF$_4$ (orange spectrum), compounds known in the literature to stabilize the filaments. Differences in the signal pattern is appreciable for the filaments containing ADP.BeF$_4$ where an overall loss is the resolution is recognizable.

Limited information was collected observing the spectra recorded on the filaments and they were mostly due to drastic changes in the filaments arrangement. It is not a coincidence that useful information were gathered when the stability during the time of sedimented filaments loaded in a rotor for ssNMR was investigated. The different ^{13}C CP MAS spectra acquired did not show any appreciable change until a collapse of part of the spectrum was observed in the experiment recorded after 90 days from the packaging of the rotor. As the EM pictures acquired on an aliquot sampled from the rotor confirmed, the effect in the spectra was due to a degradation of filaments that was occurring in the rotor Figure 11.3.

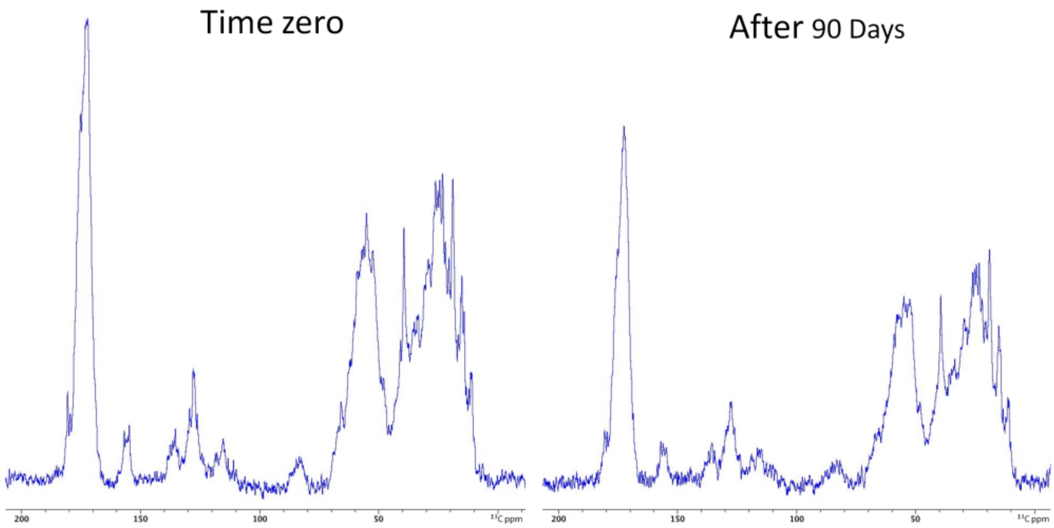

Figure 11.3 Stability over time of actin filaments polymerized in presence of phalloidin and loaded in a 4mm rotor checked by ^{13}C CP MAS experiments. A collapse in signal in the region of Cα atoms comparing the spectra acquired at time zero (left panel) and after 90 days (right panel) is clearly visible. The spectra were acquired at 10kHz spinning rate, 278K in a 400MHz Bruker magnet.

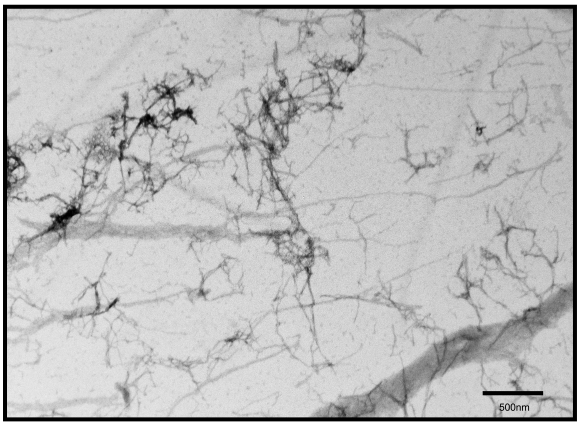

Figure 11.4 EM picture of negatively stained actin filaments containing phalloidin after two months from filling in a 4mm rotor for ssNMR. Damages and shorter filaments were recognizable in the image. The image was acquired using a FEI Tecnai T20 with a magnification of 9300x and the bar indicates 500nm.

A different approach to better understand possible improvements in the filament preparation where investigated analysing how a small protein domain able to bind the filaments affects their arrangement. It has been reported in the literature that the binding of ABPs or small compounds modifies the arrangement along the entire filament as a cooperative effect. We selected the villin headpiece domain from ABLIM2 (VHD) as ABP model due to its binding to actin filaments with high affinity (2,8μM for the WT VHD) and its generally good behaviour. The expression of different isotopic labelled versions of this protein with high yield, its easy and fast purification, its stability during the time and, most important, the availability of its almost complete assignment in the free state performed by NMR in solution made the VHD the best candidate for this study. It is important to consider that, to prepare a 4mm rotor that contains 5-6mg of labelled protein, 10-15mg of enriched VHD were mixed to 30-35mg of actin filaments and cosedimented together.

When the first VHD-F.actin complex was prepared, it was clear that the filaments were somehow affected by the binding of VHD because the appearance and density of the pellet generated was different compared to the pellet of filaments sedimented alone. A first rough optimization of the conditions to sediment the filaments was achieved by analyzing the ^{13}C-^{13}C DARR spectra generated by a sample of uniformly labelled ^{13}C-^{15}N VHD bound to the filaments. It was possible to establish the maximum speed to centrifuge the filaments (25000 rpm) and the temperature at which the spectra showed the best resolution (278K). Unfortunately, this type of experiment needs a long acquisition time to show well resolved resonances (in the order of days) and it is clearly not the best approach when several conditions have to be tested.

Searching for an alternative technique to analyse the filaments, explored ^{31}P ssNMR spectroscopy was explored. We suggested that changes in the linewidth of the signals of the nucleotide phosphates could provide information about rearrangements in the filaments upon complex formation with ABPs. Improvements in the homogeneity of the sample were defined as decreasing the linewidths of these signals and vice versa increases in the linewidth would have been considered as a decrease in the homogeneity. Nevertheless, the resolution obtained in the first ^{31}P CP MAS spectrum acquired on filaments sedimented alone was disappointing. It was not possible to recognize the two peaks from the ADP as expected, but a single signal centred at -9,8ppm with a linewidth of 324Hz was observed (Figure 11.5). Furthermore, it was necessary to acquire at least 10k scans to achieve a signal to noise ratio of 30 in this ^{31}P CP MAS spectrum recorded.

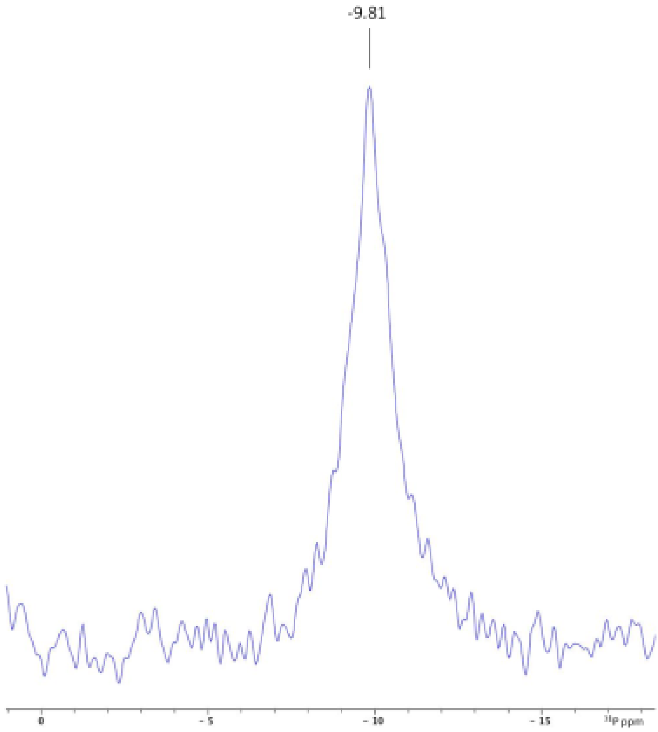

Figure 11.5 ^{31}P CP MAS spectrum of actin filaments. A single peak was recognizable in the spectrum at -9.55ppm characterized by a linewidth of near 324Hz. The spectrum was recorded at 10kHz spinning rate, 278K in a 400MHz Bruker magnet.

Before abandoning this approach, the acquisition of ^{31}P CP MAS experiments on different filament preparations was attempted hoping for possible improvements. The filaments polymerized and sedimented in presence of phalloidin or cucurbitacin E showed an improvement in the linewidth that decreased to 130Hz, but it was when the filaments polymerized in presence of $ADP.AlF_4$ were analysed that this approach started to reveal its potential. Two peaks likely resulting from the phosphate groups of ADP (centred at -11.91ppm and -9.83ppm) and a third broad signal (centred at -10.93ppm) were observable (Figure 11.6). The assignment of the two sharp signals was performed comparing their chemical shift to the one reported in literature for free ADP (P_{α} at -11.91ppm and P_{β} at -9.83ppm).

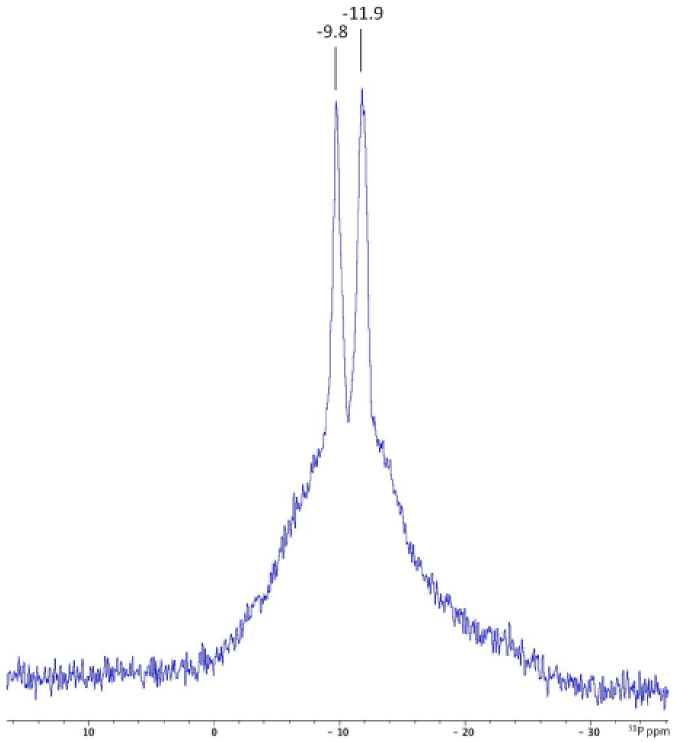

Figure 11.6 ^{31}P CP MAS spectrum of actin filaments complexed with ADP.AlF$_4$. The peaks from α (-11.91ppm) and β (-9.83ppm) phosphate were assigned referencing the assignment reported in literature for free ADP in water. A third broad peak centred at near -10.93ppm was recognizable. The spectrum was recorded at 10kHz spinning rate, 278K in a 400MHz Bruker magnet

Encouraged by the results obtained, we decided to test the potential of ^{31}P spectroscopy in the investigation of the effects of VHD binding to the filaments. The first ^{31}P CP MAS spectrum acquired on the VHD-F.actin complex showed a similar spectrum of ADP as acquired for the filaments (even if a little shifted to lower field) but with the presence of a new signal at lower field never observed before. Residual phosphate from the solution in which VHD is stored were excluded as origin of this new peak because the ^{31}P CP spectrum recorded on actin filaments stored in phosphate buffer did not show this new signal. This could mean that the binding of VHD actually affects the arrangement of filaments generating two populations of ADP resulting from two different arrangements of the pocket that experience or not the proximity of the VHD. ^{31}P-^{31}P DARR spectra recorded on this complex confirmed the presence of these two different families by the absence of correlations between the new signal and the other signals. Additionally, it was observed that the saturation of F-actin binding sites by VHD helps to generate a more homogeneous sample.

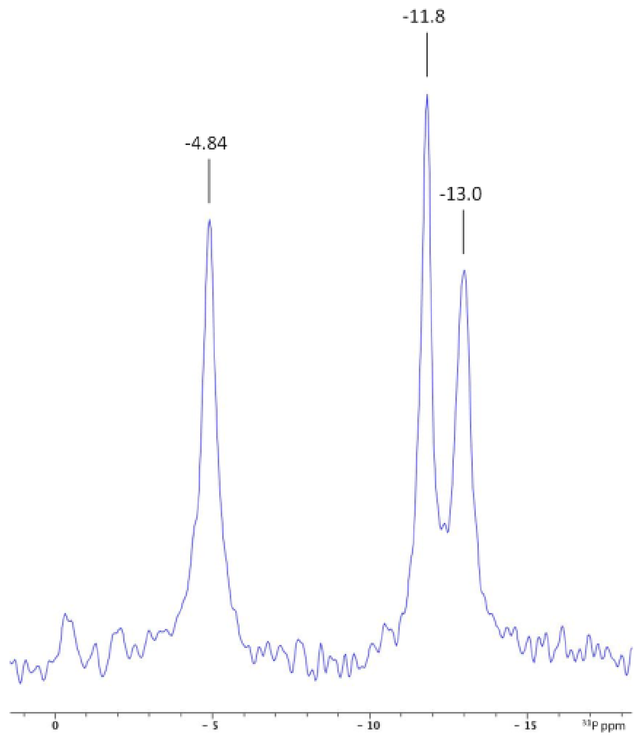

Figure 11.7 ^{31}P CP MAS spectrum of a saturated VHD-actin filaments sample. showing the three peaks centred at -4.8ppm, -11.8ppm and -13ppm. The spectrum was recorded at 10kHz spinning rate, 278K in a 400MHz Bruker magnet.

Trying to figure out if this was an isolated case or a common pattern that all ABPs share, different thin filaments complexes containing actin binding domains of proteins involved in various biological functions were tested. Thin filament complexes containing the tandem CH domain of α-actinin, calponin fragments 1-228 and 131-228 and hcLNK1 (the linker sequence between domains C1 and C2 of human cardiac myosin binding protein C) showed the same behavior and it was different from the behavior shared by the complexes containing myosin, tropomyosin, VHD and ABD1.

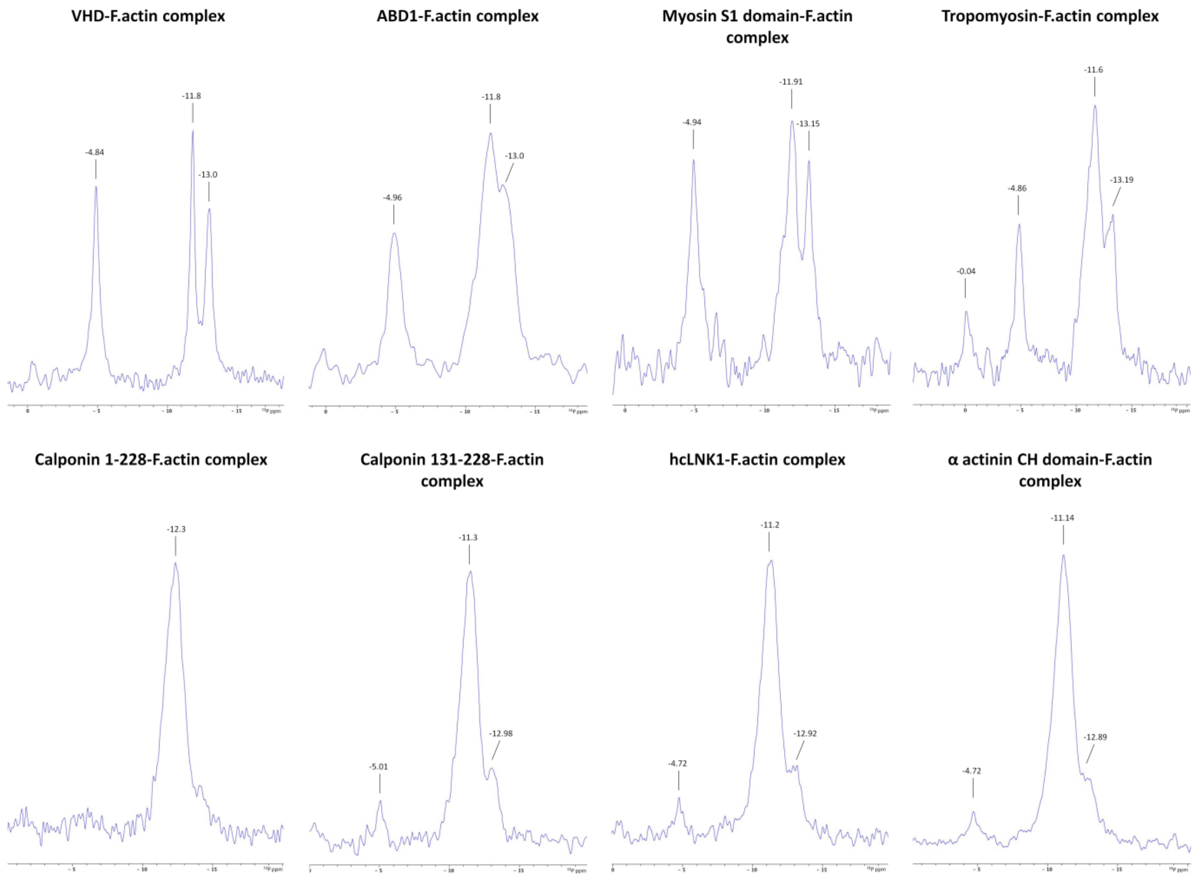

Figure 11.8 ^{31}P CP MAS spectra acquired on different thin filaments complexes. It is possible to divide the spectra in two different groups based on the pattern of signals that the complex generates. VHD-, ABD1- and myosin S1 domain-F.actin complexes show the same pattern of signals while tropomyosin-F.actin complex show an extra peak at lower field. On the other hand, α-actinin CH domain-, calponin fragments 1-228- and 131-228- and hcLNK1-F.actin complexes share the same pattern of signals.

Thin filament complex	Peaks on ^{31}P CP MAS spectrum [ppm]			
VHD-F.actin	-4.84	-11.84	-13.00	
linewidth (saturated F.actin)	83Hz	67Hz	102Hz	
ABD1-F.acttin	-4.96	-11.82	-13.00	
Linewidth	180Hz	280Hz	250Hz	
Myosin S1 domain-F.actin	-4.94	-11.91	-13.15	
Linewidth	148Hz	141Hz	154Hz	
Tropomyosin-F.actin	-0.04	-4.86	-11.6	-13.19
Linewidth	157Hz	172Hz	272Hz	148Hz
Calponin fragments 1-228-F.actin		-12.30		
Linewidth		294Hz		
Calponin fragments 131-228-F.actin	-5.01 (weak)	-11.35	-12.98 (weak)	
Linewidth	103Hz	269Hz	132Hz	
hcLNK1-F.actin	-4.72 (weak)	-11.20	-12.92 (weak)	
linewidth	137Hz	279Hz	191Hz	
α actinin CH domain-F.actin	-4.72 (weak)	-11.14	-12.92 (weak)	
linewidth	194Hz	254Hz	160Hz	

Table 11.1 Chemical shift (in ppm) of peaks contained in the ^{31}P CP MAS spectra acquired on the different thin filament complexes analysed.

Analyzing the interaction models available in the literature for the tandem CH domains of α-actinin to F.actin (Figure 1.1, left panel, PDB: 3LUE) and for the tropomyosin-myosin-F.actin complex (Figure 1.1, right panel, PDB: 4A7F), it became clear how differently the two families of actin binding domains interact with the filaments.

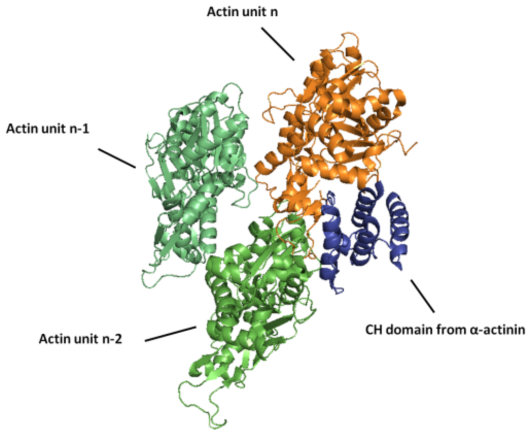

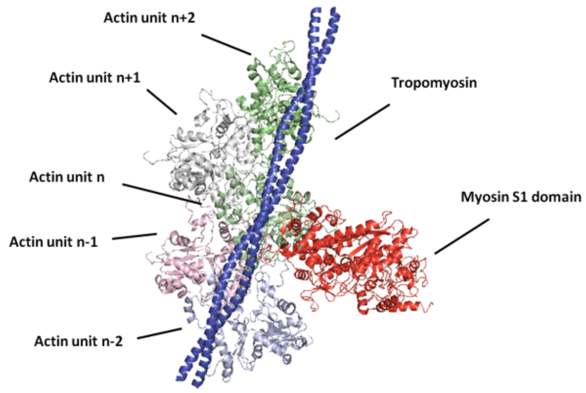

Figure 11.9 Left panel) Model representation for α-actinin CH1 domain interaction to F-actin at a resolution of 15Å. The CH1 domain (blue) interacts to the filaments at the interface of two adjacent subunits of actin [27]. Right Panel) Ribbon representation of tropomyosin-myosin-F-actin complex solved at 7.7Å. In red is highlighted the myosin S1 domain while in blue the tropomyosin pseudo-repeats 2-6. The five actin subunits are referred as n, n+1, n+2, n-1 and n-2. The models were generated in PyMol software using the tropomyosin-myosin-F.actin model solved at 7.7Å and the α-actinin CH1 domain-F.actin model deposited, respectively, on PDB as (4A7F) and (3LUE).

The CH domains interact at the interface of two adjacent subunits of actin (n and n-2) while myosin “clamps” one subunit of actin and makes contact to an adjacent subunit through several loops creating a large contact surface. On the other hand, tropomyosin envelops the entire filament following a positively charged groove on the F-actin surface. In these models, myosin and tropomyosin share a binding site on the filaments spatially close to each other while the binding site of the CH domain tandem is in a more distant region. The relative position of these ABPs on the filaments compared to the signals these complexes generate in ^{31}P spectra suggested that there is a connection between their binding site on actin filaments and their effect on the nucleotide in the clefts. As a consequence, we assumed that it would be possible to roughly predict the region on the filaments where an uncharacterized ABP binds by simply analyzing the pattern of peaks generated by the ABP-F.actin complex in a ^{31}P CP MAS experiment. It will not be possible to predict precisely at atomic resolution the actual position of the ABP on the filaments but it is possible to collect useful information that could be used as constrains in the calculation of the complex structure.

In an NMR structure calculation, it is fundamental to have available the assignment of the protein of interest. Unfortunately, the assignment performed so far on the VHD bound to the actin filaments is not complete. At the beginning of the project, almost four years ago, the 4mm rotor seemed to be the only suitable option in the study of this thin filament complex. Both the availability of only a 4mm CP MAS probe at King's College London NMR facility and the gel-like consistency of the actin sedimented made it difficult to use a thinner rotor. Thus, the limitations in the access to instruments at higher magnetic field than the 400MHz provided by the King's College London NMR facility impeded the acquisition of a dataset sufficient for the assignment of VHD bound to actin filaments.

The ^{13}C-^{13}C and ^{13}C-^{15}N correlation spectra acquired by ssNMR were characterized by a poor signal to noise ratio making it impossible to acquire any threedimensional spectra. In addition, in both ^{13}C-^{13}C and ^{13}C-^{15}N correlation spectra several signals were overlapped making it very difficult to assign them. The acquisition of spectra using VHD samples based on [1,3-^{13}C] and [2-^{13}C] labelled glycerol bound to filaments helped to resolve some resonances but it was still not sufficient to complete the assignment. Only recently, the development in ssNMR has made it possible to acquire spectra on protons at high resolution. In collaboration with Dr. Lewandowski from Warwick University, an ultrafast spinning MAS approach was attempted on uniformly back protonated ^{2}H-^{13}C-^{15}N VHD bound to filaments. Two different protocols to prepare the complex were performed and both were analysed using a 850MHz Bruker instrument equipped with a triple resonance ultrafast MAS probe. Unfortunately, both the datasets failed to produce data at high resolution because problems wits the sample affected the spectra. Nevertheless, even if the experiments recorded using 4mm and 1.3mm rotors have not yet allowed to assign all the resonances, they helped to establish a straightforward platform of experiments to efficiently approach the structural determination of a thin filament complex. It is interesting to consider that using routine ssNMR experiments it is possible to observe resonances of atoms that would require the optimization of specific sequences in solution. Consider for example the assignment of the carbonyl group on the side chains of glutamate. It would require a specific experiment in solution [96] while acquiring a simple ^{13}C-^{13}C DARR it was possible to identify the C_δ frequencies for almost all the glutamates in VHD.

	C_β [ppm]	C_γ [ppm]	C_δ [ppm]
Glu30	-	32.88	183.4
Glu36	28.35	36.6	184.25
Glu37	29.96	38.94	184.05
Glu40	29.65	35.66	183.36
Glu47	28.35	36.6	184.25
Glu48	-	36.6	184.25

Table 11.2 Chemical shift (in ppm) assigned for glutamate residue performed on VHD complex to filaments.

The last three years collecting information, investigating deeper and deeper in the VHD-F.actin complex made me think that it is finally possible to answer to the fundamental question that I think it is the core around which this project developed.

Is ssNMR spectroscopy really able to generate data at atomic resolution on a sample that is sedimented as gel-like pellet and that is not characterized by the same homogeneity as a crystallite? But more important, **is ssNMR spectroscopy really suitable in the characterization of thin filament complexes?**

Clearly the answer is positive, ssNMR spectroscopy showed the potential to successfully study thin filaments complexes. All the information collected suggests that still few optimizations in the method are required in order to establish a straightforward protocol that will efficiently approach the study of complexes in which actin filaments are involved. The possibility to obtain the structure at atomic level on actin filament complexes is almost a reality.

11.2 What we have learned on the VHD-F.actin complex so far...

It was not possible yet to determine the structure of the VHD bound to the actin filaments because its complete assignment is still missing. Thus, no docking simulation implementing the available structure of the free VHD and an available model of the filaments was tried. We assumed that it would have been more a challenging docking exercise rather than been a meaningful model calculation for this complex. Nevertheless, the implementation in this study of ssNMR spectroscopy supported by classic biologic assays makes possible to collect interesting and useful information about the VHD-F.actin complex.

Firstly, it was established that the assignment performed in solution and the partial one performed in solid state were comparable. Furthermore, an overall small perturbation in chemical shift (less than 0.3-0.4ppm) was observed for all the resonances compared. Its cause was suggested to derive from the differences in the environment between solution and solid state. The VHD residues whose resonances were not affected by the binding to the filaments were highlighted on the structure of the apo VHD as shown in Figure 11.10. It is possible to appreciate how those residues are clustered on the same part of the protein that correspond to the hydrophobic cap, the crown and the positive patch. Differently the region that correspond to the long coil at the N-terminal has no residues highlighted.

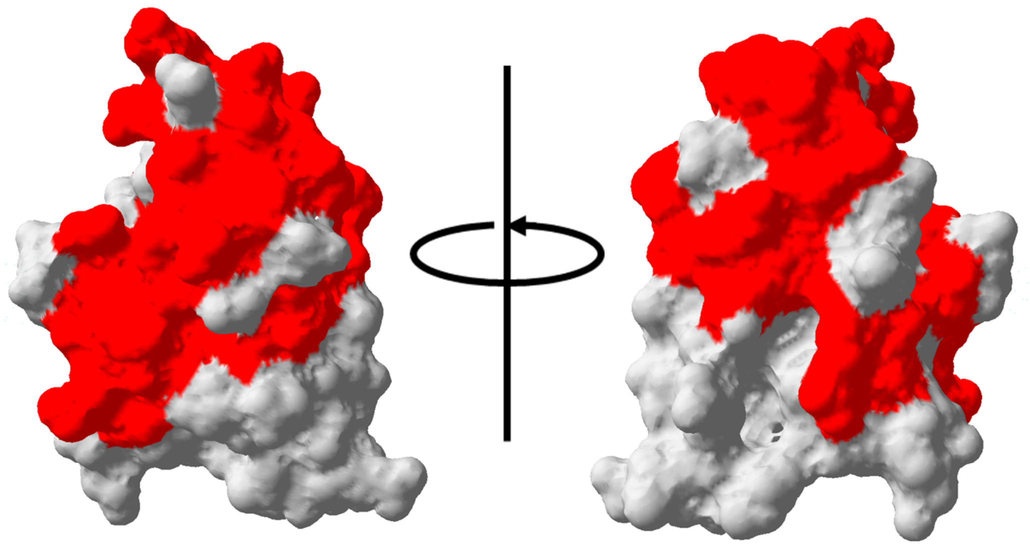

Figure 11.10 Residues assigned highlighted in red on the surface of VHD (PDB:2L3X). The majority of the residues lie on the same region of the actin structure suggesting that that this region could the region that takes contact with the filaments resulting more compact. On the other hand, it was suggested that the region at the N-terminal that included a long coil can maintain a degree of movement making the contact time for the CP longer than the rest of the protein. The surface has been calculated using Swiss PDB viewer [119].

VHD has a globular compact structure. The binding of this small domain to actin filaments could involve small structural rearrangements that would be difficult to recognize just considering chemical shift perturbation. Furthermore, almost all the resonances were affected by a small shift in their frequencies rendering even more difficult to distinguish between global shift and changes due to the binding event. It can be suggested that the VHD region including the cap, the crown and the positive patch is actually the part of the protein that take contacts with the filaments.

Comparison between the ^{15}N CP MAS experiment available and the ^{15}N assignment performed for the positively charged side chains of arginine and lysine revealed interesting information. It was observed that the chemical shift for arginine N_{ε} atoms is comparable to the one for apo VHD while the resonances of arginine N_{η} are quite different (an overall difference of 10ppm). Interestingly, the mutants of VHD R26A-R28A and R31A showed the same affinity to the filaments as the WT protein but the mutant R26A-R28A-R31A showed a lower affinity as expected. As reported in the literature [43], the presence of the positive patch is essential in maintaining the binding to the filaments at high affinity and its disruption (but keeping cap and crown unaltered) will cause the decreasing in the affinity. This suggests that the shift in arginine N_{η} atoms can be due to the binding of VHD to the actin filaments. Highlighting R26, R28 and R31 on the surface of the protein, it became evident as those residues were clustered in the portion of the protein that has been assigned and proposed to make contacts with the filaments.

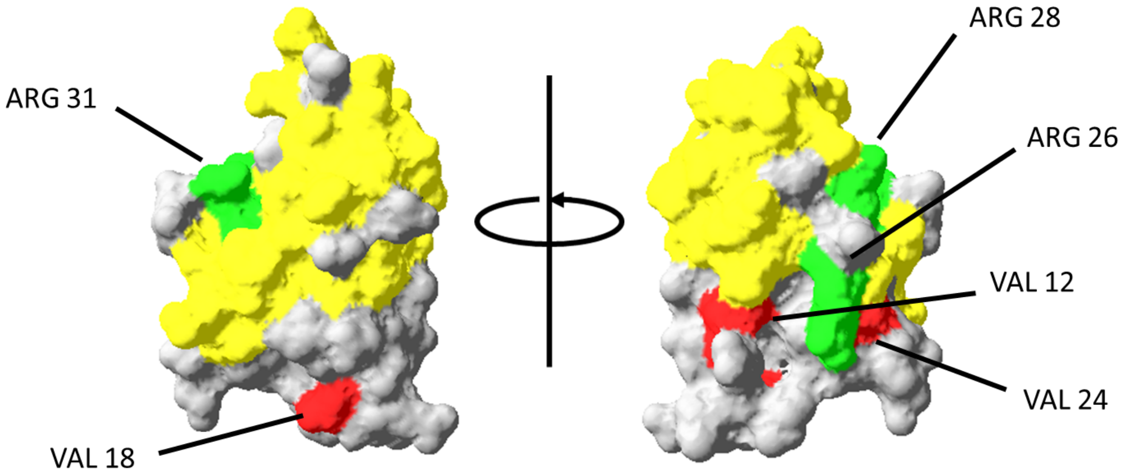

Figure 11.11 Arginine 26, 28 and 31 (green residues) highlighted on the surface of VHD (PFB:2L3X). Their mutation to alanine resulted in a decrease of the affinity to the filaments. Interestingly, these arginine residues are included in the part of protein that was assigned and was suggested to be likely involved in the binding to the filaments. Valine 12, 18 and 24 are highlighted in red while the assigned residues in yellow. The surface has been calculated using Swiss PDB viewer [119].

The model resolved by electron tomography of the structure between villin and actin filaments has been available in the literature [120] and it is in agreement with the suggested mechanism of interaction. The resolution is not reported but for electron tomography it range between 5 to 20nm. In this work, it is reported that the headpiece interaction wother a filament through its crown and the positive patch while the coil is not involved that male contacts with the residues 308-320 on the subdomain 3 of actin (Figure 11.12).

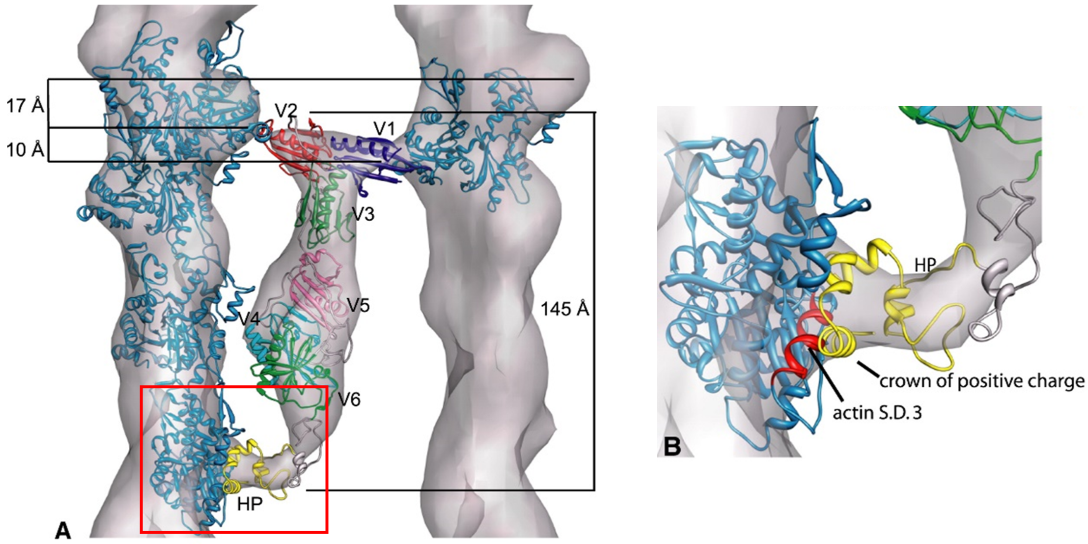

Figure 11.12 Model of villin crosslinking F-actin. (A) Placement of the villin homology model atomic coordinates within the averaged villin density and (B) the magnification of the position of the villin head piece on a filament. The head piece helix residues 62-76, which include the "crown of positive charge", are positioned towards actin and in the vicinity of helix residues 308-320 on actin subdomain 3 [120].

In this scenario the remaining part of the protein would be free to move. This would be in agreement with the fact that most of the resonances from this region of the protein are missing. This dynamic part would be characterized by a longer contact time during the CP element. The intensity for those resonances would be lower and in some cases the signal can be hidden in the background noise. It was suggested this kind of behaviour to explain the missing resonances for the CαCγ signals of valine 12, 18 and 24. Precisely, all these residues are included in the dynamic region at the N terminal of the protein. On the other hand, valine 41, contained in the region supposed to take contact with the filaments, was easily assigned (Figure 11.13 and

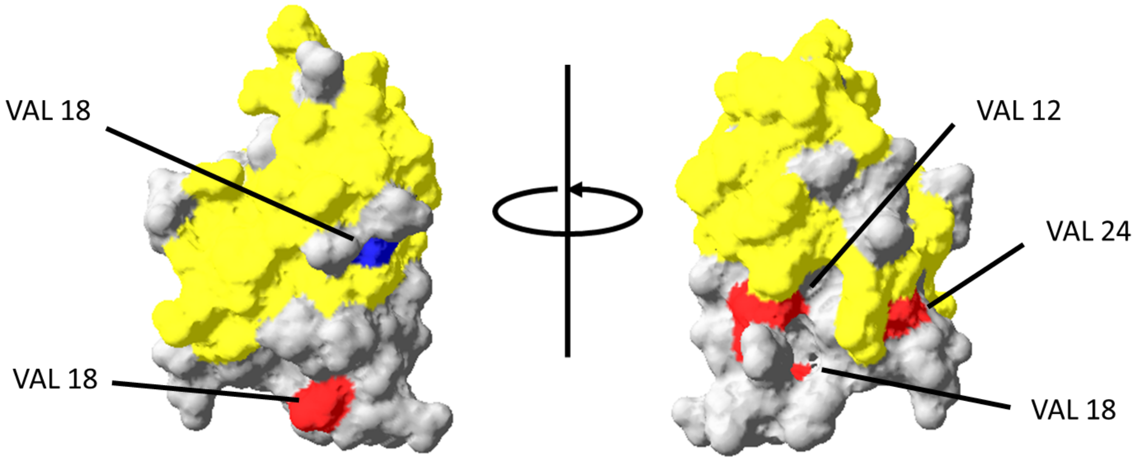

Figure 11.14).

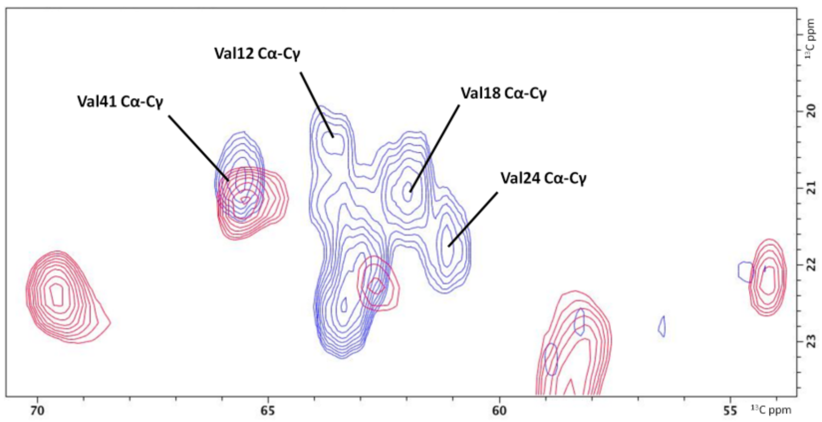

Figure 11.13 Superimposition of ^{13}C-^{13}C DARR spectrum using 20ms mixing time (red spectrum) and the ^{13}C-^{13}C projection from a HCCH TOCSY experiment (blue spectrum) of CαCγ correlation peak region for valine. The frequency for val41 was the only that was not affected by the binding of VHD to the filaments suggesting that the other valine residues are in the region of VHD surface that is involved in the binding event.

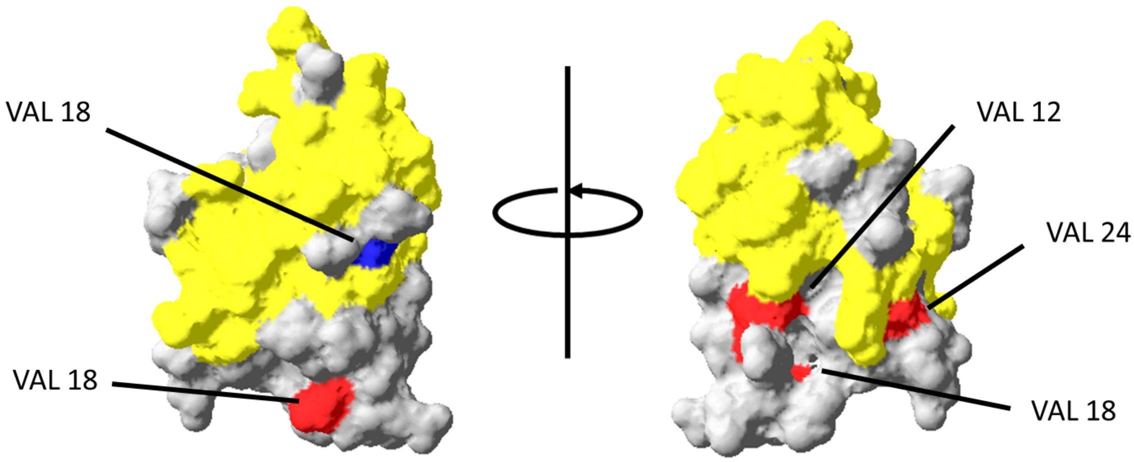

Figure 11.14 Highlighting of the valine positions on the surface of VHD. Valine 12, 18 and 24 (red) that share the same region on the surface of VHD are included in the region where only few residues were assigned unambiguously. On the other hand, valine 41 (blue) is located in the portion of the protein where most of the residues were assigned. The model was generated in Swiss PDB viewer [119] using the VHD structure deposited as on PDB (2L3X).

Unfortunately, several regions in the spectra acquired contain overlapped resonances from several residues and it was not possible to unambiguously assign them. Once the complete assignment will be available it would be possible to confirm the mechanism of binding that has been suggested.

Combining all the data obtained by the analysis of the assignment performed on the bound VHD, it was possible to determine the region on the VHD surface that is likely involved in making contacts with the filaments. In the same way, combining ^{31}P and paramagnetic ssNMR data and data from literature, it was possible to tentatively determine the region on the filaments that could be involved in the binding to the VHD.

Interesting insight on the binding site of VHD on the filaments were revealed analysing the ^{31}P CP MAS experiments. It was demonstrated that ABDs that share a close binding site on the filaments will affect the pocket containing the nucleotide in a similar manner generating the same pattern of ^{31}P signals. Myosin and VHD generate the same pattern of signals when 31P experiments were acquired while tropomyosin spectra exhibit an extra peak. This suggest that the all these three ABPs likely share a binding site on the filaments that is close in space.

In addition, the paramagnetic ssNMR data collected revealed that the VHD has to bind the filaments at more than 30Å from the position of the spin label. The tropomyosin-myosin-F.actin model (PDB: 4A7F) was modified in silico with the addition of a paramagnetic center (MTSL) covalently bound to cysteine 374 on every actin subunit. When the extent of the paramagnetic effect was estimated on the model, it was determined that the MTSL was spatially too far from both the binding site of tropomyosin (46-50Å from the spin label) and myosin (28-35Å) (Figure 11.15 and Figure 11.16).

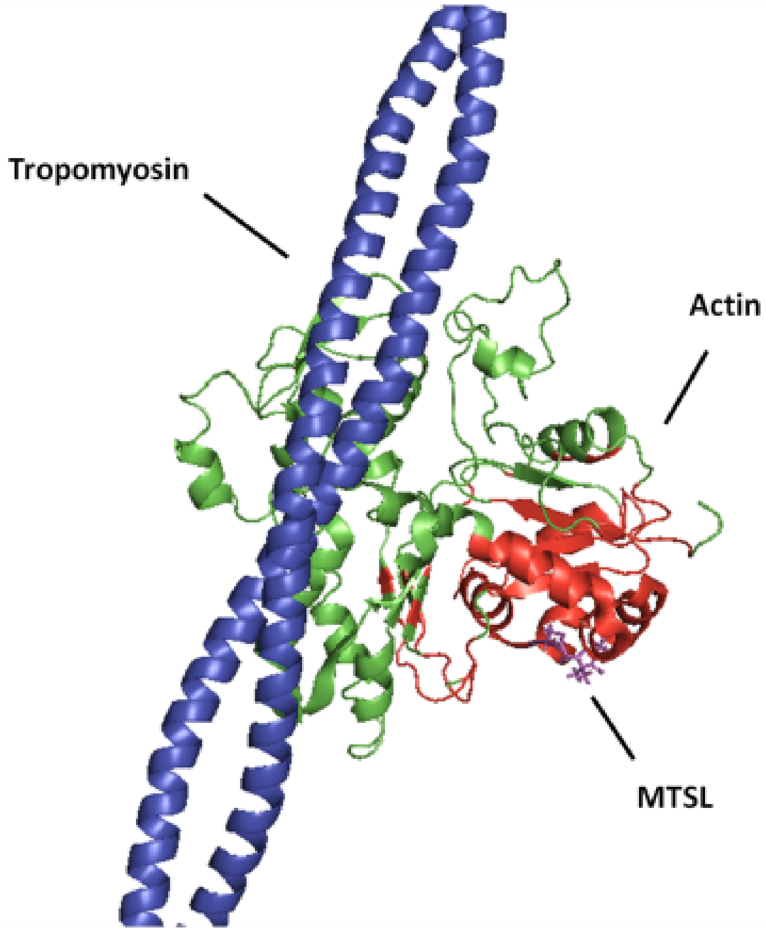

Figure 11.15 Ribbon representation of tropomyosin (blue) bound to a subunit of actin (green) modified with the covalently binding of a paramagnetic center. The molecule of MTSL is highlighted in pink and the residues closer than 25Å to it are highlighted in red. It is possible to observe that the tropomyosion is not affected by the effect of the paramagnetic center. The model was generated in PyMol software using the tropomyosin-myosin-F.actin model solved at 7.7Å deposited as on PDB (4A7F).

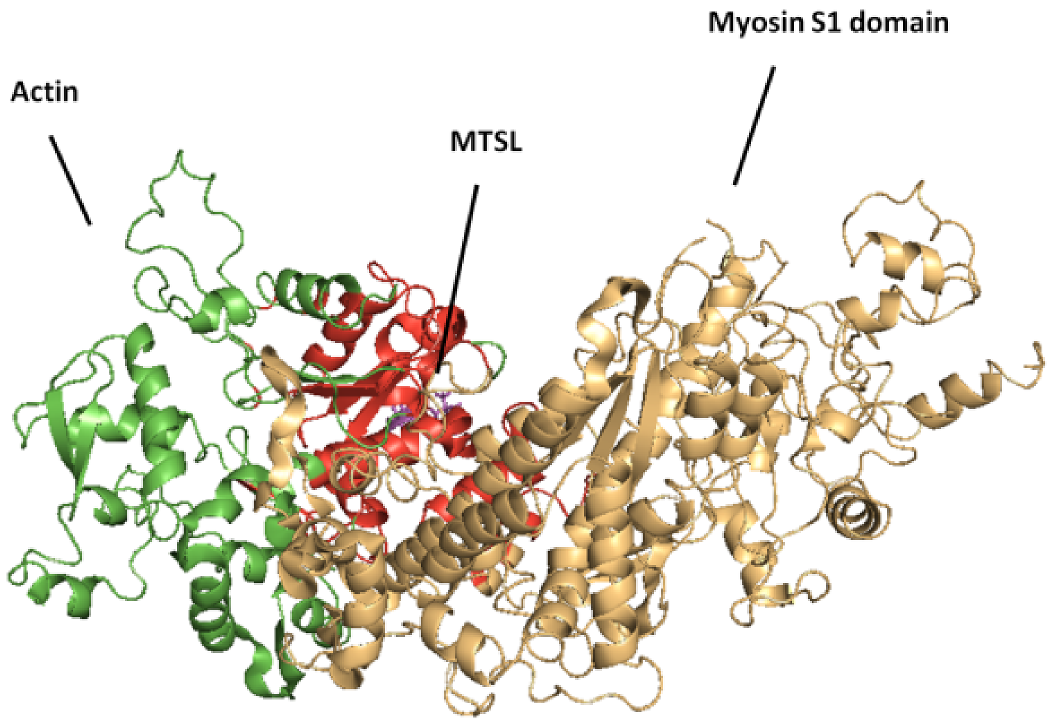

Figure 11.16 Paramagnetic effect simulation of MTSL on myosin S1 domain (light orange)-F.actin modified subunit (green). The molecule of MTSL is highlighted in pink and the residues closer than 25Å to it are highlighted in red. Several residues from the myosin S1 domain are in the region where MTSL affects. The model was generated in PyMol software using the tropomyosin-myosin-F.actin model solved at 7.7Å deposited as on PDB (4A7F).

It is reported in the literature that, tropomyosin interacts with the filaments through its negatively charged surface that take contact with a positively charged groove on the filaments (Figure 11.17) while myosin clamps the filament in a close region (Figure 11.17).

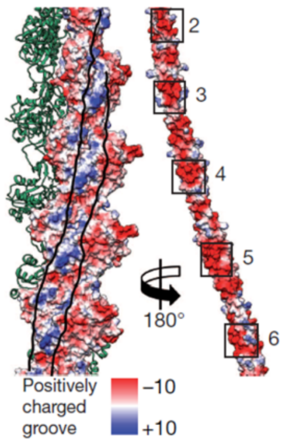

Figure 11.17 Surface of F-actin and tropomyosin (pseudo-repeats 2-6) showing their electrostatic charge (red, blue, white: negatively charged, positively charged and neutral) at pH7.5 [31]. Tropomyosin was rotated by 180° in order to show its negatively charged surface that it is involved in the binding to the positively charged patch in actin filaments.

Careful examination of the surface on actin filaments where tropomyosin and myosin make contact it was possible to define the possible region where also VHD males contacts with the filaments. VHD has to bind the filaments in a portion of the actin surface that is outside the range of influence of the spin label (blue region in Figure 11.18), but at the same time close to the regions were tropomyosin and myosin make contact with the filaments. It was also possible to eliminate the positively charged groove on actin filaments where tropomyosin binds remembering that VHD binds through the cap, the crown and the positively charged patch below the crown. Finally, the remaining region likely available for the VHD to bind to the filaments seems to overlap to the binding site for myosin (Figure 11.18). Once the structure of VHD in the complex will be available, it will be interesting to confirm the suggested region of binding and understanding the mechanism of selection between myosin and the VHD for the binding to this site.

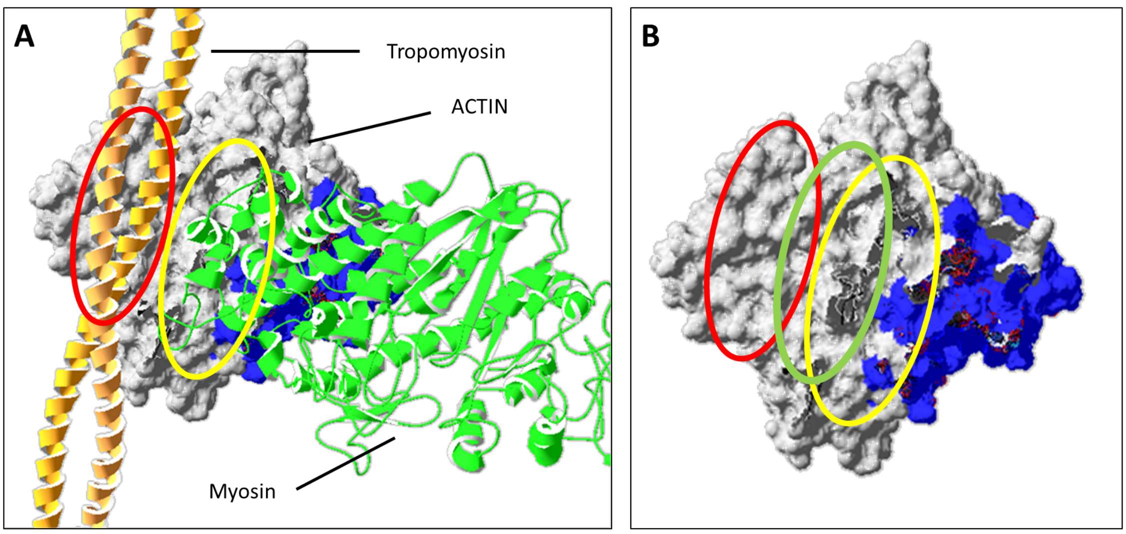

Figure 11.18 In panel A is reported the tropomyosin-myosin-F.actin complex (PDB:4A7F). In the model are highlighted the region on the actin filaments that are involved in the binding with tropomyosin (red circle) and myosin (yellow circle). In panel B is shown the surface of the same monomer of actin. The same region as panel A are reported highlighted. Their analysis helped to suggest the probable region on actin surface that is likely involved in the binding with the VHD (green circle). The ribbon representation for tropomyosin (yellow) and myosin (green) was used to allow to visualize the regions on the filaments involved in their binding. The blue residues on actin surface represent the amino acids under the effect of the paramagnetic spin label MTSL covalently bound to Cys374. The model was analyses using Swiss PDB viewer [119].

However, all these speculations are not yet conclusive and the structure at atomic resolution is still necessary to confirm these considerations, but they give an idea how ssNMR could be efficiently used to obtain a structural definition of these thin filament complexes.

11.3 …and what we can still learn.

It is clear that the final aim of this project will be the determination at atomic resolution of the structure of the VHD bound to actin filaments and, as consequence, the calculation of the first model of a thin filament complex based on data at atomic resolution. On the other hand it is interesting to consider the necessary steps that have to be taken and, more importantly, the achievements that they would implicate.

Firstly, the platform of DQ coherence experiments has to be optimized. The spectra recorded using the post-C7 pulse sequence on the uniformly labelled ^{13}C-^{15}N VHD-F.actin complex showed a low efficiency in DQ coherence generation. On the other hand, as explained during this dissertation, it is not necessary to acquire multidimensional experiments to investigate improvement in the homogeneity of the sample. Analysis of the linewidth in 1D spectra containing a few resonances is sufficient to carry out the task. This means that, as soon as the incorporation of ^{13}C-^{15}N alanine in the VHD domain will be optimized, the platform of DQ experiments will be ready to be efficiently used. The filaments polymerized in presence of the phalloidin, cucurbitacin E and the analogues of nucleotides will be cosedimented with [^{13}C-^{15}N Ala] VHD and analysed again through this platform of experiments. At the same time, different techniques to sediment the complex will be analysed. We think that a gradual and more gentle sedimentation could help to obtain a more homogeneous sample. In this new protocol, an initial gently sedimentation at low speed (4000-5000 rpm) will be followed by a centrifugation in which the speed is increased to the maximum allowed (25000 rpm for the VHD-F.actin complex before to promote the unfolding of VHD) in a continuum process. In this way, the filaments are initially gently moved to the bottom of the tube and then progressively squeezed from the majority of the buffer possibly helping to sediment a pellet in which the filaments maintain a more homogeneous packaging. The future use in this protocol of a new rotor packing device made by Giotto Biotech could improve the sample homogeneity even more. The device consists of a ultracentrifuge tube for that can hold an empty rotor at its bottom. The solution containing the complex is loaded in the tube and during the centrifugation the pellet sediments directly inside the rotor filling it. This new device could help in the optimization of a rotor packaging protocol and it could possibly avoid any mechanic damage to the sample that the current packaging protocols could cause.

Once the best conditions to sediment the filaments will be determined, it will allow the acquisition of datasets at high resolution with proton detection using the ultrafast MAS technique. This will initially help to fill the gaps in the current assignment of VHD bound to the filaments. Later, it will be possible to acquire distance constrains, perform relaxation measurements and collect PREs that will give the information that will be used to calculate the first structure of a ABP bound to filaments at atomic resolution.

To accurately determine the region on the filaments that make contacts with the VHD, the paramagnetic ssNMR protocol described will be developed following two different ideas. It is known that every subunit of actin in the filaments contain a Mg^{2+} coordinated to the nucleotide. It is already available in the literature a protocol that allows to exchange the Mg^{2+} in the cleft with Mn^{2+}[121]. The actin filaments containing Mn^{2+}, that is known to have paramagnetic properties [122], will be cosedimented with uniformly labelled ^{13}C-^{15}N VHD and ^{13}C-^{13}C DARR spectra will be recorded and analysed as explain in chapter 8. This will give an idea of the VHD distance from the nucleotide in the cleft. Recently, we started a collaboration with Dr. Rosen from UT Southwestern (University of Texas). In their publication [117], they showed the possibility to express *Drosophila* actin in *P.pastoris*. The success in actin expression has made it possible to develop a mutagenesis protocol where the sequence of actin will be modified inserting cysteine residues on its structure in difference positions. The choice between *Drosophila* or human skeletal actin isoform is still under investigation. The mutated actin will be later modified on these new cysteines with the addition of a MTSL molecule and polymerized. The filaments will be cosedimented in the presence of a uniformly labelled ^{13}C-^{15}N-2H VHD and analysed as described above. The possibility to insert cysteine residues in different regions of the actin surface will help to determine the actual position where the VHD binds. These information collected using paramagnetic NMR techniques will allow calculation a model for the VHD-F.actin complex based on data at atomic resolution.

The successful expression of actin in *P.pastoris* made possible the attempt to produce a labelled version of this protein. A [^{13}C-δ1-methyl-Ile] actin was successfully expressed

[117] leading the way to the development of a protocol for the expression of different labelled versions of actin. As mentioned above, we are collaborating with Dr. Rosen, the author of this work, and he kindly provided the construct to express in *P.pastoris* both the versions of *Drosophila* actin with or without the ability of polymerize. The construct are already stored in our freezer and transformation of X33 strain of *Pichia* are already scheduled.

The availability of different isotopic enriched version of actin will make it possible to study the thin filaments directly instead of the indirect investigation through a bound ABP. This will be the first step in the characterization of the actin filaments that, in future, can lead to the solving of the actin filament structure at atomic resolution. It will be also fundamental to accurately define the structure of thin filament complexes and, as a consequence, to define in detail how they modulate the action of actin in cells. This will give important new insights in the understanding of the role of thin filament complexes in numerous diseases and suggest potential strategy in their treatment.

Appendix A **Buffer and Medium recipes**

List of buffer recipes

FF6 wash buffer: 20mM phosphate pH 7.5, 500mM NaCl, 10mM Imidazole, 0.02% NaN_3

FF6 elution buffer: 20mM phosphate pH 7.5, 500mM NaCl, 500mM Imidazole, 0.02% NaN_3

NMR buffer (or Phosphate buffer): 20mM phosphate pH 7.5, 50mM NaCl, 2mM DDT, 0.02% NaN_3

Extraction Buffer 1: 0.3M KCl, 0,1M KH2PO4, 0.05M K_2HPO_4 and 1mM EDTA at pH6.5

G-actin buffer: 2mM Tris-HCl pH 8, 0.2mM ATP, 0.1mM DTT, 0.02% NaN_3

10x KME buffer: 0.1M Tris-HCl pH 8, 0.5M KCl, 10mM EGTA, 25mM $MgCl_2$, 0.02% NaN_3

Acting binding buffer: 10mM Hepes pH 7.2, 50mM KCl, 3.5mM $MgCl_2$, 1mM DTT, 0.02% NaN_3

Pyrene labeling buffer: 25mM Tris pH 7.5, 0.1M KCl, 2mM $MgCl_2$, 0.3mM ATP, 0.02% NaN_3

List of medium recipes

Medium	Recipe	Concentration
LB And LB agar	Yeast extract Tryptone NaCl Agar (for LB agar)	0.5% 01% 0,5% 1.5%
Minimal M9 medium	M9 salt buffer $MgSO_4$ $CaCl_2$ Glucose NH_4Cl Vitamin Solution Micronutrients H2O	20ml from 20X stock 2mM 10µM 0.2% 0.1% 1ml from 1000x 1ml from 1000x 900ml
M9 salt buffer 20x stock (1L) pH 7-7.4	Na_2HPO_4 $KHPO_4$ NaCl	120g 60g 10g
Micronutrients 1000x stock (1L)	$(NH_4)_6Mo_7O_{24}\cdot 4H_2O$ H_3BO_3 $CoCl_2\cdot 6H_2O$	3.70 mg 24.7 mg 7.14 mg

	$CuSO_4 \cdot 5H_2O$ $MnCl_2 \cdot 4H_2O$ $ZnSO_4 \cdot 7H_2O$	2.50 mg 15.8 mg 2.88 mg
Vitamins 1000x stock (1L)	Choline chloride Biotin Folic acid Riboflavin Pantothenic acid Pyridoxine HCl Thiamine HCl Nicotinamide Myo-inositol	400mg 1g 500mg 50mg 500mg 500mg 500mg 500mg 1g
MG → MM	YNB Biotin Glycerol → Methanol	1.34% $4 \cdot 10^{-5}$% 1% → 0.5%
BMG → BMM	Potassium phosphate, pH 6.0 YNB Biotin Glycerol → Methanol	100 mM 1.34% $4 \cdot 10^{-5}$% 1% → 0.5%
BMGY → BMMY	Yeast extract Peptone Potassium phosphate, pH 6.0 YNB Biotin Glycerol → Methanol	1% 2% 100mM 1.34% $4 \cdot 10^{-5}$% 1% → 0.5%
FM22	$CaSo_4$ K_2SO_4 $MgSO_4$ Biotin PTM1 Salt NH_4Cl Glucose → Methanol	0.1% 1.43% 1.17% $4 \cdot 10^{-5}$% $1 \cdot 10^{-4}$% 0.5% 5% → 0.5%
FM23	YNB Biotin $(NH_4)_2SO_4$ K_2HPO_4 KH_2PO_4 PTM1 Salt NH_4Cl Glucose → Methanol	0.8% 2mg/L 1.2% 0.3% 0.28% $2 \cdot 10^{-4}$% 1.2% 3% → 0.5%

Appendix B Validation of method for peak fitting

In order to calculate the linewidth of signals that were too close to each other, a fitting of the signals was necessarily performed. The peak fitting was performed using the "line fitting" suite provided in the academic version of ACD/Lab [77] and MestReNova [78]. The relevant parameters and the algorithm used to perform it has been described in 4.11.

Nevertheless, the results from a peak fitting can be affected by errors when the processing of spectra is not taken into consideration. The application of window functions can contribute to introduce an error in the fitting due to the improvement of the signal to noise ratio in the spectrum and the narrowing of the signal linewidth that the function provide when applied. Ideally, the peak fitting should be done on spectra processed without the help of this function. On the other hand, in many cases it is not possible to process a FID without them due to a poor signal to noise ratio that affect the experiment and will result in a spectrum of just noise.

To validate the fitting performed for this spectra it was necessary to check how the application of the exponential window function, the common function used in processing 1D spectra (and the one used to process all the 1D spectra in this dissertation), affects the calculation. For this purpose a FID is processed using different values of linebroadening, the signals is fitted using the same set up and the linewidths is calculated. The values obtained are compared to the values of linewidth calculated when no window function is applied. When the linewidth values collimate, the value of the applied linebroadening does not affect anymore the fitting performed and no error will be introduced in the calculation.

For the validation was used the ^{31}P CP MAS FID acquired on a sample containing VHD-F.actin complex in which the filaments were not saturated by the ABP. The FID was processed both without window function (Figure 1) and with an increasing value of the linebroadening, from 20Hz to 90Hz at interval of 10Hz (Figure 2). The peak fitting was performed on each spectrum processed and the values of linewidth in Hertz are listed below (Table 1).

	Linebroadening applied	Linewidth in Hz No EM	20 Hz	30 Hz	40 Hz	50 Hz
Peaks fitted	-4.9ppm	136.43	91.37	112.45	125.58	124.94
	-11.0ppm	299.28	225.06	246.44	238.70	274.67
	-13.1ppm	192.18	136.75	142.32	153.95	163.87

	Linebroadening applied	Linewidth in Hz 60 Hz	70 Hz	80 Hz	90 Hz
Peaks fitted	-4.9ppm	130.96	133.83	130.73	140.75
	-11.0ppm	292.15	299.62	299.98	300.00
	-13.1ppm	178.21	185.26	191.80	190.45

Table 1 Linewidth calculation using ACD/Lab dedicated suite. The value calculated for each spectrum processed using EM window function with increasing value of linebrodening were compared to the value calculated for the same spectrum processed without any window function. After a linebroadening of 60Hz the calculated value collimate and are comparable to the reference.

It was observed that after 60Hz the application of the window function returned values of linewidth comparable to the reference. A value of 60Hz was then used to process all the FIDs in which the linewidth was calculated. Nevertheless, a more aggressive linebroadening of 20Hz was used to produce pictures better resolved that have been included in this dissertation.

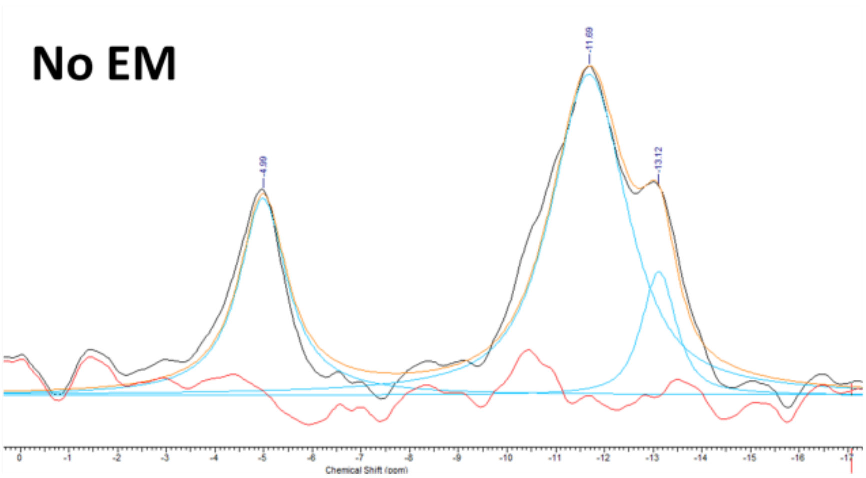

Figure 1 Output returned for the spectrum processed without window function. The black line represents the real spectrum while the other are the result from the peak fitting. Blue lines are the peaks fitted, the orange the sum of the fitted peak while the red the residual signal from the calculation. For a good fitting the orange has to be almost superimposable to the real spectrum while the residual signal has to be zero.

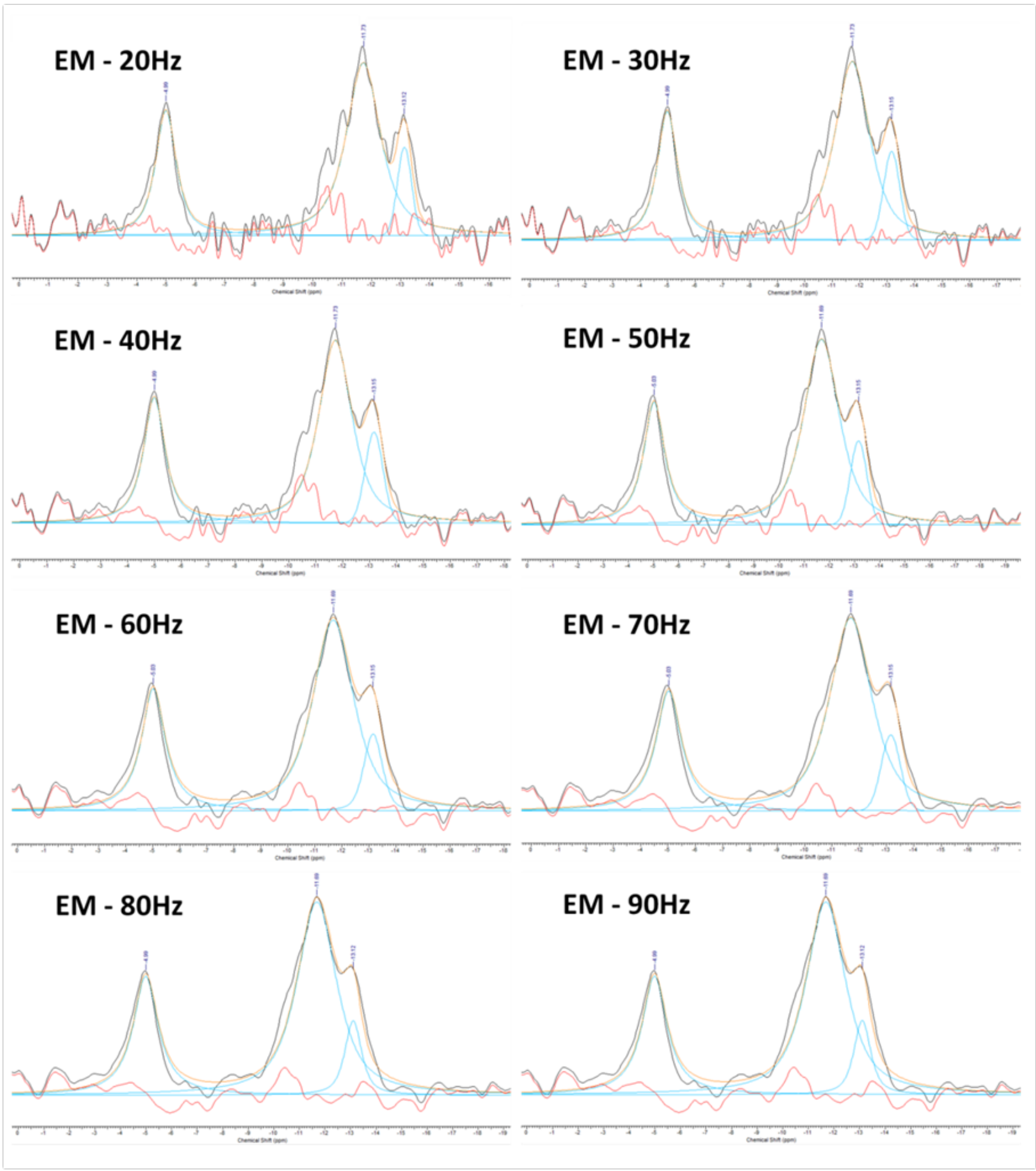

Figure 2 Output returned for the spectrum processed with increasing value of linebrodening. As hypothesized, the application of window function contributes to introduce an error in the calculation of the linewidth and only when the linebroadening applied is higher than 60Hz the calculation return value of linewidth comparable to the reference.

Appendix C R script developed to fit binding curves

The script for the calculation of the k_D between VHD and actin filaments has been developed by Dr. Pfuhl for the statistical software R. The input data are in form of a *(x,y)* table, where *x* represents the concentration of protein added to the filaments and *y* the percentage of filament saturated. The script calculates the best fitting of the curves generated by the data imported and returns the value of k_D for the binding.

```
BindFit <- function(path, file, Conc)
{  loadname <- " "
   loadname <- paste(path,file,sep="")
   titration <- read.table(loadname)
   xdata <- titration[1]
   ydata <- titration[2]
   cat("\n Titration data from :",file," \n\n")
   print(titration)
   nlsfit <- nls(V2~fbind2(Bm,V1,abs(Kd),Conc), data=titration, start=list(Kd=10.0,
      Bm=100))
   print(summary(nlsfit))
   Kd <- abs(coef(nlsfit)["Kd"])
   Bmax <- coef(nlsfit)["Bm"]
   fitx <- seq(0,max(xdata),length=100)
   fity <- fbind(Bmax,fitx,Kd,Conc)
   output1 <- paste("Kd = ",Kd," uM",sep="")
   plot(titration, main="Binding curve based on Densitometric data", sub=output1,
      type="p", pch=17, cex=1.5,xlab="conc / uM", ylab="% saturation", col="blue")
   lines(fitx,fity, col="red")
   mtext(file, side=3)}
fbind <- function(b,v,k,c)
{  res = b*((v+c+k)-sqrt(abs((v+c+k)^2-4*v*c)))/(2*c)
   return(res)}
```

Appendix D **Alignment of the sequenced DNA fragments of the VHD mutants**

The alignment has been performed using the Clustal Omega software provided by EMBL-EBI bioinformatics web [94].

```
VHD_WT                   TTCCAATCCATGCAATACAAGATCTATCCGTATGACTCCCTCATCGTCACAAACCGAATT
VHD_K61A                 TTCCAATCCATGCAATACAAGATCTATCCGTATGACTCCCTCATCGTCACAAACCGAATT
VHD_K62A_K63A            TTCCAATCCATGCAATACAAGATCTATCCGTATGACTCCCTCATCGTCACAAACCGAATT
VHD_R26A_R28A_R31A       TTCCAATCCATGCAATACAAGATCTATCCGTATGACTCCCTCATCGTCACAAACCGAATT
VHD_R26A_R28A            TTCCAATCCATGCAATACAAGATCTATCCGTATGACTCCCTCATCGTCACAAACCGAATT
VHD_R31A                 TTCCAATCCATGCAATACAAGATCTATCCGTATGACTCCCTCATCGTCACAAACCGAATT
VHD_R15A_R17A            TTCCAATCCATGCAATACAAGATCTATCCGTATGACTCCCTCATCGTCACAAACGCCATT
                         ******************************************************   ***

VHD_WT                   CGCGTGAAACTGCCCAAAGACGTGGACCGGACGAGACTGGAGAGACACTTGTCGCCCGAG
VHD_K61A                 CGCGTGAAACTGCCCAAAGACGTGGACCGGACGAGACTGGAGAGACACTTGTCGCCCGAG
VHD_K62A_K63A            CGCGTGAAACTGCCCAAAGACGTGGACCGGACGAGACTGGAGAGACACTTGTCGCCCGAG
VHD_R26A_R28A_R31A       CGCGTGAAACTGCCCAAAGACGTGGACGCCACGGCCCTGGAGGCCCACTTGTCGCCCGAG
VHD_R26A_R28A            CGCGTGAAACTGCCCAAAGACGTGGACGCCACGGCCCTGGAGAGACACTTGTCGCCCGAG
VHD_R31A                 CGCGTGAAACTGCCCAAAGACGTGGACCGGACGAGACTGGAGGCCCACTTGTCGCCCGAG
VHD_R15A_R17A            GCCGTGAAACTGCCCAAAGACGTGGACCGGACGAGACTGGAGAGACACTTGTCGCCCGAG
                            ************************   **   ******   ****************

VHD_WT                   GAGTTCCAGGAAGTGTTTGGGATGAGCATCGAGGAGTTTGACCGCCTGGCCCTCTGGAAG
VHD_K61A                 GAGTTCCAGGAAGTGTTTGGGATGAGCATCGAGGAGTTTGACCGCCTGGCCCTCTGGAAG
VHD_K62A_K63A            GAGTTCCAGGAAGTGTTTGGGATGAGCATCGAGGAGTTTGACCGCCTGGCCCTCTGGAAG
VHD_R26A_R28A_R31A       GAGTTCCAGGAAGTGTTTGGGATGAGCATCGAGGAGTTTGACCGCCTGGCCCTCTGGAAG
VHD_R26A_R28A            GAGTTCCAGGAAGTGTTTGGGATGAGCATCGAGGAGTTTGACCGCCTGGCCCTCTGGAAG
VHD_R31A                 GAGTTCCAGGAAGTGTTTGGGATGAGCATCGAGGAGTTTGACCGCCTGGCCCTCTGGAAG
VHD_R15A_R17A            GAGTTCCAGGAAGTGTTTGGGATGAGCATCGAGGAGTTTGACCGCCTGGCCCTCTGGAAG
                         ************************************************************

VHD_WT                   AGGAATGACCTTAAGAAGAAAGCCCTTTTGTTCTGATGACAGTAAAGGTGGATACGGATC
VHD_K61A                 AGGAATGACCTTGCCAAGAAAGCCCTTTTGTTCTGATGACAGTAAAGGTGGATACGGATC
VHD_K62A_K63A            AGGAATGACCTTAAGGCCGCCGCCCTTTTGTTCTGATGACAGTAAAGGTGGATACGGATC
VHD_R26A_R28A_R31A       AGGAATGACCTTAAGAAGAAAGCCCTTTTGTTCTGATGACAGTAAAGGTGGATACGGATC
VHD_R26A_R28A            AGGAATGACCTTAAGAAGAAAGCCCTTTTGTTCTGATGACAGTAAAGGTGGATACGGATC
VHD_R31A                 AGGAATGACCTTAAGAAGAAAGCCCTTTTGTTCTGATGACAGTAAAGGTGGATACGGATC
VHD_R15A_R17A            AGGAATGACCTTAAGAAGAAAGCCCTTTTGTTCTGATGACAGTAAAGGTGGATACGGATC
                         ************         ***************************************
```

Appendix E Assignment of VHD in free state performed using NMR in solution

The assignment of VHD performed by solution NMR was performed by Dr. Bruton and Dr. Pfuhl and deposited on BMRB database (ID entry 17206). All the resonances in the assignment are reported in ppm.

1 Gln	Hα	4.202
1 Gln	Hβ2	1.815
1 Gln	Hβ3	1.811
1 Gln	Hε2_1	7.391
1 Gln	Hε2_2	6.754
1 Gln	Hγ2	2.047
1 Gln	Hγ3	2.142
1 Gln	C	175.063
1 Gln	Cα	55.362
1 Gln	Cβ	29.607
1 Gln	Cγ	33.518
1 Gln	N	112.453
1 Gln	Nε2	112.466
2 Tyr	H	8.131
2 Tyr	Hα	4.397
2 Tyr	Hβ2	2.504
2 Tyr	Hβ3	2.131
2 Tyr	Hδ1	6.779
2 Tyr	Hδ2	6.779
2 Tyr	Hε1	6.687
2 Tyr	Hε2	6.687
2 Tyr	C	175.542
2 Tyr	Cα	57.026
2 Tyr	Cβ	38.872
2 Tyr	Cδ1	133.915
2 Tyr	Cδ2	133.915
2 Tyr	Cε1	118.263
2 Tyr	Cε2	118.263
2 Tyr	N	121.733
3 Lys	H	8.916
3 Lys	Hα	4.063
3 Lys	Hβ2	1.749

3 Lys	Hβ3	1.660
3 Lys	Hδ2	1.639
3 Lys	Hδ3	1.638
3 Lys	Hε2	2.820
3 Lys	Hε3	2.814
3 Lys	Hγ2	1.318
3 Lys	Hγ3	1.129
3 Lys	C	175.840
3 Lys	Cα	56.611
3 Lys	Cβ	32.873
3 Lys	Cδ	28.816
3 Lys	Cε	41.963
3 Lys	Cγ	25.100
3 Lys	N	125.174
4 Ile	H	7.973
4 Ile	Hα	4.715
4 Ile	Hβ	1.628
4 Ile	Hδ1_1	0.494
4 Ile	Hδ1_2	0.494
4 Ile	Hδ1_3	0.494
4 Ile	Hγ1_2	1.500
4 Ile	Hγ1_3	1.185
4 Ile	Hγ2_1	0.581
4 Ile	Hγ2_2	0.581
4 Ile	Hγ2_3	0.581
4 Ile	C	176.582
4 Ile	Cα	59.509
4 Ile	Cβ	37.474
4 Ile	Cδ1	11.547
4 Ile	Cγ1	27.919
4 Ile	Cγ2	17.860
4 Ile	N	124.961

5 Tyr	H	9.115
5 Tyr	Hα	4.908
5 Tyr	Hβ2	2.876
5 Tyr	Hβ3	2.313
5 Tyr	Hδ1	6.966
5 Tyr	Hδ2	6.966
5 Tyr	Hε1	6.545
5 Tyr	Hε2	6.545
5 Tyr	Cα	55.621
5 Tyr	Cβ	41.802
5 Tyr	Cδ1	133.534
5 Tyr	Cδ2	133.534
5 Tyr	Cε1	118.673
5 Tyr	Cε2	118.673
5 Tyr	N	126.648
6 Pro	Hα	4.658
6 Pro	Hβ2	2.565
6 Pro	Hβ3	2.029
6 Pro	Hδ2	3.993
6 Pro	Hδ3	3.766
6 Pro	Hγ2	2.170
6 Pro	Hγ3	2.097
6 Pro	C	178.042
6 Pro	Cα	62.193
6 Pro	Cβ	32.385
6 Pro	Cδ	50.753
6 Pro	Cγ	27.865
7 Tyr	H	10.315
7 Tyr	Hα	4.048
7 Tyr	Hβ2	3.089
7 Tyr	Hβ3	2.809
7 Tyr	Hδ1	6.931

7 Tyr	Hδ2	6.931
7 Tyr	Hε1	6.599
7 Tyr	Hε2	6.599
7 Tyr	C	176.702
7 Tyr	Cα	61.047
7 Tyr	Cβ	37.809
7 Tyr	Cδ1	133.019
7 Tyr	Cδ2	133.019
7 Tyr	Cε1	118.310
7 Tyr	Cε2	118.310
7 Tyr	N	128.942
8 Asp	H	8.641
8 Asp	Hα	3.899
8 Asp	Hβ2	2.539
8 Asp	Hβ3	2.445
8 Asp	C	177.274
8 Asp	Cα	56.669
8 Asp	Cβ	41.098
8 Asp	N	113.980
9 Ser	H	7.794
9 Ser	Hα	4.335
9 Ser	Hβ2	3.934
9 Ser	Hβ3	3.814
9 Ser	C	173.823
9 Ser	Cα	59.796
9 Ser	Cβ	64.042
9 Ser	N	112.271
10 Leu	H	7.508
10 Leu	Hα	4.077
10 Leu	Hβ2	1.642
10 Leu	Hβ3	1.385
10 Leu	Hδ1_1	0.625
10 Leu	Hδ1_2	0.625
10 Leu	Hδ1_3	0.625
10 Leu	Hδ2_1	0.317
10 Leu	Hδ2_2	0.317
10 Leu	Hδ2_3	0.317
10 Leu	Hγ	1.602
10 Leu	C	175.443
10 Leu	Cα	54.603
10 Leu	Cβ	44.090

10 Leu	Cδ1	26.623
10 Leu	Cδ2	22.112
10 Leu	Cγ	25.578
10 Leu	N	120.512
11 Ile	H	6.487
11 Ile	Hα	3.908
11 Ile	Hβ	1.508
11 Ile	Hδ1_1	0.362
11 Ile	Hδ1_2	0.362
11 Ile	Hδ1_3	0.362
11 Ile	Hγ1_2	1.151
11 Ile	Hγ1_3	0.565
11 Ile	Hγ2_1	0.388
11 Ile	Hγ2_2	0.388
11 Ile	Hγ2_3	0.388
11 Ile	C	178.512
11 Ile	Cα	62.479
11 Ile	Cβ	39.600
11 Ile	Cδ1	13.479
11 Ile	Cγ1	26.341
11 Ile	Cγ2	18.073
11 Ile	N	112.881
12 Val	H	8.412
12 Val	Hα	3.947
12 Val	Hβ	1.922
12 Val	Hγ1_1	0.563
12 Val	Hγ1_2	0.563
12 Val	Hγ1_3	0.563
12 Val	Hγ2_1	0.561
12 Val	Hγ2_2	0.561
12 Val	Hγ2_3	0.561
12 Val	C	176.518
12 Val	Cα	63.600
12 Val	Cβ	32.977
12 Val	Cγ1	21.071
12 Val	Cγ2	20.312
12 Val	N	120.733
13 Thr	H	7.275
13 Thr	Hα	4.022
13 Thr	Hβ	3.992
13 Thr	Hγ2_1	1.215

13 Thr	Hγ2_2	1.215
13 Thr	Hγ2_3	1.215
13 Thr	Cα	63.160
13 Thr	Cβ	68.722
13 Thr	Cγ2	22.536
13 Thr	N	114.032
14 Asn	Hα	4.726
14 Asn	Hβ2	2.882
14 Asn	Hβ3	2.706
14 Asn	Hδ2_1	7.714
14 Asn	Hδ2_2	6.875
14 Asn	Cα	53.445
14 Asn	Cβ	38.406
14 Asn	Nδ2	113.487
15 Arg	Hα	4.272
15 Arg	Hβ2	1.732
15 Arg	Hβ3	1.732
15 Arg	Hδ2	3.100
15 Arg	Hδ3	3.101
15 Arg	Hγ2	1.553
15 Arg	Hγ3	1.554
15 Arg	C	176.531
15 Arg	Cα	56.716
15 Arg	Cβ	30.598
15 Arg	Cδ	43.023
15 Arg	Cγ	26.931
16 Ile	H	7.794
16 Ile	Hα	4.030
16 Ile	Hβ	1.848
16 Ile	Hδ1_1	0.559
16 Ile	Hδ1_2	0.559
16 Ile	Hδ1_3	0.559
16 Ile	Hγ1_2	1.384
16 Ile	Hγ1_3	1.183
16 Ile	Hγ2_1	0.592
16 Ile	Hγ2_2	0.592
16 Ile	Hγ2_3	0.592
16 Ile	C	176.327
16 Ile	Cα	61.958
16 Ile	Cβ	38.120
16 Ile	Cδ1	12.826

16 Ile	Cγ1	27.541
16 Ile	Cγ2	17.517
16 Ile	N	117.694
17 Arg	H	7.935
17 Arg	Hα	4.251
17 Arg	Hβ2	1.774
17 Arg	Hβ3	1.774
17 Arg	Hδ2	3.141
17 Arg	Hδ3	3.141
17 Arg	Hγ2	1.546
17 Arg	Hγ3	1.546
17 Arg	C	175.947
17 Arg	Cα	56.564
17 Arg	Cβ	29.68
17 Arg	Cδ	42.978
17 Arg	Cγ	27.344
17 Arg	N	121.108
18 Val	H	7.827
18 Val	Hα	4.049
18 Val	Hβ	1.980
18 Val	Hγ1_1	0.588
18 Val	Hγ1_2	0.588
18 Val	Hγ1_3	0.588
18 Val	Hγ2_1	0.590
18 Val	Hγ2_2	0.590
18 Val	Hγ2_3	0.590
18 Val	C	175.087
18 Val	Cα	61.818
18 Val	Cβ	33.158
18 Val	Cγ1	20.889
18 Val	Cγ2	21.052
18 Val	N	119.588
19 Lys	H	8.241
19 Lys	Hα	4.273
19 Lys	Hβ2	1.631
19 Lys	Hβ3	1.714
19 Lys	Hδ2	1.607
19 Lys	Hδ3	1.607
19 Lys	Hε2	2.907
19 Lys	Hε3	2.907
19 Lys	Hγ2	1.310

19 Lys	Hγ3	1.307
19 Lys	C	175.904
19 Lys	Cα	55.284
19 Lys	Cβ	32.247
19 Lys	Cδ	28.890
19 Lys	Cε	41.758
19 Lys	Cγ	24.511
19 Lys	N	125.066
20 Leu	H	8.144
20 Leu	Hα	4.372
20 Leu	Hβ2	1.440
20 Leu	Hβ3	1.106
20 Leu	Hδ1_1	0.458
20 Leu	Hδ1_2	0.458
20 Leu	Hδ1_3	0.458
20 Leu	Hδ2_1	0.438
20 Leu	Hδ2_2	0.438
20 Leu	Hδ2_3	0.438
20 Leu	Hγ	1.485
20 Leu	Cα	52.775
20 Leu	Cβ	41.917
20 Leu	Cδ1	25.507
20 Leu	Cδ2	23.437
20 Leu	Cγ	26.725
20 Leu	N	125.353
21 Pro	Hα	4.299
21 Pro	Hβ2	2.207
21 Pro	Hβ3	1.613
21 Pro	Hδ2	3.732
21 Pro	Hδ3	2.883
21 Pro	Hγ2	1.609
21 Pro	Hγ3	1.206
21 Pro	C	177.274
21 Pro	Cα	62.518
21 Pro	Cβ	32.546
21 Pro	Cδ	50.451
21 Pro	Cγ	27.339
22 Lys	H	8.495
22 Lys	Hα	3.984
22 Lys	Hβ2	1.798
22 Lys	Hβ3	1.798

22 Lys	Hδ2	1.643
22 Lys	Hδ3	1.643
22 Lys	Hε2	2.948
22 Lys	Hε3	2.953
22 Lys	Hγ2	1.444
22 Lys	Hγ3	1.444
22 Lys	C	176.465
22 Lys	Cα	57.984
22 Lys	Cβ	32.298
22 Lys	Cδ	29.001
22 Lys	Cε	41.741
22 Lys	Cγ	24.514
22 Lys	N	120.273
23 Asp	H	8.105
23 Asp	Hα	4.486
23 Asp	Hβ2	2.941
23 Asp	Hβ3	2.554
23 Asp	C	175.640
23 Asp	Cα	53.397
23 Asp	Cβ	39.609
23 Asp	N	114.896
24 Val	H	6.943
24 Val	Hα	4.030
24 Val	Hβ	1.525
24 Val	Hγ1_1	0.216
24 Val	Hγ1_2	0.216
24 Val	Hγ1_3	0.216
24 Val	Hγ2_1	0.128
24 Val	Hγ2_2	0.128
24 Val	Hγ2_3	0.128
24 Val	C	175.226
24 Val	Cα	60.948
24 Val	Cβ	32.168
24 Val	Cγ1	21.535
24 Val	Cγ2	21.897
24 Val	N	116.559
25 Asp	H	9.742
25 Asp	Hα	4.682
25 Asp	Hβ2	3.181
25 Asp	Hβ3	2.655
25 Asp	C	177.014

25 Asp	Cα	52.446
25 Asp	Cβ	40.939
25 Asp	N	128.563
26 Arg	H	8.640
26 Arg	Hα	3.825
26 Arg	Hβ2	1.857
26 Arg	Hβ3	1.857
26 Arg	Hδ2	3.186
26 Arg	Hδ3	3.075
26 Arg	Hγ2	1.679
26 Arg	Hγ3	1.560
26 Arg	C	177.492
26 Arg	Cα	57.965
26 Arg	Cβ	29.631
26 Arg	Cδ	42.860
26 Arg	Cγ	27.801
26 Arg	N	124.916
27 Thr	H	8.724
27 Thr	Hα	4.467
27 Thr	Hβ	4.354
27 Thr	Hγ2_1	1.226
27 Thr	Hγ2_2	1.226
27 Thr	Hγ2_3	1.226
27 Thr	C	175.349
27 Thr	Cα	62.683
27 Thr	Cβ	69.415
27 Thr	Cγ2	21.804
27 Thr	N	110.779
28 Arg	H	7.714
28 Arg	Hα	4.944
28 Arg	Hβ2	1.790
28 Arg	Hβ3	1.424
28 Arg	Hδ2	3.143
28 Arg	Hδ3	3.051
28 Arg	Hγ2	1.656
28 Arg	Hγ3	1.511
28 Arg	C	176.703
28 Arg	Cα	53.737
28 Arg	Cβ	30.83
28 Arg	Cδ	43.322
28 Arg	Cγ	26.578

28 Arg	N	124.233
29 Leu	H	8.272
29 Leu	Hα	4.098
29 Leu	Hβ2	1.458
29 Leu	Hβ3	1.905
29 Leu	Hδ1_1	0.535
29 Leu	Hδ1_2	0.535
29 Leu	Hδ1_3	0.535
29 Leu	Hδ2_1	0.651
29 Leu	Hδ2_2	0.651
29 Leu	Hδ2_3	0.651
29 Leu	Hγ	1.921
29 Leu	C	178.454
29 Leu	Cα	58.349
29 Leu	Cβ	43.431
29 Leu	Cδ1	24.824
29 Leu	Cδ2	26.514
29 Leu	Cγ	26.856
29 Leu	N	120.495
30 Glu	H	10.176
30 Glu	Hα	4.133
30 Glu	Hβ2	1.933
30 Glu	Hβ3	1.831
30 Glu	Hγ2	2.360
30 Glu	Hγ3	2.263
30 Glu	C	177.116
30 Glu	Cα	58.325
30 Glu	Cγ	33.114
30 Glu	N	115.901
31 Arg	H	7.731
31 Arg	Hα	3.857
31 Arg	Hβ2	1.192
31 Arg	Hβ3	0.551
31 Arg	Hδ2	2.545
31 Arg	Hδ3	2.818
31 Arg	Hγ2	1.363
31 Arg	Hγ3	1.130
31 Arg	C	175.348
31 Arg	Cα	56.205
31 Arg	Cβ	28.935
31 Arg	Cδ	41.999

31 Arg	Cγ	27.871
31 Arg	N	119.316
32 His	H	7.703
32 His	Hα	4.443
32 His	Hβ2	3.847
32 His	Hβ3	3.336
32 His	Hδ2	7.044
32 His	Hε1	8.287
32 His	C	172.712
32 His	Cα	56.333
32 His	Cβ	29.120
32 His	Cδ2	130.421
32 His	Cε1	139.437
32 His	N	115.047
33 Leu	H	6.624
33 Leu	Hα	5.060
33 Leu	Hβ2	2.059
33 Leu	Hβ3	1.680
33 Leu	Hδ1_1	1.108
33 Leu	Hδ1_2	1.108
33 Leu	Hδ1_3	1.108
33 Leu	Hδ2_1	0.635
33 Leu	Hδ2_2	0.635
33 Leu	Hδ2_3	0.635
33 Leu	Hγ	1.924
33 Leu	C	178.490
33 Leu	Cα	53.165
33 Leu	Cβ	43.984
33 Leu	Cδ1	24.525
33 Leu	Cδ2	26.652
33 Leu	Cγ	26.868
33 Leu	N	115.408
34 Ser	H	9.940
34 Ser	Hα	4.441
34 Ser	Hβ2	4.504
34 Ser	Hβ3	4.065
34 Ser	Cα	56.109
34 Ser	Cβ	62.189
34 Ser	N	120.867
35 Pro	Hα	4.516
35 Pro	Hβ2	2.313

35 Pro	Hβ3	1.908
35 Pro	Hδ2	3.925
35 Pro	Hδ3	3.857
35 Pro	Hγ2	2.202
35 Pro	Hγ3	2.051
35 Pro	C	180.014
35 Pro	Cα	65.497
35 Pro	Cβ	31.224
35 Pro	Cδ	49.507
35 Pro	Cγ	28.099
36 Glu	H	8.772
36 Glu	Hα	4.035
36 Glu	Hβ2	2.064
36 Glu	Hβ3	1.923
36 Glu	Hγ2	2.446
36 Glu	Hγ3	2.216
36 Glu	C	179.679
36 Glu	Cα	60.496
36 Glu	Cβ	28.623
36 Glu	Cγ	37.112
36 Glu	N	117.055
37 Glu	H	8.015
37 Glu	Hα	4.100
37 Glu	Hβ2	2.128
37 Glu	Hβ3	1.890
37 Glu	Hγ2	2.493
37 Glu	Hγ3	2.111
37 Glu	C	177.932
37 Glu	Cα	60.163
37 Glu	Cβ	29.827
37 Glu	Cγ	39.142
37 Glu	N	120.774
38 Phe	H	9.410
38 Phe	Hα	3.648
38 Phe	Hβ2	3.263
38 Phe	Hβ3	2.996
38 Phe	Hδ1	7.097
38 Phe	Hδ2	7.097
38 Phe	Hε1	7.012
38 Phe	Hε2	7.012
38 Phe	Hζ	6.805

38 Phe	C	177.651
38 Phe	Cα	62.845
38 Phe	Cβ	39.553
38 Phe	Cδ1	132.801
38 Phe	Cδ2	132.801
38 Phe	Cε1	131.276
38 Phe	Cε2	131.276
38 Phe	Cζ	129.218
38 Phe	N	121.510
39 Gln	H	7.872
39 Gln	Hα	4.140
39 Gln	Hβ2	2.214
39 Gln	Hβ3	2.047
39 Gln	Hε2_1	7.295
39 Gln	Hε2_2	6.565
39 Gln	Hγ2	2.238
39 Gln	Hγ3	2.351
39 Gln	C	179.315
39 Gln	Cα	58.334
39 Gln	Cβ	27.553
39 Gln	Cδ	179.561
39 Gln	Cγ	33.133
39 Gln	N	116.948
39 Gln	Nε2	109.970
40 Glu	H	7.465
40 Glu	Hα	3.882
40 Glu	Hβ2	1.991
40 Glu	Hβ3	2.089
40 Glu	Hγ2	2.241
40 Glu	Hγ3	2.127
40 Glu	C	178.030
40 Glu	Cα	59.030
40 Glu	Cβ	29.743
40 Glu	Cγ	35.790
40 Glu	N	119.937
41 Val	H	8.077
41 Val	Hα	3.178
41 Val	Hβ	1.119
41 Val	Hγ1_1	-0.052
41 Val	Hγ1_2	-0.052
41 Val	Hγ1_3	-0.052

41 Val	Hγ2_1	-0.494
41 Val	Hγ2_2	-0.494
41 Val	Hγ2_3	-0.494
41 Val	C	177.566
41 Val	Cα	65.379
41 Val	Cβ	32.099
41 Val	Cγ1	21.025
41 Val	Cγ2	20.717
41 Val	N	118.390
42 Phe	H	8.408
42 Phe	Hα	4.307
42 Phe	Hβ2	2.776
42 Phe	Hβ3	2.335
42 Phe	Hδ1	6.207
42 Phe	Hδ2	6.207
42 Phe	Hε1	6.424
42 Phe	Hε2	6.424
42 Phe	Hζ	6.561
42 Phe	C	176.858
42 Phe	Cα	59.489
42 Phe	Cβ	40.015
42 Phe	Cδ1	132.141
42 Phe	Cδ2	132.141
42 Phe	Cε1	129.889
42 Phe	Cε2	129.889
42 Phe	Cζ	127.549
42 Phe	N	113.570
43 Gly	H	8.091
43 Gly	Hα2	3.903
43 Gly	Hα3	3.903
43 Gly	C	173.007
43 Gly	Cα	46.361
43 Gly	N	108.977
44 Met	H	7.573
44 Met	Hα	4.731
44 Met	Hβ2	2.331
44 Met	Hβ3	2.156
44 Met	Hε1	2.119
44 Met	Hε2	2.119
44 Met	Hε3	2.119
44 Met	Hγ2	2.737

44 Met	Hγ3	2.225
44 Met	C	172.092
44 Met	Cα	53.588
44 Met	Cβ	34.376
44 Met	Cε	16.562
44 Met	Cγ	29.188
44 Met	N	113.741
45 Ser	H	8.477
45 Ser	Hα	4.715
45 Ser	Hβ2	4.237
45 Ser	Hβ3	3.973
45 Ser	C	176.467
45 Ser	Cα	56.946
45 Ser	Cβ	65.851
45 Ser	N	112.450
46 Ile	H	8.721
46 Ile	Hα	3.319
46 Ile	Hβ	0.122
46 Ile	Hδ1_1	0.247
46 Ile	Hδ1_2	0.247
46 Ile	Hδ1_3	0.247
46 Ile	Hγ1_2	0.540
46 Ile	Hγ1_3	0.542
46 Ile	Hγ2_1	0.377
46 Ile	Hγ2_2	0.377
46 Ile	Hγ2_3	0.377
46 Ile	C	176.010
46 Ile	Cα	64.393
46 Ile	Cβ	37.226
46 Ile	Cδ1	14.262
46 Ile	Cγ1	29.244
46 Ile	Cγ2	16.168
46 Ile	N	123.820
47 Glu	H	8.050
47 Glu	Hα	3.950
47 Glu	Hβ2	1.930
47 Glu	Hβ3	1.767
47 Glu	Hγ2	2.160
47 Glu	Hγ3	2.270
47 Glu	C	179.559
47 Glu	Cα	59.791

47 Glu	Cβ	28.593
47 Glu	Cγ	36.938
47 Glu	N	120.765
48 Glu	H	7.219
48 Glu	Hα	3.796
48 Glu	Hβ2	2.007
48 Glu	Hβ3	2.199
48 Glu	Hγ2	2.240
48 Glu	Hγ3	2.239
48 Glu	C	179.150
48 Glu	Cα	58.750
48 Glu	Cβ	29.912
48 Glu	Cγ	37.097
48 Glu	N	118.111
49 Phe	H	8.331
49 Phe	Hα	4.083
49 Phe	Hβ2	3.290
49 Phe	Hβ3	2.903
49 Phe	Hδ1	7.379
49 Phe	Hδ2	7.379
49 Phe	Hε1	6.236
49 Phe	Hε2	6.236
49 Phe	Hζ	5.478
49 Phe	C	176.947
49 Phe	Cα	60.941
49 Phe	Cβ	40.366
49 Phe	Cδ1	132.870
49 Phe	Cδ2	132.870
49 Phe	Cε1	130.990
49 Phe	Cε2	130.990
49 Phe	Cζ	129.383
49 Phe	N	123.947
50 Asp	H	8.431
50 Asp	Hα	4.273
50 Asp	Hβ2	2.531
50 Asp	Hβ3	2.525
50 Asp	C	177.493
50 Asp	Cα	56.066
50 Asp	Cβ	40.302
50 Asp	N	116.461
51 Arg	H	7.042

51 Arg	Hα	4.136
51 Arg	Hβ2	1.878
51 Arg	Hβ3	1.704
51 Arg	Hδ2	3.146
51 Arg	Hδ3	3.081
51 Arg	Hγ2	1.852
51 Arg	Hγ3	1.551
51 Arg	C	177.377
51 Arg	Cα	56.423
51 Arg	Cβ	30.968
51 Arg	Cδ	43.628
51 Arg	Cγ	27.873
51 Arg	N	116.016
52 Leu	H	7.404
52 Leu	Hα	4.058
52 Leu	Hβ2	0.616
52 Leu	Hβ3	1.669
52 Leu	Hδ1_1	0.389
52 Leu	Hδ1_2	0.389
52 Leu	Hδ1_3	0.389
52 Leu	Hδ2_1	0.456
52 Leu	Hδ2_2	0.456
52 Leu	Hδ2_3	0.456
52 Leu	Hγ	1.825
52 Leu	C	176.995
52 Leu	Cα	53.909
52 Leu	Cβ	42.729
52 Leu	Cδ1	26.251
52 Leu	Cδ2	22.001
52 Leu	Cγ	25.636
52 Leu	N	120.459
53 Ala	H	8.150
53 Ala	Hα	4.056
53 Ala	Hβ1	1.119
53 Ala	Hβ2	1.119
53 Ala	Hβ3	1.119
53 Ala	C	178.349
53 Ala	Cα	51.724
53 Ala	Cβ	18.885
53 Ala	N	123.361
54 Leu	H	8.694

54 Leu	Hα	3.668
54 Leu	Hβ2	1.831
54 Leu	Hβ3	1.524
54 Leu	Hδ1_1	0.626
54 Leu	Hδ1_2	0.626
54 Leu	Hδ1_3	0.626
54 Leu	Hδ2_1	0.617
54 Leu	Hδ2_2	0.617
54 Leu	Hδ2_3	0.617
54 Leu	C	178.106
54 Leu	Cα	58.736
54 Leu	Cβ	41.398
54 Leu	Cδ1	25.553
54 Leu	Cδ2	23.085
54 Leu	N	124.353
55 Trp	H	8.044
55 Trp	Hα	4.302
55 Trp	Hβ2	3.451
55 Trp	Hβ3	3.198
55 Trp	Hδ1	7.453
55 Trp	Hε1	10.300
55 Trp	Hε3	7.385
55 Trp	HH2	7.201
55 Trp	Hζ2	7.451
55 Trp	Hζ3	7.094
55 Trp	C	177.881
55 Trp	Cα	59.254
55 Trp	Cβ	26.656
55 Trp	Cδ1	127.996
55 Trp	Cε3	121.387
55 Trp	CH2	125.299
55 Trp	Cζ2	115.001
55 Trp	Cζ3	122.754
55 Trp	N	114.222
55 Trp	Nε1	129.910
56 Lys	H	5.948
56 Lys	Hα	3.537
56 Lys	Hβ2	1.351
56 Lys	Hβ3	0.276
56 Lys	Hδ2	1.482
56 Lys	Hδ3	1.390

56 Lys	Hε2	2.722
56 Lys	Hε3	2.836
56 Lys	Hγ2	0.453
56 Lys	Hγ3	0.625
56 Lys	C	178.130
56 Lys	Cα	57.638
56 Lys	Cβ	31.110
56 Lys	Cδ	28.614
56 Lys	Cε	41.532
56 Lys	Cγ	24.553
56 Lys	N	124.104
57 Arg	H	7.736
57 Arg	Hα	3.374
57 Arg	Hβ2	1.693
57 Arg	Hβ3	1.398
57 Arg	Hδ2	2.543
57 Arg	Hδ3	2.962
57 Arg	Hε	6.394
57 Arg	Hγ2	-0.184
57 Arg	Hγ3	0.608
57 Arg	C	179.019
57 Arg	Cα	60.312
57 Arg	Cβ	30.634
57 Arg	Cδ	43.916
57 Arg	Cγ	28.435
57 Arg	N	119.689
57 Arg	Nε	108.780
58 Asn	H	8.397
58 Asn	Hα	4.562
58 Asn	Hβ2	2.852
58 Asn	Hβ3	2.559
58 Asn	Hδ2_1	7.661
58 Asn	Hδ2_2	6.945
58 Asn	C	177.757
58 Asn	Cα	55.513
58 Asn	Cβ	37.077
58 Asn	Cγ	174.835
58 Asn	N	116.293
58 Asn	Nδ2	110.219
59 Asp	H	7.946
59 Asp	Hα	4.384

59 Asp	Hβ2	2.833
59 Asp	Hβ3	2.728
59 Asp	C	179.166
59 Asp	Cα	58.104
59 Asp	Cβ	41.532
59 Asp	N	122.930
60 Leu	H	8.410
60 Leu	Hα	4.136
60 Leu	Hβ2	2.321
60 Leu	Hβ3	1.712
60 Leu	Hδ1_1	0.673
60 Leu	Hδ1_2	0.673
60 Leu	Hδ1_3	0.673
60 Leu	Hδ2_1	0.680
60 Leu	Hδ2_2	0.680
60 Leu	Hδ2_3	0.680
60 Leu	Hγ	1.959
60 Leu	C	181.121
60 Leu	Cα	57.918
60 Leu	Cβ	42.052
60 Leu	Cδ2	22.494
60 Leu	Cγ	27.045
60 Leu	N	119.199
61 Lys	H	8.763
61 Lys	Hα	3.993
61 Lys	Hβ2	2.108
61 Lys	Hβ3	1.869
61 Lys	Hδ2	1.367
61 Lys	Hδ3	1.367
61 Lys	Hε2	2.887
61 Lys	Hε3	3.127
61 Lys	Hγ2	0.580
61 Lys	Hγ3	0.657
61 Lys	C	178.388
61 Lys	Cα	61.260
61 Lys	Cβ	31.615
61 Lys	Cε	42.630
61 Lys	Cγ	24.686
61 Lys	N	119.499
62 Lys	H	8.606
62 Lys	Hα	4.147

62 Lys	Hβ2	1.917
62 Lys	Hβ3	1.917
62 Lys	Hδ2	1.448
62 Lys	Hδ3	1.448
62 Lys	Hε2	2.374
62 Lys	Hε3	2.374
62 Lys	Hγ2	1.282
62 Lys	Hγ3	1.160
62 Lys	C	181.046
62 Lys	Cα	60.176
62 Lys	Cβ	32.134
62 Lys	Cδ	29.281
62 Lys	Cε	41.401
62 Lys	Cγ	26.056
62 Lys	N	121.435
63 Lys	H	7.888
63 Lys	Hα	4.000
63 Lys	Hβ2	1.940
63 Lys	Hβ3	1.940
63 Lys	Hδ2	1.644
63 Lys	Hδ3	1.644
63 Lys	Hε2	2.956
63 Lys	Hε3	2.956
63 Lys	Hγ2	1.568
63 Lys	Hγ3	1.426
63 Lys	C	177.192
63 Lys	Cα	59.186
63 Lys	Cβ	32.162
63 Lys	Cδ	28.923
63 Lys	Cε	41.659
63 Lys	Cγ	25.568
63 Lys	N	121.604
64 Ala	H	7.514
64 Ala	Hα	4.195
64 Ala	Hβ1	1.053
64 Ala	Hβ2	1.053
64 Ala	Hβ3	1.053
64 Ala	C	176.529
64 Ala	Cα	51.407
64 Ala	Cβ	19.880
64 Ala	N	117.839
65 Leu	H	7.860
65 Leu	Hα	4.192
65 Leu	Hβ2	2.480
65 Leu	Hβ3	1.624
65 Leu	Hδ1_1	0.624
65 Leu	Hδ1_2	0.624
65 Leu	Hδ1_3	0.624
65 Leu	Hδ2_1	0.642
65 Leu	Hδ2_2	0.642
65 Leu	Hδ2_3	0.642
65 Leu	Hγ	1.481
65 Leu	C	175.926
65 Leu	Cα	56.108
65 Leu	Cβ	38.491
65 Leu	Cδ1	25.841
65 Leu	Cδ2	22.588
65 Leu	Cγ	26.726
65 Leu	N	114.376
66 Leu	H	8.403
66 Leu	Hα	4.707
66 Leu	Hβ2	1.973
66 Leu	Hβ3	1.440
66 Leu	Hδ1_1	0.680
66 Leu	Hδ1_2	0.680
66 Leu	Hδ1_3	0.680
66 Leu	Hδ2_1	0.569
66 Leu	Hδ2_2	0.569
66 Leu	Hδ2_3	0.569
66 Leu	Hγ	1.877
66 Leu	C	173.977
66 Leu	Cα	52.770
66 Leu	Cβ	43.086
66 Leu	Cδ1	27.278
66 Leu	Cδ2	23.628
66 Leu	Cγ	25.695
66 Leu	N	117.033
67 Phe	H	7.324
67 Phe	Hα	4.398
67 Phe	Hβ2	2.749
67 Phe	Hβ3	2.900
67 Phe	Hδ1	7.189
67 Phe	Hδ2	7.189
67 Phe	Hε1	7.370
67 Phe	Hε2	7.370
67 Phe	Hζ	7.324
67 Phe	Cα	59.555
67 Phe	Cβ	42.124
67 Phe	Cδ1	132.195
67 Phe	Cδ2	132.195
67 Phe	Cε1	132.011
67 Phe	Cε2	132.011
67 Phe	Cζ	130.422
67 Phe	N	124.611

Bibliography

1. Oda, T. and Y. Maeda, *Multiple Conformations of F-actin.* Structure, 2010. **18**(7): p. 761-7.
2. Oda, T., et al., *The nature of the globular- to fibrous-actin transition.* Nature, 2009. **457**(7228): p. 441-5.
3. Pollard, T.D. and J.A. Cooper, *Actin, a Central Player in Cell Shape and Movement.* Science (New York, N.Y.), 2009. **326**(5957): p. 1208-1212.
4. Blanchoin, L., et al., *Actin Dynamics, Architecture, and Mechanics in Cell Motility.* Physiological Reviews, 2014. **94**(1): p. 235-263.
5. Hild, G., B. Bugyi, and M. Nyitrai, *Conformational dynamics of actin: effectors and implications for biological function.* Cytoskeleton (Hoboken), 2010. **67**(10): p. 609-29.
6. Dominguez, R. and K.C. Holmes, *Actin Structure and Function.* Annual review of biophysics, 2011. **40**: p. 169-186.
7. Kabsch, W., et al., *Atomic structure of the actin: DNase I complex.* Nature, 1990. **347**(6288): p. 37-44.
8. Oriol, C., C. Dubord, and F. Landon, *Crystallization of native striated-muscle actin.* FEBS Letters, 1977. **73**(1): p. 89-91.
9. Yoshidome, T., et al., *Free-energy function based on an all-atom model for proteins.* Proteins: Structure, Function, and Bioinformatics, 2009. **77**(4): p. 950-961.
10. Lodish H, B.A., Zipursky SL, et al., *The Dynamics of Actin Assembly.* Molecular Cell Biology, 2000. **4th edition**: p. Section 18.2.
11. Atkinson, S.J., M.A. Hosford, and B.A. Molitoris, *Mechanism of Actin Polymerization in Cellular ATP Depletion.* Journal of Biological Chemistry, 2004. **279**(7): p. 5194-5199.
12. Korn, E., M. Carlier, and D. Pantaloni, *Actin polymerization and ATP hydrolysis.* Science, 1987. **238**(4827): p. 638-644.
13. Holmes, K.C., et al., *Atomic model of the actin filament.* Nature, 1990. **347**(6288): p. 44-49.
14. T D Pollard, a. and J.A. Cooper, *Actin and Actin-Binding Proteins. A Critical Evaluation of Mechanisms and Functions.* Annual Review of Biochemistry, 1986. **55**(1): p. 987-1035.
15. Van Troys, M., J. Vandekerckhove, and C. Ampe, *Structural modules in actin-binding proteins: towards a new classification.* Biochimica et Biophysica Acta (BBA) - Molecular Cell Research, 1999. **1448**(3): p. 323-348.
16. Dos Remedios, C.G., et al., *Actin Binding Proteins: Regulation of Cytoskeletal Microfilaments.* Physiological Reviews, 2003. **83**(2): p. 433-473.
17. Schrodinger, *The PyMOL Molecular Graphics System, Version 1.8*. 2015.
18. Galkin, V.E., et al., *Remodeling of actin filaments by ADF/cofilin proteins.* Proc Natl Acad Sci U S A, 2011. **108**(51): p. 20568-72.
19. Burtnick, L.D., et al., *Structure of the N-terminal half of gelsolin bound to actin: roles in severing, apoptosis and FAF.* The EMBO Journal, 2004. **23**(14): p. 2713-2722.
20. Schutt, C.E., et al., *The structure of crystalline profilin□[beta]-actin.* Nature, 1993. **365**(6449): p. 810-816.

21. Pfuhl, M., S. Al-Sarayreh, and M. El-Mezgueldi, *The Calponin Regulatory Region Is Intrinsically Unstructured: Novel Insight into Actin-Calponin and Calmodulin-Calponin Interfaces Using NMR Spectroscopy.* Biophysical Journal, 2011. **100**(7): p. 1718-1728.
22. Bramham, J., et al., *Solution Structure of the Calponin CH Domain and Fitting to the 3D-Helical Reconstruction of F-Actin:Calponin.* Structure, 2002. **10**(2): p. 249-258.
23. Ferjani, I., et al., *Two distinct regions of calponin share common binding sites on actin resulting in different modes of calponin-actin interaction.* Biochim Biophys Acta, 2010. **1804**(9): p. 1760-7.
24. Stradal, T., et al., *CH domains revisited.* FEBS Letters, 1998. **431**(2): p. 134-137.
25. Sjöblom, B., J. Ylänne, and K. Djinović-Carugo, *Novel structural insights into F-actin-binding and novel functions of calponin homology domains.* Current Opinion in Structural Biology, 2008. **18**(6): p. 702-708.
26. Moores, C.A., N.H. Keep, and J. Kendrick-Jones, *Structure of the utrophin actin-binding domain bound to F-actin reveals binding by an induced fit mechanism1.* Journal of Molecular Biology, 2000. **297**(2): p. 465-480.
27. Galkin, V.E., et al., *Opening of tandem calponin homology domains regulates their affinity for F-actin.* Nature structural & molecular biology, 2010. **17**(5): p. 614-616.
28. Lodish H, B.A., Zipursky SL, et al., *Myosin: The Actin Motor Protein.* Molecular Cell Biology, 2000. **4th edition**: p. Section 18.3.
29. Geeves, M.A. and K.C. Holmes, *The Molecular Mechanism of Muscle Contraction*, in *Advances in Protein Chemistry*. 2005, Academic Press. p. 161-193.
30. Behrmann, E., et al., *Structure of the Rigor Actin-Tropomyosin-Myosin Complex.* Cell, 2012. **150**(2): p. 327-338.
31. von der Ecken, J., et al., *Structure of the F-actin-tropomyosin complex.* Nature, 2015. **519**(7541): p. 114-117.
32. Lewis, W.G. and L.B. Smillie, *The amino acid sequence of rabbit cardiac tropomyosin.* The Journal of biological chemistry, 1980. **255**(14): p. 6854-6859.
33. Muhlrad, A., et al., *Antagonistic effects of cofilin, beryllium fluoride complex, and phalloidin on subdomain 2 and nucleotide-binding cleft in F-actin.* Biophys J, 2006. **91**(12): p. 4490-9.
34. Cooper, J.A., *Effects of cytochalasin and phalloidin on actin.* The Journal of Cell Biology, 1987. **105**(4): p. 1473-1478.
35. Orbán, J., et al., *Noncooperative Stabilization Effect of Phalloidin on ADP.BeF(x)- and ADP.AlF(4)-Actin Filaments.* Biochemistry, 2008. **47**(15): p. 4530-4534.
36. Sörensen, P.M., et al., *The Natural Product Cucurbitacin E Inhibits Depolymerization of Actin Filaments.* ACS Chemical Biology, 2012. **7**(9): p. 1502-1508.
37. Laing, N.G., et al., *Mutations and Polymorphisms of the Skeletal Muscle α-Actin Gene (ACTA1).* Human mutation, 2009. **30**(9): p. 1267-1277.
38. Sparrow, J.C., et al., *Muscle disease caused by mutations in the skeletal muscle alpha-actin gene (ACTA1).* Neuromuscular Disorders. **13**(7): p. 519-531.
39. Berman, H.M., et al., *The Protein Data Bank.* Nucleic Acids Research, 2000. **28**(1): p. 235-242.
40. Phillips, L., et al., *Actin dynamics studied by solid-state NMR spectroscopy.* European Biophysics Journal, 1991. **19**(3): p. 147-155.

41. Ahmed, M.A., et al., *Induced secondary structure and polymorphism in an intrinsically disordered structural linker of the CNS: solid-state NMR and FTIR spectroscopy of myelin basic protein bound to actin.* Biophys J, 2009. **96**(1): p. 180-91.
42. Klahre, U., et al., *Villin-Like Actin-Binding Proteins Are Expressed Ubiquitously in Arabidopsis.* Plant Physiology, 2000. **122**(1): p. 35-48.
43. Vardar, D., et al., *Villin-type headpiece domains show a wide range of F-actin-binding affinities.* Cell Motility and the Cytoskeleton, 2002. **52**(1): p. 9-21.
44. Vardar, D., et al., *NMR structure of an F-actin-binding "headpiece" motif from villin1.* Journal of Molecular Biology, 1999. **294**(5): p. 1299-1310.
45. Barrientos, T., et al., *Two Novel Members of the ABLIM Protein Family, ABLIM-2 and -3, Associate with STARS and Directly Bind F-actin.* Journal of Biological Chemistry, 2007. **282**(11): p. 8393-8403.
46. Fogl, C., et al., *A structural and functional dissection of the cardiac stress response factor MS1.* Proteins, 2012. **80**(2): p. 398-409.
47. Keeler, J., *Understanding NMR Spectroscopy*. 2010: John Wiley and Sons.
48. Bloembergen, N., E.M. Purcell, and R.V. Pound, *Relaxation Effects in Nuclear Magnetic Resonance Absorption.* Physical Review, 1948. **73**(7): p. 679-712.
49. Anne E. McDermott, T.P., *Solid State NMR Studies of Biopolymers*. 2010: John Wiley and Sons.
50. Levitt, M.H., *Spin Dynamics: Basics of Nuclear Magnetic Resonance*. 2nd ed. 2008: John Wiley and Sons.
51. Duer, M.J., *The Basics of Solid-State NMR*, in *Solid-State NMR Spectroscopy Principles and Applications*. 2007, Blackwell Science Ltd. p. 1-72.
52. Mehring, M., R.G. Griffin, and J.S. Waugh, *19F Shielding Tensors from Coherently Narrowed NMR Powder Spectra.* The Journal of Chemical Physics, 1971. **55**(2): p. 746-755.
53. Mehring, M., *Internal Spin Interactions and Rotations in Solids*, in *eMagRes*. 2007, John Wiley & Sons, Ltd.
54. Gunter Gauglitz, D.S.M., *Handbook of Spectroscopy, 4 Volume Set*. Vol. 3. 2014: John Wiley and Sons.
55. Burum, D.P., *Cross Polarization in Solids*, in *eMagRes*. 2007, John Wiley & Sons, Ltd.
56. G., F. *The Effect of Magic Angle Spinning and High Power 1H Decoupling on 13C Cross Polarization NMR Experiments*. 2009; Available from: http://u-of-o-nmr-facility.blogspot.co.uk/2009/01/effect-of-magic-angle-spinning-and-high.html.
57. Ernst, M., A. Samoson, and B.H. Meier, *Low-power decoupling in fast magic-angle spinning NMR.* Chemical Physics Letters, 2001. **348**(3–4): p. 293-302.
58. Ernst, M., et al., *Low-Power High-Resolution Solid-State NMR of Peptides and Proteins.* Journal of the American Chemical Society, 2004. **126**(15): p. 4764-4765.
59. Conte, P. and A.E. Berns, *Dynamics of Cross Polarization in Solid State Nuclear Magnetic Resonance Experiments of Amorphous and Heterogeneous Natural Organic Substances.* Analytical Sciences, 2008. **24**(9): p. 1183-1188.
60. Baldus, M., et al., *Cross polarization in the tilted frame: assignment and spectral simplification in heteronuclear spin systems.* Molecular Physics, 1998. **95**(6): p. 1197-1207.

61. Zhang, Z., et al., *Dual-band selective double cross polarization for heteronuclear polarization transfer between dilute spins in solid-state MAS NMR.* Journal of magnetic resonance (San Diego, Calif. : 1997), 2012. **217**: p. 92-99.
62. Takegoshi, K., S. Nakamura, and T. Terao, *13C–1H dipolar-assisted rotational resonance in magic-angle spinning NMR.* Chemical Physics Letters, 2001. **344**(5–6): p. 631-637.
63. Higman, V.A. *Protein NMR - A Practical Guide*. 2012 21-11-2012; Available from: http://www.protein-nmr.org.uk/.
64. Levitt, M.H., *Symmetry-Based Pulse Sequences in Magic-Angle Spinning Solid-State NMR*, in *eMagRes*. 2007, John Wiley & Sons, Ltd.
65. Marley, J., M. Lu, and C. Bracken, *A method for efficient isotopic labeling of recombinant proteins.* Journal of Biomolecular NMR, 2001. **20**(1): p. 71-75.
66. Gasteiger E., H.C., Gattiker A., Duvaud S., Wilkins M.R., Appel R.D., Bairoch A., *Protein Identification and Analysis Tools on the ExPASy Server*, in *(In) John M. Walker (ed): The Proteomics Protocols Handbook*, H. Press, Editor. 2005. p. pp. 571-607
67. Pardee, J.D. and J.A. Spudich, *Purification of muscle actin.* Methods Cell Biol., 1982. **24**: p. 271-289.
68. Sorensen, P.M., et al., *The natural product cucurbitacin E inhibits depolymerization of actin filaments.* ACS Chem Biol, 2012. **7**(9): p. 1502-8.
69. Cooper, J.A., S.B. Walker, and T.D. Pollard, *Pyrene actin: documentation of the validity of a sensitive assay for actin polymerization.* Journal of Muscle Research & Cell Motility, 1983. **4**(2): p. 253-262.
70. Criddle, A.H., M.A. Geeves, and T. Jeffries, *The use of actin labelled with N-(1-pyrenyl)iodoacetamide to study the interaction of actin with myosin subfragments and troponin/tropomyosin.* Biochemical Journal, 1985. **232**(2): p. 343-349.
71. Team, R.D.C., *R: A Language and Environment for Statistical Computing*. 2008, R Foundation for Statistical Computing.
72. Taylor, R.E., *Setting up13C CP/MAS experiments.* Concepts in Magnetic Resonance, 2004. **22A**(1): p. 37-49.
73. Zhou, D.H., *Fast Magic Angle Spinning for Protein Solid-State NMR Spectroscopy*, in *eMagRes*. 2007, John Wiley & Sons, Ltd.
74. Hohwy, M., et al., *Fivefold symmetric homonuclear dipolar recoupling in rotating solids: Application to double quantum spectroscopy.* The Journal of Chemical Physics, 1999. **110**(16): p. 7983-7992.
75. Hohwy, M., et al., *Broadband dipolar recoupling in the nuclear magnetic resonance of rotating solids: A compensated C7 pulse sequence.* The Journal of Chemical Physics, 1998. **108**(7): p. 2686-2694.
76. Vranken, W.F., et al., *The CCPN data model for NMR spectroscopy: Development of a software pipeline.* Proteins: Structure, Function, and Bioinformatics, 2005. **59**(4): p. 687-696.
77. *ACD/NMR Processor Academic Edition*. Advance Chemistry Development, Inc.: Toronto, On, Canada.
78. Carlos Cobas, S.D., Nikolay Larin, Isaac Iglesias, Cristina Geada, Felipe Seoane, Maruxa Sordo et Pablo Monj, *MestReNova*, M.R. S.L., Editor. 2015.

79. Lian, L.-Y. and D.A. Middleton, *Labelling approaches for protein structural studies by solution-state and solid-state NMR.* Progress in Nuclear Magnetic Resonance Spectroscopy, 2001. **39**(3): p. 171-190.
80. Higman, V., et al., *Assigning large proteins in the solid state: a MAS NMR resonance assignment strategy using selectively and extensively 13C-labelled proteins.* Journal of Biomolecular NMR, 2009. **44**(4): p. 245-260.
81. Nand, D., et al., *Fractional deuteration applied to biomolecular solid-state NMR spectroscopy.* J Biomol NMR, 2012. **52**(2): p. 91-101.
82. Brown, S.P., *Applications of high-resolution 1H solid-state NMR.* Solid State Nuclear Magnetic Resonance, 2012. **41**(0): p. 1-27.
83. Zech, S.G., A.J. Wand, and A.E. McDermott, *Protein Structure Determination by High-Resolution Solid-State NMR Spectroscopy: Application to Microcrystalline Ubiquitin.* Journal of the American Chemical Society, 2005. **127**(24): p. 8618-8626.
84. Castellani, F., et al., *Structure of a protein determined by solid-state magic-angle-spinning NMR spectroscopy.* Nature, 2002. **420**(6911): p. 98-102.
85. Hong, M. and K. Jakes, *Selective and extensive 13C labeling of a membrane protein for solid-state NMR investigations.* Journal of Biomolecular NMR, 1999. **14**(1): p. 71-74.
86. Hiller, M., et al., *[2,3-13C]-labeling of Aromatic ResiduesGetting a Head Start in the Magic-Angle-Spinning NMR Assignment of Membrane Proteins.* Journal of the American Chemical Society, 2008. **130**(2): p. 408-409.
87. Tanio, M., et al., *Amino acid-selective isotope labeling of proteins for nuclear magnetic resonance study: Proteins secreted by Brevibacillus choshinensis.* Analytical Biochemistry, 2009. **386**(2): p. 156-160.
88. O'Grady, C., et al., *One-step amino acid selective isotope labeling of proteins in prototrophic Escherichia coli strains.* Analytical Biochemistry, 2012. **426**(2): p. 126-128.
89. Visegrady, B., et al., *The effect of phalloidin and jasplakinolide on the flexibility and thermal stability of actin filaments.* FEBS Lett, 2004. **565**(1-3): p. 163-6.
90. Bertini, I., et al., *Solid-state NMR of proteins sedimented by ultracentrifugation.* Proc Natl Acad Sci U S A, 2011. **108**(26): p. 10396-9.
91. Pinheiro, T.J.T. and A. Watts, *Lipid Specificity in the Interaction of Cytochrome c with Anionic Phospholipid Bilayers Revealed by Solid-State 31P NMR.* Biochemistry, 1994. **33**(9): p. 2451-2458.
92. Toke, O., et al., *Secondary Structure and Lipid Contact of a Peptide Antibiotic in Phospholipid Bilayers by REDOR.* Biophysical Journal, 2004. **87**(1): p. 662-674.
93. Potrzebowski, M.J., et al., *Distance measurements in disodium ATP hydrates by means of 31P double quantum two-dimensional solid-state NMR spectroscopy.* J Magn Reson, 2006. **179**(2): p. 173-81.
94. Larkin, M.A., et al., *Clustal W and Clustal X version 2.0.* Bioinformatics, 2007. **23**(21): p. 2947-2948.
95. Wüthrich, K., *Protein structure determination in solution by NMR spectroscopy.* Journal of Biological Chemistry, 1990. **265**(36): p. 22059-62.
96. Oktaviani, N.A., et al., *100% complete assignment of non-labile (1)H, (13)C, and (15)N signals for calcium-loaded Calbindin D(9k) P43G.* Biomol NMR Assign, 2011. **5**(1): p. 79-84.

97. Bertani, P., J. Raya, and B. Bechinger, *15N chemical shift referencing in solid state NMR.* Solid State Nuclear Magnetic Resonance, 2014. **61–62**: p. 15-18.
98. Schanda, P., *Solid-state NMR studies of protein dynamics: New approaches and applications to crystalline proteins and large molecular assemblies.* Life Sciences [q-bio], 2015.
99. Meng, J., et al., *High-Resolution Crystal Structures of Villin Headpiece and Mutants with Reduced F-Actin Binding Activity†,‡.* Biochemistry, 2005. **44**(36): p. 11963-11973.
100. Liu, Y., et al., *Variation in proton affinity of the guanidino group between free and blocked arginine.* Amino Acids, 2007. **33**(1): p. 145-50.
101. Werbeck, N.D., J. Kirkpatrick, and D.F. Hansen, *Probing Arginine Side-Chains and Their Dynamics with Carbon-Detected NMR Spectroscopy: Application to the 42 kDa Human Histone Deacetylase 8 at High pH.* Angewandte Chemie International Edition, 2013. **52**(11): p. 3145-3147.
102. Clore, G.M. and J. Iwahara, *Theory, practice, and applications of paramagnetic relaxation enhancement for the characterization of transient low-population states of biological macromolecules and their complexes.* Chem Rev, 2009. **109**(9): p. 4108-39.
103. Koehler, J. and J. Meiler, *Expanding the utility of NMR restraints with paramagnetic compounds: Background and practical aspects.* Progress in Nuclear Magnetic Resonance Spectroscopy, 2011. **59**(4): p. 360-389.
104. Knight, M.J., et al., *Magic Angle Spinning NMR of Paramagnetic Proteins.* Accounts of Chemical Research, 2013. **46**(9): p. 2108-2116.
105. Constantine, K.L., *Evaluation of Site-Directed Spin Labeling for Characterizing Protein-Ligand Complexes Using Simulated Restraints.* Biophysical Journal, 2001. **81**(3): p. 1275-1284.
106. Keizers, P.H.J. and M. Ubbink, *Paramagnetic tagging for protein structure and dynamics analysis.* Progress in Nuclear Magnetic Resonance Spectroscopy, 2011. **58**(1–2): p. 88-96.
107. Jaroniec, C.P., *Solid-state nuclear magnetic resonance structural studies of proteins using paramagnetic probes.* Solid State Nuclear Magnetic Resonance, 2012. **43–44**: p. 1-13.
108. Sengupta, I., P.S. Nadaud, and C.P. Jaroniec, *Protein Structure Determination with Paramagnetic Solid-State NMR Spectroscopy.* Accounts of Chemical Research, 2013. **46**(9): p. 2117-2126.
109. Zhu, K., et al., *Docking Covalent Inhibitors: A Parameter Free Approach To Pose Prediction and Scoring.* Journal of Chemical Information and Modeling, 2014. **54**(7): p. 1932-1940.
110. Cregg, J., *Introduction*, in *Pichia Protocols*, J. Cregg, Editor. 2007, Humana Press. p. 1-10.
111. De Schutter, K., et al., *Genome sequence of the recombinant protein production host Pichia pastoris.* Nat Biotech, 2009. **27**(6): p. 561-566.
112. Zhang, W., M. Inan, and M. Meagher, *Fermentation strategies for recombinant protein expression in the methylotrophic yeastPichia pastoris.* Biotechnology and Bioprocess Engineering, 2000. **5**(4): p. 275-287.
113. Macauley-Patrick, S., et al., *Heterologous protein production using the Pichia pastoris expression system.* Yeast, 2005. **22**(4): p. 249-270.

114. Cregg, J., et al., *Recombinant protein expression in Pichia pastoris.* Molecular Biotechnology, 2000. **16**(1): p. 23-52.
115. Perrin, B.J. and J.M. Ervasti, *The Actin Gene Family: Function Follows Isoform.* Cytoskeleton (Hoboken, N.j.), 2010. **67**(10): p. 630-634.
116. Cregg, J.M., et al., *Pichia pastoris as a host system for transformations.* Molecular and Cellular Biology, 1985. **5**(12): p. 3376-3385.
117. Clark, L., et al., *Methyl labeling and TROSY NMR spectroscopy of proteins expressed in the eukaryote Pichia pastoris.* Journal of Biomolecular NMR, 2015. **62**(3): p. 239-245.
118. Purcell, E.M., H.C. Torrey, and R.V. Pound, *Resonance Absorption by Nuclear Magnetic Moments in a Solid.* Physical Review, 1946. **69**(1-2): p. 37-38.
119. Guex, N. and M.C. Peitsch, *SWISS-MODEL and the Swiss-Pdb Viewer: An environment for comparative protein modeling.* ELECTROPHORESIS, 1997. **18**(15): p. 2714-2723.
120. Hampton, C.M., et al., *The 3D Structure of Villin as an Unusual F-Actin Crosslinker.* Structure. **16**(12): p. 1882-1891.
121. Grazi, E., *54Mn2+ as a tracer of the polymerization of actin. Intermediate oligomers condense to give F-actin.* Biochemical Journal, 1984. **223**(3): p. 571-576.
122. Jagannadham, A.V. and P. Venkateswarlu, *Electron paramagnetic resonance of Mn2+ in NaF single crystals.* Proceedings of the Indian Academy of Sciences - Section A, 1969. **69**(2): p. 67-77.